Synthesis, Characterisation and Photocatalytic Activity of Porous Silicon-based Materials

Ting Li

A thesis submitted in fulfilment of the requirements for the degree of Doctor of Philosophy of the University of East Anglia.

School of Chemistry

University of East Anglia

Norwich, United Kingdom

September 2017

Declaration

I declare that the research contained in the thesis, submitted for the degree of Doctor of Philosophy, is original, except where due reference is made to other authors, and has not previously been submitted by me for a degree at this or any other universities.

Ting Li

Abstract

As a free and abundant alternative energy source, the use of sunlight to store and transfer energy is of great importance to a clean and sustainable future. Aiming for an environmentally and economically friendly approach to utilizing solar energy, metal-free, earth-abundant mesoporous silicon with hydrogen termination were developed via inexpensive electrochemical etching. By means of a range of characterisation tools, a detailed structural analysis was established, showing a large surface area, open porous system and abundant quantum confined Si nanocrystallites of which the morphological properties can be controllably tuned through adjusting etching parameters and wafer resistivity. As a result, an excellent efficiency in degrading methyl orange under visible light irradiation was achieved in the following photocatalytic study, which also revealed the influence of different structural factors on the photocatalytic performance by affecting mass transport, light absorption and photoexcited charge recombination. The photocatalytic mechanism of mesoporous silicon in methyl orange degradation was also investigated in this research, with insights gained into the electronic band properties, photocatalytic oxidation facilitated by the generation of reactive oxygen species and the roles of surface hydrides on the degradation pathways of methyl orange. By coupling with graphitic carbon nitride (g-C_3N_4) nanosheets, the formed heterostructure showed an enhanced degradation activity towards methyl orange under visible light illumination. An exciton-related pathway was proposed to explain the promoted reducing power of the surface hydrides upon irradiation with or without the participation of g-C_3N_4. In general, this work highlighted the potentiality of H-terminated mesoporous silicon in photocatalytic applications and deepened the understanding of its photocatalytic mechanism and degradation behaviour for future exploration of porous silicon-based photocatalysts.

Table of Contents

Chapter 2: Materials and Experimental Details

Chapter 3: Controllable Generation of Mesoporous Silicon with Large Surface Area by Electrochemical Etching

List of Schemes

List of Tables

List of Figures

List of Abbreviations

1D	One Dimensional
2D	Two Dimensional
3D	Three Dimensional
ATR	Attenuated Total Reflectance
BEs	Binding Energies
BET	Brunauer–Emmett–Teller theory
BJH	Barrett-Joyner-Halenda approach
C/N	Carbon/nitrogen ratio
CB	Conduction Band
CO_2	Carbon dioxide
COFs	Covalent Organic Frameworks
DCM	Dichloromethane
DMPD	Dimethyl-4-phenylenediamine
DOS	Density of States
DSC	Differential Scanning Calorimetry
e^-	Electron carriers
E_{CB}	Conduction band potential
EDX	Energy Dispersive X-ray
E_g	Bandgap energy
EM	Electron Microscopy
E_m	Emission wavelength
eV	Electron Volt
E_{VB}	Valence band potential
E_x	Excitation wavelength
F^-	Fluoride ion
FE-SEM	Field Emission Scanning Electron Microscopy
FTIR	Fourier Transform Infrared Spectroscopy
g-C_3N_4	Graphitic carbon nitride
h^+	Hole carriers
H_2O_2	Hydrogen peroxide
HF	Hydrofluoric acid
HPS	Boron-doped p-type Si (0.001-0.01 Ω·cm)
HRTEM	High-Resolution Transmission Electron Microscope
H-terminated	Hydrogen-terminated
IR	Infrared Spectroscopy
IUPAC	International Union of Pure and Applied Chemistry
I-V	Current-Voltage
J	Etching current density
J_{ps}	Electropolishing critical value
k	Reaction rate constant

KOH	Potassium hydroxide
LN	Liquid nitrogen
m/z	Mass-to-charge ratio
MACE	Metal-Assisted Chemical Etching
Mg	Magnesium
MO	Methyl orange ($C_{14}H_{14}N_3NaO_3S$)
MOFs	Metal-Organic Frameworks
mpSi	Mesoporous silicon
MW	Molecular Weight
NSs	Nanosheets
NHE	Normal Hydrogen Electrode
NWs	Nanowires
$O_2^{\cdot -}$	Superoxide radical anion
·OH	Hydroxyl radical
$^1O_2$	Singlet oxygen
p/p_0	Relative pressure
PL	Photoluminescence Spectroscopy
PS	Boron-doped p-type Si (1-10 Ω·cm)
pSi	Porous silicon
PSZ	Pore Size Distribution
PTFE	Polytetrafluoroethylene
QCE	Quantum Confinement Effect
QDs	Quantum Dots
QY	Quantum yield (ϕ_F)
ROSs	Reactive Oxygen Species
SiO_2	Silicon oxides
SAED	Selected Area Diffraction
SEM	Scanning Electron Microscopy
Si	Silicon
SiH	Silicon monohydride
SiH_2	Silicon dihydride
SiH_3	Silicon trihydride
SiH_x (x = 1, 2, 3)	Silicon hydrides
SSA	Specific surface area
t	Etching time
TEM	Transmission Electron Microscopy
TEOA	Triethanolamine
TGA	Thermogravimetric Analysis
TOC	Total Organic Carbon
UV-Vis	Ultraviolet-Visible Absorption Spectroscopy
VB	Valence Band
XPS	X-ray Photoelectron Spectroscopy
XRD	X-ray Diffraction
η	Decomposition efficiency

Acknowledgements

I would like to express my very great appreciation to my supervisory team at UEA, especially my principal supervisor, Dr Yimin Chao for giving me this great opportunity to challenge and improve myself, for his valuable and constructive suggestions during the planning and development of this research work, and for his rich personal experiences and sincere life advices unreservedly shared with me that have enlightened me in numerous ways. The willingness of him and his wife to give their time so generously has been very much appreciated. My thanks also extends to my secondary supervisor, Prof Andy Cammidge for his kindness to listen and to guide. His priceless advice has been a great help in every aspect of this work and this thesis.

I also would like to offer my special thanks to Prof Gregory Wildgoose, Dr Andrew Mayes in Chemistry department, Dr Sheng Qi from School of Pharmacy, Dr Congxiao Shang from School of Environmental Sciences who so generously provided me with various instruments in their labs for sample preparation and characterisation included in this work.

I am immensely thankful to John Brindle and Bertrand Leze from School of Environmental Sciences for their technical help and much appreciated contribution to the data collection in this thesis.

I am also particularly grateful to Prof Hualong Xu from Fudan University who I have always aspired to be since I was an undergraduate, for his patient guidance, enthusiastic encouragement and useful critiques of this research work. And Jun Li, Qiang Zhang from King Abdullah University of Science and Technology for their contribution to the data collection as well.

To my lovely colleagues, Dr Qi Wang, Dr Shane Ashby, Dr Jayshree Ahire, Dr Mehrnaz Behray, Ruoxi Liu, Tiezheng Bian, Ashley Marsh, Chenghao Yue, I would like to express my sincere gratitude for their passionate spirit and open-mindedness, for their helpfulness and considerate thoughts, and for sharing the big and small life moments together.

To my dearest family and friends, especially my parents, Ying He and Anluo Li, for everything, for their love and care, for their support and encouragement, for their belief and trust, for their patience and sacrifice so that I can follow my own heart, for always being there and all in all for being my mum and dad. I could not thank them enough and I will never be.

Lastly, I would like to thank UEA deeply for the International Student Scholarship that had supported me all through my PhD study.

Chapter 1

Introduction

Abstract

Porous materials are first described in three fundamental categories: micro-, meso- and macro-porous. Various aspects of porous silicon are overviewed including the general knowledge, discovery history, fabrication strategies, modifiable properties and various applications in catalysis, bio-related and energy storage fields. The history, polymer structure, synthesis and photocatalytic applications of graphitic carbon nitride (g-C_3N_4) are also reviewed. The condition of water pollution and currently available solutions are discussed. Given this, the objectives of this research and thesis structure are outlined.

1.1 Porous solids

Porous solids are materials consisting of an amorphous or crystalline framework with void spaces, e.g. cavities, channels or interstices. Porous materials of varying structural features and chemical characteristics are of fundamental importance in the areas of science and technology. Many natural substances such as rocks and soil, biological tissues (diatom, butterfly, leaf etc.) as shown in Figure 1.1 can be considered as porous media that have shaped the world around us with their distinctive porous structures and functionalities.

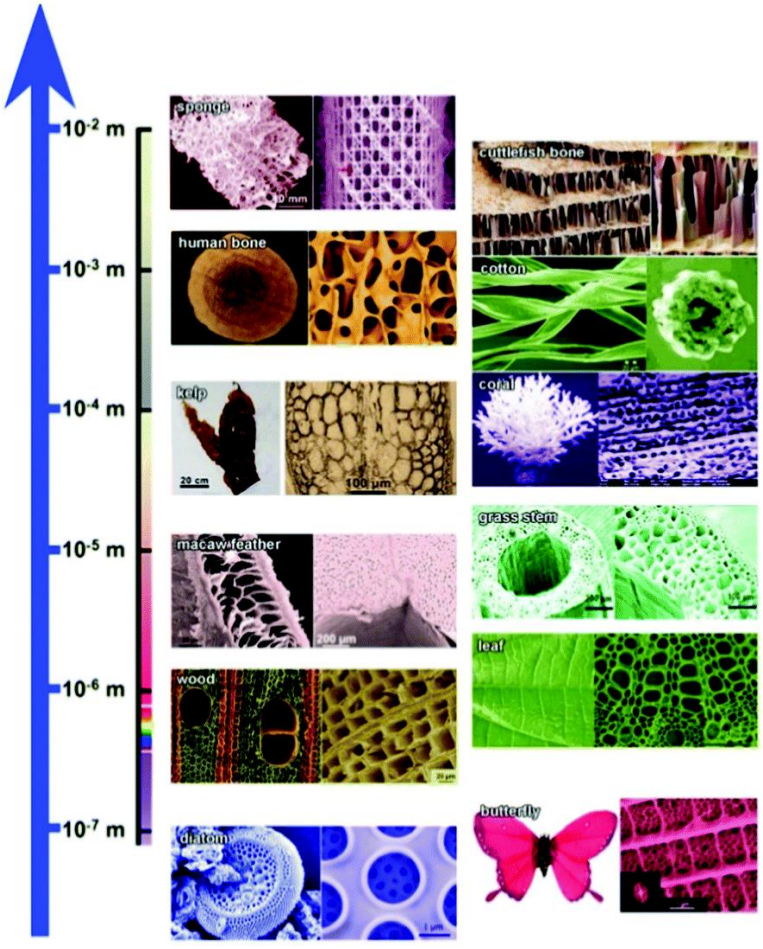

Figure 1.1 Overview of natural porous materials, placed alongside the length scale according to their critical dimensions. The SEM or OM images of original biological porous structures are shown from bottom to up: diatom, butterfly, wood, leaf, macaw feather, grass stem, kelp, coral, cotton, human bone, cuttlefish bone, and sponge. Reprinted with permission from ref. [1]. Copyright 2011, Wiley-VCH.

Inspired by the delicate morphologies of natural substances and their various levels of hierarchies, a broad class of artificial organic/inorganic porous materials with various functionalities (acidic, basic, oxidative, reductive, inert, conducting, semiconducting etc.) are discovered and applied in a variety of fields, ranging from separation to catalysis and from energy to life sciences.[2] By controlling the size of the pore below 100 nm, the formed porous material also referred to as nanoporous material has drawn extensive research interests from almost every aspect of the scientific community, carrying the hope of leading to the next breakthrough of human intelligence and technological revolution. Rationally designing the efficient structure of nanomaterial relative to its application is challenging but also greatly rewarding. As physics, computing science and engineering markedly advance, chemistry remains a central part of this historical nanomaterial-era.

According to the length scale of pore dimensions, nanoporous materials are classified into three categories: materials containing pores with diameter less than 2 nm are called microporous material, materials with pores between 2-50 nm are typically termed mesoporous material, and materials with pores greater than 50 nm are called macroporous material.[3] The characteristics of a porous material depend on not only its chemical composition and crystal structure, but also are defined by the structural morphology as illustrated in the discussion below.

1.1.1 Microporous materials

Microporous materials, such as zeolites, carbons, amorphous glasses, metal-organic frameworks (MOFs), covalent organic frameworks (COFs) have caught widespread attention owing to their practical and potential uses in catalysis, separation, gas storage, sensing and biological applications. For example, zeolites have been widely used in oil-refining industries as catalysts since the late 1950s.[4-5] Zeolites are crystalline aluminosilicates with three-dimensional microporous structures. One of the defining features of zeolites is the inherent shape selectivity by its long diffusion channel system in molecular dimension (typically 2-8 Å).[6] The shape selectivity has this remarkable “molecular sieving” effect, which only permits the molecules that fit inside

the pores to be exclusively processed by the active sites located on the internal surface, as shown in Figure 1.2. One of the most famous examples is the shape-selective xylene isomerization catalysed by HZSM-5 zeolite, which strongly favours the production and outward diffusion of p-xylene, the isomer with the smallest dimension.[7]

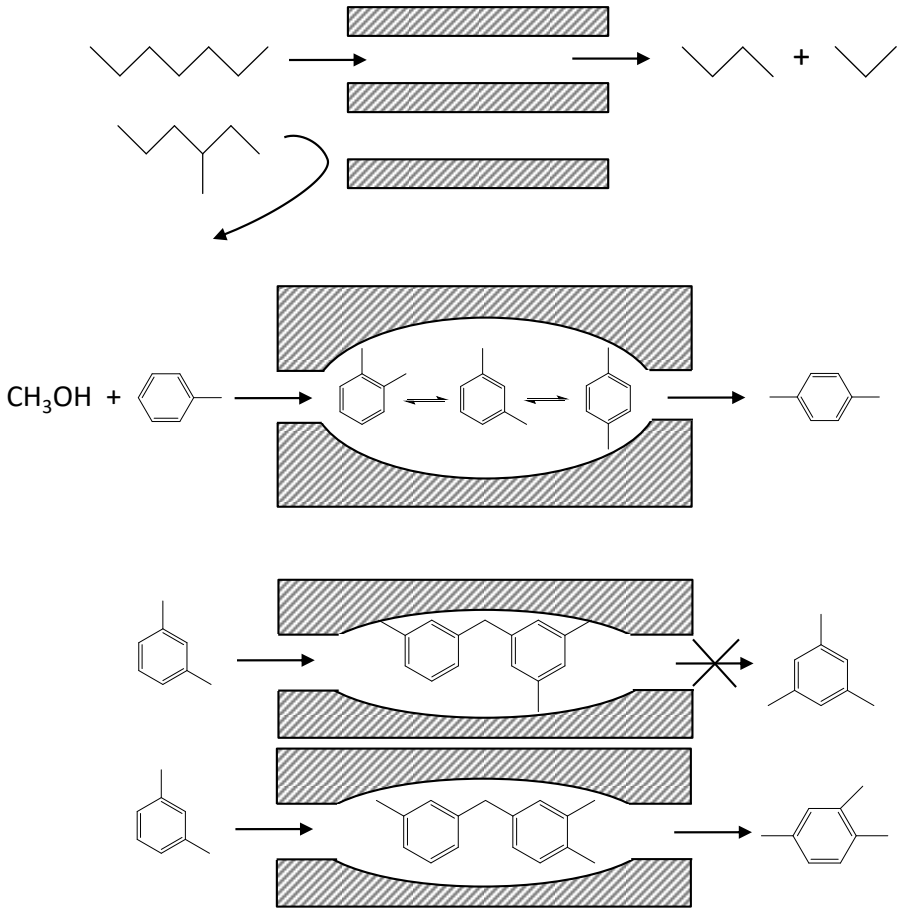

Figure 1.2 Unique shape selectivity imposed by zeolite structure.

However, the intrinsic micropore system of conventional zeolites could also serve as the material's weakness as well as the strength for allowing shape selectivity. It imposes a severe diffusion barrier and hence extremely limits their applications and efficacy in liquid phase reactions due to the restricted space inside the pores where most active sites reside. Different strategies have been developed to increase the surface availability while retaining its vital functionality. For example, by largely

reducing the crystal size to nanometre scale, more active sites are relocated on the external surface becoming accessible to bulky substrates that are unlikely to enter the micropores due to their molecular size.[8] By introducing additional porosity in the mesopore size region (2–50 nm), a hierarchical structure can be constructed in the zeolite matrix which is a promising route for effectively enhancing the mass transport inside the porous network and largely improving their values in technological applications.[9-10]

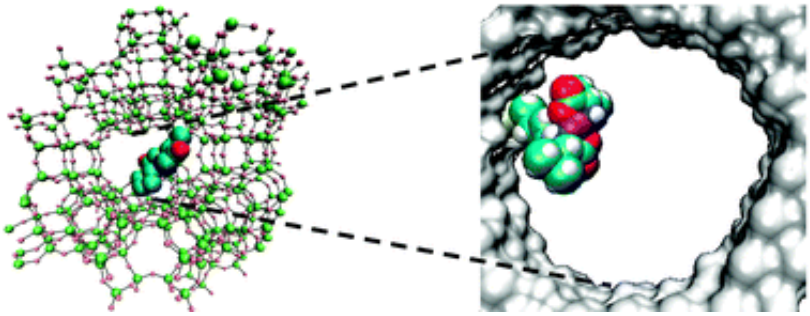

Figure 1.3 Schematic diagram of the accessibility of micropore and mesopore. Reprinted with permission from ref. [11]. Copyright 2011, Royal Society of Chemistry.

1.1.2 Mesoporous materials

As one of the most important branches of porous materials, mesoporous materials are well acknowledged for the significantly improved molecular mobility in the porous structure over conventional microporous materials. Outstanding progress has been made in the development of mesoporous materials of which the chemical varieties have been extensively enriched over the years.[12] A wide class of substances including silica, alumina, transitional metal compounds (e.g. oxides, sulfides, nitrides, and phosphates), carbon, silicon, organic polymer etc. have been sufficiently explored.[13-15] Their signature structural features such as high surface-to-volume ratio, wide range of mesoscale pore dimension, high accessibility, released diffusion limitation, and high storage capacity effectively promote their applications in various fields such as catalysis, immobilization, adsorption, separation, sensors, energy and life sciences that

were once vastly dominated by the microporous counterparts. For example, the large surface area of ordered mesoporous silica (OMS) that is often recognized as one of the most exciting discoveries in material synthesis[9], is largely exploited in supporting functional nano-species such as metal nanoparticles used in heterogeneous catalysis and bio-active molecules e.g. enzymes, drugs in biological applications.

1.1.3 Macroporous materials

Although above-mentioned mesoporous materials are very capable of providing easier access with lower resistance for guest species, in viscous systems or in the presence of very large molecules, very slow diffusion rate could still be resulted. Thus, macroporous material with large pore size often in the range of 50 nm - 1.5 µm is very useful in resolving the transport limitation. Besides, macroporous materials also possess unique physicochemical properties. For example, their very large pore diameter comparable to the visible light wavelength can effectively reinforce the light harvesting efficiency through light scattering effect, making them ideal candidates for photoelectrical applications, including dye-sensitized solar cells (DSSCs), photoelectrochemical (PEC) cells, photocatalysis etc.[16] Meanwhile, macroporous materials are also well known for their mechanical robustness and good thermal, chemical stabilities. However, a significant setback induced by the hollow structure and large inner voids is the inherent low interface area owned by macroporous materials, profoundly limiting their efficiency in various applications.[17-20] Many efforts have thus been made in increasing the specific surface area of macroporous structures by growing secondary building blocks onto the macroporous framework, such as low dimensional nanoparticles, nanowires, nanorods, etc.[21-22]

1.1.4 Hierarchically structured porous materials

Materials with hierarchical porous structures, whose pores exist on different length scales from micro to meso to macro, have been explored to improve the efficiency of conventional micro-/meso-/macroporous materials.[10] By integrating the morphological advantages on different micro-, meso- and macroscopic levels, the hierarchically porous materials would offer a desirable combination of high internal surface areas and convenient molecular transport.[23] Therefore, it is expected to propel the development of functional porous materials with remarkable properties for a wide variety of emerging applications.[24] However, the ability to engineer the hierarchy, morphology and chemical composition of the porous materials at different length scales is still very limited and insufficiently reproducible. As a result, simple porous systems are still largely relied on in practical applications and mechanistic studies. Through investigating the relationship between synthesis/processing, structure/composition, and properties, the performance of nanoporous materials can be optimized.

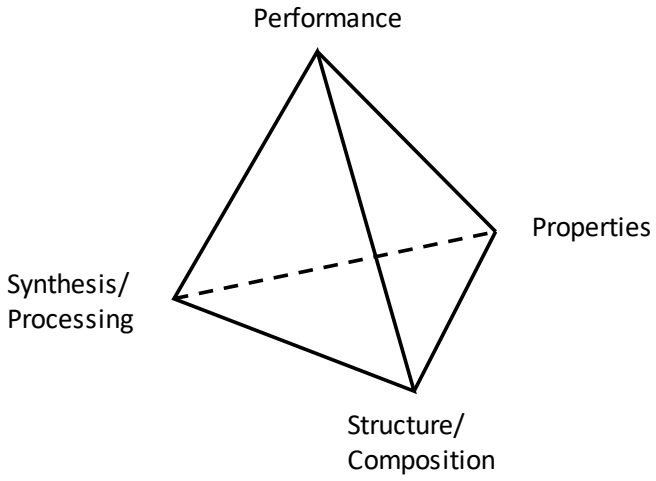

Figure 1.4 The interrelationship among synthesis/processing, structure/composition, properties, and performance.

1.2 Porous silicon

1.2.1 Background of porous silicon

Silicon (Si) was discovered by Jöns Jacob Berzelius, a Swedish chemist, in 1824 by heating chips of potassium in a silica container and then carefully washing away the residual by-products. The origin of the name is from the Latin “silex” or “silicis” which means flint. Silicon is the seventh most abundant element in the universe and the second most abundant element in the Earth’s crust, constituting 27.7% of the Earth’s crust by mass, which is only second to oxygen. The natural forms of Si are principally found as silicon oxides (SiO_2) or silicates in various minerals such as sand, rock, flint, clay and in photosynthesising algae called diatoms. Alongside the daily uses of Si-containing glass and silicon rubber etc., Si is also the material foundation of solid-state electronic devices, marking crystalline Si as the most commonly used semiconductor by far. Pure crystalline Si has a diamond cubic crystal structure of which the unit cell is displayed in Figure 1.5. Every Si atom within the crystal lattice has four nearest neighboring atoms. The length of Si-Si covalent bond is 2.35 Å and the strength is 226 $kJ \cdot mol^{-1}$.[25] The lattice constant (a) is 5.431 Å.

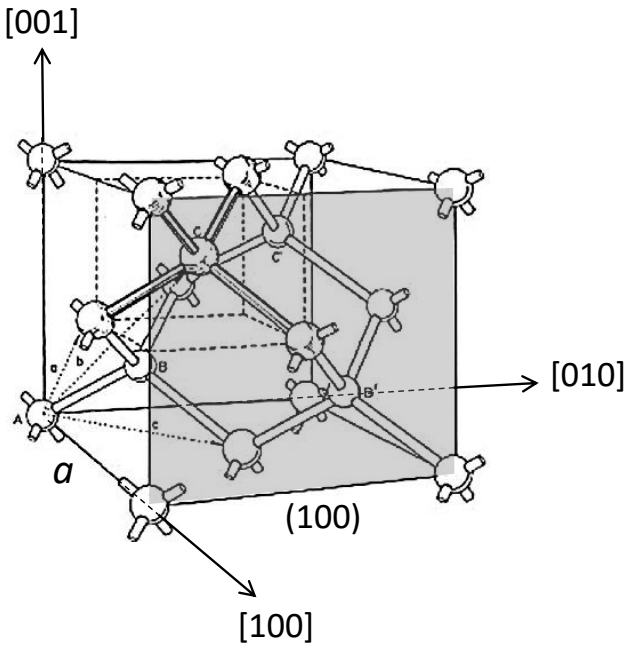

Figure 1.5 The diamond cubic crystal structure of Si.

Porous silicon (pSi) is a form of solid silicon that contains small channels connecting to the surface and running within the matrix. It has become one of the most popular porous materials available to date because of its outstanding and unique set of physiochemical properties. According to IUPAC recommendations, it can be classified as microporous silicon (< 2 nm), mesoporous silicon (2-50 nm) and classical macroporous silicon (> 50 nm) based on the length scale of pore dimension.[26] Although in the pSi literature these terms have often been loosely applied to pSi as opposed to the strict criteria used in describing porous carbon, silica mentioned in 1.1.

Together with one-dimensional Si nanowires (Si NWs) and zero-dimensional Si nanoparticles or quantum dots (QDs), silicon nanostructures have become a research hot point in recent years known as the most important semiconductor materials. Fundamental properties, such as environmental benignity, earth abundancy, cost-competitiveness, non-toxicity, and bio-degradability significantly promote the development of porous silicon and other nanostructured Si materials in optoelectronics, sensing, energy storage and bio-medical applications in which many other characteristics also play an important part, such as size-dependent optical properties, sensibility, compatibility with the existing microelectronic industry and convenient surface chemistry.

1.2.2 Outline history of porous silicon

Porous silicon was accidentally discovered by the Uhlirs at Bell Labs, USA in the mid-1950s when carrying out electropolishing experiments.[27] Instead of a shiny smooth surface as expected, they observed the generation of hydrogen gas in the HF-based solution and the etched surface developed “a matte black, brown or red deposit”, as shown in Figure 1.6. However, presuming this was silicon oxide, the interesting finding was just reported as a technical note without further investigation at that time. It was not until 1970s and 1980s, porous silicon became a material of interest as the high surface area was used as a model in spectroscopic studies of crystalline silicon surface and as a precursor to generate thick oxide layers on silicon.

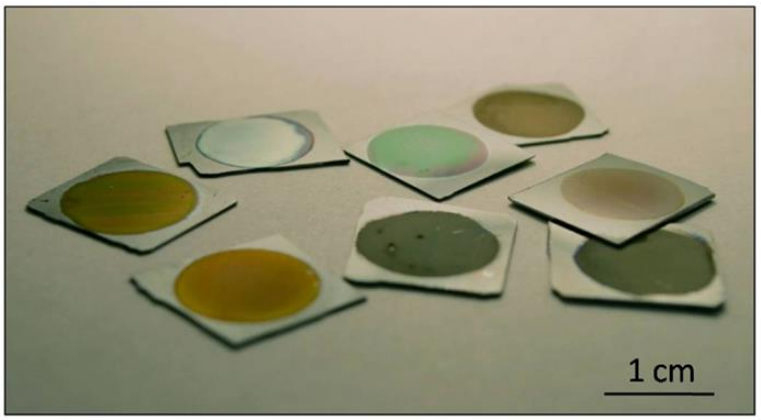

Figure 1.6 Image of various pSi samples prepared at different etching conditions. Reprinted with permission from ref. [32]. Copyright, 2015. Hernández-Montelongo, Muñoz-Noval, García-Ruíz, Torres-Costa, Martín-Palma and Manso-Silván.

The interest exploded after the landmark discovery made by Canham, Gösele and Lehmann in the early 1990s when they observed the bright red-orange photoluminescence at room temperature from silicon nanoparticles embedded within the porous structure,[29-30] leading to intensive focus on creating porous silicon-based optoelectronics. However, the progress was not very impressive because of the low electroluminescence efficiency.[31-32]

In 1999, laser adsorption/ionization on pSi was first observed, implying its possible application in mass spectrometry.[33] In 2001, the ability of photoexcited pSi to generate singlet oxygen in solution was discovered, which makes it a good photosensitizer and promising candidate for cancer theranostics.[34] More recently, remarkable progress in exploiting pSi as metal nanoparticles substrate used in surface enhanced Raman spectroscopy (SERS),[35-38] as photonic crystal sensor,[39-41] as photoactive material in converting solar energy,[42-50] as anodic material for rechargeable Lithium-ion battery,[51-56] as bio-imaging agent and drug delivery vehicle[57-61] have been achieved by worldwide studies, which have significantly promoted the application of porous silicon in many other areas and also inspired the work of ours.

1.2.3 Fabrication of porous silicon

A variety of preparation methods have been developed to fabricate porous silicon with diverse morphologies and surface topographies, which can be divided into two main categories, known as top-down and bottom-up approaches.

Top–down approaches include various etching-based methods with the use of a homogeneous, macroscopic Si precursor, such as single-crystalline Si wafer that is often employed in an electrochemical etching method, notably the most popular method for Si porosification.[62] Using a combination of lithography, deposition and etching steps, a number of alternative top-down methods have also been developed which include stain etching,[63] metal-assisted chemical etching (MACE),[64-66] reactive ion etching (RIE),[67] and laser ablation.[68] Among them, the MACE method is widely employed for its simplicity and controllability in preparing pSi and more often Si NWs.

Alternatively, porous silicon can also be generated through various bottom-up approaches such as thermal annealing,[69] magnesiothermic reduction,[51, 70-71] magnetron sputtering,[72] and ion implantation.[73] In contrast to the top-down routes that use sculpting or etching to carve structures from a large piece of Si material, bottom-up methods are usually template-assisted and grow the porous structure from Si atoms and Si-based molecules (e.g. silica, silane, silicon halides) in an additive manner. For example, by varying the microscopic structure of silica template, pSi with well-controlled 3D morphology can be readily synthesised through the shape-preserving magnesiothermic reduction method.

1.2.3.1 Electrochemical etching

Among all the preparation methods, electrochemical etching is the most popular for pSi preparation. It is simple, low-cost, versatile, therefore applied successfully across physics, chemistry, engineering and material sciences.[74] As a classic top-down method, pSi with wide ranges of morphologies and porosities can be reproducibly attained by anodic etching Si crystal in hydrofluoric acid (HF) containing electrolyte solution in electrochemical cell under an external bias voltage.

Normally, silicon does not dissolve but if an external current flows through the system, electrochemical etching will occur. This means that a specific chemical redox reaction occurs at the Si/solution interface the nature of which is fundamental to the electrochemical formation of pSi. Figure 1.7 shows the typical current-voltage (*I–V*) curve for Si in aqueous HF. Although the exact *I*, *V* values vary upon the Si wafer properties and electrolyte concentration, the main shape of the curve remains consistent. At high anodic overpotentials, the Si surface is subject to electropolishing and retains a smooth and planar morphology. In contrast, under low anodic polarization, channels that penetrate deeply into the solid crystal dominate the surface morphology.[32, 75] From the initial exponential rise of the *I-V* curve to the first small peak which is known as electropolishing current (J_{ps}), lies the formation regime for pSi.

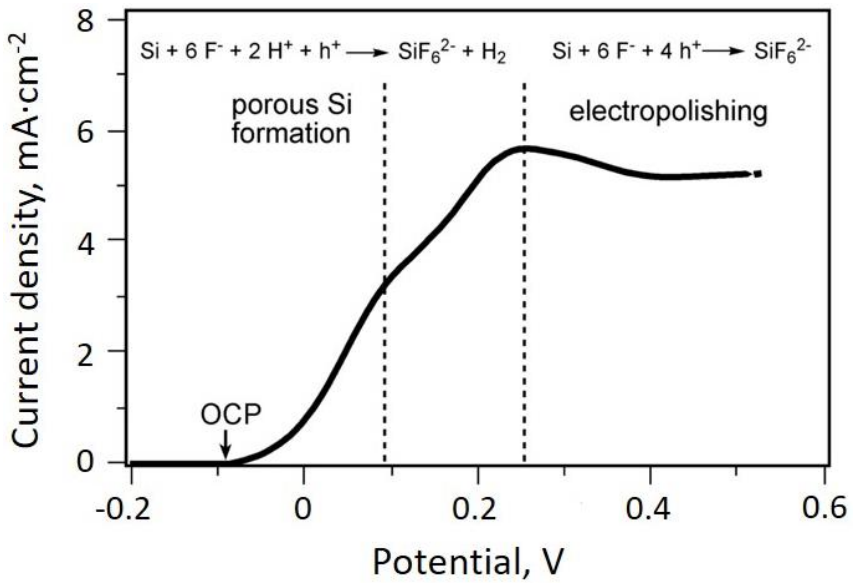

Figure 1.7 Characteristic *I–V* curve for moderately doped p-type silicon in 1% HF electrolyte. Reprinted with permission from ref. [76]. Copyright 2012, Wiley-VCH.

During pSi formation, two electrons per dissolved Si atom participate in the interfacial charge transfer, while the remaining two of the total four available electrons undergo a corrosive hydrogen generation. The occurring anodic semi-reaction during pSi formation is shown below (Equation 1.1).

$$Si + 6HF \longrightarrow H_2SiF_6 + H_2 + 2H^+ + 2e^- \qquad \text{Equation 1.1}$$

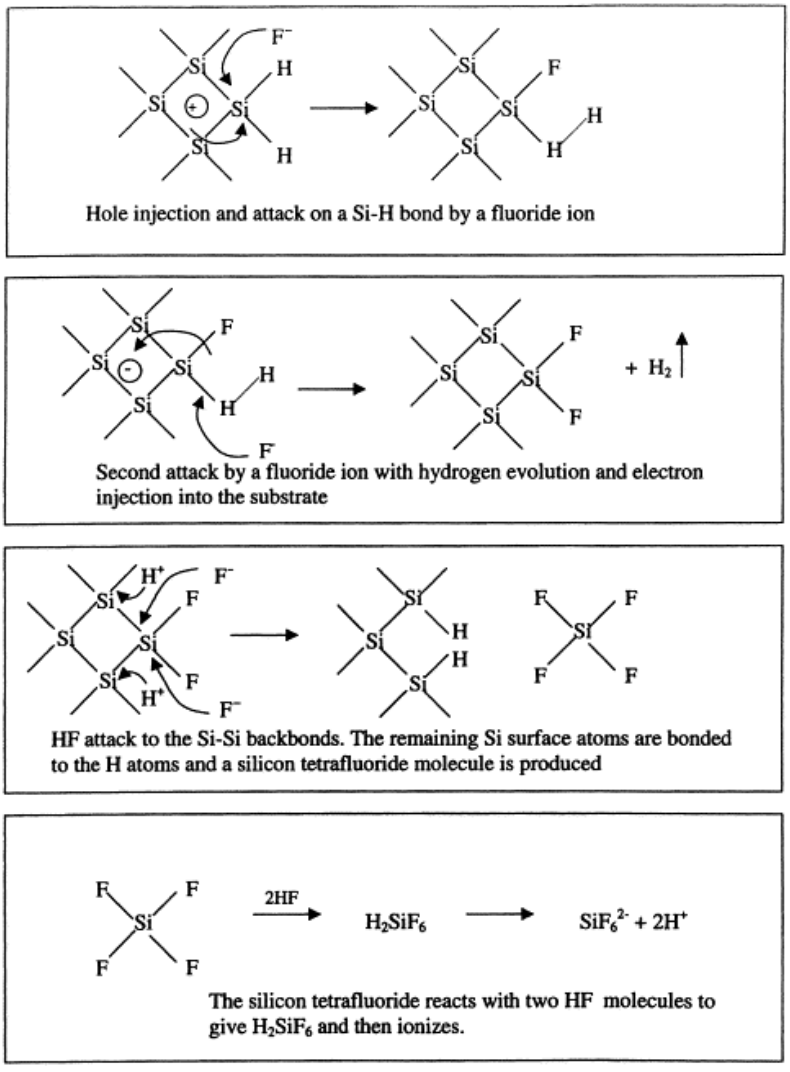

Figure 1.8 Silicon dissolution scheme proposed by Lehmann and Gösele. Reprinted with permission from ref. [77]. Copyright 2000, Elsevier Science B.V.

This two-electron electrochemical reaction and the resulting silicon surface change were further explained in the dissolution mechanism proposed by Lehmann and Gösele, which is so far the most accepted (Figure 1.8).[30] The oxidizing equivalents that

start the electrochemical dissolution and pore formation are valence band holes (h^+), driven to the surface by the applied electric field and by charge diffusion. The migration of charge carriers is preferentially directed towards the pore bottoms because of the enhanced electric field at pore tips that have the smallest radius of curvature. Once a hole makes it to a surface Si atom, the atom is susceptible to attack by nucleophilic F^- in the solution. As a result, pore walls which are sufficiently distant from the tips are largely passivated, therefore pores are generated in the silicon crystal and propagate through time.[76]

In summary, the supply of valence band holes at the surface, the presence of active pore tips, and the external current density which should be lower than the electropolishing critical value (J_{ps}) are the basic requirements to be fulfilled for the occurrence of electrochemical pore formation.[78] By altering anodization conditions, the structural features of pSi are adjustable with relative ease.[74] Meanwhile, the properties of initial Si wafer subjected to electrochemical etching also matter to the resultant porous structure greatly.

1.2.3.2 Metal-assisted chemical etching

Metal-assisted chemical etching (MACE) is a recently developed anisotropic wet-etching method.[79] In the presence of HF and an oxidative agent, catalysed by noble metals (Pt, Pd, Au, Ag), silicon can be etched to form required structures such as 1D Si NWs[80] and 3D pSi[81] with various morphologies. Compared to the anisotropic nature of electrochemical etching along the [100] direction (Figure 1.5), the etching direction in MACE can be controlled on the [100] and non-[100] directions.[62]

During deposition, a compound containing metal ions, such as $AgNO_3$ or $HAuCl_4$, is added to a HF-H_2O_2 solution. Upon attachment to the silicon substrate, noble metal ions acquire electrons (e^-) from the silicon valence band (VB) and are reduced to form seed nuclei, which develop into nanoparticles. Concurrently, these ions inject holes underneath the silicon causing oxidation into SiO or SiO_2, which are then removed by

HF etchant. By the continuous formation of silicon oxide underneath the metal particles and the corresponding removal action by the HF, the metal particles sink into the silicon and create porous structures (Figure 1.9). Once the desired surface structures are created, the metal nanoparticles can be removed by HNO_3, followed by a cleaning process.[82]

MACE-fabricated pSi structure often has a black look, suggesting an improved antireflection and light trapping property that can be exploited in enhancing the solar cell efficiency in PV industry.[83] It is also being intensively applied in the preparation of Si-based anodic material used in Li-ion batteries.[84] However, as the homogeneity of the initial metal deposition in size and place distribution is usually quite poor, the level of control is relatively limited.[66]

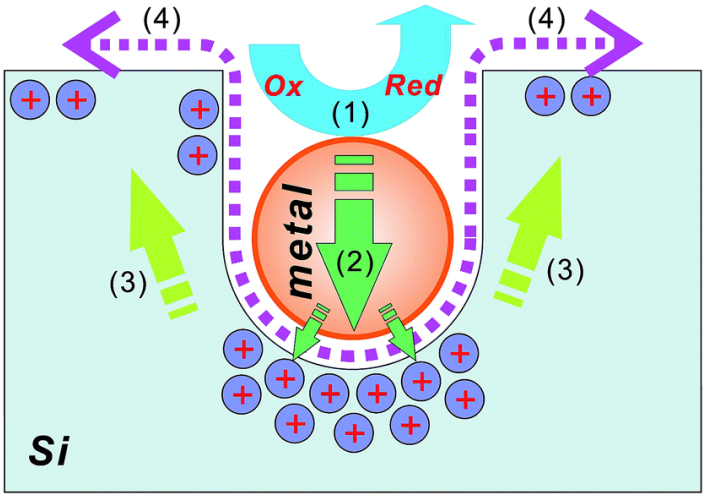

Figure 1.9 An illustration of the metal-assisted chemical etch process: (1) the reduction of an oxidative agent (such as H_2O_2) catalysed by a noble metal particle; (2) the injection of the holes generated during the reduction reaction, into the silicon substrate, with the highest hole concentration underneath the metal particle; (3) the migration of holes to silicon sidewalls and surfaces; and (4) the removal of oxidized silicon via HF. Reprinted from ref. [82] - Published by The Royal Society of Chemistry.

1.2.3.3 In-situ magnesiothermic reduction

$$2Mg\,(g) + SiO_2\,(s) \xrightarrow[650\,^{\circ}C]{\Delta} 2MgO\,(s) + Si\,(s) \qquad \text{Equation 1.2}$$

As Equation 1.2 points out, when magnesium powder (Mg) and silica powder are well mixed and heated above 650°C under inert atmosphere, the melting temperature of Mg, silica can be converted into silicon replicas with identical porous network.[70] In contrast to the conventional carbothermal reduction of silica, which operates at temperatures above 1500°C,[85] the magnesiothermic reaction takes place at much lower temperature region thus preserves the complex structure of silica in the final pSi product. Another advantage of this method is that a vast range of artificial and natural silica (diatom frustule,[70] rice husk,[86] etc.) can be transformed into pSi nanostructures via this strategy. Owing to the simplicity and versatility, magnesiothermic reduction has been used in diverse applications such as sensor,[87] bio-medical therapy,[88] Li-ion batteries[51] and photocatalysis[46].

However, magnesiothermic reduction has a critical limitation caused by unavoidable incomplete reduction that results in low yield of pSi. In order to force silica reduction to completion, a substantial excess of Mg powder is often required which leads to degradation or even collapse of the structure by further reacting with the as-generated silicon to form magnesium silicide (Mg_2Si) at high temperatures (Equation 1.3).[85, 89]

$$2Mg\,(g) + Si\,(s) \xrightarrow{\Delta} Mg_2Si\,(s) \qquad \text{Equation 1.3}$$

1.2.4 Modification of porous silicon

As mentioned above porous silicon can be produced via various synthetic approaches of which each of the capability and speciality is also reflected on the resultant porous structure, distinguishing in various aspects such as the structural morphology, shape, surface chemistry and chemical composition. However, in many cases the as-formed properties are not ideal, thus a range of physical and chemical post-treatments can be applied in adjusting these crucial factors separately or collectively.

1.2.4.1 Morphological modification of porous silicon

Morphological control of porous material is vitally important in realizing its functionality as known from the previous discussion about porous solids in 1.1. The characteristics of a nanoporous material are deeply interlocked with its surface and pore properties, depending on the size, geometry and connectivity of the pores. As well as largely determined by the used preparation method and Si precursor, they can also be tailored to meet the needs of the application via tuning the synthesis parameters, which affect the formation process of porous silicon significantly.

For example, the morphological properties of electrochemically etched porous silicon can be adjusted effectively by changing the etching conditions, or electrolyte compositions.[90] Meanwhile the crystal orientation and doping conditions of Si wafer also have strong influence on the final structure.[91] As these variables are standardised and well-controlled, this endows electrochemical etching method superior advantages over other methods which is also contributed by the fact that the pore formation is largely defined by the pre-determined conditions.[92] For p-type Si wafer with doping density 1×10^{17} cm^{-3}, the porosity of porous silicon can be adjusted from 60% to 80% by increasing the etching current density from 3 to 300 $mA \cdot cm^{-2}$.[93] As found in another study of p-type Si wafer with a resistivity range of 9.0-13.0 Ω·cm, the measured macropore diameter is proportional to the square root of etching current density.[94] The following example clearly highlights the effect of dopant on pore texture in porous silicon films. Under the same conditions of current density

(50 mA·cm^{-2}), etching time (300 s), and electrolyte composition (3:1 aqueous HF: ethanol), Figure 1.10A shows the cross-section SEM image of porous silicon made from a (100)-orientated n-type Si wafer, featured by parallel macropores. While for a (100)-orientated p-type Si wafer, porous silicon is densely packed with small pores that are too small to be resolved properly in the image (Figure 1.10B).[76]

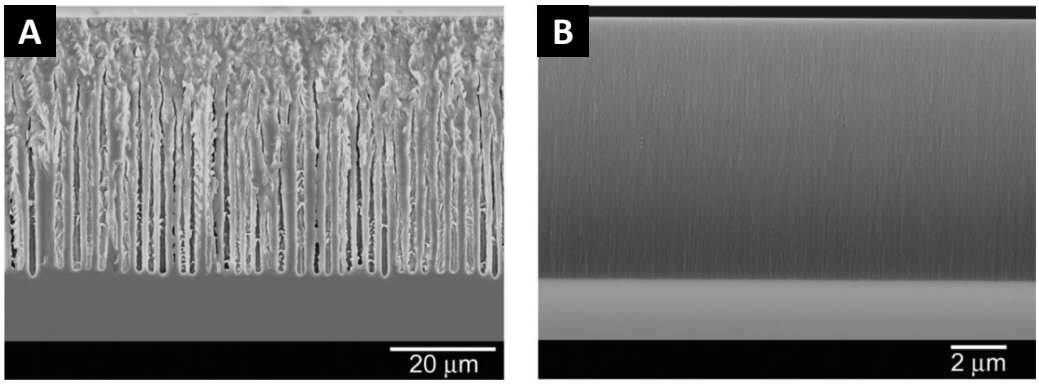

Figure 1.10 Cross-section SEM images of porous silicon prepared via electrochemical etching of n-type (A) and p-type (B) Si wafer. Reprinted with permission from ref. [76]. Copyright 2012, Wiley-VCH.

It is often of interest to generate porous silicon with a high surface area in many applications that potentially involve interfacial interactions, such as optoelectronics, catalysis, drug delivery systems, and lithium-ion batteries. Since macroporous silicon has an inherently low surface-to-volume ratio, efforts have mainly been focused on developing micro-/mesoporous silicon structures. Ruike et al. reported a finely porous meso-structure of Si prepared from a lightly boron-doped (dopant density 7×10^{14}/cm^3) crystalline Si wafer by anodization (10 mA·cm^{-2}) in mildly concentrated HF solution exhibited a specific surface area of 590 m^2·g^{-1} and mean pore size around 3.1 nm.[95] A similar value of surface area was also reported in a later study which achieved 570 m^2·g^{-1} in amorphous mesoporous silicon from a sodiothermically reduced silica template (NaY zeolite) with pore size distribution centred at 11.2 nm, further leading to a high supercapacitive performance.[96] Another bottom-up self-templating synthesis

of mesoporous crystalline Si from a gaseous precursor ($SiCl_4$) was also developed which shows high surface area up to 580 $m^2 \cdot g^{-1}$ and enhanced photocatalytic efficiency in hydrogen generation.[48] By adding different additives (hydrochloric acid, sulphuric acid, ammonium dodecyl sulfate) into the HF containing electrolyte, highly porous silicon film with 1125 $m^2 \cdot g^{-1}$ (pore diameter 4.2 nm) and pSi particles with 864 $m^2 \cdot g^{-1}$ (pore size in 2.8 - 3.2 nm region) were obtained on p-type Si wafer with resistivity 1 - 5 Ω·cm through electrochemical etching and supercritical drying with CO_2 solvent in order to maintain the integrity of the etched micro-/mesoporosity during electrolyte removal.[97-98]

1.2.4.2 Shape modification of porous silicon

The natural form of porous silicon produced by bottom-up approaches is usually powder-like particles. In contrast, as crystalline Si wafers are often employed as precursor in etching-based approaches in the preparation of porous silicon, as-etched porous silicon is often supported by the unetched part of the Si wafer in the form of porous thin film, a continuous bulky phase that can also be "lifted off" the substrate. As an advantage, the chip-bound shape could open up the opportunities of porous silicon prepared by top-down methods to be utilized in microelectromechanical systems (MEMS) applications, especially the electrochemical etching method for its excellent controllability.

For broader uses, porous silicon microparticles and nanoparticles are also desirable.[99-100] Common methods to prepare them involve physical grinding, ball-milling[101-103] or ultrasonication.[104-106] Since the resulting particle size distribution is relatively broad, extra sieving step is often required. With the emergence of various new post-treatments, such as pulsed electrochemical etching,[103, 107] high-pressure microfluidization,[108] the yield of porous silicon nanoparticles can be further improved with greater size control.

1.2.4.3 Surface modification of porous silicon

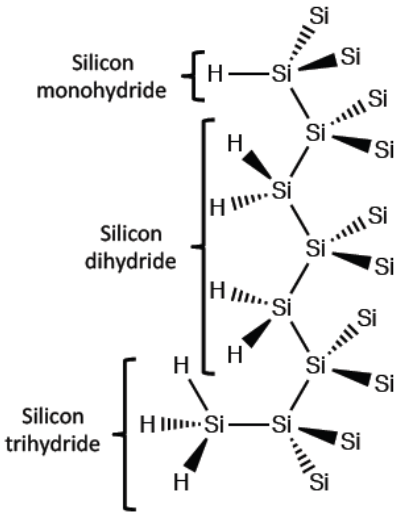

Figure 1.11 Schematic diagram of the silicon hydrides (SiH, SiH_2 and SiH_3) formed on the surface of as-etched porous silicon.

Porous silicon outscores many other nanostructured Si for its unique porous structure and large surface area, which means the surface properties are as important as the bulk properties. In general, the surface of porous silicon fabricated by etching-based approaches is often populated with Si-H bonds, as shown in Figure 1.11, resulting in a hydride-passivated surface environment. These hydrides species are metastable and thus can be transformed through various ways of oxidation, carbonization, hydrosilylation, to enhance the stability,[109-110] modify the surface hydrophobicity/hydrophilicity,[111-112] adjust the porous structure[113-115] or optical properties[116-117] and to functionalize pSi with useful features via ligand grafting which include alkene, alkyne, aldehyde etc.[118-119] As a result, the surface chemistry of porous silicon has been profoundly enriched which facilitates the development of porous silicon-based multicomponent and multifunctional systems.

1.2.5 Applications of porous silicon

Due to the unique morphological structure and surface functionality, porous silicon is widely applied in a broad range of fields of which a glimpse can be caught in the discussion above in 1.2.2. Here, three potential applications that are attracting increasing research attentions are described.

1.2.5.1 Heterogeneous catalysis

The large surface-to-volume ratio, open porous network, unique surface chemistry, and semiconducting properties of pSi provide a solid structural basis for the material to be utilized in catalytic/photocatalytic conversions as inert catalyst substrate or as active photocatalyst.

1.2.5.1.1 Porous silicon as catalyst support

As we know in heterogeneous catalysis, the catalyst support has huge influences on the catalytic performance and catalyst lifetime. A high specific surface area is greatly appreciated, as that would improve the dispersity and stability of active catalysts, increase the loading capacity, and exposes more reaction sites on the catalyst surfaces. Much work have been dedicated to this area by making use of nanostructured Si, e.g. Si NWs,[120-122] pSi[123-126] in anchoring active catalyst/photocatalyst species, most commonly metal nanoparticles (e.g. Ag, Cu, Pt, Au), for the reduction of nitroaromatics,[125-126] CO oxidation,[124] selective oxidation of hydrocarbons[127-128] and ethanol steaming reforming etc.[123] Apart from the structural advantages, the SiH_x species on the surface of pSi also enable the in-situ reduction of metal ions into metallic catalyst without the need for additional reducing agent.[125-126, 128] As a semiconductor, pSi may also influence the electronic state of metal clusters through exciton-plasmon interaction and consequently affects the catalytic activity.[125]

1.2.5.1.2 Porous silicon as photocatalyst

The sun delivers about 3 × 10^{24} J of energy to the Earth's surface per year, which is about 4 orders of magnitude larger than the energy annually consumed by humans all over the world. Visible light (400-700 nm) accounts for 43% of the solar energy that reaches the surface of the Earth while UV light (290-400 nm) only compose less than 5% of the incident solar energy. Thus, much work in recent years have been devoted to developing advanced materials for harvesting the visible light energy to drive photochemical reactions. Promoted by the wide applications of Si in photovoltaic cells and the emergence of various nanostructures, silicon-based photocatalysts have been greatly developed in recent years.[50]

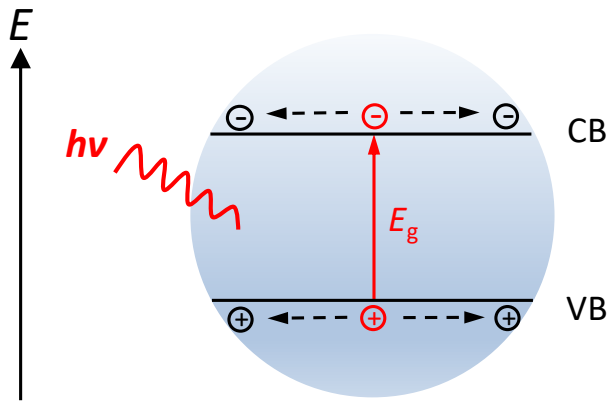

Figure 1.12 Diagram of the band structure of semiconductor with electron excitation.

As shown in Figure 1.12, the ability of harvesting incident photons is determined by the bandgap (E_g) of semiconductor, which means the energy gap between the maximum of the valence band (VB) and the minimum of the conduction band (CB). Bulk crystalline Si with a diamond cubic structure has an indirect bandgap of around 1.1 eV which means a broad light absorption up to 1100 nm of the solar spectrum (Figure 1.13), making it a promising candidate in utilizing the solar energy. However, the narrow band gap of bare Si also implies very close band edges that limits its photocatalytic applications. The reductive and oxidative capacities of photogenerated electrons and holes are dependent on the band potential of CB and VB respectively.

Through nanoscaling, the energy difference between CB and VB can be increased effectively, leading to a better photoredox capability.

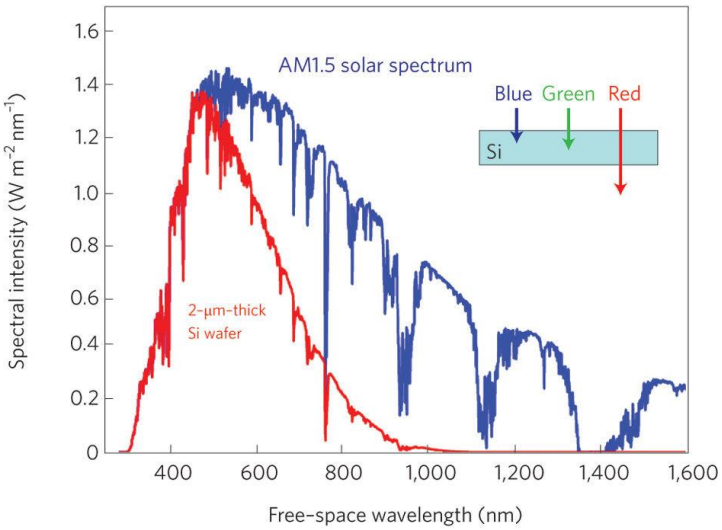

Figure 1.13 AM1.5 solar spectrum, together with a graph that indicates the solar energy absorbed in a 2-µm-thick crystalline Si film (assuming single-pass absorption and no reflection). Reprinted with permission from ref. [129]. Copyright 2010, Nature Publishing Group.

Due to the quantum confinement caused by the Si nanocrystallites formed on the porous framework, the bandgap energy of electrochemically etched pSi is effectively enlarged to 1.8-2.2 eV.[47] As a result, visible light photons with energies equal to and higher than the bandgap level can be absorbed by porous silicon resulting in the excitation of electrons from the valence band to the conduction band by overcoming the transition barrier. After the charge separation, the photoexcited electrons (e^-) and holes (h^+) then migrate to the surfaces of pSi from the inner bulk phase and are donated to substrate molecules in liquid phase which results in interfacial charge transfer and half reaction of reduction and/or oxidation. The reductive and oxidative capacities of photogenerated electrons and holes are dependent on the band potential of CB and VB respectively. As seen in Figure 1.14, the above mentioned charge transfer pathway is among various other possibilities of photoinduced charge recombination which can be generally divided as non-radiative recombination and radiative recombination, the latter of which gives rise to the light emitting property of porous silicon, as further illustrated in 1.2.5.2.

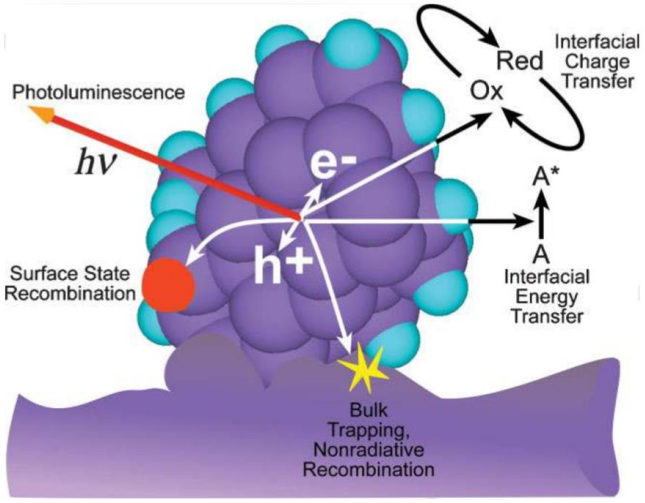

Figure 1.14 Schematic diagram depicting the radiative and non-radiative recombination pathways available to a Si nanocrystallite in porous silicon. Reprinted with permission from ref. [60]. Copyright 2009, Wiley-VCH.

As earth-abundant, metal-free and visible-light responsive, Si-based photocatalysts (pSi, Si NWs, Si nanoparticles etc.) have drawn widespread attention in fuel production, organic synthesis, waste treatment and environmental remediation.[42-46, 48-49, 122, 130-147] Mao et al. reported the electrochemically etched Si electrodes exhibit higher energy conversion efficiencies than Si electrodes due to the formation of a pSi layer which suppressed charge recombination at the Si/electrolyte interface and stabilizes the electrodes against photocorrosion.[148] As good photosensitizers, pSi and Si nanocrystals are also used in generating singlet oxygen.[34] The photocatalytic ability of Si NWs and Si QDs in CO_2 photoreduction,[130, 140] water splitting,[47, 134, 137, 139] aqueous dye degradation (methyl red,[130, 144, 146] rhodamine B,[131, 145] indigo carmine,[132] rose Bengal,[136] methylene blue,[134] methyl orange[43]), selective oxidation of benzene,[130, 146] benzoic alcohol,[131] and reduction of Cr (VI)[135] under visible light irradiation have also been demonstrated in various studies. One of the studies on Si QDs suggests a size-dependent photocatalytic activity for different reactions as 1-2 nm Si QDs is capable in degrading methyl red and reducing CO_2 while 3-4 nm Si QDs shows little activity (Figure 1.15). This was explained by the authors that the former QDs have more energy to induce those photochemical reactions than the latter ones due to the wider band gap.[130] Another study comparing

the photocatalytic performance of porous Si NWs and nonporous Si NWs prepared with MACE method in methyl red photodegradation shows nanoporous Si NWs have better photocatalytic activity as a result of the higher surface area, pore volume and stronger light absorption.[144] As implied, by controlling the surface and band gap of nanostructured Si, more efficient Si NWs, QDs-based photocatalyst can be developed.

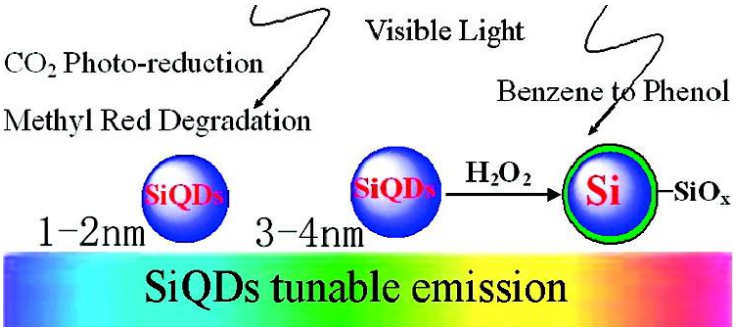

Figure 1.15 Different diameter Si QDs for different reactions. Reprinted with permission from ref. [130]. Copyright 2007, American Chemical Society.

While the physical structure is not much of a concern for the low dimensional Si QDs and NWs which is also one of the reasons why their photocatalytic applications are mostly investigated, porous silicon has much more complex micro- and nano-structural features in terms of internal/external surfaces, pore size, pore interconnectivity, pore volume and the size distribution of Si nanocrystallites on the pore walls. Understandably, these factors not only affect the electronic band structure and optical properties of pSi but also have huge influences on the photochemical reaction kinetics by regulating the absorption and diffusion behaviours of reactant molecules. Compared to the widely studied Si QDs and NWs, the photocatalytic performance of pSi and pSi-based materials have been less intensively investigated despite the larger surface area that it possesses. A very broad absorption across the entire UV, visible light and near-IR range was widely recorded in a number of pSi research[49, 149-150] which is partly due to the existence of a wide spread of band gaps, as demonstrated by the large and inhomogeneous lineshape of its visible emission band.[77] Further studies suggest the light absorption in water can be further enhanced by the nanoporous

structure by providing broadband anti-reflection which improves the photon conversion efficiency (Figure 1.16).[151] The visible-light-driven activities in solar water splitting,[47-48] photodegradation of methyl orange,[44] phenol,[49] nitroaromatics, CO_2 reduction[152] have been broadly discussed in literature, exhibiting a promising potentiality in H_2 generation, pollution control and water purification under visible light irradiation which can be further promoted by increasing the surface area or adjusting the porous structure.

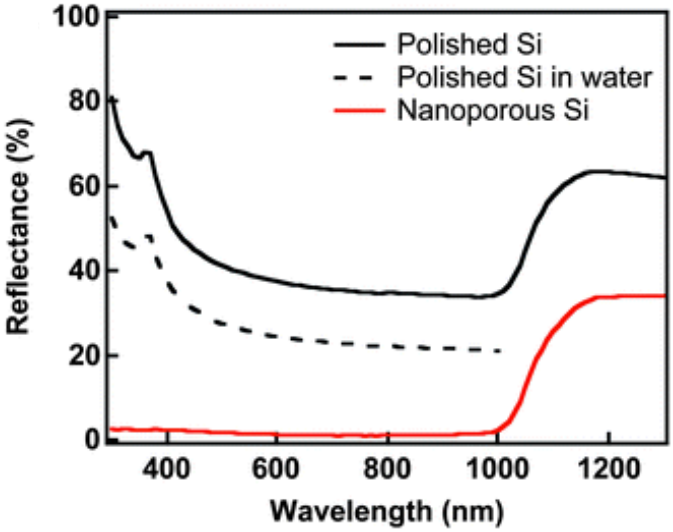

Figure 1.16 The measured total hemispherical optical reflectance of polished and nanoporous Si in air, and the calculated reflectance of polished Si in water. Nanoporous Si shows broadband anti-reflection properties with optical reflectance < 2% over whole solar spectrum. The polished Si reflects about 25% of sunlight at the Si–water interface. Reprinted with permission from ref. [151]. Copyright 2011, Royal Society of Chemistry.

Although the actual photocatalytic mechanisms of Si QDs, Si NWs and pSi are still largely unknown, some insights have already been shed on the importance of the surface termination. In the study carried out by Shao et al., hydrogen-terminated Si NWs exhibited even better photocatalytic activity than Pd-, Au-, Rh- or Ag-modified ones in the degradation of rhodamine B which was ascribed to the effect of hydrogen termination on accelerating photoexcited electrons and holes separation.[131] Similar effects were also proposed in other research in explaining the photocatalytic

behaviours of H-terminated Si QDs, Si NWs and pSi. As Megouda et al. reported, the significance of surface hydrides was also shown in the control experiment of oxidized Si NWs of which the photocatalytic activity in photodegradation of rhodamine B was much lower than that of the hydrogenated sample.[145] Since a hydrogen atom has a large Pauling electron negative value of 2.2, this effect is attributed to the electron-deficiency of H atoms in surface hydrides (SiH_x), which may serve as an electron sink to improve charge separation.[145] Meanwhile, by washing with HF, it was found that the HF-treated Si NWs are more efficient than the as-synthesized ones because of the increased H surface coverage in addition to the original ones.[144] A closer look at the nature of surface species provided by Liu et al. confirms the strong dependence of photocatalytic activity of Si NWs on the surface hydrides, which was revealed as a dynamic interplay of charge distribution and surface reactions. As Si-H can not only trap photoexcited electrons from the bulk but also undergoes bond cleavage in forming H_2 gas in the water splitting process. In the meantime, the Si-OH formed on the surface enters into competition with Si-H on the electron extraction, hindering the H_2 generation.[137]

On the other hand, in the study performed by Kang et al., H-terminated Si QDs were catalytically inactive in the first 2 hours of the photochemical reaction and gradually recovered their photocatalytic capability in benzene hydroxylation after being oxidized to Si/SiO_x core-shell structure which was interpreted as the assistance of SiO_x in the process of the generation of active oxygen species. Another paper also demonstrated that the hydrogen termination was not a prerequisite for the degradation activity of Si NWs in the degradation of indigo carmine.[153]

As mentioned in 1.2.4.3, surface modification of pSi can be conducted through ligand grafting by bridging with the surface hydrides. In fact, pSi is also employed as reducing agent in converting CO_2[152, 154], nitrobenzene derivatives etc.[155] The reactivity of Si-H is also documented in several photocatalysis experiments as dye molecules (e.g. methyl red, methyl orange, and methylene blue) were reduced in the absence of light presumably through hydrogen transfer although how the photocatalytic pathway would be affected by this event was not explored further.[44-45, 144, 156] Another important fact to be considered is that the hydrogen function is also known to be

affected by various external factors (UV laser,[157] ultrasonic agitation,[158] heat,[159] energetic ion[160]) and varied by the surface topography of nanostructured Si as well.[118, 161]

1.2.5.2 Biomedical applications of porous silicon

A clear advantage of Si materials applied in biological research is their natural biocompatibility, biodegradability and bioresorbability.[162-163] Promoted by the high surface area, unique porous structure and adjustable surface functionalities, porous silicon has embraced remarkable success acting as a drug delivery vector used in cancer treatment, featuring a high drug loading, controlled and sustained release.[99, 164-165] As indicated in Figure 1.14, porous silicon can also emit tuneable photoluminescence at room temperature through radiative recombination of photoexcited electrons and holes which has prompted a vast number of studies on the development of cell imaging agents[61, 166] and photoluminescence-based biosensors.[60, 167] Also inspired by the photoactivity, the use of pSi in photothermo- and photodynamic therapies has received increasing attention.[100, 168-169]

1.2.5.3 Energy storage applications of porous silicon

Taking advantage of the high theoretical specific capacity of silicon (4200 $mAh \cdot g^{-1}$) and the anti-pulverization ability endowed by the void spaces in the porous structure, porous silicon has been extensively explored as anode material for the next generation of lithium-ion batteries, with improved capacity and cycling performance as reported.[53-55, 71, 170] Although this application is also structure-sensitive, the basic requirement is mainly about the voids inside pSi to accommodate the drastic volume expansion during Li^+ insertion and extraction. Thus, the magnesiothermic reduction approach is widely adopted for pSi preparation in battery research for its versatility and cost effectiveness.[171-175]

1.3 Graphitic carbon nitride materials

Ever since the defining moment of the isolation of graphene from graphite in 2004,[176] a wide spectrum of two-dimensional (2D) nanomaterials including graphene[177-179] and non-graphene layered materials such as transitional-metal dichalcogenides[180-182] and hexagonal boron nitride (h-BN)[183] have attracted tremendous interests because of the new functionalities and applications that emerge upon 2D confinement.[184] A significant amount of effort has in particular been devoted to the development of 2D graphitic carbon nitride (g-C_3N_4) which has shown promising prospects in various fields of energy applications, light-emitting and sensing etc.[185-191]

1.3.1 General background of graphitic carbon nitride

Carbon nitrides (C_3N_4), is a subclass of covalent organic frameworks (COFs) composed of binary C, N-based polymeric materials.[192] The first synthesis of a chain-like C_3N_4 derivative, melon, was reported by Berzelius and Liebig in 1834 (Figure 1.17(d)) and it is regarded as one of the oldest synthetic polymers in human history.[193] Carbon nitrides can exist in several allotropes with diverse properties including α-C_3N_4, β-C_3N_4, cubic-C_3N_4, pseudocubic-C_3N_4, and graphitic-C_3N_4.[185, 194] Demonstrated by Liu et al., the diamond-like β-C_3N_4 allotrope was discovered to be of comparative hardness and low compressibility as that of diamond.[195] While graphitic C_3N_4 (g-C_3N_4) was found to be energetically favoured relative to other phases and is regarded as the most stable allotrope of carbon nitrides under ambient conditions based on both theoretical and experimental studies.[196-197] Besides, it has many advantages such as reliable chemical and thermal stability, high level of hardness, resistance to wear, bio-compatibility and special electronic properties due to the unique tectonic structure motif.[194] Thus, it has attracted the focus of most carbon nitride oriented research.[185, 188]

Possessing a two-dimensional (2D) layered structure, g-C_3N_4 can be viewed as an analogue of graphite, more precisely, as a high level of N-doped graphite-like framework consisting of a π-conjugated system through sp^2 hybridized C and N atoms on the plane. As shown in Figure 1.17, its polymeric network (e) is formed by the

condensation of tri-*s*-triazine/heptazine (c) subunits, widely accepted as the basic building units, connected through planar tertiary amino groups with periodic vacancies in the lattice.[198] As such, the electronic properties of g-C_3N_4 is distinctly different from graphite as characterised as a wide-bandgap semiconductor while graphite has excellent conductivity in the dimensions of the layers.

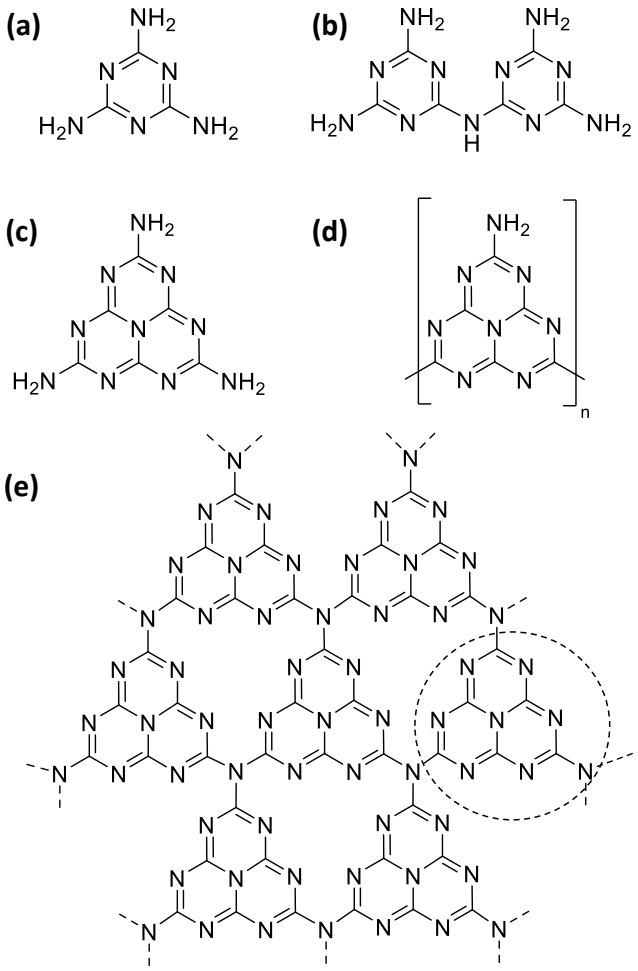

Figure 1.17 Structures of (a) melamine, (b) melam, (c) melem, (d) melon and (e) g-C_3N_4 network with tri-*s*-triazine as tectons.

One of the main advantages of g-C_3N_4 is its straightforward synthesis using a cheap and easily available starting material. Many nitrogen-rich precursors can be thermally polymerized into a g-C_3N_4 framework through a combination of polyaddition and

polycondensation, to name just a few, such as urea,[199-200] thiourea,[201] cyanamide,[202] dicyandiamide,[203-204] and melamine.[205-206] Taken melamine as an example (Figure 1.17), the reaction starts with condensation of melamine (a) that eliminates ammonia and forms a dimer called melam (b). Melam is then converted into tri-*s*-triazine called melem (c) which forms the 2D planar structure (e) via polymerization at approximately 520°C and stack into layered g-C_3N_4 through hydrogen bonds and van der Waals interplanar forces.[194]

1.3.2 Photocatalytic applications of graphitic carbon nitride

The first photocatalytic result of g-C_3N_4 semiconductor was published in 2009 by Wang et al. that revealed its photocatalytic activity in water splitting under visible light irradiation.[207] Since then, it has attracted worldwide research interests in exploiting the ability in harnessing solar energy and rapidly became a "star" material of significant importance in various fields, such as water splitting,[208] CO_2 fixation,[209-210] pollutant elimination.[185, 187, 211]

As limited by the low surface area (2-10 $m^2 \cdot g^{-1}$), poor absorption at longer wavelengths and poor charge mobility, much progress in recent years has been made in improving the photon conversion efficiency and facilitating an easier mass transfer process from four different directions of electronic structure modulation, crystal structure engineering, nanostructure design, and heterostructure construction.[194] In respect of nanostructure design, different exfoliation strategies (e.g. thermal oxidation,[212-214] mechanical exfoliation,[215-218] chemical exfoliation[219-221]) for synthesising 2D g-C_3N_4 nanosheets have been developed and proved to be efficient in improving the photocatalytic performance as a result of enlarged surface area and widened bandgap.[222] A variety of g-C_3N_4 based heterostructures have also emerged which can be categorized as: metal-free heterojunction, g-C_3N_4/single metal oxide (sulfide), g-C_3N_4/composite oxide, g-C_3N_4/halide, g-C_3N_4/noble metal, and g-C_3N_4-based complex system.[223] As suggested by these efforts, the potential of g-C_3N_4 in photocatalysis is still not yet fulfilled and in need of new perspectives to pave the way for a greener future.

1.4 Dye pollution and elimination

Over 10,000 different synthetic dyes are used widely in textile, pharmaceutical, cosmetics, paper industries, constituting one of the largest groups of organic compounds with serious environmental risks.[224] Due to improper operation or accidental leakage, about 15% of the total world production of dyes up to 200,000 tons is lost and released into water bodies during production, storage, transportation and usage.[225] Due to the high stability, most of these escaped dyes tend to persist in the natural environment, causing severe water pollution problems and ecological damages.

The distinctive colour of the dye is caused by the chromophore-containing centre in its molecular structure that are based on diverse functional groups, such as azo, anthraquinone, methane, nitro, arilmethane, carbonyl etc.[226] With respect to the number and production volumes, azo dyes are the largest group of colorants, dominating 60-70% of all organic dyes annually produced worldwide.[227] Due to their toxicity and mutagenic effect, they are banned throughout the world. However, their uses continue today because of their low cost and other properties in food, paper, leather and paints. Thus, removal and treatment of azo dyes from wastewater presents a difficult task.

Since the azo dyes are almost non-destructive by the conventional biological treatments and physical treatments are also ineffective considering the cost of adsorbent agents, chemical methods especially heterogeneous photocatalysts are significantly important as the solution to the existing and future water challenges for various reasons. The photocatalysts are mostly made of substances that can be accounted as available, inexpensive and non-toxic. The removal of organic contaminants in aqueous systems can be done without involving other agents, and carried out under ambient or mild conditions. More importantly, by utilizing sunlight, the wastewater can be constantly cleaned by reusing the same photocatalyst. The elimination efficiency is therefore largely dependent on the activity and recyclability of photocatalyst. With the advent of more advanced nanotechnologies, more and more

efficient nanomaterials will be developed and contribute to the rebalance of the out-of-balance relationship of the natural environment and human society.

1.5 Research objectives

From the discussion above, it is clear that solar energy utilization is of utmost importance in resolving various aspects of global challenges the world is now facing, to meet soaring energy demand, to tackle climate change, to solve the deteriorating pollution crisis and most of all, to establish a sustainable society for us all. Thus, the overall aim of this research is to search for an earth-abundant and eco-friendly system that can utilize solar energy to eliminate environmental pollutants efficiently and cost-effectively.

To approach the goal, we focused on exploiting porous silicon and porous silicon-based heterojunctions with graphitic carbon nitride (g-C_3N_4). Inspired by the previous findings on the surface area of catalysts, the first research objective is to prepare mesoporous silicon with a large surface area and tuneable porous structure by an electrochemical etching method and understand the morphological features and physiochemical properties. Secondly, we are interested in the structural effects on the photocatalytic performance of mesoporous silicon and the photocatalytic mechanism as well. Finally, the combination of porous silicon and g-C_3N_4 nanosheets is to be investigated in the hope of broadening the options for greener photocatalysis.

1.6 Thesis outline

According to these three objectives, this thesis is divided into 6 chapters in total.

Chapter 1 introduces the research background, concludes the state-of-the-art research progress of porous silicon and graphitic carbon nitride materials, highlights the importance of photocatalysis in dye degradation.

Chapter 2 overviews the experimental procedures for the preparation, modification, characterisation and photocatalytic analysis of porous silicon and graphitic carbon nitride materials, with a general discussion of the method principles correspondingly.

Chapter 3 showcases the high surface area and unique morphologies of mesoporous silicon, implies the potential applications in heterogeneous catalysis, biomedicines and energy storage.

Chapter 4 evaluates the photocatalytic activity of mesoporous silicon in dye degradation under visible light irradiation, reveals the varied effects of structural factors in reaction kinetics, and discusses the photocatalytic behaviours and mechanisms of porous silicon as well.

Chapter 5 demonstrates the performance of mesoporous silicon/graphitic carbon nitride nanosheets composited material in dye degradation under visible light irradiation.

Chapter 6 summarizes the primary contributions of this research, and provides suggestions for future work in this area.

1.7 References

1. Su, B.-L.; Sanchez, C.; Yang, X.-Y., *Hierarchically Structured Porous Materials*. Wiley-VCH Verlag & Co. KGaA: Germany, Weinheim, 2011.

2. Yang, X.-Y.; Chen, L.-H.; Li, Y.; Rooke, J. C.; Sanchez, C.; Su, B.-L., Hierarchically porous materials: synthesis strategies and structure design. *Chem. Soc. Rev.* **2017,** *46* (2), 481-558.

3. Sing, K. S. W., Reporting physisorption data for gas/solid systems with special reference to the determination of surface area and porosity (Recommendations 1984). *Pure Appl. Chem.* **1985,** *57* (4), 603-619.

4. Valtchev, V.; Majano, G.; Mintova, S.; Perez-Ramirez, J., Tailored crystalline microporous materials by post-synthesis modification. *Chem. Soc. Rev.* **2013,** *42* (1), 263-290.

5. Navrotsky, A.; Trofymluk, O.; Levchenko, A. A., Thermochemistry of microporous and mesoporous materials. *Chem. Rev.* **2009,** *109* (9), 3885-3902.

6. Csicsery, S. M., Shape-selective catalysis in zeolites. *Zeolites* **1984,** *4* (3), 202-213.

7. Collins, D. J.; Medina, R. J.; Davis, B. H., Xylene isomerization by ZSM-5 zeolite catalyst. *Can. J. Chem. Eng.* **1983,** *61* (1), 29-35.

8. Yan, Y.; Guo, X.; Zhang, Y.; Tang, Y., Future of nano-/hierarchical zeolites in catalysis: gaseous phase or liquid phase system. *Catal. Sci. Technol.* **2015,** *5* (2), 772-785.

9. Corma, A., From microporous to mesoporous molecular sieve materials and their use in catalysis. *Chem. Rev.* **1997,** *97* (6), 2373-2420.

10. Perez-Ramirez, J.; Christensen, C. H.; Egeblad, K.; Christensen, C. H.; Groen, J. C., Hierarchical zeolites: enhanced utilisation of microporous crystals in catalysis by advances in materials design. *Chem. Soc. Rev.* **2008,** *37* (11), 2530-2542.

11. Xuereb, D. J.; Raja, R., Design strategies for engineering selectivity in bio-inspired heterogeneous catalysts. *Catal. Sci. Technol.* **2011,** *1* (4), 517-534.

12. Yang, Z.; Lu, Y.; Yang, Z., Mesoporous materials: tunable structure, morphology and composition. *Chem. Commun.* **2009,** (17), 2270-2277.

13. Moritz, M.; Geszke-Moritz, M., Mesoporous materials as multifunctional tools in biosciences: principles and applications. *Mater Sci Eng C Mater Biol Appl* **2015,** *49*, 114-151.

14. Hoffmann, F.; Cornelius, M.; Morell, J.; Froba, M., Silica-based mesoporous organic-inorganic hybrid materials. *Angew. Chem. Int. Ed.* **2006,** *45* (20), 3216-3251.

15. Liang, C.; Li, Z.; Dai, S., Mesoporous carbon materials: synthesis and modification. *Angew. Chem. Int. Ed.* **2008,** *47* (20), 3696-3717.

16. Chen, H.-Y.; Xu, Y.-F.; Kuang, D.-B.; Su, C.-Y., Recent advances in hierarchical macroporous composite structures for photoelectric conversion. *Energy Environ. Sci.* **2014,** *7* (12), 3887-3901.

17. Wang, B.; Prinsen, P.; Wang, H.; Bai, Z.; Wang, H.; Luque, R.; Xuan, J., Macroporous materials: microfluidic fabrication, functionalization and applications. *Chem. Soc. Rev.* **2017,** *46* (3), 855-914.

18. Stein, A.; Schroden, R. C., Colloidal crystal templating of three-dimensionally ordered macroporous solids: materials for photonics and beyond. *Curr. Opin. Solid State Mater. Sci.* **2001,** *5* (6), 553-564.

19. Nardecchia, S.; Carriazo, D.; Ferrer, M. L.; Gutierrez, M. C.; del Monte, F., Three dimensional macroporous architectures and aerogels built of carbon nanotubes and/or graphene: synthesis and applications. *Chem. Soc. Rev.* **2013,** *42* (2), 794-830.

20. Carreon, M. A.; Guliants, V. V., Ordered meso- and macroporous binary and mixed metal oxides. *Eur. J. Inorg. Chem.* **2005,** *2005* (1), 27-43.

21. Ahn, S. H.; Kim, D. J.; Chi, W. S.; Kim, J. H., Hierarchical double-shell nanostructures of TiO_2 nanosheets on SnO_2 hollow spheres for high-efficiency, solid-state, dye-sensitized solar cells. *Adv. Funct. Mater.* **2014,** *24* (32), 5037-5044.

22. Kim, H. N.; Moon, J. H., Enhanced photovoltaic properties of Nb_2O_5-coated TiO_2 3D ordered porous electrodes in dye-sensitized solar cells. *ACS Appl Mater Interfaces* **2012,** *4* (11), 5821-5825.

23. Lee, J.; Kim, J.; Hyeon, T., Recent progress in the synthesis of porous carbon materials. *Adv. Mater.* **2006,** *18* (16), 2073-2094.

24. Sun, M. H.; Huang, S. Z.; Chen, L. H.; Li, Y.; Yang, X. Y.; Yuan, Z. Y.; Su, B. L., Applications of hierarchically structured porous materials from energy storage and conversion, catalysis, photocatalysis, adsorption, separation, and sensing to biomedicine. *Chem. Soc. Rev.* **2016,** *45* (12), 3479-3563.

25. Neergaard Waltenburg, H.; Yates, J. T., Surface chemistry of silicon. *Chem. Rev.* **1995,** *95* (5), 1589-1673.

26. Thommes, M.; Kaneko, K.; Neimark, A. V.; Olivier, J. P.; Rodriguez-Reinoso, F.; Rouquerol, J.; Sing, K. S. W., Physisorption of gases, with special reference to the evaluation of surface area and pore size distribution (IUPAC Technical Report). *Pure Appl. Chem.* **2015,** *87* (9-10), 1051-1069.

27. Uhlir, A., Electrolytic shaping of germanium and silicon. *Bell Syst. Tech. J.* **1956,** *35* (2), 333-347.

28. Hernandez-Montelongo, J.; Munoz-Noval, A.; Garcia-Ruiz, J. P.; Torres-Costa, V.; Martin-Palma, R. J.; Manso-Silvan, M., Nanostructured porous silicon: the winding road from photonics to cell scaffolds - a review. *Front Bioeng Biotechnol.* **2015,** *3*: 60.

29. Canham, L. T., Silicon quantum wire array fabrication by electrochemical and chemical dissolution of wafers. *Appl. Phys. Lett.* **1990,** *57* (10), 1046-1048.

30. Lehmann, V.; Gosele, U., Porous silicon formation - a quantum wire effect. *Appl. Phys. Lett.* **1991,** *58* (8), 856-858.

31. Hirschman, K. D.; Tsybeskov, L.; Duttagupta, S. P.; Fauchet, P. M., Silicon-based visible light-emitting devices integrated into microelectronic circuits. *Nature* **1996,** *384* (6607), 338-341.

32. Cullis, A. G.; Canham, L. T.; Calcott, P. D. J., The structural and luminescence properties of porous silicon. *J. Appl. Phys.* **1997,** *82* (3), 909-965.

33. Wei, J.; Buriak, J. M.; Siuzdak, G., Desorption-ionization mass spectrometry on porous silicon. *Nature* **1999,** *399* (6733), 243-246.

34. Fujii, M.; Nishimura, N.; Fumon, H.; Hayashi, S.; Kovalev, D.; Goller, B.; Diener, J., Dynamics of photosensitized formation of singlet oxygen by porous silicon in aqueous solution. *J. Appl. Phys.* **2006,** *100* (12), 124302.

35. Novara, C.; Lamberti, A.; Chiadò, A.; Virga, A.; Rivolo, P.; Geobaldo, F.; Giorgis, F., Surface-enhanced Raman spectroscopy on porous silicon membranes decorated with Ag nanoparticles integrated in elastomeric microfluidic chips. *RSC. Adv.* **2016,** *6* (26), 21865-21870.

36. Virga, A.; Rivolo, P.; Frascella, F.; Angelini, A.; Descrovi, E.; Geobaldo, F.; Giorgis, F., Silver nanoparticles on porous silicon: approaching single molecule detection in resonant SERS regime. *J. Phys. Chem. C* **2013,** *117* (39), 20139-20145.

37. Chan, S.; Kwon, S.; Koo, T. W.; Lee, L. P.; Berlin, A. A., Surface-enhanced raman scattering of small molecules from silver-coated silicon nanopores. *Adv. Mater.* **2003,** *15* (19), 1595-1598.

38. Lin, H.; Mock, J.; Smith, D.; Gao, T.; Sailor, M. J., Surface-enhanced raman scattering from silver-plated porous silicon. *J. Phys. Chem. B* **2004,** *108* (31), 11654-11659.

39. Harraz, F. A., Porous silicon chemical sensors and biosensors: A review. *Sens Actuators B Chem.* **2014,** *202*, 897-912.

40. Kilian, K. A.; Bocking, T.; Gooding, J. J., The importance of surface chemistry in mesoporous materials: lessons from porous silicon biosensors. *Chem. Commun.* **2009,** (6), 630-640.

41. Priolo, F.; Gregorkiewicz, T.; Galli, M.; Krauss, T. F., Silicon nanostructures for photonics and photovoltaics. *Nat. Nanotechnol.* **2014,** *9* (1), 19-32.

42. Li, T.; Li, J.; Zhang, Q.; Blazeby, E.; Shang, C.; Xu, H.; Zhang, X.; Chao, Y., Hydrogen-terminated mesoporous silicon monoliths with huge surface area as alternative Si-based visible light-active photocatalysts. *RSC Adv.* **2016,** *6* (75), 71092-71099.

43. Guan, B.; Sun, Y.; Li, X.; Wang, J.; Chen, S.; Schweizer, S.; Wang, Y.; Wehrspohn, R. B., Conversion of bulk metallurgical silicon into photocatalytic nanoparticles by copper-assisted chemical etching. *ACS Sustain. Chem. Eng.* **2016,** *4* (12), 6590-6599.

44. Xu, H.; Xiao, H.; Pei, H.; Cui, J.; Hu, W., Photodegradation activity and stability of porous silicon wafers with (100) and (111) oriented crystal planes. *Microporous Mesoporous Mater.* **2015,** *204*, 251-256.

45. Xu, H.; Pei, H.; Xiao, H.; Hu, W., Degradation mechanism of hydrogen-terminated porous silicon in the presence and in the absence of light. *AIP Adv.* **2015,** *5* (6), 067125.

46. Wang, J.-F.; Chen, J.-S.; Zhou, Z.-F., Preparation of porous silicon by sodiothermic reduction of zeolite and photoactivation for benzene oxidation. *Eur. J. Inorg. Chem.* **2015,** *2015* (8), 1330-1333.

47. Chandrasekaran, S.; Nann, T.; Voelcker, N. H., Nanostructured silicon photoelectrodes for solar water electrolysis. *Nano Energy* **2015,** *17*, 308-322.

48. Dai, F.; Zai, J.; Yi, R.; Gordin, M. L.; Sohn, H.; Chen, S.; Wang, D., Bottom-up synthesis of high surface area mesoporous crystalline silicon and evaluation of its hydrogen evolution performance. *Nat. Commun.* **2014,** *5*, 3605.

49. Su, J.; Yu, H.; Quan, X.; Chen, S.; Wang, H., Hierarchically porous silicon with significantly improved photocatalytic oxidation capability for phenol degradation. *Appl. Catal. B* **2013,** *138-139*, 427-433.

50. Liu, G.; Niu, P.; Cheng, H. M., Visible-light-active elemental photocatalysts. *ChemPhysChem* **2013,** *14* (5), 885-892.

51. Kim, H.; Han, B.; Choo, J.; Cho, J., Three-dimensional porous silicon particles for use in high-performance lithium secondary batteries. *Angew. Chem. Int. Ed. Engl.* **2008,** *47* (52), 10151-10154.

52. Li, X.; Gu, M.; Hu, S.; Kennard, R.; Yan, P.; Chen, X.; Wang, C.; Sailor, M. J.; Zhang, J. G.; Liu, J., Mesoporous silicon sponge as an anti-pulverization structure for high-performance lithium-ion battery anodes. *Nat. Commun.* **2014,** *5*, 4105.

53. Zhang, Z.; Wang, Y.; Ren, W.; Tan, Q.; Zhong, Z.; Su, F., Low-cost synthesis of porous silicon via ferrite-assisted chemical etching and their application as Si-based anodes for Li-ion batteries. *Adv. Electronic Mater.* **2015,** *1* (4), 140059.

54. Lu, Z.; Liu, N.; Lee, H. W.; Zhao, J.; Li, W.; Li, Y.; Cui, Y., Nonfilling carbon coating of porous silicon micrometer-sized particles for high-performance lithium battery anodes. *ACS Nano* **2015,** *9* (3), 2540-2547.

55. Wada, T.; Ichitsubo, T.; Yubuta, K.; Segawa, H.; Yoshida, H.; Kato, H., Bulk-nanoporous-silicon negative electrode with extremely high cyclability for lithium-ion batteries prepared using a top-down process. *Nano Lett.* **2014,** *14* (8), 4505-4510.

56. Su, X.; Wu, Q. L.; Li, J. C.; Xiao, X. C.; Lott, A.; Lu, W. Q.; Sheldon, B. W.; Wu, J., Silicon-based nanomaterials for lithium-ion batteries: A Review. *Adv. Energy Mater.* **2014,** *4* (1), 1300882.

57. Kotkovskiy, G. E.; Kuzishchin, Y. A.; Martynov, I. L.; Chistyakov, A. A.; Nabiev, I., The photophysics of porous silicon: technological and biomedical implications. *Phys. Chem. Chem. Phys.* **2012,** *14* (40), 13890-13902.

58. Ahire, J. H.; Wang, Q.; Coxon, P. R.; Malhotra, G.; Brydson, R.; Chen, R.; Chao, Y., Highly luminescent and nontoxic amine-capped nanoparticles from porous silicon: synthesis and their use in biomedical imaging. *ACS Appl. Mater. Interfaces* **2012**, 4(6), 3285-3292.

59. Gu, L.; Park, J. H.; Duong, K. H.; Ruoslahti, E.; Sailor, M. J., Magnetic luminescent porous silicon microparticles for localized delivery of molecular drug payloads. *Small* **2010,** *6* (22), 2546-2552.

60. Sailor, M. J.; Wu, E. C., Photoluminescence-based sensing with porous silicon films, microparticles, and nanoparticles. *Adv. Funct. Mater.* **2009,** *19* (20), 3195-3208.

61. Gu, L.; Hall, D. J.; Qin, Z.; Anglin, E.; Joo, J.; Mooney, D. J.; Howell, S. B.; Sailor, M. J., In vivo time-gated fluorescence imaging with biodegradable luminescent porous silicon nanoparticles. *Nat. Commun.* **2013,** *4*, 2326.

62. Santos, A.; Kumeria, T., Electrochemical etching methods for producing porous silicon. **2015,** *220*, 1-36.

63. Vázsonyi, É.; Szilágyi, E.; Petrik, P.; Horváth, Z. E.; Lohner, T.; Fried, M.; Jalsovszky, G., Porous silicon formation by stain etching. *Thin Solid Films* **2001,** *388* (1-2), 295-302.

64. Huang, Z.; Geyer, N.; Werner, P.; de Boor, J.; Gosele, U., Metal-assisted chemical etching of silicon: a review. *Adv. Mater.* **2011,** *23* (2), 285-308.

65. Toor, F.; Miller, J. B.; Davidson, L. M.; Nichols, L.; Duan, W.; Jura, M. P.; Yim, J.; Forziati, J.; Black, M. R., Nanostructured silicon via metal assisted catalyzed etch (MACE): chemistry fundamentals and pattern engineering. *Nanotechnology* **2016,** *27* (41), 412003.

66. Wang, Y.; Wang, T.; Da, P.; Xu, M.; Wu, H.; Zheng, G., Silicon nanowires for biosensing, energy storage, and conversion. *Adv. Mater.* **2013,** *25* (37), 5177-5195.

67. Lai, M.; Parish, G.; Liu, Y.; Keating, A. J., Reactive ion etching of porous silicon for MEMS applications. *IEEE* **2010**, 169-170.

68. Laiho, R.; Pavlov, A., Preparation of porous silicon films by laser ablation. *Thin Solid Films* **1995,** *255* (1-2), 9-11.

69. Lee, J. I.; Lee, K. T.; Cho, J.; Kim, J.; Choi, N. S.; Park, S., Chemical-assisted thermal disproportionation of porous silicon monoxide into silicon-based multicomponent systems. *Angew. Chem. Int. Ed. Engl.* **2012,** *51* (11), 2767-2771.

70. Bao, Z.; Weatherspoon, M. R.; Shian, S.; Cai, Y.; Graham, P. D.; Allan, S. M.; Ahmad, G.; Dickerson, M. B.; Church, B. C.; Kang, Z.; Abernathy, H. W., 3rd; Summers, C. J.; Liu, M.; Sandhage, K. H., Chemical reduction of three-dimensional silica micro-assemblies into microporous silicon replicas. *Nature* **2007,** *446* (7132), 172-175.

71. Ge, M.; Fang, X.; Rong, J.; Zhou, C., Review of porous silicon preparation and its application for lithium-ion battery anodes. *Nanotechnology* **2013,** *24* (42), 422001.

72. Caballero-Hernandez, J.; Godinho, V.; Lacroix, B.; Jimenez de Haro, M. C.; Jamon, D.; Fernandez, A., Fabrication of optical multilayer devices from porous silicon coatings with closed porosity by magnetron sputtering. *ACS Appl. Mater. Interfaces* **2015,** *7* (25), 13889-97.

73. Kozlovskii, V. V.; Kozlov, V. A.; Lomasov, V. N., Modification of semiconductors with proton beams. A review. *Semiconductors* **2000,** *34* (2), 123-140.

74. Canham, L., *Handbook of porous silicon*. Springer International Publishing: 2014.

75. Föll, H.; Christophersen, M.; Carstensen, J.; Hasse, G., Formation and application of porous silicon. *Mater. Sci. Eng. R* **2002,** *39* (4), 93-141.

76. Michael, S., Fundamentals of porous silicon preparation. 2012; pp 1-42.

77. Bisi, O.; Ossicini, S.; Pavesi, L., Porous silicon: a quantum sponge structure for silicon based optoelectronics. *Surf. Sci. Rep.* **2000,** *38* (1-3), 1-126.

78. Zhang, G. X., Porous silicon: morphology and formation mechanisms. In *Modern Aspects of Electrochemistry*, Springer: New York, 2006; Vol. 39, pp 65-133.

79. Li, X.; Bohn, P. W., Metal-assisted chemical etching in HF/H_2O_2 produces porous silicon. *Appl. Phys. Lett.* **2000,** *77* (16), 2572-2574.

80. Peng, K.; Yan, Y.; Gao, S.; Zhu, J., Dendrite-assisted growth of silicon nanowires in electroless metal deposition. *Adv. Funct.l Mater.* **2003,** *13* (2), 127-132.

81. Liu, Y.; Chen, B.; Cao, F.; Chan, H. L. W.; Zhao, X.; Yuan, J., One-pot synthesis of three-dimensional silver-embedded porous silicon micronparticles for lithium-ion batteries. *J. Mater. Chem.* **2011,** *21* (43), 17083-17086.

82. Liu, X.; Coxon, P. R.; Peters, M.; Hoex, B.; Cole, J. M.; Fray, D. J., Black silicon: fabrication methods, properties and solar energy applications. *Energy Environ. Sci.* **2014,** *7* (10), 3223-3263.

83. Li, X., Metal assisted chemical etching for high aspect ratio nanostructures: A review of characteristics and applications in photovoltaics. *Curr. Opin. Solid State Mater. Sci.* **2012,** *16* (2), 71-81.

84. McSweeney, W.; Geaney, H.; O'Dwyer, C., Metal-assisted chemical etching of silicon and the behavior of nanoscale silicon materials as Li-ion battery anodes. *Nano Research* **2015,** *8* (5), 1395-1442.

85. Ji, X.; He, G.; Andrei, C.; Nazar, L. F., Gentle reduction of SBA-15 silica to its silicon replica with retention of morphology. *RSC Adv.* **2014,** *4* (42), 22048-22052.

86. Liu, N.; Huo, K.; McDowell, M. T.; Zhao, J.; Cui, Y., Rice husks as a sustainable source of nanostructured silicon for high performance Li-ion battery anodes. *Sci. Rep.* **2013,** *3*, 1919.

87. Zhu, J.; Liu, R.; Xu, J.; Meng, C., Preparation and characterization of mesoporous silicon spheres directly from MCM-48 and their response to ammonia. *J. Mater. Sci.* **2011,** *46* (22), 7223-7227.

88. Guo, M.; Zou, X.; Ren, H.; Muhammad, F.; Huang, C.; Qiu, S.; Zhu, G., Fabrication of high surface area mesoporous silicon via magnesiothermic reduction for drug delivery. *Microporous Mesoporous Mater.* **2011,** *142* (1), 194-201.

89. Kim, K. H.; Lee, D. J.; Cho, K. M.; Kim, S. J.; Park, J. K.; Jung, H. T., Complete magnesiothermic reduction reaction of vertically aligned mesoporous silica channels to form pure silicon nanoparticles. *Sci. Rep.* **2015,** *5*, 9014.

90. Kumar, P.; Huber, P., Effect of etching parameter on pore size and porosity of electrochemically formed nanoporous silicon. *J. Nanomater.* **2007,** *2007*, 1-4.

91. Kim, H.; Cho, N., Morphological and nanostructural features of porous silicon prepared by electrochemical etching. *Nanoscale Res. Lett.* **2012,** *7* (1), 408.

92. Xifré Pérez, E. Design, fabrication and characterization of porous silicon multilayer optical devices. Universitat Rovira i Virgili., 2007.

93. Lehmann, V., *Electrochemistry of Silicon: Instrumentation, Science, Materials and Applications*. Wiley-VCH Verlag GmbH: 2002.

94. Peckham, J.; Andrews, G. T., Effect of anodization current density on pore geometry in macroporous silicon. *Semicond. Sci. Technol.* **2013,** *28* (10), 105027.

95. Ruike, M.; Houzouji, M.; Motohashi, A.; Murase, N.; Kinoshita, A.; Kaneko, K., Pore structure of porous silicon formed on a lightly doped crystal silicon. *Langmuir* **1996,** *12* (20), 4828-4831.

96. Wang, J. F.; Wang, K. X.; Du, F. H.; Guo, X. X.; Jiang, Y. M.; Chen, J. S., Amorphous silicon with high specific surface area prepared by a sodiothermic reduction method for supercapacitors. *Chem. Commun.* **2013,** *49* (44), 5007-5009.

97. Loni, A.; Canham, L. T.; Defforge, T.; Gautier, G., Supercritically-dried porous silicon powders with surface areas exceeding 1000 m^2/g. *ECS J. Solid State Sci. Technol.* **2015,** *4* (8), 289-292.

98. Loni, A.; Defforge, T.; Caffull, E.; Gautier, G.; Canham, L. T., Porous silicon fabrication by anodisation: Progress towards the realisation of layers and powders with high surface area and micropore content. *Microporous Mesoporous Mater.* **2015,** *213*, 188-191.

99. Venuta, A.; Wolfram, J.; Shen, H.; Ferrari, M., Post-nano strategies for drug delivery: multistage porous silicon microvectors. *J. Mater. Chem. B* **2017,** *5* (2), 207-219.

100. Stojanovic, V.; Cunin, F.; Durand, J. O.; Garcia, M.; Gary-Bobo, M., Potential of porous silicon nanoparticles as an emerging platform for cancer theranostics. *J. Mater. Chem. B* **2016,** *4* (44), 7050-7059.

101. Bimbo, L. M.; Sarparanta, M.; Santos, H. A.; Airaksinen, A. J.; Makila, E.; Laaksonen, T.; Peltonen, L.; Lehto, V. P.; Hirvonen, J.; Salonen, J., Biocompatibility of thermally hydrocarbonized porous silicon nanoparticles and their biodistribution in rats. *ACS Nano* **2010,** *4* (6), 3023-3032.

102. Salonen, J.; Laitinen, L.; Kaukonen, A. M.; Tuura, J.; Bjorkqvist, M.; Heikkila, T.; Vaha-Heikkila, K.; Hirvonen, J.; Lehto, V. P., Mesoporous silicon microparticles for oral drug delivery: loading and release of five model drugs. *J. Control Release* **2005,** *108* (2-3), 362-374.

103. Nissinen, T.; Ikonen, T.; Lama, M.; Riikonen, J.; Lehto, V.-P., Improved production efficiency of mesoporous silicon nanoparticles by pulsed electrochemical etching. *Powder Technol.* **2016,** *288*, 360-365.

104. Pace, S.; Sciacca, B.; Geobaldo, F., Surface modification of porous silicon microparticles by sonochemistry. *RSC Adv.* **2013,** *3* (41), 18799-18802.

105. McInnes, S. J.; Michl, T. D.; Delalat, B.; Al-Bataineh, S. A.; Coad, B. R.; Vasilev, K.; Griesser, H. J.; Voelcker, N. H., "Thunderstruck": plasma-polymer-coated porous silicon microparticles as a controlled drug delivery system. *ACS Appl. Mater. Interfaces* **2016,** *8* (7), 4467-4476.

106. Kim, T.; Braun, G. B.; She, Z.-g.; Hussain, S.; Ruoslahti, E.; Sailor, M. J., Composite porous silicon–silver nanoparticles as theranostic antibacterial agents. *ACS Appl. Mater. Interfaces* **2016,** *8* (44), 30449-30457.

107. Qin, Z.; Joo, J.; Gu, L.; Sailor, M. J., Size control of porous silicon nanoparticles by electrochemical perforation etching. *Part. Part. Syst. Char.* **2014,** *31* (2), 252-256.

108. Roberts, D. S.; Estrada, D.; Yagi, N.; Anglin, E. J.; Chan, N. A.; Sailor, M. J., Preparation of photoluminescent porous silicon nanoparticles by high-pressure microfluidization. *Part. Part. Syst. Char.* **2017,** *34* (3), 1600326.

109. Boukherroub, R.; Wayner, D. D. M.; Sproule, G. I.; Lockwood, D. J.; Canham, L. T., Stability enhancement of partially-oxidized porous silicon nanostructures modified with ethyl undecylenate. *Nano Lett.* **2001,** *1* (12), 713-717.

110. Lees, I. N.; Lin, H.; Canaria, C. A.; Gurtner, C.; Sailor, M. J.; Miskelly, G. M., Chemical stability of porous silicon surfaces electrochemically modified with functional alkyl species. *Langmuir* **2003,** *19* (23), 9812-9817.

111. Wang, M.; Hartman, P. S.; Loni, A.; Canham, L. T.; Bodiford, N.; Coffer, J. L., Influence of surface chemistry on the release of an antibacterial drug from nanostructured porous silicon. *Langmuir* **2015,** *31* (22), 6179-85.

112. Velleman, L.; Shearer, C. J.; Ellis, A. V.; Losic, D.; Voelcker, N. H.; Shapter, J. G., Fabrication of self-supporting porous silicon membranes and tuning transport properties by surface functionalization. *Nanoscale* **2010,** *2* (9), 1756-1761.

113. Secret, E.; Wu, C. C.; Chaix, A.; Galarneau, A.; Gonzalez, P.; Cot, D.; Sailor, M. J.; Jestin, J.; Zanotti, J. M.; Cunin, F.; Coasne, B., Control of the pore texture in nanoporous silicon via chemical dissolution. *Langmuir* **2015,** *31* (29), 8121-8128.

114. Secret, E.; Leonard, C.; Kelly, S. J.; Uhl, A.; Cozzan, C.; Andrew, J. S., Size control of porous silicon-based nanoparticles via pore-wall thinning. *Langmuir* **2016,** *32* (4), 1166-1170.

115. Fry, N. L.; Boss, G. R.; Sailor, M. J., Oxidation-induced trapping of drugs in porous silicon microparticles. *Chem. Mater.* **2014,** *26* (8), 2758-2764.

116. Joo, J.; Cruz, J. F.; Vijayakumar, S.; Grondek, J.; Sailor, M. J., Photoluminescent porous Si/SiO_2 core/shell nanoparticles prepared by borate oxidation. *Adv. Funct. Mater.* **2014,** *24* (36), 5688-5694.

117. Song, J. H.; Sailor, M. J., Dimethyl sulfoxide as a mild oxidizing agent for porous silicon and its effect on photoluminescence. *Inorg. Chem.* **1998,** *37* (13), 3355-3360.

118. Buriak, J. M., Organometallic chemistry on silicon and germanium Surfaces. *Chem. Rev.* **2002,** *102* (5), 1271-1308.

119. Jarvis, K. L.; Barnes, T. J.; Prestidge, C. A., Surface chemistry of porous silicon and implications for drug encapsulation and delivery applications. *Adv. Colloid. Interface Sci.* **2012,** *175*, 25-38.

120. Amdouni, S.; Coffinier, Y.; Szunerits, S.; Zaïbi, M. A.; Oueslati, M.; Boukherroub, R., Catalytic activity of silicon nanowires decorated with silver and copper nanoparticles. *Semicond. Sci. Technol.* **2016,** *31* (1), 014011.

121. Zhang, C.; Chen, P.; Liu, J.; Zhang, Y.; Shen, W.; Xu, H.; Tang, Y., Ag microparticles embedded in Si nanowire arrays: a novel catalyst for gas-phase oxidation of high alcohol to aldehyde. *Chem. Commun.* **2008,** (28), 3290-3292.

122. Liao, F.; Wang, T.; Shao, M., Silicon nanowires: applications in catalysis with distinctive surface property. *J. Mater. Sci. Mater. Electron.* **2015,** *26* (7), 4722-4729.

123. Llorca, J.; Casanovas, A.; Trifonov, T.; Rodriguez, A.; Alcubilla, R., First use of macroporous silicon loaded with catalyst film for a chemical reaction: A microreformer for producing hydrogen from ethanol steam reforming. *J. Catal.* **2008,** *255* (2), 228-233.

124. Polisski, S.; Goller, B.; Wilson, K.; Kovalev, D.; Zaikowskii, V.; Lapkin, A., In situ synthesis and catalytic activity in CO oxidation of metal nanoparticles supported on porous nanocrystalline silicon. *J. Catal.* **2010,** *271* (1), 59-66.

125. Halim, M.; Tan, W.; Bakar, N.; Bakar, M., Surface characteristics and catalytic activity of copper deposited porous silicon powder. *Materials* **2014,** *7* (12), 7737-7751.

126. Liu, X.; Cheng, H.; Cui, P., Catalysis by silver nanoparticles/porous silicon for the reduction of nitroaromatics in the presence of sodium borohydride. *Appl. Surf. Sci.* **2014,** *292*, 695-701.

127. Tsang, C. H.; Liu, Y.; Kang, Z.; Ma, D. D.; Wong, N. B.; Lee, S. T., Metal (Cu, Au)-modified silicon nanowires for high-selectivity solvent-free hydrocarbon oxidation in air. *Chem. Commun.* **2009,** (39), 5829-5831.

128. Zhang, Y.; Han, X.; Liu, R.; Liu, Y.; Huang, H.; Zhang, J.; Yu, H.; Kang, Z., Tunable metal/silicon hybrid dots catalysts for hydrocarbon selective oxidation. *J. Phys. Chem. C* **2012,** *116* (38), 20363-20367.

129. Atwater, H. A.; Polman, A., Plasmonics for improved photovoltaic devices. *Nat. Mater.* **2010,** *9* (3), 205-213.

130. Kang, Z.; Tsang, C. H.; Wong, N. B.; Zhang, Z.; Lee, S. T., Silicon quantum dots: a general photocatalyst for reduction, decomposition, and selective oxidation reactions. *J. Am. Chem. Soc.* **2007,** *129* (40), 12090-12091.

131. Shao, M.; Cheng, L.; Zhang, X.; Ma, D. D.; Lee, S. T., Excellent photocatalysis of HF-treated silicon nanowires. *J. Am. Chem. Soc.* **2009,** *131* (49), 17738-17739.

132. Qu, Y.; Zhong, X.; Li, Y.; Liao, L.; Huang, Y.; Duan, X., Photocatalytic properties of porous silicon nanowires. *J. Mater. Chem.* **2010,** *20* (18), 3590-3594.

133. Oh, I.; Kye, J.; Hwang, S., Enhanced photoelectrochemical hydrogen production from silicon nanowire array photocathode. *Nano Lett.* **2012,** *12* (1), 298-302.

134. Ghosh, R.; Giri, P. K., Efficient visible light photocatalysis and tunable photoluminescence from orientation controlled mesoporous Si nanowires. *RSC Adv.* **2016,** *6* (42), 35365-35377.

135. Fellahi, O.; Barras, A.; Pan, G.-H.; Coffinier, Y.; Hadjersi, T.; Maamache, M.; Szunerits, S.; Boukherroub, R., Reduction of Cr(VI) to Cr(III) using silicon nanowire arrays under visible light irradiation. *J. Hazard. Mater.* **2016,** *304*, 441-447.

136. Ameen, S.; Park, D.-R.; Shin, H. S., Silicon nanowires arrays for visible light driven photocatalytic degradation of rose bengal dye. *J. Mater. Sci. Mater. Electron.* **2016,** *27* (10), 10460-10467.

137. Liu, D.; Li, L.; Gao, Y.; Wang, C.; Jiang, J.; Xiong, Y., The nature of photocatalytic "water splitting" on silicon nanowires. *Angew. Chem. Int. Ed. Engl.* **2015,** *54* (10), 2980-2985.

138. Chandrasekaran, S.; McInnes, S. J. P.; Macdonald, T. J.; Nann, T.; Voelcker, N. H., Porous silicon nanoparticles as a nanophotocathode for photoelectrochemical water splitting. *RSC Adv.* **2015,** *5* (104), 85978-85982.

139. Chandrasekaran, S.; Macdonald, T. J.; Gerson, A. R.; Nann, T.; Voelcker, N. H., Boron-doped silicon diatom frustules as a photocathode for water splitting. *ACS Appl. Mater. Interfaces* **2015,** *7* (31), 17381-17387.

140. Peng, F.; Wang, J.; Ge, G. L.; He, T.; Cao, L. X.; He, Y. H.; Ma, H.; Sun, S. Q., Photochemical reduction of CO_2 catalyzed by silicon nanocrystals produced by high energy ball milling. *Mater. Lett.* **2013,** *92*, 65-67.

141. Meekins, B. H.; Lin, Y. C.; Manser, J. S.; Manukyan, K.; Mukasyan, A. S.; Kamat, P. V.; McGinn, P. J., Photoactive porous silicon nanopowder. *ACS Appl. Mater. Interfaces* **2013,** *5* (8), 2943-2951.

142. Liu, R.; Yuan, G. B.; Joe, C. L.; Lightburn, T. E.; Tan, K. L.; Wang, D. W., Silicon nanowires as photoelectrodes for carbon dioxide fixation. *Angew. Chem. Int. Ed.* **2012,** *51* (27), 6709-6712.

143. Lee, H. Y.; Ryu, J.; Kim, J. H.; Lee, S. H.; Park, C. B., Biocatalyzed artificial photosynthesis by hydrogen-terminated silicon nanowires. *ChemSusChem* **2012,** *5* (11), 2129-2132.

144. Wang, F. Y.; Yang, Q. D.; Xu, G.; Lei, N. Y.; Tsang, Y. K.; Wong, N. B.; Ho, J. C., Highly active and enhanced photocatalytic silicon nanowire arrays. *Nanoscale* **2011,** *3* (8), 3269-3276.

145. Megouda, N.; Cofininier, Y.; Szunerits, S.; Hadjersi, T.; Elkechai, O.; Boukherroub, R., Photocatalytic activity of silicon nanowires under UV and visible light irradiation. *Chem. Commun.* **2011,** *47* (3), 991-993.

146. Lian, S. Y.; Tsang, C. H. A.; Kang, Z. H.; Liu, Y.; Wong, N.; Lee, S. T., Hydrogen-terminated silicon nanowire photocatalysis: Benzene oxidation and methyl red decomposition. *Mater. Res. Bull.* **2011,** *46* (12), 2441-2444.

147. Kang, Z.; Liu, Y.; Lee, S. T., Small-sized silicon nanoparticles: new nanolights and nanocatalysts. *Nanoscale* **2011,** *3* (3), 777-791.

148. Mao, D.; Kim, K. J.; Tsuo, Y. S.; Frank, A. J., Improved efficiency and stability of silicon photocathodes by electrochemical etching. *J. Phys. Chem.* **1995,** *99* (11), 3643-3647.

149. Xiao, W.; Jin, X.; Chen, G. Z., Up-scalable and controllable electrolytic production of photo-responsive nanostructured silicon. *J. Mater. Chem. A* **2013,** *1* (35), 10243-10250.

150. Betty, C. A.; Sasikala, R.; Jayakumar, O. D.; Sakuntala, T.; Tyagi, A. K., Photoelectrochemical properties of porous silicon based novel photoelectrodes. *Prog. Photovoltaics Res. Appl.* **2011,** *19* (3), 266-274.

151. Oh, J.; Deutsch, T. G.; Yuan, H.-C.; Branz, H. M., Nanoporous black silicon photocathode for H_2 production by photoelectrochemical water splitting. *Energy Environ. Sci.* **2011,** *4* (5), 1690-1694.

152. Sun, W.; Qian, C.; He, L.; Ghuman, K. K.; Wong, A. P. Y.; Jia, J.; Jelle, A. A.; O'Brien, P. G.; Reyes, L. M.; Wood, T. E.; Helmy, A. S.; Mims, C. A.; Singh, C. V.; Ozin, G. A., Heterogeneous reduction of carbon dioxide by hydride-terminated silicon nanocrystals. *Nat. Commun.* **2016,** *7*, 12553.

153. Cao, Y.; Gu, X. Y.; Yu, H. K.; Zeng, W.; Liu, X.; Jiang, S. H.; Li, Y. S., Degradation of organic dyes by Si/SiO_x core-shell nanowires: Spontaneous generation of superoxides without light irradiation. *Chemosphere* **2016,** *144*, 836-841.

154. Dasog, M.; Kraus, S.; Sinelnikov, R.; Veinot, J. G. C.; Rieger, B., CO_2 to methanol conversion using hydride terminated porous silicon nanoparticles. *Chem. Commun.* **2017,** *53* (21), 3114-3117.

155. Xu, Y.; Wang, L.; Jiang, W.; Wang, H.; Yao, J.; Guo, Q.; Yuan, L.; Chen, H., Silicon nanowire arrays - a new catalyst for the reduction of nitrobenzene derivatives. *ChemCatChem* **2013,** *5* (12), 3788-3793.

156. Ye, M.; Qian, C.; Sun, W.; He, L.; Jia, J.; Dong, Y.; Zhou, W., Dye colour switching by hydride-terminated silicon particles and its application as an oxygen indicator. *J. Mater. Chem. C* **2016,** *4* (20), 4577-4583.

157. Miyauchi, Y.; Sano, H.; Mizutani, G., Numerical analysis of second harmonic intensity images of a H–Si(111) surface after UV light pulse irradiation. *Appl. Surf. Sci.* **2008,** *255* (5), 3442-3446.

158. Chen, Z. H.; Tang, Y. B.; Liu, Y.; Kang, Z. H.; Zhang, X. J.; Fan, X.; Lee, C. S.; Bello, I.; Zhang, W. J.; Lee, S. T., Dye degradation induced by hydrogen-terminated silicon nanowires under ultrasonic agitations. *J. Appl. Phys.* **2009,** *105* (3), 034307.

159. Manilov, A. I.; Skryshevsky, V. A., Hydrogen in porous silicon — A review. *Mater. Sci. Eng.,B* **2013,** *178* (15), 942-955.

160. Vendamani, V. S.; Khan, S. A.; Dhanunjaya, M.; Pathak, A. P.; Rao, S. V. S. N., Energetic ion induced desorption of hydrogen from porous silicon studied by on-line elastic recoil detection analysis. *Microporous Mesoporous Mater.* **2017,** *246*, 81-88.

161. Stewart, M. P.; Buriak, J. M., Exciton-mediated hydrosilylation on photoluminescent nanocrystalline silicon. *J. Am. Chem. Soc.* **2001,** *123* (32), 7821-7830.

162. Tzur-Balter, A.; Shatsberg, Z.; Beckerman, M.; Segal, E.; Artzi, N., Mechanism of erosion of nanostructured porous silicon drug carriers in neoplastic tissues. *Nat. Commun.* **2015,** *6*, 6208.

163. Low, S. P.; Voelcker, N. H.; Canham, L. T.; Williams, K. A., The biocompatibility of porous silicon in tissues of the eye. *Biomaterials* **2009,** *30* (15), 2873-2880.

164. Wu, C. C.; Hu, Y.; Miller, M.; Aroian, R. V.; Sailor, M. J., Protection and delivery of anthelmintic protein Cry5B to nematodes using mesoporous silicon particles. *ACS Nano* **2015,** *9* (6), 6158-6167.

165. Savage, D. J.; Liu, X.; Curley, S. A.; Ferrari, M.; Serda, R. E., Porous silicon advances in drug delivery and immunotherapy. *Curr. Opin. Pharmacol.* **2013,** *13* (5), 834-841.

166. Park, J. H.; Gu, L.; von Maltzahn, G.; Ruoslahti, E.; Bhatia, S. N.; Sailor, M. J., Biodegradable luminescent porous silicon nanoparticles for in vivo applications. *Nat. Mater.* **2009,** *8* (4), 331-336.

167. Gupta, B.; Zhu, Y.; Guan, B.; Reece, P. J.; Gooding, J. J., Functionalised porous silicon as a biosensor: emphasis on monitoring cells in vivo and in vitro. *Analyst* **2013,** *138* (13), 3593-3615.

168. Lee, C.; Kim, H.; Hong, C.; Kim, M.; Hong, S. S.; Lee, D. H.; Lee, W. I., Porous silicon as an agent for cancer thermotherapy based on near-infrared light irradiation. *J. Mater. Chem.* **2008,** *18* (40), 4790-4795.

169. Hong, C.; Lee, J.; Zheng, H.; Hong, S. S.; Lee, C., Porous silicon nanoparticles for cancer photothermotherapy. *Nanoscale Res. Lett.* **2011,** *6* (1), 321.

170. Xiao, Q.; Gu, M.; Yang, H.; Li, B.; Zhang, C.; Liu, Y.; Liu, F.; Dai, F.; Yang, L.; Liu, Z.; Xiao, X.; Liu, G.; Zhao, P.; Zhang, S.; Wang, C.; Lu, Y.; Cai, M., Inward lithium-ion breathing of hierarchically porous silicon anodes. *Nat. Commun.* **2015,** *6*, 8844.

171. Zuo, X.; Xia, Y.; Ji, Q.; Gao, X.; Yin, S.; Wang, M.; Wang, X.; Qiu, B.; Wei, A.; Sun, Z.; Liu, Z.; Zhu, J.; Cheng, Y. J., Self-templating construction of 3D hierarchical macro-/mesoporous silicon from 0D silica nanoparticles. *ACS Nano* **2017,** *11* (1), 889-899.

172. Liang, J.; Li, X.; Hou, Z.; Zhang, W.; Zhu, Y.; Qian, Y., A deep reduction and partial oxidation strategy for fabrication of mesoporous Si anode for lithium ion batteries. *ACS Nano* **2016,** *10* (2), 2295-2304.

173. Choi, S.; Bok, T.; Ryu, J.; Lee, J.-I.; Cho, J.; Park, S., Revisit of metallothermic reduction for macroporous Si: compromise between capacity and volume expansion for practical Li-ion battery. *Nano Energy* **2015,** *12*, 161-168.

174. Wu, P.; Wang, H.; Tang, Y.; Zhou, Y.; Lu, T., Three-dimensional interconnected network of graphene-wrapped porous silicon spheres: in situ magnesiothermic reduction synthesis and enhanced lithium-storage capabilities. *ACS Appl. Mater. Interfaces* **2014,** *6* (5), 3546-3552.

175. Xing, A.; Zhang, J.; Bao, Z.; Mei, Y.; Gordin, A. S.; Sandhage, K. H., A magnesiothermic reaction process for the scalable production of mesoporous silicon for rechargeable lithium batteries. *Chem. Commun.* **2013,** *49* (60), 6743-6745.

176. Novoselov, K. S.; Geim, A. K.; Morozov, S. V.; Jiang, D.; Zhang, Y.; Dubonos, S. V.; Grigorieva, I. V.; Firsov, A. A., Electric field effect in atomically thin carbon films. *Science* **2004,** *306* (5696), 666-669.

177. Geim, A. K.; Novoselov, K. S., The rise of graphene. *Nat. Mater.* **2007,** *6* (3), 183-191.

178. Rao, C. N.; Sood, A. K.; Subrahmanyam, K. S.; Govindaraj, A., Graphene: the new two-dimensional nanomaterial. *Angew. Chem. Int. Ed. Engl.* **2009,** *48* (42), 7752-7777.

179. Zhang, N.; Zhang, Y.; Xu, Y. J., Recent progress on graphene-based photocatalysts: current status and future perspectives. *Nanoscale* **2012,** *4* (19), 5792-5813.

180. Hinnemann, B.; Moses, P. G.; Bonde, J.; Jorgensen, K. P.; Nielsen, J. H.; Horch, S.; Chorkendorff, I.; Norskov, J. K., Biomimetic hydrogen evolution: MoS_2 nanoparticles as catalyst for hydrogen evolution. *J. Am. Chem. Soc.* **2005,** *127* (15), 5308-5309.

181. Jaramillo, T. F.; Jorgensen, K. P.; Bonde, J.; Nielsen, J. H.; Horch, S.; Chorkendorff, I., Identification of active edge sites for electrochemical H_2 evolution from MoS_2 nanocatalysts. *Science* **2007,** *317* (5834), 100-102.

182. Gao, M. R.; Xu, Y. F.; Jiang, J.; Yu, S. H., Nanostructured metal chalcogenides: synthesis, modification, and applications in energy conversion and storage devices. *Chem. Soc. Rev.* **2013,** *42* (7), 2986-3017.

183. Golberg, D.; Bando, Y.; Huang, Y.; Terao, T.; Mitome, M.; Tang, C.; Zhi, C., Boron nitride nanotubes and nanosheets. *ACS Nano* **2010,** *4* (6), 2979-2993.

184. Bhimanapati, G. R.; Lin, Z.; Meunier, V.; Jung, Y.; Cha, J.; Das, S.; Xiao, D.; Son, Y.; Strano, M. S.; Cooper, V. R.; Liang, L.; Louie, S. G.; Ringe, E.; Zhou, W.; Kim, S. S.; Naik, R. R.; Sumpter, B. G.; Terrones, H.; Xia, F.; Wang, Y.; Zhu, J.; Akinwande, D.; Alem, N.; Schuller, J. A.; Schaak, R. E.; Terrones, M.; Robinson, J. A., Recent advances in two-dimensional materials beyond graphene. *ACS Nano* **2015,** *9* (12), 11509-11539.

185. Ong, W.-J.; Tan, L.-L.; Ng, Y. H.; Yong, S.-T.; Chai, S.-P., Graphitic carbon nitride (g-C_3N_4)-based photocatalysts for artificial photosynthesis and environmental remediation: are we a step closer to achieving sustainability? *Chem. Rev.* **2016,** *116* (12), 7159-7329.

186. Thomas, A.; Fischer, A.; Goettmann, F.; Antonietti, M.; Müller, J.-O.; Schlögl, R.; Carlsson, J. M., Graphitic carbon nitride materials: variation of structure and morphology and their use as metal-free catalysts. *J. Mater. Chem.* **2008,** *18* (41), 4893-4908.

187. Lam, S. M.; Sin, J. C.; Mohamed, A. R., A review on photocatalytic application of g-C_3N_4/semiconductor (CNS) nanocomposites towards the erasure of dyeing wastewater. *Mater. Sci. Semicond. Process.* **2016,** *47*, 62-84.

188. Liu, J.; Wang, H.; Antonietti, M., Graphitic carbon nitride "reloaded": emerging applications beyond (photo)catalysis. *Chem. Soc. Rev.* **2016,** *45* (8), 2308-2326.

189. Mamba, G.; Mishra, A. K., Graphitic carbon nitride (g-C_3N_4) nanocomposites: A new and exciting generation of visible light driven photocatalysts for environmental pollution remediation. *Appl. Catal., B.* **2016,** *198*, 347-377.

190. Feng, L.; He, F.; Yang, G.; Gai, S.; Dai, Y.; Li, C.; Yang, P., NIR-driven graphitic-phase carbon nitride nanosheets for efficient bioimaging and photodynamic therapy. *J. Mater. Chem. B* **2016,** *4* (48), 8000-8008.

191. Liu, J.-W.; Luo, Y.; Wang, Y.-M.; Duan, L.-Y.; Jiang, J.-H.; Yu, R.-Q., Graphitic carbon nitride nanosheets-based ratiometric fluorescent probe for highly sensitive detection of H_2O_2 and glucose. *ACS Appl. Mater. Interfaces* **2016,** *8* (49), 33439-33445.

192. Sakaushi, K.; Antonietti, M., Carbon- and nitrogen-based organic frameworks. *Acc. Chem. Res.* **2015,** *48* (6), 1591-1600.

193. Liebig, J., *Annalen* **1834,** *10* (10).

194. Zheng, Y.; Lin, L.; Wang, B.; Wang, X., Graphitic carbon nitride polymers toward sustainable photoredox catalysis. *Angew. Chem. Int. Ed. Engl.* **2015,** *54* (44), 12868-12884.

195. Liu, A. Y.; Cohen, M. L., Prediction of new low compressibility solids. *Science* **1989,** *245* (4920), 841-842.

196. Kroke, E.; Schwarz, M.; Horath-Bordon, E.; Kroll, P.; Noll, B.; Norman, A. D., Tri-s-triazine derivatives. Part I. From trichloro-tri-s-triazine to graphitic C_3N_4 structures. *New J. Chem.* **2002,** *26* (5), 508-512.

197. Sehnert, J.; Baerwinkel, K.; Senker, J., Ab initio calculation of solid-state NMR spectra for different triazine and heptazine based structure proposals of g-C_3N_4. *J. Phys. Chem. B* **2007,** *111* (36), 10671-10680.

198. Gong, Y.; Li, M.; Wang, Y., Carbon nitride in energy conversion and storage: recent advances and future prospects. *ChemSusChem* **2015,** *8* (6), 931-946.

199. Yew, Y. T.; Lim, C. S.; Eng, A. Y. S.; Oh, J.; Park, S.; Pumera, M., Electrochemistry of layered graphitic carbon nitride synthesised from various precursors: searching for catalytic effects. *ChemPhysChem* **2016**, *17* (4), 481-488.

200. Zheng, Y.; Zhang, Z.; Li, C., A comparison of graphitic carbon nitrides synthesized from different precursors through pyrolysis. *J. Photochem. Photobiol. A* **2017,** *332*, 32-44.

201. Zhang, G.; Zhang, J.; Zhang, M.; Wang, X., Polycondensation of thiourea into carbon nitride semiconductors as visible light photocatalysts. *J. Mater. Chem.* **2012,** *22* (16), 8083-8091.

202. Zhu, Y.; Li, X.; Zhu, M., Mesoporous graphitic carbon nitride as photo-catalyst for oxidative desulfurization with oxygen. *Catal. Commun.* **2016,** *85*, 5-8.

203. Fang, J.; Fan, H.; Zhu, Z.; Kong, L. B.; Ma, L., "Dyed" graphitic carbon nitride with greatly extended visible-light-responsive range for hydrogen evolution. *J. Catal.* **2016,** *339*, 93-101.

204. Xu, J.; Wang, Y.; Shang, J.-K.; Jiang, Q.; Li, Y.-X., Synthesis of mesoporous carbon nitride via a novel detemplation method and its superior performance in base-catalyzed reactions. *Catal. Sci. Technol.* **2016,** *6* (12), 4192-4200.

205. Yan, S. C.; Li, Z. S.; Zou, Z. G., Photodegradation performance of g-C_3N_4 fabricated by directly heating melamine. *Langmuir* **2009,** *25* (17), 10397-10401.

206. Zhang, Y.; Pan, Q.; Chai, G.; Liang, M.; Dong, G.; Zhang, Q.; Qiu, J., Synthesis and luminescence mechanism of multicolor-emitting g-C_3N_4 nanopowders by low temperature thermal condensation of melamine. *Sci. Rep.* **2013,** *3*, 1943.

207. Wang, X.; Maeda, K.; Thomas, A.; Takanabe, K.; Xin, G.; Carlsson, J. M.; Domen, K.; Antonietti, M., A metal-free polymeric photocatalyst for hydrogen production from water under visible light. *Nat. Mater.* **2009,** *8* (1), 76-80.

208. Liang, Q.; Li, Z.; Huang, Z. H.; Kang, F.; Yang, Q. H., Holey graphitic carbon nitride nanosheets with carbon vacancies for highly improved photocatalytic hydrogen production. *Adv. Funct. Mater.* **2015,** *25* (44), 6885-6892.

209. Xu, J.; Shang, J.-K.; Jiang, Q.; Wang, Y.; Li, Y.-X., Facile alkali-assisted synthesis of g-C_3N_4 materials and their high-performance catalytic application in solvent-free cycloaddition of CO_2 to epoxides. *RSC Adv.* **2016,** *6* (60), 55382-55392.

210. Tan, X.; Kou, L.; Tahini, H. A.; Smith, S. C., Conductive graphitic carbon nitride as an ideal material for electrocatalytically switchable CO_2 capture. *Sci. Rep.* **2015,** *5*, 17636.

211. Sun, L.; Yang, M.; Huang, J.; Yu, D.; Hong, W.; Chen, X., Freestanding graphitic carbon nitride photonic crystals for enhanced photocatalysis. *Adv. Funct. Mater.* **2016**, *26* (27), 4943-4950.

212. Niu, P.; Zhang, L.; Liu, G.; Cheng, H.-M., Graphene-like carbon nitride nanosheets for improved photocatalytic activities. *Adv. Funct. Mater.* **2012,** *22* (22), 4763-4770.

213. Qiu, P.; Chen, H.; Xu, C.; Zhou, N.; Jiang, F.; Wang, X.; Fu, Y., Fabrication of an exfoliated graphitic carbon nitride as a highly active visible light photocatalyst. *J. Mater. Chem. A* **2015,** *3* (48), 24237-24244.

214. Han, Q.; Wang, B.; Gao, J.; Cheng, Z.; Zhao, Y.; Zhang, Z.; Qu, L., Atomically thin mesoporous nanomesh of graphitic C_3N_4 for high-efficiency photocatalytic hydrogen evolution. *ACS Nano* **2016,** *10* (2), 2745-2751.

215. Zhang, X.; Xie, X.; Wang, H.; Zhang, J.; Pan, B.; Xie, Y., Enhanced photoresponsive ultrathin graphitic-phase C_3N_4 nanosheets for bioimaging. *J. Am. Chem. Soc.* **2013,** *135* (1), 18-21.

216. Han, Q.; Hu, C.; Zhao, F.; Zhang, Z.; Chen, N.; Qu, L., One-step preparation of iodine-doped graphitic carbon nitride nanosheets as efficient photocatalysts for visible light water splitting. *J. Mater. Chem. A* **2015,** *3* (8), 4612-4619.

217. Han, Q.; Zhao, F.; Hu, C. G.; Lv, L. X.; Zhang, Z. P.; Chen, N.; Qu, L. T., Facile production of ultrathin graphitic carbon nitride nanoplatelets for efficient visible-light water splitting. *Nano Res.* **2015,** *8* (5), 1718-1728.

218. Zhu, K. X.; Wang, W. J.; Meng, A.; Zhao, M.; Wang, J. H.; Zhao, M.; Zhang, D. L.; Jia, Y. P.; Xu, C. H.; Li, Z. J., Mechanically exfoliated g-C_3N_4 thin nanosheets by ball milling as high performance photocatalysts. *RSC Adv.* **2015,** *5* (69), 56239-56243.

219. Chen, L.; Huang, D.; Ren, S.; Dong, T.; Chi, Y.; Chen, G., Preparation of graphite-like carbon nitride nanoflake film with strong fluorescent and electrochemiluminescent activity. *Nanoscale* **2013,** *5* (1), 225-230.

220. Xu, J.; Zhang, L.; Shi, R.; Zhu, Y., Chemical exfoliation of graphitic carbon nitride for efficient heterogeneous photocatalysis. *J. Mater. Chem. A* **2013,** *1* (46), 14766-14772.

221. Shi, L.; Chang, K.; Zhang, H.; Hai, X.; Yang, L.; Wang, T.; Ye, J., Drastic enhancement of photocatalytic activities over phosphoric acid protonated porous g-C_3N_4 nanosheets under visible light. *Small* **2016,** *12* (32), 4431-4439.

222. Zhang, J.; Chen, Y.; Wang, X., Two-dimensional covalent carbon nitride nanosheets: synthesis, functionalization, and applications. *Energy Environ. Sci.* **2015,** *8* (11), 3092-3108.

223. Zhao, Z.; Sun, Y.; Dong, F., Graphitic carbon nitride based nanocomposites: a review. *Nanoscale* **2015,** *7* (1), 15-37.

224. Zollinger, H., *Color Chemistry: Synthesis, Properties of Organic Dyes and Pigments*. USA: VCH Publishers: New York, 1987.

225. Houas, A., Photocatalytic degradation pathway of methylene blue in water. *Appl. Catal. B* **2001,** *31* (2), 145-157.

226. Drumond Chequer, F. M.; de Oliveira, G. A. R.; Anastacio Ferraz, E. R.; Carvalho, J.; Boldrin Zanoni, M. V.; de Oliveir, D. P., Textile dyes: dyeing process and environmental impact. **2013**.

227. Bafana, A.; Devi, S. S.; Chakrabarti, T., Azo dyes: past, present and the future. *Environ. Rev.* **2011,** *19*, 350-371.

Chapter 2

Materials and Experimental Details

Abstract

The fundamental part of our work is based on the synthesis and characterization of semiconductor material of interest including mesoporous silicon, graphitic carbon nitride (g-C_3N_4) and their hybrid composites. The preparation methods and related experimental variables used for sample production and modification are depicted in detail. A general discussion of the characterization techniques featured in this study is provided. Lastly, photocatalytic experiments and analytic methods are included.

2.1 Materials

2.1.1 Silicon wafers

Boron-doped p-type monocrystalline Si wafers were used in the electrochemical preparation of mesoporous silicon with various porous morphologies studied in this research. The wafer specifications (crystal orientation, electrical resistivity, diameter, thickness etc.) are summarized in Table 2.1, which includes both moderately doped and heavily doped Si wafers, labelled as PS and HPS respectively.

Table 2.1 Specifications of the silicon wafers used in the preparation of mesoporous silicon.

	PS	**HPS**
Dopant	Boron / p-type	Boron / p-type
Orientation	(100) ± 0.5 ˚	(100) ± 0.9 ˚
Resistivity / Ω·cm	1-10	0.001-0.01
Diameter / mm	100 ± 0.3	100 ± 0.3
Thickness / μm	525 ± 25	300 ± 25
Single side polished	Yes	Yes
Backside etched	Yes	Yes
Manufacturer	Compart Technology U.K.	Virginia Semiconductor USA

2.1.2 Chemical reagents and materials

The chemical reagents and other materials used in this research are listed in Table 2.2. All chemicals were used as received unless otherwise stated.

Table 2.2 List of chemical reagents and materials used in this study.

Substance	Grade	Source
Acetone	≥ 99.5%	Sigma-Aldrich
Allyl mercaptan (C_3H_6S)	60%	Sigma-Aldrich
Calcium chloride hexahydrate ($CaCl_2{\cdot}6H_2O$)	98%	Sigma-Aldrich
Dichloromethane (DCM)	≥ 99.8%	Sigma-Aldrich
Diethyl ether	2% ethyl alcohol	Sigma-Aldrich
Distilled water	Thermo Scientific NanoPure purification system	Produced on site
Ethanol (C_2H_5OH)	≥ 99.8%	Sigma-Aldrich
Hexane	≥ 95%	Sigma-Aldrich
Hydrofluoric acid (HF)	48-51 wt. % in water	Acros Organics
Hydrogen peroxide (H_2O_2)	30% (*w*/*w*) in H_2O	Sigma-Aldrich
Isopropyl alcohol (C_3H_7OH)	≥ 99.7%	Sigma-Aldrich
Melamine ($C_3H_6N_6$)	99%	Sigma-Aldrich
Methyl orange ($C_{14}H_{14}N_3NaO_3S$)	MW 327.33	Fluka Analytical
Potassium hydroxide (KOH)	≥ 85%, MW 56.11	Fisher Chemical
Silicon powder	99.95%, 60 nm	*io-li-tec* nanomaterials
Silicon dioxide, nanopowder (SiO_2)	99.5%, 5-15 nm (BET)	Sigma-Aldrich
Silicone oil	For oil bath (-50˚C to 200˚C)	Sigma-Aldrich
Sulfanilic acid	99%	Sigma-Aldrich
Toluene	99.8%	Sigma-Aldrich
Triethanolamine	≥ 99.0%	Sigma-Aldrich

2.2 Experimental methods

This section summarizes the experimental procedures with corresponding chemicals and apparatus related to the preparation and modification of mesoporous silicon (2.2.1) and graphitic carbon nitride materials (2.2.2), followed by the synthesis of the mesoporous silicon/graphitic carbon nitride composites as outlined in 2.2.3.

2.2.1 Mesoporous silicon (mpSi)

2.2.1.1 Preparation of mpSi by electrochemical etching

The crystalline wafer (PS and HPS) was first cut into small square-shaped Si chips of dimensions 1.3 cm × 1.3 cm using a diamond scribe pen to match the configuration of the etching cell. Prior to the porosification, Si chips were first ultrasonically degreased in ethanol and then dipped into dilute HF/ethanol solution in a petri dish at room temperature to remove the insulating surface oxides.

For each etching experiment, one so-obtained oxide-free Si chip was used. It was mounted at the bottom of a custom-made Teflon cell using an O-ring, along with a platinum plate acting as current collector. A schematic diagram of the electrochemical cell was presented in Scheme 2.1. This allowed about 1 cm^2 of the Si wafer surface (polished side) to be exposed to the homogeneously mixed electrolyte solution composed of equivalent volume of 48-51% HF aqueous solution and absolute ethanol. The addition of ethanol can increase the wettability and assist the removal of H_2 evolved at the Pt cathode thus creating a uniform porous structure on the Si chip. A tungsten (W) coil was placed under the Pt plate to connect with a Keithley Sourcemeter Model 2601, which provided a constant external current to drive the continuous etching process.

After etching, the electrolyte solution was removed and disposed of in a waste bottle containing calcium chloride ($CaCl_2$). Then the etched Si chip was carefully transferred to a Schlenk flask under nitrogen atmosphere and dried under vacuum for 4-6 hours at room temperature until all the liquid residues were completely removed. After drying,

the mpSi sample was stored under a nitrogen atmosphere in the same Schlenk flask to avoid degradation prior to use.

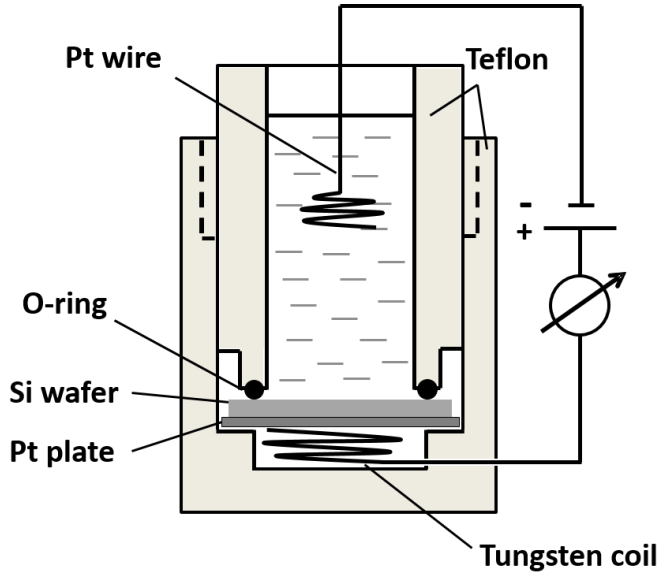

Scheme 2.1 Schematic diagram of the two-electrode electrochemical etching cell employed in the preparation of mesoporous silicon.

Table 2.3 Etching parameters of mesoporous silicon samples mainly studied in this work.

Mesoporous silicon	**Etching current density (*J*) / mA·cm^{-2}**	**Etching time (*t*) / min**
PS-30-15	30	15
PS-60-05	60	05
PS-60-15	60	15
HPS-150-05	150	05
HPS-150-10	150	10
HPS-200-05	200	05

Etching conditions such as etching current density (*J,* mA·cm^{-2}) and etching time (*t,* min) can be adjusted conveniently on Keithley Sourcemeter and a variety of mpSi materials were manufactured via the route above using varied *J* and *t*, named as "PS-*J*-*t*" or

"HPS-*J*-*t*", representing the different Si wafer type (PS/HPS, Table 2.1) used in the preparation. For reference, the major mpSi samples heavily involved in this work are listed above in Table 2.3.

Scheme 2.2 shows the typical "CD disk" appearance and physical dimensions of the as-etched mpSi layer. As mentioned above, the etched area on the Si chip was pre-determined by the cell configuration, as a 1.1 cm diameter circle shape. Another feature is the thickness (*h*) of the mpSi layer, which greatly depends on the exact etching parameters (*J* and *t*). The total volume of mpSi disk can be calculated following Equation 2.1.

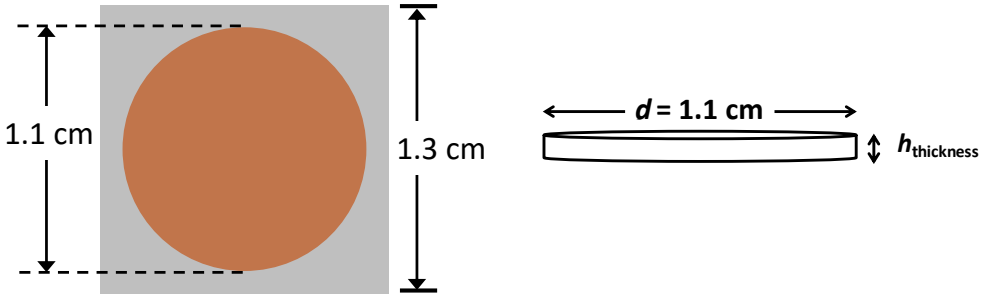

Scheme 2.2 Schematic diagram of as-etched mesoporous silicon formed on Si chip by electrochemical etching.

$$V = \pi \left(\frac{d}{2} \right)^2 \cdot h_{\text{thickness}} \qquad \text{Equation 2.1}$$

2.2.1.2 Preparation of mpSi disks and microflakes

As seen in Scheme 2.3, after electrochemical etching (Step 1), mpSi was formed and it was processed directly by a procedure known as "lift-off" to generate a free-standing mpSi disk (PS/HPS-*J*-*t*-D, Step 2).[1] By enlarging the pores at the pore tip, neighbouring pores will eventually overlap and completely undercut the mpSi layer from the wafer at

the bottom.[2] The resulting disks were collected and sonicated into microparticles (PS/HPS-*J*-*t*-F, Step 3). Detailed descriptions of the processing procedures are as follows.

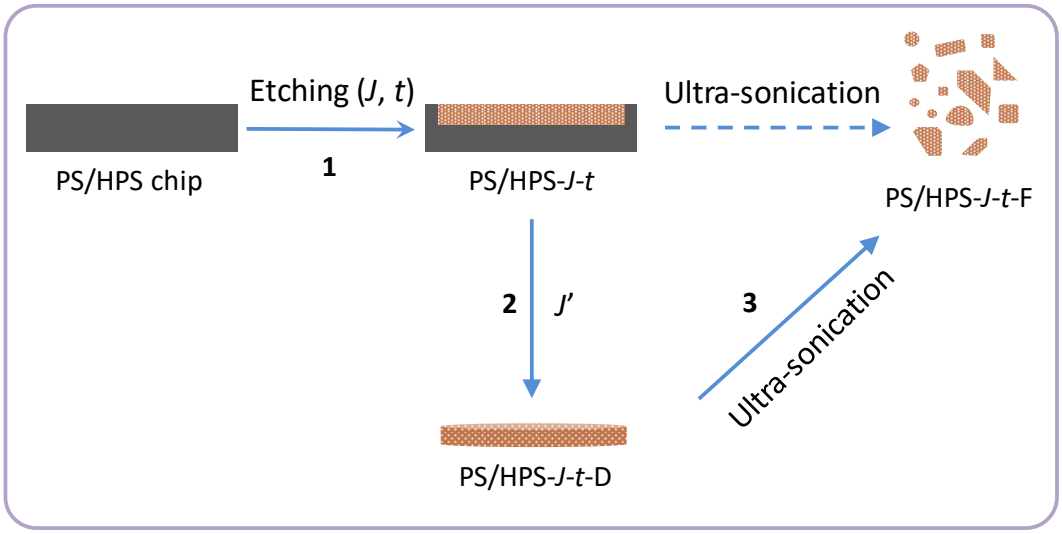

Scheme 2.3 Processing routes for mesoporous silicon disks and microflakes.

The electrochemical etching cell with the chip bound mpSi was refilled with dilute HF solution (3% by volume of 48% aqueous HF in ethanol) right after the removal of HF electrolyte used in the preparation of mpSi. Then 4 $mA \cdot cm^{-2}$ external current (*J'*) was supplied for 30-125 s. Once finished, the chip was lifted out of the etching cell and any liquid residue on the wafer surface was gently absorbed by filter papers (Whatman™, 90 mm). Thereafter it was dipped into hexane to obtain the free standing mpSi disk by reducing the adherence to Si chip, followed by drying under vacuum for 12 hours at room temperature and stored under nitrogen atmosphere prior to use.

Dried mpSi disks were then collected in a glass vial containing 10-15 mL DCM, which was constantly stirred using a magnetic stir bar to enhance the processing volume of the microtip sonicator (Apollo Electronics, output level 4). During sonication, the glass vial was continuously placed in ice bath to prevent heat build-up. Powdered mpSi were recovered after 30 min sonication by evaporating the solvent under vacuum and dried in a vacuum oven (Fistreem Ltd.) at 80˚C overnight.

2.2.1.3 Surface oxidation

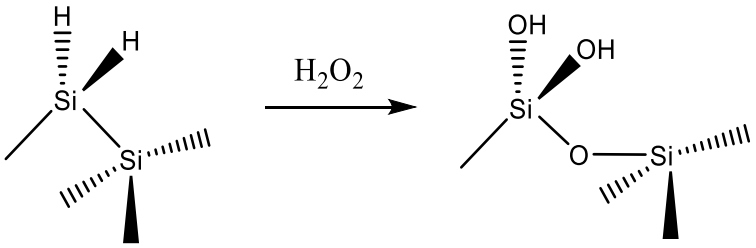

Scheme 2.4 Surface oxidization reaction for porous silicon oxidized by H_2O_2.

Silicon hydrides on the surface of mpSi pores have a dramatic influence on the photocatalytic behaviour. In this study, H_2O_2 was used to quench these species, as its use is simple and efficient (Scheme 2.4). In a plastic petri dish or a plastic centrifuge tube for free standing samples, mpSi was soaked in dilute H_2O_2 aqueous solution (4 wt. %) under static condition for 2-4 hours. The treated mpSi samples (PS/HPS-*J*-*t*-[O]) were rinsed with ethanol and distilled water after being separated from H_2O_2, and dried in a vacuum oven at 80 ˚C overnight.

2.2.1.4 Surface hydrosilylation

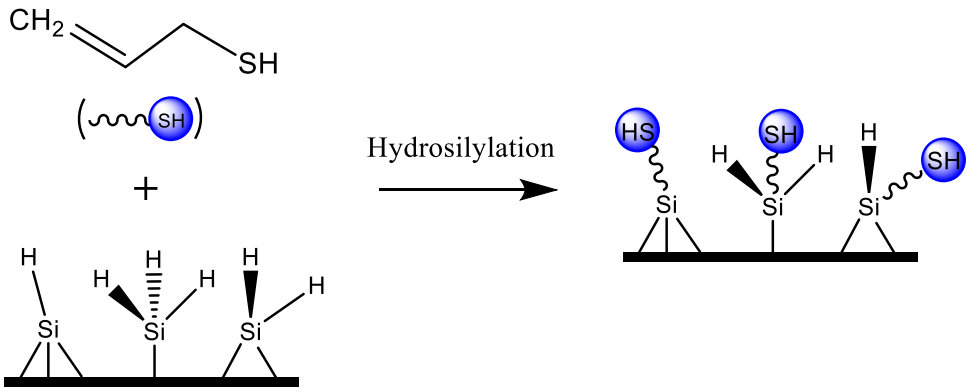

Scheme 2.5 Schematic diagram of grafting allyl mercaptan onto H-terminated mesoporous silicon via thermal hydrosilylation reaction.

As proposed, allyl mercaptan (C_3H_5SH) was intended to be grafted onto the surface of mesoporous silicon because of the potential applications of thiol-functionalized mpSi in many areas as drug delivery vector or catalyst support.[3-5] Through an addition reaction between Si-H bonds on the mpSi surface and the alkene group of the ligand molecules, Si-C bridges can be formed and hence covalently link the thiols to the silicon surface, as seen in Scheme 2.5. In this study, thermal energy was introduced to overcome the reaction barrier of which the reaction process can be interpreted as a radical mechanism[6] as outlined in Scheme 2.6. At higher temperature, the reaction occurs through homolytic cleavage of a surface Si-H group to produce a silicon radical which immediately reacts with an olefin molecule and forms a Si-C bond which links the molecule onto the surface. The carbon-based radical then abstracts a hydrogen atom from a neighbouring Si-H group on the surface.

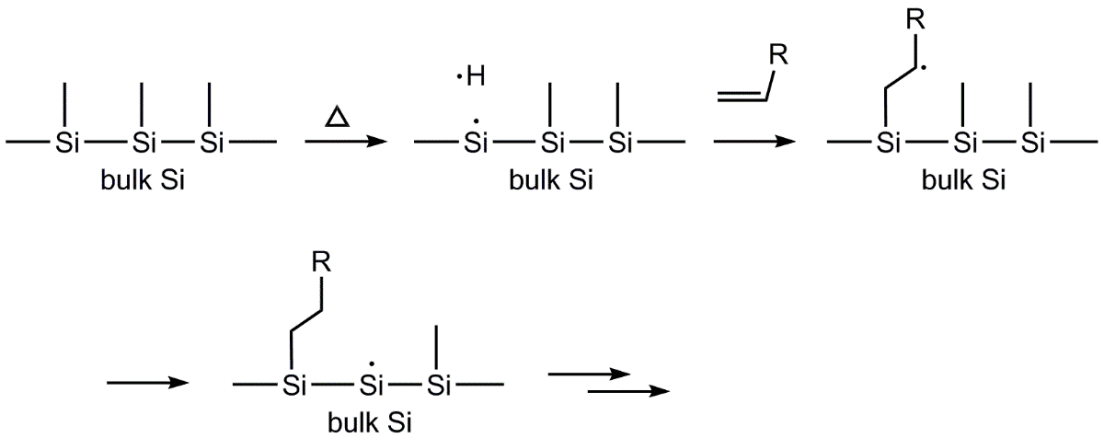

Scheme 2.6 Reaction mechanism for radical-based hydrosilylation.

A silicone oil bath (max 200°C) was used for heating the Schlenk flask containing mpSi (PS/HPS-*J*-*t*) and a mixture of toluene and allyl mercaptan. The flask was heated to reflux under a nitrogen atmosphere and maintained for 12-48 hours as indicated in Chapter 3.

The mixture of toluene and allyl mercaptan with mpSi were sealed in a Teflon lined stainless steel autoclave (50 mL) and heated in a conventional oven (GenLab Ltd.) at temperatures up to 200˚C.

A domestic multi-mode microwave oven (Hinari, Max 800 Watt) was used to heat the reaction mixture contained in a borosilicate glass vial. Three power modes (Full/Medium/Low) are available and the Medium powder mode was used throughout the experiment. As shown in Figure 2.1, microwave irradiation was applied at regular intervals to enable the dissipation of thermal energy released under microwave field for safety reasons. By using professional microwave reactors designed for research purposes, it may not be necessary through real-time temperature control.[7-9]

After each experiment, the reactor was first cooled to room temperature. The excess of unreacted and physisorbed reagent was removed by rinsing with diethyl ether. Samples were dried under a stream of N_2.

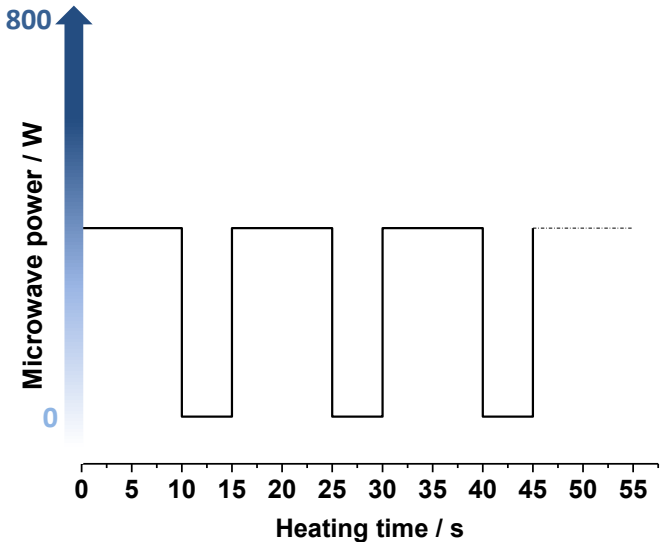

Figure 2.1 Microwave power in the microwave-assisted surface modification of mesoporous silicon with allyl mercaptan. For each cycle, the system was heated for 10 s under microwave irradiation and then the microwave irradiation was stopped for 5 s.

2.2.2 Graphitic carbon nitride materials (g-C_3N_4)

2.2.2.1 Synthesis of g-C_3N_4 bulk powders

In this work, graphitic carbon nitride was synthesised through thermal polycondensation of melamine as reported previously.[10-13] In a typical synthetic process, 2.5 g of melamine

was put into an alumina boat covered by Al foil and was subsequently annealed at T = 550˚C for 2 hours (t) at a heating rate of 10 ˚C·min^{-1} (ΔT) in a tube furnace (Carbolite model CTF-121651550) in static air. After cooling to room temperature, the yellow coloured products were then ground into powders as shown in Figure 2.2.

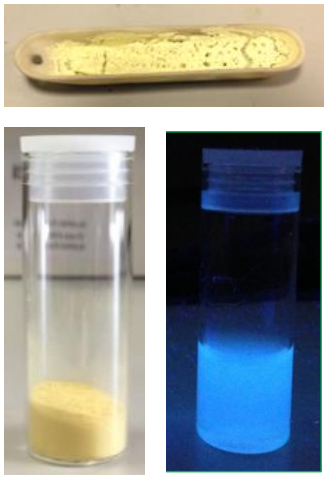

Figure 2.2 Photographs of as-synthesized graphitic carbon nitride after pyrolysis of melamine and grinding and its aqueous dispersion under 365 nm UV lamp at room temperature.

2.2.2.2 Synthesis of g-C_3N_4 nanosheets

As inspired by the methods employed in the delamination of layered materials (graphite, MoS_2 etc.),[14] free standing g-C_3N_4 nanosheets (g-C_3N_4 NSs) were prepared by one-pot exfoliation of the bulk g-C_3N_4 solids as obtained above through simple sonication in a polar solvent. Many studies devoted to this purpose often involve the pre-treatment of protonation by using caustic chemicals such as H_2SO_4,[15-16] HNO_3,[17-18] HCl,[19] H_3PO_4[20] etc. to assist the peeling process. Although this strategy could reduce the sonication time, the overall preparation time required is actually extended. Thus we simplified the procedure to use only a solvent, such as distilled water,[21] methanol, acetone, DMSO, THF etc.[22] to minimize the environmental impact and promote the delamination of g-C_3N_4. As revised from the previously reported approach,[23] isopropanol was adopted as the dispersion medium here as it was found to be more efficient than water and acetone in our preliminary experiments.

Typically, 100 mg bulk g-C_3N_4 powders were added into 100 mL round bottom flask with 50 mL isopropanol and then sonicated for 10 hours at ambient conditions. Then the suspension was centrifuged at 3000 rpm for 10 min to remove aggregated large particles, giving rise to a homogeneously dispersed g-C_3N_4 nanosheets solution with a light-yellow colour and can be stably stored for days. For the solid sample, the supernatant was next centrifuged at 14000 rpm for 10 min and re-dispersed in 25 mL H_2O, and taken to a freeze-dryer at -80˚C under reduced pressure 10 Pa for 3 days.

2.2.3 Porous silicon/carbon nitride composites (mpSi/g-C_3N_4 NSs)

Free standing mesoporous silicon microflakes were fabricated following the procedures mentioned above in 2.2.1 and used in the preparation of mpSi/g-C_3N_4 NSs composite via liquid phase impregnation. 20 mg mpSi powders were added into 0.5 mL, 2.0 mL, 8.0 mL of the condensed isopropanol dispersion of g-C_3N_4 NSs obtained above (10 mg·mL^{-1}) with subsequent addition of 9.5 mL, 8.0 mL, 2.0 mL acetone to keep a constant mixture volume as 10 mL. Then it was stirred overnight at room temperature before evaporating the organic solvent under vacuum and annealed in a conventional vacuum oven at 70˚C overnight. The compositional ratio of mpSi/g-C_3N_4 NSs composite was varied with *m*(Si):*m*(g-C_3N_4) as 4:1, 1:1 and 1:4 respectively.

2.3 Characterisation techniques

A range of imaging and spectroscopic techniques was employed to identify and characterise the morphological features and physiochemical properties of obtained materials studied in this research. The basic principles and instrumental parameters are described as follows.

2.3.1 Electron microscopy

Electron microscopy is one of the most widely used techniques in material characterisation for the ability to record the physical appearance of materials up to atomic details. It also reveals information about the elemental composition of the materials by detecting the X-rays produced by the interaction of the electrons with sample matter. As indicated in Figure 2.3, a variety of signals can be detected and analysed after the incident e-beam hits the sample depending on required structural and compositional information.

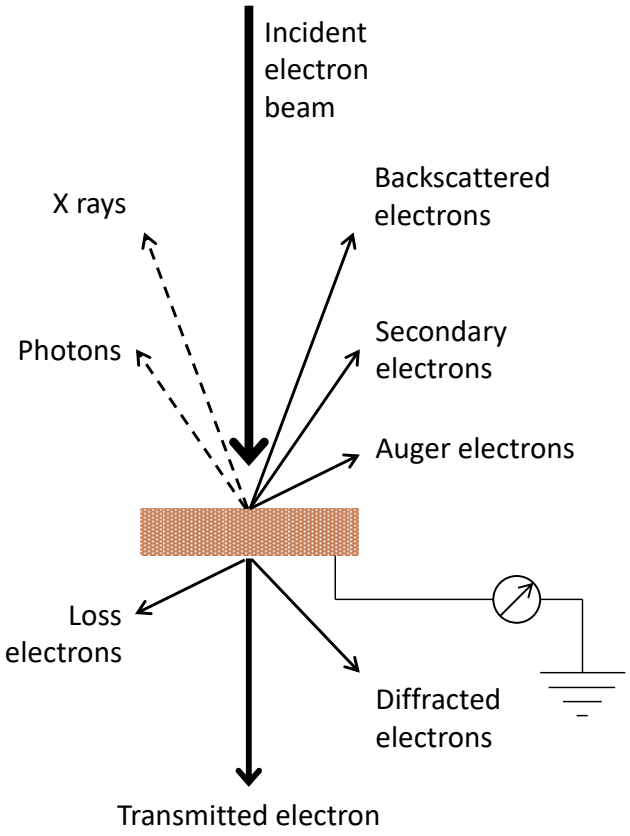

Figure 2.3 Detectable signals from the interaction of incident electron beam with sample material under investigation in electron microscopy.

2.3.1.1 Scanning electron microscopy (SEM) and field emission scanning electron microscopy (FE-SEM)

By detecting the yield of secondary or backscattered electrons as a function of the position of the focused e-beam, the surface region of sample material can be imaged directly through a quick scanning.[24] Due to shadowing of emitted electrons by rough surfaces, secondary electron images (SEI) can provide an excellent view of surface topography. While backscattered electron images can reveal valuable information on the chemical composition because of the sensitivity of backscattering to the atomic number of the target atoms. The elemental composition can be further measured by elemental analysis using energy dispersive X-ray (EDX) technique of the SEM and FE-SEM facilities.

In this thesis, all plane-view and cross section images were taken mainly under SEI mode on a JEOL JSM 5900LV (SEM), and FEI Helios Nanolab 400S (FE-SEM). Samples were fixed by a double-sided adhesive carbon tape on an aluminium specimen stub specified for electron microscope use. The acceleration voltage was 20 kV for SEM and 5 kV for FE-SEM. The magnification was varied up to 10k for SEM and 500k for FE-SEM. The high magnification and spatial resolution of FE-SEM facilitated the observation of the very fine structural features of the materials.

2.3.1.2 High-resolution transmission electron microscope (HRTEM)

Transmission electron microscopy (TEM) is used to provide some of the most detailed information on the internal structure of the material. As shown in Figure 2.3, when a sample of interest is irradiated by e-beam, a fraction of electrons passes through it without suffering much energy loss. The amount of energy lost depends on the sample thickness under scope. An image of the sample is thus impressed into the transmitted electrons and is then magnified by subsequent electromagnetic lenses. Similar to SEM and FE-SEM, TEM can also carry out elemental analysis such as EDX analysis, and electron energy loss spectroscopy (EELS) on very small regions of a sample.[24] It can also record selected area diffraction pattern (SAED analysis) which allows important

evaluation of the crystallinity of the specimen and determination of the crystallographic phases.[25] While the more advanced HRTEM technique could further extend the imaging capability of traditional TEM and improve the data quality substantially by making use of the high-energy electron beams and superior atomic resolution.

In this thesis, bright-field images and diffraction patterns were acquired with an FEI Titan 80-300 microscope equipped with a high-brightness Schottky-field emission electron source and working voltage of 300 kV. All mpSi samples for the TEM observations were prepared by suspending them in ethanol and dip-casted onto Cu-coated TEM grids. Particle size and interplanar spacing measurements were performed by using Gatan Digital Micrograph version 3.6.4.

2.3.2 X-ray powder diffraction (XRD)

Wide-angle XRD is very useful in analysing the bulk crystallinity of nanomaterials. By monitoring the elastic scattering of X-ray photons by atoms in a periodic lattice, crystallographic phases and lattice parameters can be identified according to Bragg's law as expressed in the Bragg formula below.

$$n\lambda = 2d\sin\theta \qquad \text{Equation 2.2}$$

In Equation 2.2, n is an integer representing the orders of the diffraction, λ is the wavelength of the X-ray, θ is Bragg angle, the half of the deviation of the diffracted beam, and d is the interplanar spacing for a lattice plane.[26]

For crystal size below 100 nm, the narrow diffraction lines from perfect crystals become broadened due to incomplete destructive interference in scattering directions where the X-ray is out of phase. Thus the mean size of nanocrystallites (τ) can be calculated based on Scherrer's formula (Equation 2.3).[27] The width of diffraction peaks (β) carries

information on the dimensions of the reflecting planes related to crystal sizes. *k* is the shape factor that depends on the specific shape and size distribution of the crystalline cluster. In this work it was adopted as the typical value of 0.9 for spherical particles.[28]

$$t = \frac{kl}{b\cos q} \qquad \text{Equation 2.3}$$

In this thesis, XRD patterns were recorded on a Thermo ARL Xtra diffractometer with Cu Kα radiation (λ = 1.540562 Å) at 45 kV and 40 mA. All scans were made in a 2θ range of 30-80° with a step size of 0.01° and a step time of 1 s using aluminium sample holders. Scherrer calculation was performed by using MDI Jade version 5.0.

2.3.3 Nitrogen adsorption-desorption isotherms

The properties of surface area, pore size and size distribution in porous materials is crucial in understanding the physiochemical/optical/electrical behaviours of semiconductors. Among various methods for pore determination, low temperature gas adsorption is a popular tool in analysing the complete range of micro- and mesopores, which has already been successfully applied in the characterisation of a variety of porous solids with different morphologies and chemical compositions.[29-30] It is based on physisorption, which is a very common general phenomenon and occurs when gas molecules (adsorbate) are brought into contact with the surface of a solid material (adsorbent) through the van der Waals forces. This process can be generally divided into stages that include micropore filling, monolayer-multilayer formation, pore condensation for typical micro-mesoporous materials.[30] At a given temperature and adsorbate gas e.g. 77 K for N_2, the gas adsorption and desorption behaviours at each of these stages are primarily governed by the geometrical factors of the solid sample investigated. Its surface and porous structure are therefore distinguishable by the shape

of physisorption isotherms and associated hysteresis loops, defined by the IUPAC recommendations published in 2015.[31]

In this thesis, nitrogen sorption isotherms were performed at 77 K on a Quantachrome Autosorb-1. Each chip of mpSi was cut into two pieces to be able to fit into the sample cell (inner d. 10 mm), while free standing powder samples were used directly. Before each measurement, samples were outgassed under vacuum at elevated temperature overnight to eliminate any adsorbed moisture. The specific surface area was acquired from the adsorption branch via the application of Brunauer-Emmett-Teller theory (BET).[32] The traditional linear range P/P_0 = 0.05 to 0.3 was adopted to derive the BET plot. The micropore analysis was conducted using the *t*-plot method. The data points used for this method were in the normal t-plot range P/P_0 = 0.2-0.7. The Barrett-Joyner-Halenda (BJH) approach was used to predict the pore size distribution.[33] The total pore volume was obtained from the amount of gas adsorbed at P/P_0 = 0.96. All the calculations were computed using Quantachrome AS1WIN version 2.11.

The mass of as-etched pSi was evaluated by subtracting the mass of unetched silicon (m_1) from the initial weight (m_0) taken after electrochemical etching. Due to the more strained nature of Si-Si bond in porous structure, m_1 was derived by dissolving pSi in dilute KOH aqueous solution (5% *w*/*v*). Both values were measured after degassing at 150˚C under vacuum overnight by using the outgassing station with which the Quantachrome Autosorb-1 is equipped.

2.3.4 Fourier transform infrared spectroscopy (FTIR)

Infrared spectroscopy is a simple and sensitive spectroscopic method widely used in both organic and inorganic chemistry, as well as in semiconductor research. By detecting the position (wavenumber, cm^{-1}) and intensity of characteristic vibrational absorption bands, the chemical composition can be identified. The raw data recorded is then turned into the actual transmittance or absorbance spectrum, by a data-processing technique called Fourier transform. The IR spectrum of solid-state sample can be directly collected as solid by using attenuated total reflectance technique (ATR). Sample is pressed against

the face of a single crystal (ATR crystal). The infrared radiation passes through the crystal and only interacts with the sample at the interface between the two materials.
In this thesis, FTIR measurements were carried out using PerkinElmer Spectrum 400 equipped with an ATR accessory. Each IR spectrum was averaged over 32 scans with a resolution of 4 cm^{-1}.

2.3.5 Raman scattering

Raman spectroscopy is a fast and non-destructive tool to investigate the vibrational and electronic properties of materials as well as the inner stress, strain and disorders.[34] By studying the first order Raman spectra, the crystalline, amorphous or nano-crystalline nature of semiconductor materials can be verified.[35] The physics behind Raman scattering in semiconductors is based on the inelastic interaction of incident photons with lattice oscillations i.e. phonons, that are sensitive to internal or external perturbations. In crystalline materials, the Raman scattering is restricted to near zone centred phonons (ZCP). But in the case of nanostructured materials, other phonons also contribute due to phonon confinement in a finite dimension, inducing a variation in the line-shape of the first order Raman spectrum.[36] Many studies have been carried out to explain the Raman spectra of various silicon nanostructures, showing a shift in the peak position towards lower energy accompanied by a spectral broadening.[37-41]

In this thesis, Raman scattering spectra of mpSi samples were collected on Bruker FRA 106 spectrometer with a Ge detector (cooled with LN) and 1064 nm Nd-YAG laser for fluorescence-free excitation. Low laser power was maintained throughout the measurements to avoid local heating effects.

2.3.6 X-ray photoelectron spectroscopy (XPS)

XPS is an important surface analysis technique, based on the photoelectric effect revealed by Einstein in 1905. By measuring the kinetic energy of photoelectrons (E_k), combining with the known value of the energy of incoming X-ray photons ($h\lambda$), the

binding energy of each of the emitted electron (E_b) can be determined using Equation 2.4,[24] which is not only element specific but also contains chemical information. The work function term ϕ is an adjustable instrumental correction factor dependent on both the spectrometer and the material. Since the energy levels of core electrons depend on the chemical state of the atom. Thus, XPS can not only provide the composition of the surface region but also supply important information about the chemical environments (i.e. binding states, oxidation states) of surface atoms (H and He excluded).

$$E_b = h\lambda - E_k - \phi \qquad \text{Equation 2.4}$$

XPS measurements were carried out on a K-Alpha XPS instrument (Thermo Scientific) at NEXUS nanolab. Samples were drop cast onto a clean gold substrate (10 mm × 10 mm). The film was introduced into a loadlock attached to an UHV chamber in which the typical pressure was maintained below 5 × 10^{-9} mbar. All spectra were acquired at normal emission with Al Kα radiation at 1486.6 eV and a spot size of 400 µm. A pass energy of 200 eV and step size of 0.4 eV was used for the survey spectra and a pass energy of 40 eV and step size of 0.1 eV was used for high-resolution spectra. In all photoemission spectra, binding energies (BEs) were referred to the Au $4f_{7/2}$ line measured on a gold foil in direct contact with the sample, which was at 84 eV. Correction for charge shifts was done by using the carbon contamination with a C 1s binding energy of 285.0 eV. XPS data analysis and peak fitting was conducted using CasaXPS version 2.3.

2.3.7 Thermogravimetric analysis

Thermogravimetric analysis (TGA) is a conventional thermoanalytical method of measuring the mass of a sample as it is submitted to a controlled temperature program in a defined atmosphere. By simultaneously measuring the heat flow (Differential Scanning Calorimetry) to the same sample in a single experiment, TGA-DSC curves are produced which can be analysed to evaluate the thermal stability, to determine the

composition, to explore the thermal behaviours such as phase transitions, desorption, decomposition, oxidation etc. of the sample substance.[42]

In this thesis, the thermal properties of graphitic carbon nitride powders and nanosheets were examined by TGA-DSC (Mettler Toledo, DSC 1). For each measurement, the sample was heated in a 70 µL Pt crucible from 25°C to 1000°C with the heating rate as 10 °C·min^{-1} under a nitrogen atmosphere (20 mL·min^{-1}).

2.3.8 Optical measurements

The optical properties of semiconductor materials are a great part of the unique set of physical and chemical properties, and the drive of numerous studies in broad range of fields of optoelectronics, cell imaging, sensors and solar energy conversion.

2.3.8.1 Ultraviolet-visible absorption spectroscopy (UV-Vis)

Ultraviolet-visible absorption spectroscopy (UV-Vis) monitors the absorption of photons in ultraviolet-visible region by molecules or semiconductors as a result of electronic transition from the ground state to an excited state. It is a heavily used tool in analytical chemistry and shows its advantage in characterising the optical and electronic properties of semiconductor materials. Electron-hole pairs in the crystalline matrix of semiconductor can be separated by absorbing photons matched with its bandgap (E_g). As a result, electrons are excited to the conduction band (CB) while the positive charged holes remain in its lower valence band. The process is so-called photoexcitation and lays the foundation for the capability of semiconductor in storing and converting solar energy. As strongly affected by the quantum confinement effect induced by the very small dimension of the crystallite size, the absorbed photon energy or wavelength can be altered by varying the crystallite size which directly affects the size-dependent bandgap level.[43-45] In practice, this principle is often used to widen the bandgap of narrow bandgap semiconductors e.g. Si by decreasing the nanocrystal size to enhance the optical response across a broad range of spectrum.[46-48]

In this thesis, UV-Vis absorption spectra were collected on Shimadzu UV-1800 spectrometer under ambient conditions. A wavelength range of 200-800 nm was scanned at 0.5 nm intervals. Samples were dispersed in H_2O or DCM (230 nm cut-off) in a 10 mm × 10 mm quartz cuvette. Sample spectra were obtained after subtracting the spectrum of the solvent. Data analysis was done using UVProbe version 2.50.

2.3.8.2 Photoluminescence spectroscopy (PL)

Initiated by photoexcitation mentioned above, the absorbed photons of a particular wavelength are rapidly re-emitted, through the radiative recombination of photoexcited electrons on CB band (excited state) and holes on VB band (ground state). As indicated in the Jablonski diagram shown in Figure 2.4, many electron transition processes may occur before the emission event, such as internal conversion, vibrational relaxation, and intersystem crossing, the latter of which results in the generation of phosphorescence by altering the spin multiplicity ($S_1 \rightarrow T_1$ state). In the meantime, for crystalline semiconducting systems, the exciton movement is also strongly influenced by extrinsic effects, such as structural distortion, lattice disorder, and variation of the chemical composition, acting as radiative recombination centres for the free photoinduced charge carriers.[49] Also affected by the size-dependent quantum confinement effect, PL emission spectrum of Si is also strongly related to the nanocrystals.[2, 40] Although the origin of the photoluminescence of porous Si is still debatable, extensive research efforts have been devoted to this topic.[50-52] The general agreement is that both localized defects at the interface and the quantum confinement of excitons account for the light-emitting phenomenon.[50]

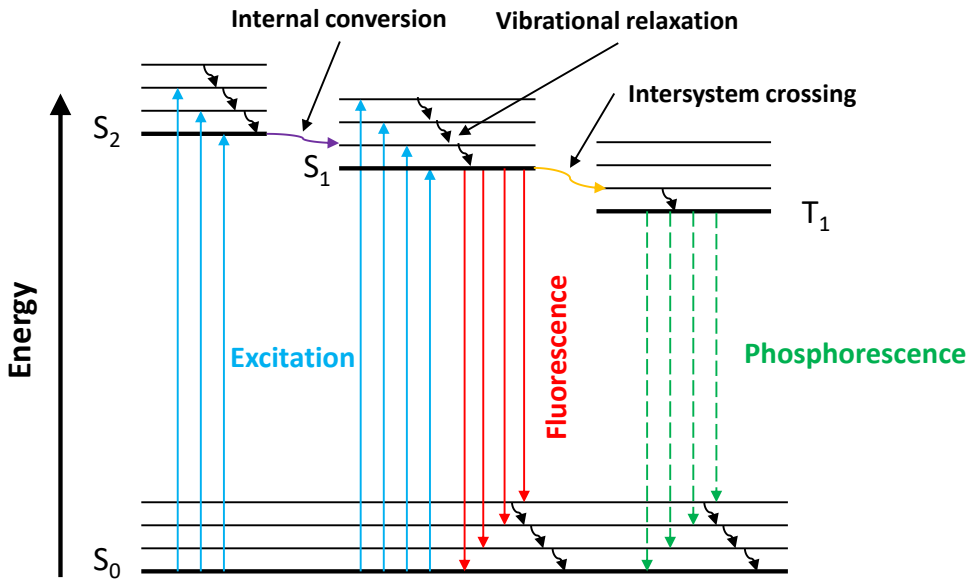

Figure 2.4 Jablonski diagram representing various electronic and molecular processes that occur after photoexcitation.

In this thesis, PL spectra were recorded on a Perkin-Elmer LS55 spectrometer under ambient conditions. Samples were dispersed in H_2O or DCM in a 10 mm × 10 mm quartz cuvette. The excitation wavelength was 320 nm and a 390 nm cut-off filter was applied. For mpSi, the excitation slit width (Ex) was set to 10 nm and the emission slit width (Em) was 15 nm. For g-C_3N_4, the Ex and Em values were set as 2.5 nm and 10 nm respectively. For mpSi/ g-C_3N_4 composite, they were set as 10 nm and 5 nm respectively. Sample spectra were corrected by subtracting the spectrum of the solvent. PL spectroscopic data was processed using FL WinLab 4.00.03.

2.3.8.3 Quantum yield (QY)

As known from the discussion above, excited electrons can return to lower energy level through different mechanisms including fluorescence. By comparing the number of photons absorbed (UV-Vis absorbance) with the photons emitted through fluorescence (PL emission intensity), the light emitting ability of semiconductor materials can be assessed. The ratio is known as quantum yield (QY, ϕ_F). The most common method for QY calculation involves the use of well-characterised standard sample with known QY

value at similar excitation wavelength as the test sample which, if possible, emits in the similar region as well. The QY value of fluorescent samples can be derived according to the following equation.

$$\phi_{\mathrm{F}} = \phi_{\mathrm{ref}}\left(\frac{Grad_{\mathrm{x}}}{Grad_{\mathrm{ref}}}\right)\left(\frac{\eta^{2}_{\mathrm{x}}}{\eta^{2}_{\mathrm{ref}}}\right) \qquad \text{Equation 2.5}$$

In Equation 2.5, the subscripts ref and x denote reference sample and test sample, respectively. *Grad* is the gradient from the plot of integrated fluorescence intensity versus UV-Vis absorbance. η represents the refractive index of the solvent.

In our study, quinine sulfate in 0.1M H_2SO_4 was used as reference. For both the standard sample and test sample, the plot of integrated fluorescence intensity versus absorbance was composed of six data points from solutions of which the respective UV-Vis absorbance was recorded as around 0, 0.02, 0.04, 0.06, 0.08 and 0.10.

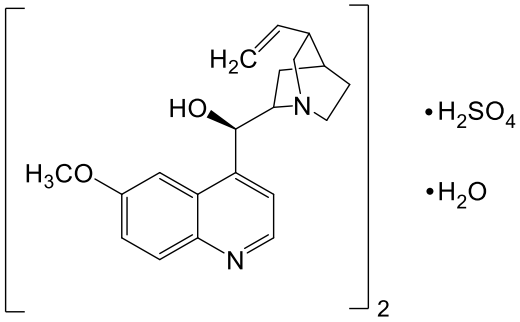

Scheme 2.7 Molecular structure of quinine sulfate.

2.4 Photocatalytic study

This section includes a detailed description of the photodegradation experiment and the engaged analysis methods in the measurements of reaction kinetics, organic carbon content, active species and photocatalyst lifetime as discussed below.

2.4.1 Photodegradation experiment

The visible-light-active photocatalytic activities of various semiconductor materials (mesoporous silicon, graphitic carbon nitride and their coupled composites) prepared by above-mentioned methods were evaluated by photodegradation of organic dyes under visible light irradiation. Among them, methyl orange (MO) was used in our experiments as a model contaminant because of its minimized photosensitization by visible light photons.[53]

A homemade photoreactor equipped with two 8 W fluorescent lamps (OSRAM) was used throughout the analysis which also had a fan installed on top of the wood frame to increase air circulation. The temperature variation inside the photoreactor under fan-assisted air flow was found to be considerably smaller than the ambient temperature during photocatalytic experiment, thus no other cooling system was employed. Sample (*m*, mg) was added in a glass vial or beaker containing certain volume (*V*, mL) of aqueous solution of methyl orange with initial concentration as C_0 (30-50 µmol·L^{-1}). A magnetic bar and stirrer were used throughout the experiment to constantly stir the solution phase. Then the vessel was positioned between the two fluorescent lamps in the chamber at a distance of 10 cm. At certain intervals (30 min for example), an aliquot of MO solution was taken for absorbance measurement in a UV-Vis absorption spectrometer (Shimadzu, UV1800) under ambient conditions using the same instrumental parameters mentioned in 2.3.8.1. For powder samples, prior to illumination, the reaction system was sonicated for 15 min to suspend the photocatalyst particles and the MO aliquot was also centrifuged to ensure a clear solution for UV-Vis measurement. While for monolithic samples, since the solution was naturally free of any solids, the centrifugation step was not necessary so the UV-Vis measurement was directly carried out on the dye solution that had been sampled. Besides, the suspension was also magnetically stirred for 1 hour in the dark to establish the adsorption-desorption equilibrium with the organic substrate. For comparison, the behaviours of our samples toward MO in the absence of external irradiation were also studied using the same photoreactor with the lamps switched off and by following the same experimental procedure mentioned above. Other experimental details including the

sample mass, initial dye concentration etc. will be elaborated in each experimental section of the following chapters.

2.4.2 Kinetic analysis

In the field of heterogeneous photocatalysis, the reaction process is often interpreted as kinetically controlled by the diffusion of initial substrate in the solution phase and follows Langmuir-Hinshelwood type or pseudo first order reaction model of which the mathematical expression is presented as follows.

$$r = -\frac{\mathrm{d[MO]}}{\mathrm{d}t} = k[\mathrm{MO}] \qquad \text{Equation 2.6}$$

$$\ln\frac{[\mathrm{MO}]_t}{[\mathrm{MO}]_0} = -kt \qquad \text{Equation 2.7}$$

As seen in the Equation 2.6 and Equation 2.7, *k* is the rate constant and can be realized by plotting ln ($[MO]_t/[MO]_0$) vs. *t* to yield the gradient. According to Beer-Lambert law, the concentration of an absorbing species is linearly proportional to the absorption intensity recorded in the UV-Vis absorption spectrum. Therefore, by simply monitoring the absorbance decay of MO molecules as a function of irradiation time, the first order reaction rate (*k*) of MO degradation in the presence of photocatalyst can be determined.

$$\ln\frac{\mathrm{Abs(MO)}_t}{\mathrm{Abs(MO)}_0} = -kt \qquad \text{Equation 2.8}$$

2.4.3 Total organic carbon analysis

Total carbon analysis (TOC) is a very important chemical analytical method in detecting contaminants in water, assessing the quality of drinking water and water for pharmaceutical use as well. It is a sensitive and non-specific measurement of all organics present in the sample. In photocatalysis, this technique is often used to determine the photomineralization efficiency of organic substrates by detecting the carbon content that remains in the photoredox system.

In this thesis, TOC was detected by using a Skalar Formacs CA16 TOC analyser. Typically, a test sample was injected from an auto sampler into a high temperature combustion furnace. In the reactor, at a temperature of 850°C, TOC was converted to CO_2 by catalytic oxidation of cobalt chromium and cerium oxide as catalyst to help the reaction to completion. A flow of Zero Grade Air transported the CO_2 product to a non-dispersive infrared detector (NDIR) where the amount of CO_2 was determined by IR detection at 4.2 µm.

2.4.4 Active species analysis

After band-to-band excitation, the photo-induced charge carriers are able to migrate to the surface of semiconductor and participate in redox reactions by reacting with $O_2/H_2O/OH^-$ existing in the system to generate a variety of active species, such as superoxide radical anion ($O_2^{\cdot-}$), hydroxyl radical (·OH), singlet oxygen ($^1O_2$), hydrogen peroxide (H_2O_2), known as reactive oxygen species (ROSs)[54] that are primarily responsible for the photocatalytic oxidation of organic dyes in aqueous solution.[55] The behaviours of these active species are good indicators of the electronic band structure and photocatalytic mechanism of semiconductor photocatalyst.[56-59] Detection methods include electron spin resonance (ESR) spectroscopy,[60-61] chemiluminescence,[62-63] mass spectroscopy[64-65] and scavengers.[66-67]

In this thesis, the involvement of $\cdot O_2^-$, ·OH, h^+ in the visible light driven photodegradation of MO were investigated by using ethanol, 2-propanol, and triethanolamine (TEOA) as quenchers. In each experiment, 1 mmol of quencher, ethanol (58 µL), 2-propanol (76 µL),

TEOA (149 mg) was added into the photocatalytic system which was thereafter irradiated and began the scavenging activities under visible light irradiation. The role of dissolved oxygen in the formation of ROSs was also tested by bubbling high purity N_2 through MO solution to ensure that the solution was N_2 saturated and the reaction was operated under anoxic conditions.

2.4.5 Lifetime study

As we know, the lifetime of photocatalyst is one of the most crucial factor determining its efficiency and applicability, which is often interpreted as the ability to be photocatalytically active in certain numbers of reaction cycles.

In this thesis, the lifetime of mesoporous silicon in MO photodegradation was assessed during visible light irradiation. After a photocatalytic experiment, it was recovered by immersing in 5 wt. % aqueous HF for 2 min and subsequently washed four times with distilled water, followed by drying at 80°C for 12 h under vacuum to remove the residual reactant prior to the next reaction cycle.

2.5 Summary

In general, inexpensive, eco-friendly and upscalable approaches were used in this research for the synthesis and modification of semiconductor materials (silicon, carbon nitride) that are widely recognized as low cost, metal-free and earth abundant. Given this, electrochemical etching was employed in the preparation of mpSi with various morphologies and properties. g-C_3N_4 was synthesized through one-step thermal polycondensation of melamine followed by ultrasonication to gain exfoliated nanosheets, which was to be composited with mpSi via simple impregnation. The simplicity, availability and controllability of these preparation methods are highly valued in this work as exhibited in the following chapters.

2.6 References

1. Sailor, M. J., Fundamentals of porous silicon preparation. In *Porous Silicon in Practice: Prepration, Chracterization and Applications*. Wiley, 2012; pp 1-42.

2. Secret, E.; Leonard, C.; Kelly, S. J.; Uhl, A.; Cozzan, C.; Andrew, J. S., Size control of porous silicon-based nanoparticles via pore-wall thinning. *Langmuir* **2016,** *32* (4), 1166-1170.

3. Walcarius, A.; Etienne, M.; Bessière, J., Rate of access to the binding sites in organically modified silicates. 1. Amorphous silica gels grafted with amine or thiol Groups. *Chem. Mater.* **2002,** *14* (6), 2757-2766.

4. Wang, C.; Flynn, N. T.; Langer, R., Controlled structure and properties of thermoresponsive nanoparticle–hydrogel composites. *Adv. Mater.* **2004,** *16* (13), 1074-1079.

5. Yang, H.; Wang, Y.; Huang, H.; Gell, L.; Lehtovaara, L.; Malola, S.; Hakkinen, H.; Zheng, N., All-thiol-stabilized Ag_{44} and $Au_{12}Ag_{32}$ nanoparticles with single-crystal structures. *Nat. Commun.* **2013,** *4*, 2422.

6. Buriak, J. M., Organometallic chemistry on silicon and germanium surfaces. *Chem. Rev.* **2002,** *102* (5), 1271-1308.

7. Kappe, C. O., How to measure reaction temperature in microwave-heated transformations. *Chem. Soc. Rev.* **2013,** *42* (12), 4977-4990.

8. Obermayer, D.; Damm, M.; Kappe, C. O., Design and evaluation of improved magnetic stir bars for single-mode microwave reactors. *Org. Biomol. Chem.* **2013,** *11* (30), 4949-4956.

9. Obermayer, D.; Kappe, C. O., On the importance of simultaneous infrared/fiber-optic temperature monitoring in the microwave-assisted synthesis of ionic liquids. *Org. Biomol. Chem.* **2010,** *8* (1), 114-121.

10. Yan, S. C.; Li, Z. S.; Zou, Z. G., Photodegradation performance of g-C_3N_4 fabricated by directly heating melamine. *Langmuir* **2009,** *25* (17), 10397-10401.

11. Mo, Z.; She, X.; Li, Y.; Liu, L.; Huang, L.; Chen, Z.; Zhang, Q.; Xu, H.; Li, H., Synthesis of g-C_3N_4 at different temperatures for superior visible/UV photocatalytic performance and photoelectrochemical sensing of MB solution. *RSC Adv.* **2015,** *5* (123), 101552-101562.

12. Papailias, I.; Giannakopoulou, T.; Todorova, N.; Demotikali, D.; Vaimakis, T.; Trapalis, C., Effect of processing temperature on structure and photocatalytic properties of g-C_3N_4. *Appl. Surf. Sci.* **2015,** *358*, 278-286.

13. Zheng, Y.; Zhang, Z.; Li, C., A comparison of graphitic carbon nitrides synthesized from different precursors through pyrolysis. *J. Photochem. Photobiol. A* **2017,** *332*, 32-44.

14. Coleman, J. N.; Lotya, M.; O'Neill, A.; Bergin, S. D.; King, P. J.; Khan, U.; Young, K.; Gaucher, A.; De, S.; Smith, R. J.; Shvets, I. V.; Arora, S. K.; Stanton, G.; Kim, H. Y.; Lee, K.; Kim, G. T.; Duesberg, G. S.; Hallam, T.; Boland, J. J.; Wang, J. J.; Donegan, J. F.; Grunlan, J. C.; Moriarty, G.; Shmeliov, A.; Nicholls, R. J.; Perkins, J. M.; Grieveson, E. M.; Theuwissen, K.; McComb, D. W.; Nellist, P. D.; Nicolosi, V., Two-dimensional nanosheets produced by liquid exfoliation of layered materials. *Science* **2011,** *331* (6017), 568-571.

15. Xu, J.; Zhang, L.; Shi, R.; Zhu, Y., Chemical exfoliation of graphitic carbon nitride for efficient heterogeneous photocatalysis. *J. Mater. Chem. A* **2013,** *1* (46), 14766-14772.

16. Guo, X.; Wang, Y.; Wu, F.; Ni, Y.; Kokot, S., Preparation of protonated, two-dimensional graphitic carbon nitride nanosheets by exfoliation, and their application as a fluorescent probe for trace analysis of copper(II). *Microchimica Acta* **2015,** *183* (2), 773-780.

17. Chen, L.; Huang, D.; Ren, S.; Dong, T.; Chi, Y.; Chen, G., Preparation of graphite-like carbon nitride nanoflake film with strong fluorescent and electrochemiluminescent activity. *Nanoscale* **2013,** *5* (1), 225-230.

18. Lin, L. S.; Cong, Z. X.; Li, J.; Ke, K. M.; Guo, S. S.; Yang, H. H.; Chen, G. N., Graphitic-phase C_3N_4 nanosheets as efficient photosensitizers and pH-responsive drug nanocarriers for cancer imaging and therapy. *J. Mate. Chem. B* **2014,** *2* (8), 1031-1037.

19. Ma, T. Y.; Tang, Y.; Dai, S.; Qiao, S. Z., Proton-functionalized two-dimensional graphitic carbon nitride nanosheet: an excellent metal-/label-free biosensing platform. *Small* **2014,** *10* (12), 2382-2389.

20. Shi, L.; Chang, K.; Zhang, H.; Hai, X.; Yang, L.; Wang, T.; Ye, J., Drastic enhancement of photocatalytic activities over phosphoric acid protonated porous g-C_3N_4 Nanosheets under visible light. *Small* **2016,** *12* (32), 4431-4439.

21. Zhang, X.; Xie, X.; Wang, H.; Zhang, J.; Pan, B.; Xie, Y., Enhanced photoresponsive ultrathin graphitic-phase C_3N_4 nanosheets for bioimaging. *J. Am. Chem. Soc.* **2013,** *135* (1), 18-21.

22. Zhang, J.; Chen, Y.; Wang, X., Two-dimensional covalent carbon nitride nanosheets: synthesis, functionalization, and applications. *Energy Environ. Sci.* **2015,** *8* (11), 3092-3108.

23. Yang, S.; Gong, Y.; Zhang, J.; Zhan, L.; Ma, L.; Fang, Z.; Vajtai, R.; Wang, X.; Ajayan, P. M., Exfoliated graphitic carbon nitride nanosheets as efficient catalysts for hydrogen evolution under visible light. *Adv. Mater.* **2013,** *25* (17), 2452-2456.

24. Pavesi, L.; Turan, R., *Silicon Nanocrystals: Fundamentals, Synthesis and Applications*. Wiley: 2010.

25. Bisi, O.; Ossicini, S.; Pavesi, L., Porous silicon: a quantum sponge structure for silicon based optoelectronics. *Surf. Sci. Rep.* **2000,** *38* (1-3), 1-126.

26. Bragg, W. H.; Bragg, W. L., The Reflection of X-rays by Crystals. *Proceedings of the Royal Society A: Mathematical, Physical and Engineering Sciences* **1913,** *88* (605), 428-438.

27. Patterson, A. L., The scherrer formula for X-Ray particle size determination. *Phys. Rev.* **1939,** *56* (10), 978-982.

28. Stokes, A. R.; Wilson, A. J. C., A method of calculating the integral breadths of Debye-Scherrer lines: generalization to non-cubic crystals. *Mathematical Proceedings of the Cambridge Philosophical Society* **1944,** *40* (02), 197-198.

29. Thommes, M., Physical adsorption characterization of nanoporous materials. *Chem. Ing. Tech.* **2010,** *82* (7), 1059-1073.

30. Cychosz, K. A.; Guillet-Nicolas, R.; García-Martínez, J.; Thommes, M., Recent advances in the textural characterization of hierarchically structured nanoporous materials. *Chem. Soc. Rev.* **2017,** *46* (2), 389-414.

31. Thommes, M.; Kaneko, K.; Neimark, A. V.; Olivier, J. P.; Rodriguez-Reinoso, F.; Rouquerol, J.; Sing, K. S. W., Physisorption of gases, with special reference to the evaluation of surface area and pore size distribution (IUPAC Technical Report). *Pure Appl. Chem.* **2015,** *87* (9-10), 1051-1069.

32. Brunauer, S.; Emmett, P. H.; Teller, E., Adsorption of gases in multimolecular layers. *J. Am. Chem. Soc.* **1938,** *60* (2), 309-319.

33. Groen, J. C.; Peffer, L. A. A.; Pérez-Ramírez, J., Pore size determination in modified micro- and mesoporous materials. Pitfalls and limitations in gas adsorption data analysis. *Microporous Mesoporous Mater.* **2003,** *60* (1-3), 1-17.

34. Gouadec, G.; Colomban, P., Raman Spectroscopy of nanomaterials: How spectra relate to disorder, particle size and mechanical properties. *Prog. Cryst. Growth Charact. Mater.* **2007,** *53* (1), 1-56.

35. Richter, H.; Wang, Z. P.; Ley, L., The one phonon Raman spectrum in microcrystalline silicon. *Solid State Commun.* **1981,** *39* (5), 625-629.

36. Zi, J.; Zhang, K.; Xie, X., Comparison of models for Raman spectra of Si nanocrystals. *Phys. Rev. B* **1997,** *55* (15), 9263-9266.

37. Yang, M.; Huang, D.; Hao, P.; Zhang, F.; Hou, X.; Wang, X., Study of the Raman peak shift and the linewidth of light-emitting porous silicon. *J. Appl. Phy.* **1994,** *75* (1), 651.

38. Zi, J.; Buscher, H.; Falter, C.; Ludwig, W.; Zhang, K. M.; Xie, X. D., Raman shifts in Si nanocrystals. *Appl. Phys. Lett.* **1996,** *69* (2), 200-202.

39. Zuk, J.; Kulik, M.; Andrews, G. T.; Kiefte, H.; Clouter, M. J.; Goulding, R.; Rich, N. H.; NossarzewskaOrlowska, E., Characterization of porous silicon by Raman scattering and photoluminescence. *Thin Solid Films* **1997,** *297* (1-2), 106-109.

40. Kumar, P., Effect of silicon crystal size on photoluminescence appearance in porous silicon. *ISRN Nanotechnology* **2011,** *2011*, 1-6.

41. Kosović, M.; Gamulin, O.; Balarin, M.; Ivanda, M.; Đerek, V.; Ristić, D.; Marciuš, M.; Ristić, M., Phonon confinement effects in Raman spectra of porous silicon at non-resonant excitation condition. *J. Raman Spectrosc.* **2014,** *45* (6), 470-475.

42. Vyazovkin, S., Thermogravimetric analysis. In *Characterization of Materials*, 2012; pp 1-12.

43. Scholes, G. D.; Jones, M.; Kumar, S., Energetics of photoinduced electron-transfer reactions decided by quantum confinement. *J. Phys. Chem. C* **2007,** *111* (37), 13777-13785.

44. Canham, L. T., Silicon quantum wire array fabrication by electrochemical and chemical dissolution of wafers. *Appl. Phys. Lett.* **1990,** *57* (10), 1046-1048.

45. Lehmann, V.; Gosele, U., Porous silicon formation - a quantum wire effect. *Appl. Phys. Lett.* **1991,** *58* (8), 856-858.

46. Jana, A.; Lawrence, K. N.; Teunis, M. B.; Mandal, M.; Kumbhar, A.; Sardar, R., Investigating the control by quantum confinement and surface ligand coating of photocatalytic efficiency in chalcopyrite copper indium diselenide nanocrystals. *Chem. Mater.* **2016,** *28* (4), 1107-1120.

47. Robel, I.; Kuno, M.; Kamat, P. V., Size-dependent electron injection from excited CdSe quantum dots into TiO_2 nanoparticles. *J. Am. Chem. Soc.* **2007,** *129* (14), 4136-4137.

48. Kang, Z.; Tsang, C. H.; Wong, N. B.; Zhang, Z.; Lee, S. T., Silicon quantum dots: a general photocatalyst for reduction, decomposition, and selective oxidation reactions. *J. Am. Chem. Soc.* **2007,** *129* (40), 12090-12091.

49. Romero, J. J.; Llansola-Portolés, M. J.; Dell'Arciprete, M. L.; Rodríguez, H. B.; Moore, A. L.; Gonzalez, M. C., Photoluminescent 1–2 nm sized silicon nanoparticles: a surface-dependent system. *Chem. Mater.* **2013,** *25* (17), 3488-3498.

50. Sailor, M. J.; Wu, E. C., Photoluminescence-based sensing with porous silicon films, microparticles, and nanoparticles. *Adv. Funct. Mater.* **2009,** *19* (20), 3195-3208.

51. Kotkovskiy, G. E.; Kuzishchin, Y. A.; Martynov, I. L.; Chistyakov, A. A.; Nabiev, I., The photophysics of porous silicon: technological and biomedical implications. *Phys. Chem. Chem. Phys.* **2012,** *14* (40), 13890-13902.

52. Mughal, A.; El Demellawi, J. K.; Chaieb, S., Band-gap engineering by molecular mechanical strain-induced giant tuning of the luminescence in colloidal amorphous porous silicon nanostructures. *Phys. Chem. Chem. Phys.* **2014,** *16* (46), 25273-25279.

53. Rochkind, M.; Pasternak, S.; Paz, Y., Using dyes for evaluating photocatalytic properties: a critical review. *Molecules* **2014,** *20* (1), 88-110.

54. Krumova, K.; Cosa, G., Chapter 1. Overview of Reactive Oxygen Species. In *Singlet Oxygen: Applications in Biosciences and Nanosciences*, 2016; Vol. 1, pp 1-21.

55. Chen, C.; Ma, W.; Zhao, J., Semiconductor-mediated photodegradation of pollutants under visible-light irradiation. *Chem. Soc. Rev.* **2010,** *39* (11), 4206-4219.

56. Prihod'ko, R. V.; Soboleva, N. M., Photocatalysis: oxidative processes in water treatment. *J. Chem.* **2013,** *2013*, 1-8.

57. Spasiano, D.; Marotta, R.; Malato, S.; Fernandez-Ibanez, P.; Di Somma, I., Solar photocatalysis: Materials, reactors, some commercial, and pre-industrialized applications. A comprehensive approach. *Appl. Catal. B* **2015,** *170*, 90-123.

58. Dong, S.; Feng, J.; Fan, M.; Pi, Y.; Hu, L.; Han, X.; Liu, M.; Sun, J.; Sun, J., Recent developments in heterogeneous photocatalytic water treatment using visible light-responsive photocatalysts: a review. *RSC Adv.* **2015,** *5* (19), 14610-14630.

59. Hoffmann, M. R.; Martin, S. T.; Choi, W. Y.; Bahnemann, D. W., Environmental applications of semiconductor photocatalysis. *Chem. Rev.* **1995,** *95* (1), 69-96.

60. Hirakawa, T.; Kominami, H.; Ohtani, B.; Nosaka, Y., Mechanism of photocatalytic production of active oxygens on highly crystalline TiO_2 particles by means of chemiluminescent probing and ESR spectroscopy. *J. Phys. Chem. B* **2001,** *105* (29), 6993-6999.

61. Nosaka, Y.; Kishimoto, M.; Nishino, J., Factors governing the initial process of TiO_2 photocatalysis studied by means of in-situ Electron Spin Resonance measurements. *J. Phys. Chem. B* **1998,** *102* (50), 10279-10283.

62. Ishibashi, K.-i.; Fujishima, A.; Watanabe, T.; Hashimoto, K., Generation and deactivation processes of superoxide formed on TiO_2 film illuminated by very weak UV light in air or water. *J. Phys. Chem. B* **2000,** *104* (20), 4934-4938.

63. Nosaka, Y.; Yamashita, Y.; Fukuyama, H., Application of chemiluminescent probe to monitoring superoxide radicals and hydrogen peroxide in TiO_2 photocatalysis. *J. Phys. Chem. B* **1997,** *101* (30), 5822-5827.

64. Li, W.; Li, D.; Lin, Y.; Wang, P.; Chen, W.; Fu, X.; Shao, Y., Evidence for the active species involved in the photodegradation process of methyl orange on TiO_2. *J. Phys. Chem. C* **2012,** *116* (5), 3552-3560.

65. Baiocchi, C.; Brussino, M. C.; Pramauro, E.; Prevot, A. B.; Palmisano, L.; Marcì, G., Characterization of methyl orange and its photocatalytic degradation products by HPLC/UV–VIS diode array and atmospheric pressure ionization quadrupole ion trap mass spectrometry. *Int. J. Mass Spectrom.* **2002,** *214* (2), 247-256.

66. Xu, Y.; Jing, L.; Chen, X.; Ji, H.; Xu, H.; Li, H.; Li, H.; Zhang, Q., Novel visible-light-driven Fe_2O_3/Ag_3VO_4 composite with enhanced photocatalytic activity toward organic pollutants degradation. *RSC Adv.* **2016,** *6* (5), 3600-3607.

67. Jiang, Z.; Zhu, C.; Wan, W.; Qian, K.; Xie, J., Constructing graphite-like carbon nitride modified hierarchical yolk–shell TiO_2 spheres for water pollution treatment and hydrogen production. *J. Mater. Chem. A* **2016,** *4* (5), 1806-1818.

Chapter 3

Controllable Generation of Mesoporous Silicon with Large Surface Area by Electrochemical Etching

Abstract

As earth-abundant and low cost, elemental silicon has attracted numerous research efforts in developing novel devices for various uses. Among different Si nanostructures, nanoporous silicon has been extensively studied for its vast potential over a broad spectrum of applications. In this study, mesoporous silicon with diverse surface and pore properties have been fabricated via electrochemical etching. The hydrogen termination, huge surface area and open mesoporous structure hold much promise for a superior performance anticipated in a variety of areas.

3.1 Overview

Owing to its semiconductor nature and outstanding structural characteristics, nanoporous silicon (pSi) has been extensively investigated in applications ranging from optoelectronics to various emerging fields. Due to the high theoretical capacity and anti-pulverization ability, pSi is a promising candidate as anode materials for high performance Li-ion rechargeable batteries.[1-5] The biocompatibility, biodegradability and light-emitting ability of pSi have also inspired growing interest in biomedical research, as a novel bio-imaging agent,[6-8] a drug delivery vector,[9-11] etc. Recent decades have also witnessed tremendous efforts in developing pSi-based sensors for detection of toxic gases, heavy metal ions, bio-active molecules.[12-14] Its unique optical and electrical properties further led to a wider field of applications in heterogeneous catalysis ranging from energy conversion to environmental remediation.[15-18]

At the heart of these applications, the morphological characteristics of pSi are of utmost importance, determining the overall performance in various research fields. The distribution of pore size is particularly crucial in the application of pSi as it strongly influences the diffusion kinetics of substrate molecules especially in liquid phase and thereby regulates the access to the internal surface.[19-20] In previous studies of porous solids, a meso-scale pore dimension is proved efficient in accommodating guest species while also maintaining a relatively high surface-to-volume ratio. The surface area, especially internal surface area of porous materials is also a significantly important structural factor and a larger value could contribute dramatically to the performance of the material with a greater loading capacity, a better sensibility and a longer working lifetime.[15, 21-22]

In this chapter, we aim to fabricate mesoporous silicon (mpSi) with high surface area and a tuneable porous system via an electrochemical etching method. As will be demonstrated, the highest value of specific surface area reached up to 994.4 $m^2 \cdot g^{-1}$ with the pore size distributed primarily between 3-4 nm. Mesoporous silicon with larger mesopores in the range of 7-10 nm were also generated in our study although the surface area was accordingly reduced, but still up to 467 $m^2 \cdot g^{-1}$.

By means of FE-SEM, HRTEM, XRD, ATR-IR, Raman and nitrogen adsorption analysis, the morphological and physiochemical properties of mesoporous silicon materials were thoroughly examined. The varied effects of etching conditions (etching current density, etching time) and dopant concentration on crystallinity, surface and pore features, as well as microscopic morphological figures of the resulting porous Si matrix were investigated.

Furthermore, several post-treatments were explored to modify the shape and surface environment of mpSi. Highly porous free-standing disks/microflakes were successfully gained via pulse etching and sonication. The surface chemistry of mesoporous silicon was altered by microwave-assisted thermal hydrosilylation, which yielded thiol-capped mpSi for the first time using allyl mercaptan as precursor under microwave electromagnetic field.

3.2 Experimental section

3.2.1 Mesoporous silicon preparation (mpSi)

Mesoporous silicon samples (PS/HPS-*J*-*t*) were fabricated by galvanostatic anodization of silicon wafers in ethanoic HF acid under ambient conditions. Moderately doped and heavily doped Si wafers (PS and HPS) were applied in the preparation of PS-*J*-*t* and HPS-*J*-*t* samples, respectively, following a similar anodic etching process as described in Chapter 2.

Table 3.1 Etching parameters for producing mesoporous silicon materials involved in Chapter 3.

Mesoporous silicon	**Etching current density (*J*) / mA·cm^{-2}**	**Etching time (*t*) / min**
PS-10-15	10	15
PS-30-15	30	15
PS-60-05	60	05
PS-60-15	60	15
HPS-60-15	60	15
HPS-150-05	150	05
HPS-150-10	150	10
HPS-150-15	150	15

3.2.2 Free-standing mpSi preparation

HPS-150-10 and PS-60-15 were employed in the "lift-off" experiment and treated with sonication to prepare free-standing mpSi disks (PS/HPS-*J*-*t*-D) and microflakes (PS/HPS-*J*-*t*-F).

Table 3.2 Preparation conditions for free standing mesoporous silicon materials investigated in Chapter 3.

		HPS-150-10-D	**HPS-150-10-F**	**PS-60-15-F**
Disk sample	Current density / mA·cm^{-2}	4	4	4
	Etching time / s	125	125	125
Microflake sample	Output level*	/	4	4
	Sonication mode	/	Constant	Constant
	Sonication time / min	/	30	30

* Microtip sonicator, purchased from Apollo Electronics, output level 1-10.

3.2.3 Thiol-capped mpSi preparation

PS-60-05 was used in the capping experiments with allyl mercaptan (CH_2=$CHCH_2SH$) to synthesize thiol-capped mpSi materials. Three different heating methods were employed as mentioned below. Detailed descriptions of each experimental procedure can be found in Chapter 2.

Table 3.3 Experimental details of thiol-capping experiments of PS-60-05.

	PS-60-05-RF	**PS-60-05-AC**	**PS-60-05-MW**
Heating approach	Oil bath	Conventional Oven	Microwave oven
Allyl mercaptan / mL	2	2	2
Dry toluene / mL	10	10	5
Reaction temperature / °C	ca. 110	200	N.A.
Reaction time	12 h-48 h	24 h	6 min
Atmosphere	N_2	Air	N_2

3.2.4 Material characterisation

The surface morphology, internal structure and layer thickness of mpSi were determined by various imaging techniques (SEM, FE-SEM and HRTEM). XRD patterns were recorded to reflect the crystalline nature of porous framework. The chemical composition of as-etched mpSi and modified mpSi samples was distinguished by ATR-IR, Raman and XPS spectroscopy. A quantitative evaluation of the surface and pore features (S_{BET}, V_{pore} and d_{pore}) was performed on various mpSi samples using low-temperature nitrogen sorption isotherms at 77 K. All measurement parameters were the same as outlined in Chapter 2 unless otherwise stated.

3.3 Results and discussion

3.3.1 Microscopic morphology of PS-mpSi

Electron microscopic images of as-etched moderately doped mpSi were first presented in this section to show the main structural characteristics possessed by the highly porous Si samples prepared via electrochemical etching, taking PS-60-15 as an example.

3.3.1.1 FE-SEM images of PS-mpSi

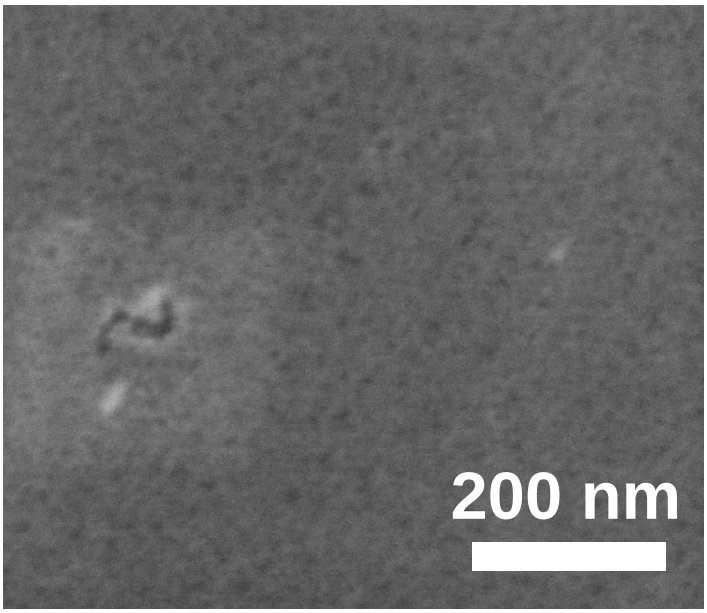

Figure 3.1 Top view FE-SEM image of PS-60-15.

The top surface of PS-60-15 was first examined by means of FE-SEM. As shown in Figure 3.1, numerous nanoholes with varied sizes, mostly less than 10 nm, were visualized with a homogeneous spatial distribution and very narrow interpore distances. These nanopores were formed as neighbouring silicon atoms were rapidly dissolved into soluble substances in HF solution under the external voltage bias during electrochemical etching. Some large holes and cracks were also observed on the surface that many factors could contribute to, such as unevenly distributed etching

current, surface tensions and unavoidable mechanical force during handling etc. On the other hand, these features were more normally seen in PS-60-15 compared to other PS samples etched under different conditions, which indicated a poorer mechanical stability of PS-60-15 resulting from its highly porous structure.

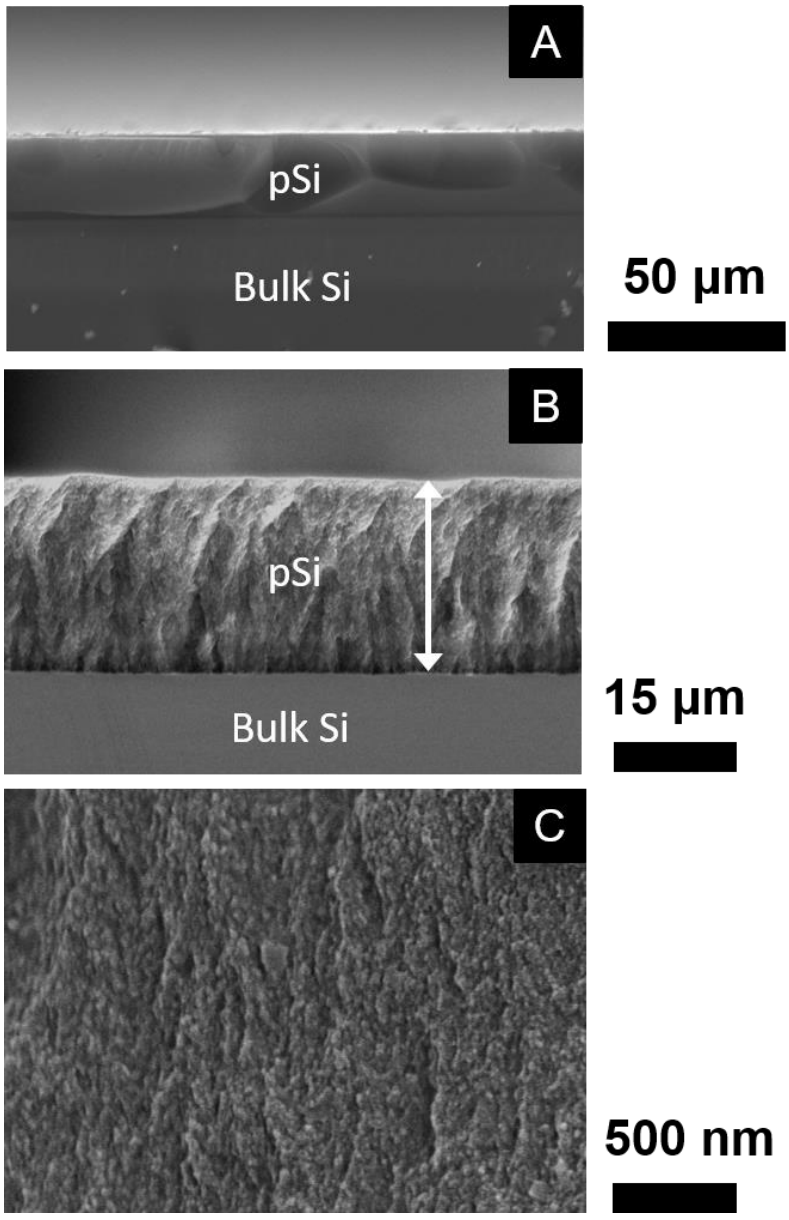

Figure 3.2 Cross section SEM (A) and FE-SEM (B and C) images of PS-60-15.

Figure 3.2 demonstrates the cross section morphology of PS-60-15. A layer of porous silicon was formed above the un-etched Si wafer, with two straight boundary lines

lying between mpSi/Si and mpSi/outer environment. The thickness of the layer was consistent and the value was estimated as 23.66 ± 0.20 µm. The internal structure was further revealed in Figure 3.2C, showing abundant nanosized Si filaments and particulates embedded on the internal structure, implying the very large surface area possessed by PS-60-15. According to quantum confinement theory, these ultra-small Si structural figures are known to have huge impact on the optical properties of pSi.[23-27]

3.3.1.2 HRTEM images of PS-mpSi

As displayed in Figure 3.3, a highly porous network with a matrix of isolated silicon nanocrystallites was characterised in PS-60-15. Consequently, only amorphous rings were detected in the SAED pattern (Figure 3.3D). Lattice fringes of silicon nanocrystallites in irregular sizes and shapes were also discovered at various framework locations as pointed out in Figure 3.3E and F. The sizes of the Si nanocrystallites embedded on the internal surface were mostly less than 5 nm, indicating the significance of quantum confinement effects on the electronic properties.[28]

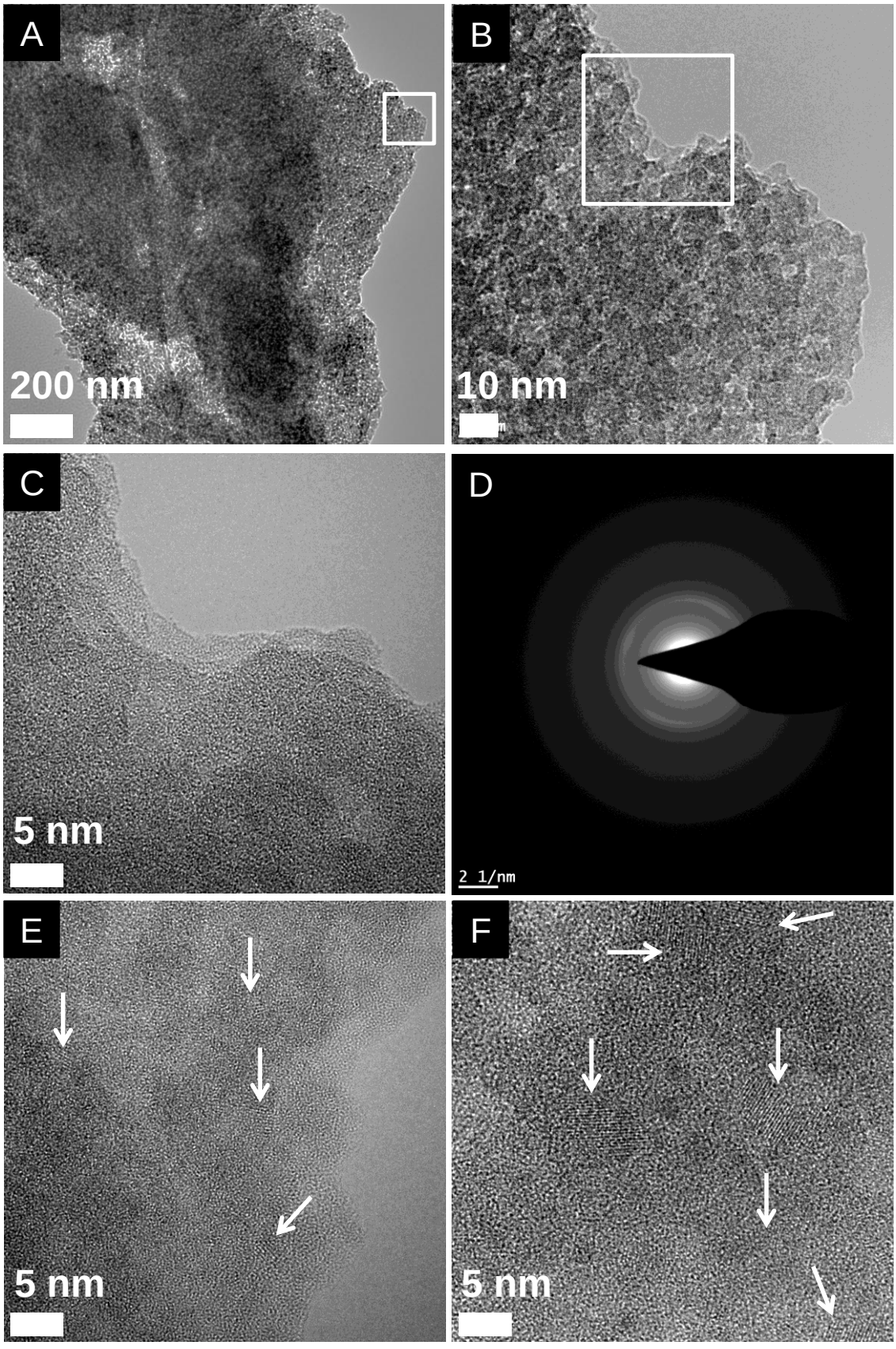

Figure 3.3 HRTEM images (A, B, C, E, and F) and SAED pattern (D) of PS-60-15. Arrows in E and F represent the lattice fringes of Si nanocrystallites in the framework.

3.3.2 Structural effects of etching current density

To examine the effects of etching current density, in addition to PS-60-15, PS-10-15 and PS-30-15 were also prepared under current densities of 10 $mA \cdot cm^{-2}$ and 30 $mA \cdot cm^{-2}$, respectively. The etching time was constant at 15 min. As seen in Figure 3.4, PS-10-15 appeared to have a golden brown colour while PS-30-15 became more reddish and it was further darkened for PS-60-15. This is likely due to the varied refractive index of porous Si in relation to the porosity and layer thickness.

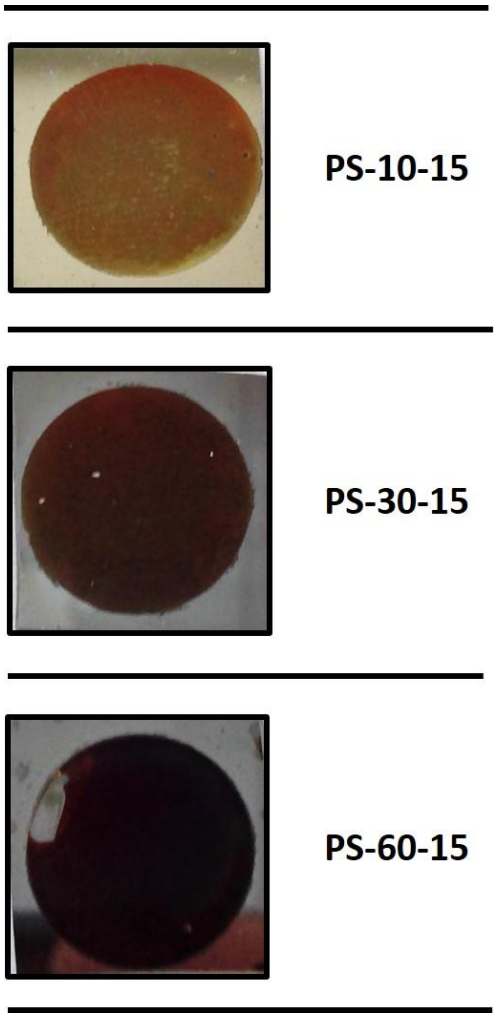

Figure 3.4 Photographs of PS-10-15, PS-30-15 and PS-60-15.

As shown in Figure 3.5, the mpSi layer became thicker with the increasing etching current density, 5.8 µm for PS-10-15, 20.7 µm for PS-30-15 and 23.7 µm for PS-60-15. The etching rate was accelerated under higher etching current density.

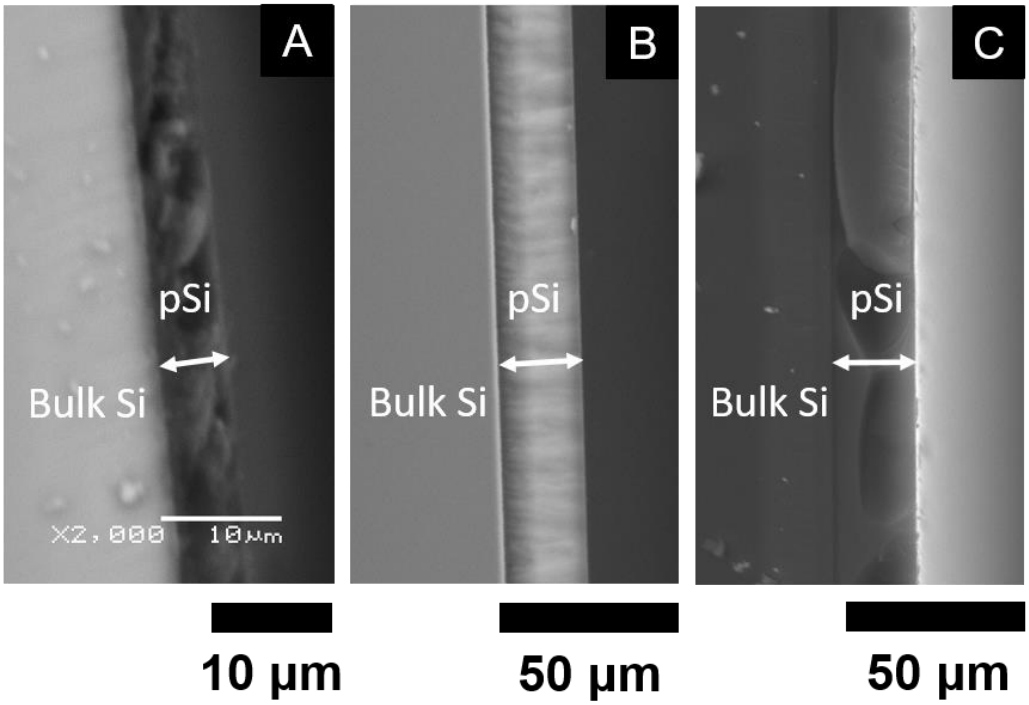

Figure 3.5 Cross sectional SEM images of PS-10-15 (A), PS-30-15 (B) and PS-60-15 (C).

3.3.2.1 XRD patterns of PS-mpSi

As shown in Figure 3.6, the main feature observed in the XRD patterns of PS-10-15, PS-30-15 and PS-60-15 was a broad diffraction peak centred at 69.1˚, which is attributable to the (400) crystal plane of silicon.[29] This result is consistent with the crystal orientation of the moderately doped silicon wafer used for mpSi preparation via electrochemical etching (Figure 3.7). However, the (400) peak intensity of mpSi samples was significantly weakened suggesting reduced crystallinity after electrochemical etching. Various extents of (400) peak broadening were also identified, corresponding to the physical dimension of Si nanocrystals constituting the framework. By applying Scherrer's Equation,[30] it was determined to be 11.22 nm, 7.08 nm and 5.48 nm for PS-10-15, PS-30-15 and PS-60-15 respectively. Thus, as etching current

density increases, the size of Si nanocrystals reduces, which could lead to a higher surface area and enlarged bandgap of mpSi, and eventually affect the behaviour and activity of mpSi. According to the prevalent pore-forming mechanisms, these Si nanocrystallites are shaped by the occurrence of three processes during electrochemical etching, i.e. electrochemical etching itself, chemical dissolution and QCE.[25, 31]

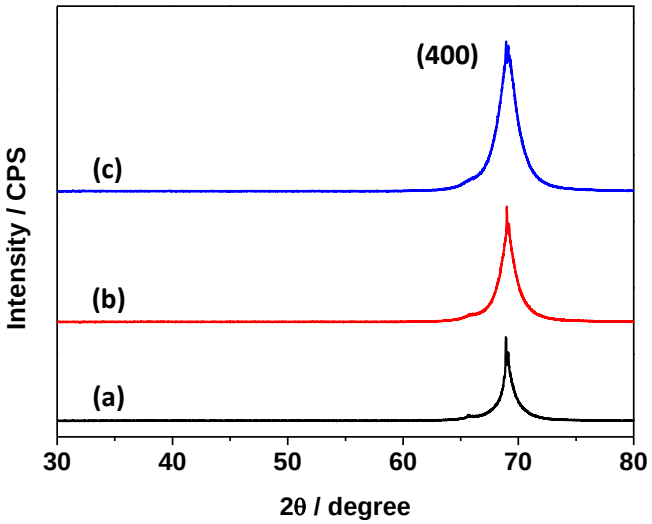

Figure 3.6 XRD patterns of PS-10-15 (a), PS-30-15 (b) and PS-60-15 (c).

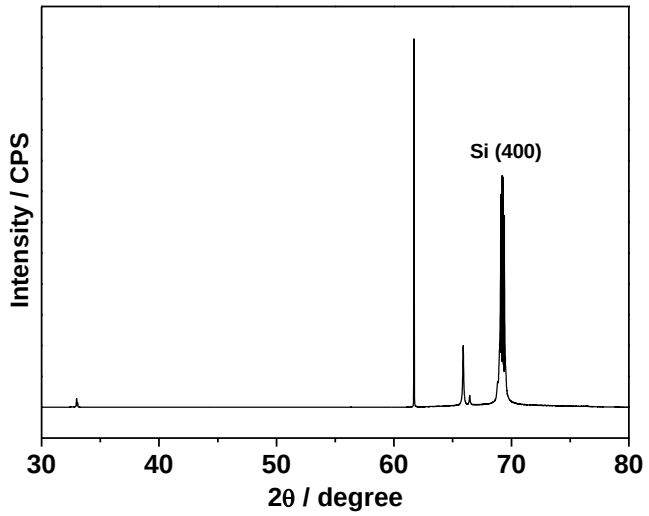

Figure 3.7 XRD pattern of a moderately doped *p*-type silicon wafer (diffraction signals maximized at 61.7˚ and 65.9˚ are the Si (400) diffraction contributed by the residual Cu Kα and Ni Kα).

3.3.2.2 Raman scattering of PS-mpSi

Figure 3.8 shows the Raman scattering spectra of mpSi materials. Each mpSi sample shows an optical phonon band in the 450-600 cm^{-1} range. In the spectrum of PS-10-15, the band (a) was symmetrically distributed at 519 cm^{-1} with a Lorentzian lineshape, which slightly redshifted to lower energy side compared to a well-defined Si crystal (521 cm^{-1}) due to phonon confinement. And it further redshifted to 513 cm^{-1} and became asymmetrically broadened as etching current density was increased, as shown in the spectra of PS-30-15 (b) and PS-60-15 (c), which can be explained by the existence of smaller Si nanocrystallites contained in their porous structures, in agreement with the previous XRD results.

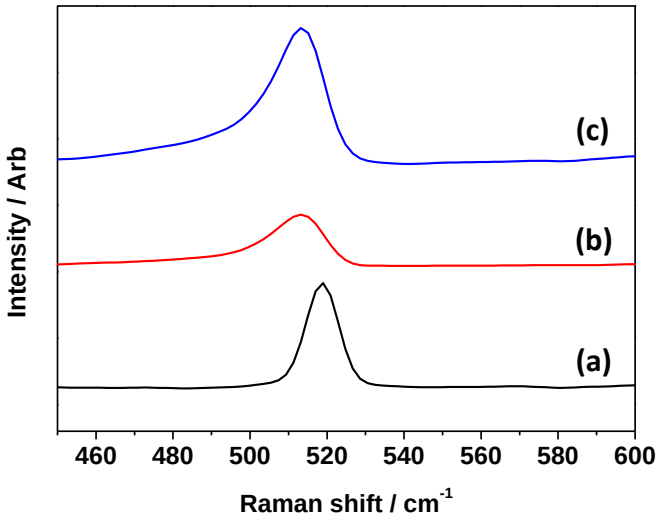

Figure 3.8 Raman spectra of PS-10-15 (a), PS-30-15 (b) and PS-60-15 (c); laser wavelength 1064 nm, laser power 30 mW.

3.3.2.3 ATR-IR spectra of PS-mpSi

Figure 3.9 presents the ATR-IR spectra of PS-10-15 (a), PS-30-15 (b) and PS-60-15 (c), consisting of six characteristic Si-H peaks in each spectrum. The absorptions at 664 cm^{-1} and 910 cm^{-1} originate from Si-H wagging and scissoring modes. The IR signals at 2087 cm^{-1}, 2110 cm^{-1}, and 2139 cm^{-1} were the stretching modes of SiH, SiH_2 and SiH_3,

respectively.[32] As implied, freshly prepared mpSi surface was successfully passivated by chemically bound hydrogen atoms as a result of electrochemical etching. As etching current density increased, the absorption intensity of SiH_x signals at 2087, 2110, and 2139 cm^{-1} also increased, signifying an enhanced hydrogen coverage on the surface. Notably, neither Si-O stretching peak in the range of 1000-1200 cm^{-1} nor any signals around 2260 cm^{-1} from SiO_ySiH_x ($x + y = 4$, $x = 1, 2, 3$) complexes were detected, indicating the surface of mpSi was free of identifiable oxide phases.

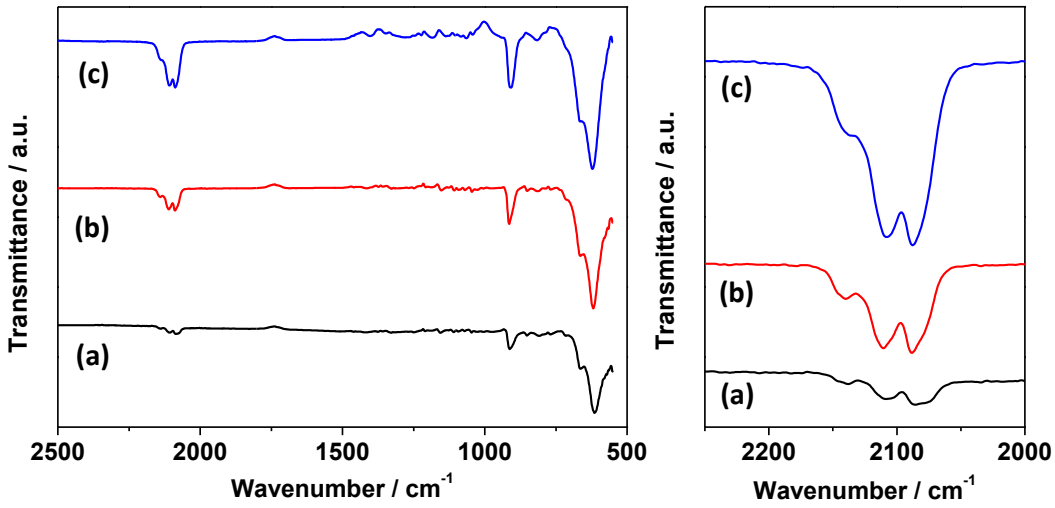

Figure 3.9 ATR-IR spectra of freshly made PS-10-15 (a), PS-30-15 (b) and PS-60-15 (c).

To verify the reproducibility of the electrochemical etching method, the IR spectra of two PS-30-15 samples were compared. For each sample, IR spectra were taken at three spots (S1, S2 and S3) on the surface as displayed in Figure 3.10. Although it has been documented that FTIR of porous silicon often vary in certain respects, even after being made under identical conditions,[26] in our experiments, each corresponding IR peak in the IR spectra of PS-30-15a and PS-30-15b was located at similar position regardless of the sites the IR signals were collected from. Although the peak intensity was slightly different because of the variation in the force used for pressing sample material against ATR crystal in an effort to ensure the best signal-to-noise ratio of the spectra.

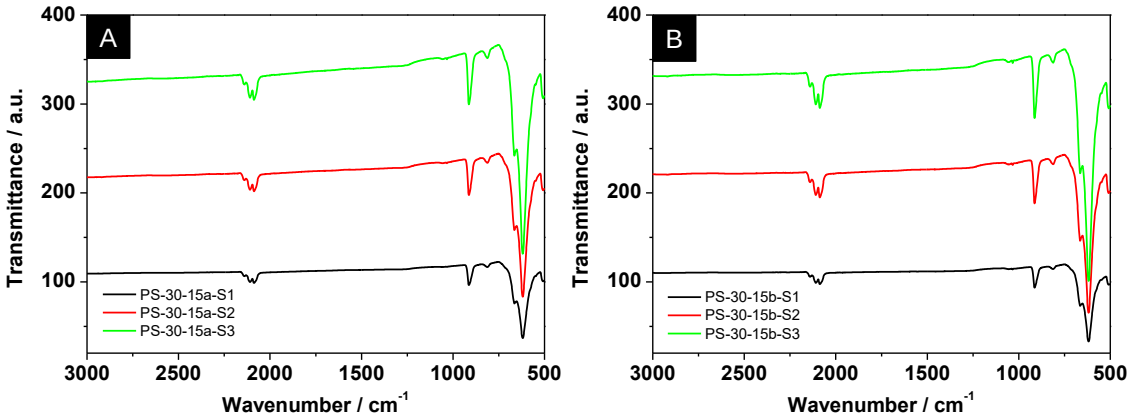

Figure 3.10 ATR-IR spectra collected at three different surface sites (S1, S2 and S3) of two PS-30-15 samples (A and B) prepared under identical conditions by electrochemical etching.

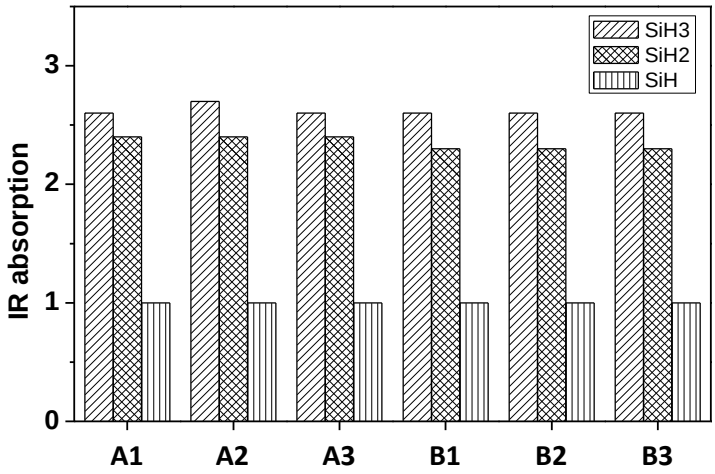

Figure 3.11 Normalized IR absorption intensity of silicon tri-hydrides at 2140 cm^{-1}, di-hydrides at 2110 cm^{-1} and mono-hydride at 2088 cm^{-1} derived from the IR spectra of PS-30-15 in Figure 3.10.

Figure 3.11 demonstrates the ratio of tri- (SiH_3) at 2140 cm^{-1}, bi- (SiH_2) at 2110 cm^{-1} to mono- (SiH) hydride at 2088 cm^{-1} derived from Figure 3.10, which is known to be indicative of the roughness/shape of Si nanocrystallites contained in porous silicon structures. As seen, the ratios were consistent among them, representing the high level of reproducibility of electrochemical etching method.

3.3.2.4 Nitrogen sorption analysis of PS-mpSi

The surface and pore properties of mpSi materials were further characterised by means of low-temperature gas adsorption. Nitrogen sorption isotherms of PS-10-15, PS-30-15 and PS-60-15 were presented respectively in Figure 3.12, Figure 3.13 and Figure 3.14. According to IUPAC classification,[33] a Type IV(a) isotherm was identified with the capillary condensation step occurring at relative pressure P/P_0 ~ 0.4, which is typical for mesoporous materials.

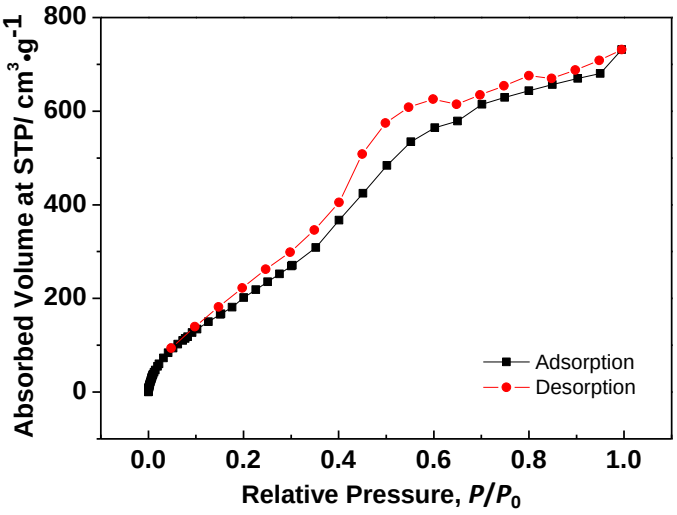

Figure 3.12 Nitrogen sorption isotherms of PS-10-15.

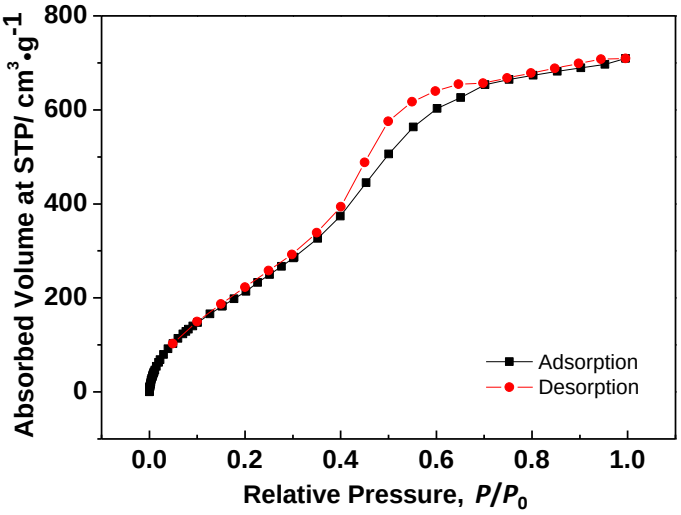

Figure 3.13 Nitrogen sorption isotherms of PS-30-15.

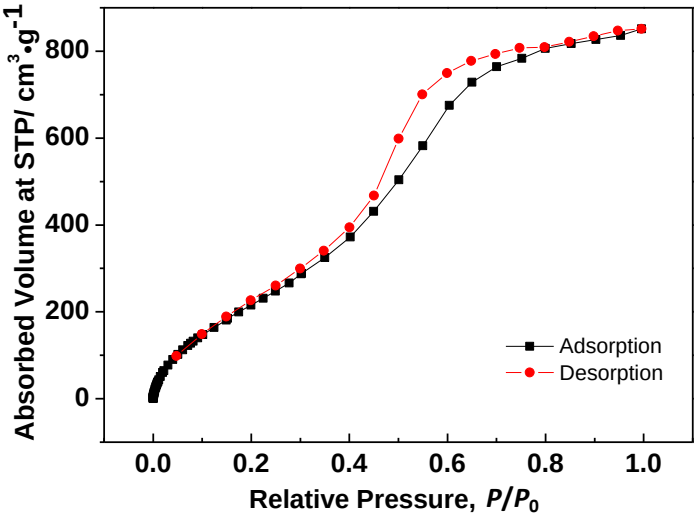

Figure 3.14 Nitrogen sorption isotherms of PS-60-15.

Table 3.4 Textural properties of moderately doped mesoporous silicon derived from nitrogen sorption isotherms.

Samples	S_{BET} / $m^2 \cdot g^{-1}$	V_{meso} / $cm^3 \cdot g^{-1}$	d_{pore} / nm
PS-10-15	887.1	1.09	3.07
PS-30-15	907.0	1.04	3.43
PS-60-15	994.4	1.36	3.82
PS-60-05	819.2	1.08	3.84
Ball milled Si powder	14.67	0.03	7.80
Commercial silica powder	658.0	0.78	4.94
SBA-15	848.4	1.07	7.81

As shown in Table 3.4, as etching current density increased, the specific surface area, pore volume and average pore size also increased representing an increasing porosity of the resulting Si structure. All PS samples showed an exceptionally high specific surface area. Especially for PS-60-15, it reached up to 994.4 $m^2 \cdot g^{-1}$, which is only second to the highest reported value of porous silicon to date (1125 $m^2 \cdot g^{-1}$).[34] For comparison, crystalline silicon powders were also prepared by ball milling Si chips,

which is widely used to achieve size reduction and surface area expansion of Si materials. As shown in Figure 3.15, after ball milling, Si microparticles in a broad size distribution were produced and its specific surface area measure by N_2 adsorption was merely 14.67 $m^2 \cdot g^{-1}$. Amorphous silica powder and order mesoporous silica e.g. SBA-15 are greatly valued for their abundant surface area. According to Figure 3.16, the specific surface area of amorphous silica and SBA-15 was determined as 658.0 $m^2 \cdot g^{-1}$ and 848.4 $m^2 \cdot g^{-1}$ respectively which are lower than mesoporous silicon.

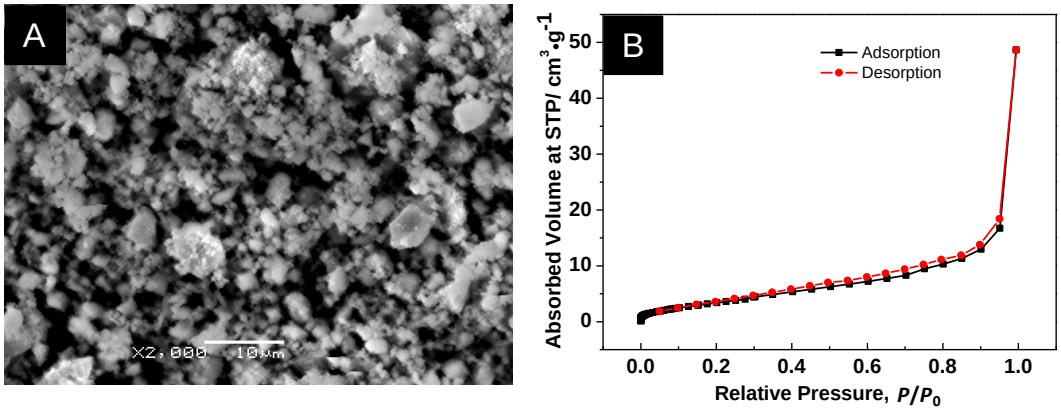

Figure 3.15 SEM image (A) and nitrogen sorption isotherms (B) of Si powders obtained by high energy ball mill.

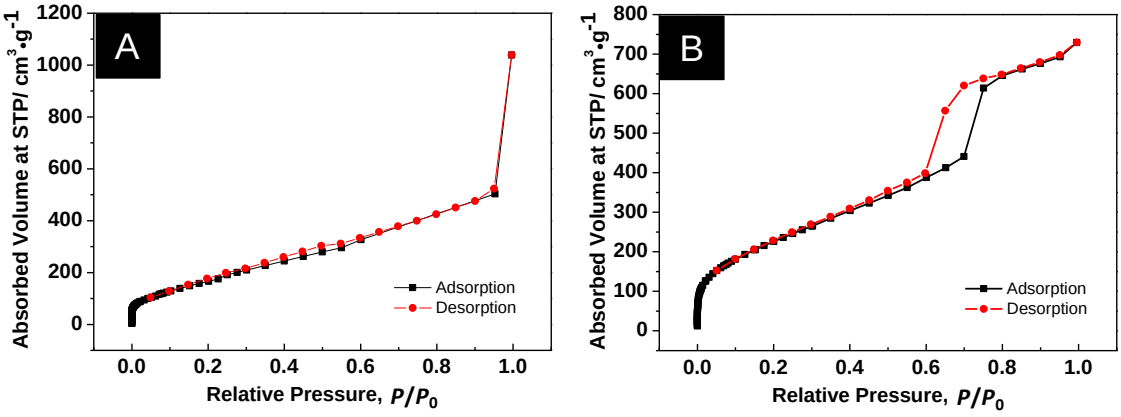

Figure 3.16 Nitrogen sorption isotherms of amorphous silica commercially purchased (A) and ordered mesoporous silica SBA-15 (B).

Apart from surface area, pore size distribution is also an important factor to be considered in the application of porous materials. As exhibited in Table 3.4, the diameter of mesopores increased from 3.07 to 3.82 nm by increasing the etching current density from 10 to 60 $mA \cdot cm^{-2}$. Due to the limitation of BJH analysis method, the pore size distribution curve was measured above 3 nm as displayed in Figure 3.17. As etching current density increased, the curve became gradually broader and also exhibited a small portion of larger mesopores around 7-10 nm for PS-10-15 and PS-30-15 samples.

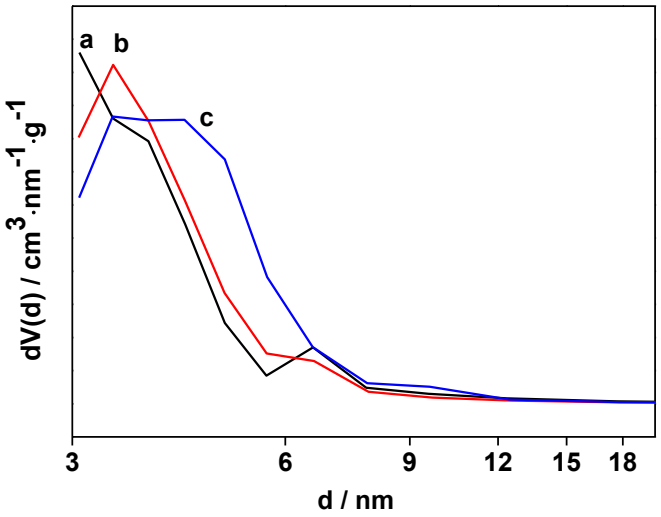

Figure 3.17 Pore size distribution curves of PS-10-15 (a), PS-30-15 (b) and PS-60-15 (c) acquired by BJH approach using adsorption branch.

3.3.3 Structural effects of etching time

As another important factor, etching time also has direct impact on the formation of mesoporous silicon as discussed below.

3.3.3.1 Layer thickness of PS-mpSi

Figure 3.18 summarizes the cross sectional SEM images of various PS samples fabricated under different etching time (A: PS-10-02, B: PS-10-05, C: PS-10-15, D: PS-10-25, E: PS-10-30, F: PS-10-35, G: PS-10-40; H: PS-60-05, I: PS-60-10). The layer

thickness was then plotted as a function of the etching duration as shown in Figure 3.19. An etching time-dependent increase in the layer thickness was observed as anodic etching process prolonged under constant 10 $mA \cdot cm^{-2}$ or 60 $mA \cdot cm^{-2}$. The non-linearity is likely due to the depletion of HF electrolyte which affected the etch rate during electrochemical etching.

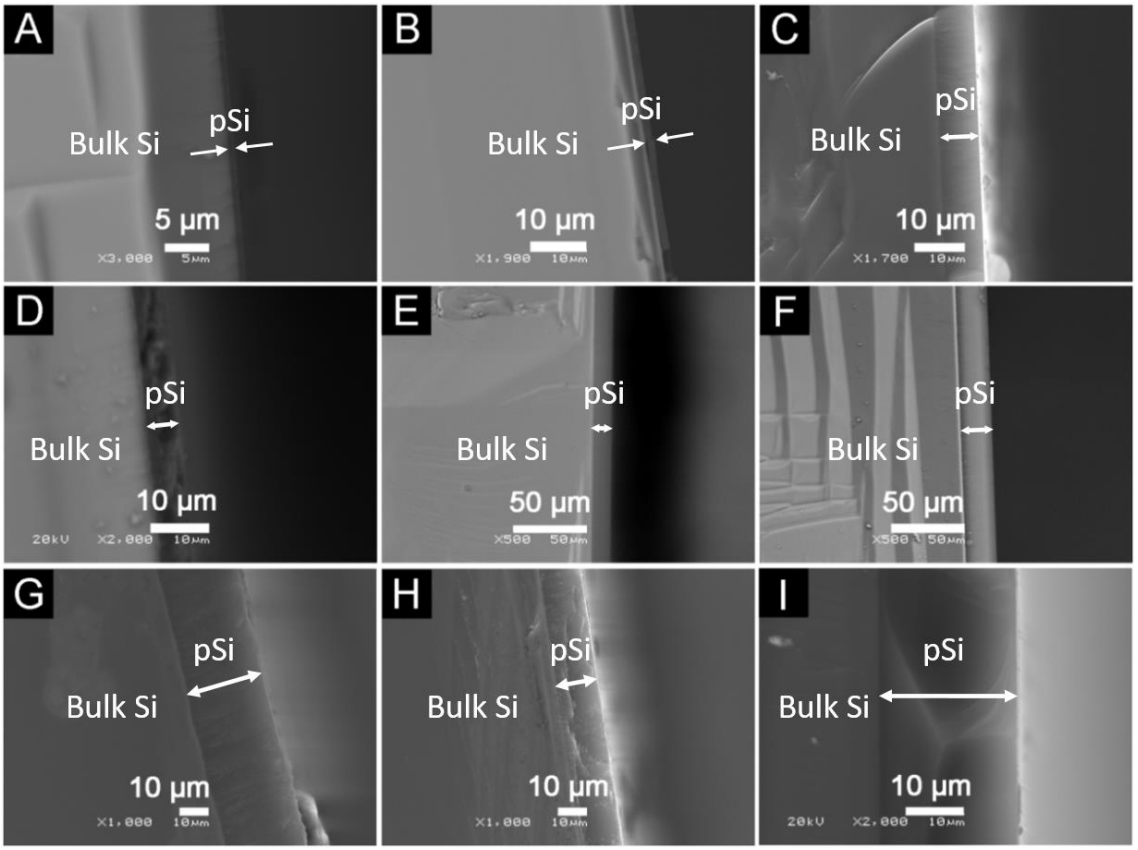

Figure 3.18 Cross sectional SEM micrographs of PS samples (A) PS-10-02, (B)PS-10-05, (C) PS-10-15, (D) PS-10-25, (E) PS-10-30, (F) PS-10-35, (G) PS-10-40, (H) PS-60-05, (I) PS-60-10, respectively.

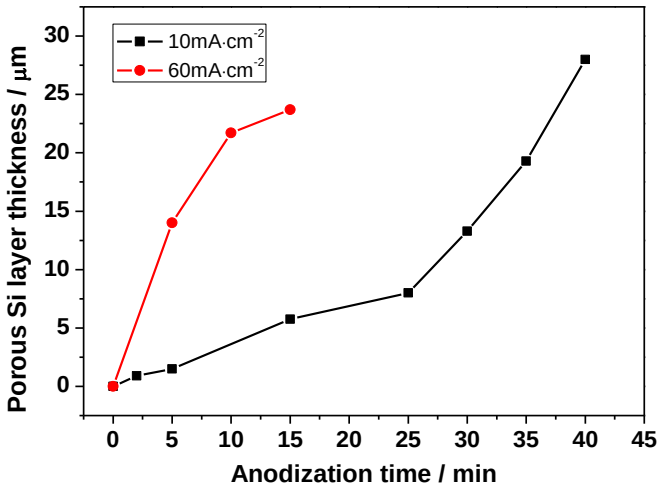

Figure 3.19 Plots of layer thickness against etching time for mesoporous silicon prepared under 10 mA·cm^{-2} (square) or 60 mA·cm^{-2} (circle).

3.3.3.2 Surface and pore properties of PS-mpSi

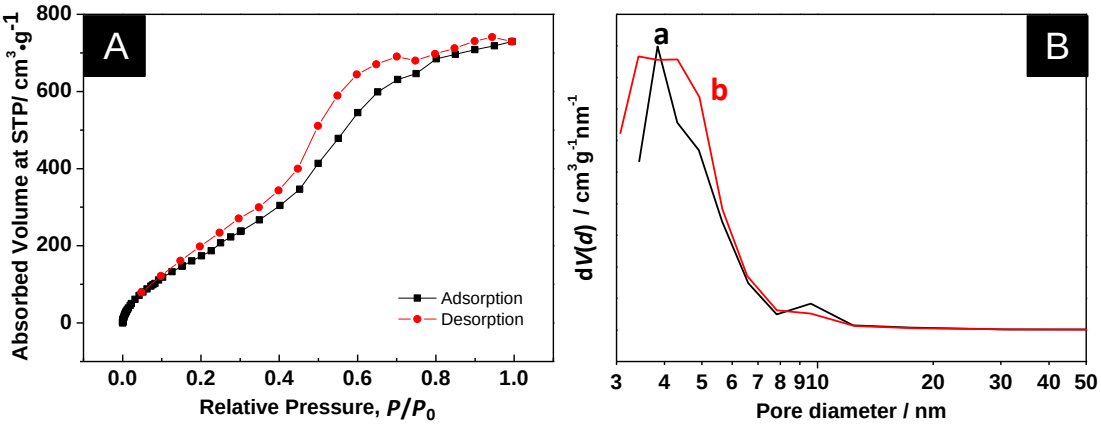

Figure 3.20 Nitrogen sorption isotherms (A) of PS-60-05 and pore size distribution curves (B) of PS-60-05 (a) and PS-60-15 (b).

To further reveal the effects of etching time, PS-60-05 was introduced into this study and its structure was characterised by nitrogen adsorption and XRD as demonstrated in Figure 3.20 and Figure 3.21. Type-IV curves with H2 hysteresis loop was featured in the nitrogen sorption isotherms of PS-60-05 with the capillary condensation occurring at relative pressure P/P_0 ~ 0.4. According to Table 3.4, its S_{BET} and V_{meso} were derived

as 819.2 $m^2 \cdot g^{-1}$ and 1.08 $cm^3 \cdot g^{-1}$. Compared to PS-60-15, it is clear to see that under constant etching current density (60 $mA \cdot cm^{-2}$), longer etching time leads to larger surface area and pore volume of the final mpSi structure. While the effect of etching duration on the average pore dimension is very limited. As indicated in Figure 3.20B, the PSZ curves of PS-60-05 and PS-60-15 were maximized at similar position, 3.84 nm for PS-60-05, 3.82 nm for PS-60-15.

3.3.3.3 Crystallite size of PS-mpSi

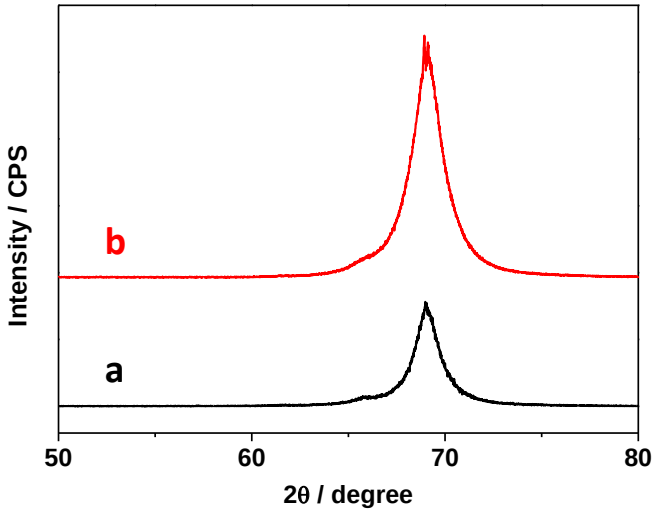

Figure 3.21 XRD patterns of PS-60-05 (a) and PS-60-15 (b)

As stated previously, the average size of Si nanocrystals can be measured based on Scherrer's Equation and it was 6.57 nm and 5.48 nm for PS-60-05 and PS-60-15, according to their XRD data above (Figure 3.21). As electrochemical etching extended, the size of the Si nanocrystallites was reduced although the pore dimension was unchanged, which confirms the influence of etching time on the microstructural characteristics of the resulting mpSi. This result also explains the larger specific surface area possessed by PS-60-15 as revealed above due to the smaller Si nanocrystallites created on the pore walls than PS-60-05.

To understand the effects of etching time, the PS-60-05 sample can be considered in the following discussion as an early stage of the formation process of PS-60-15 during electrochemical etching. As known, after 60 $mA \cdot cm^{-2}$ was applied, mesopores were gradually formed in the crystalline Si chip in the vertical direction along the [100] direction. As it progressed, the produced porous structure of Si was also immersed in the electrolyte solution and subject to the chemical corrosion of HF etchant during electrochemical process, causing the dissolution of Si mass on the pore walls which led to a gradual decrease of the size of the nanocrystallites embedded on the surface as revealed in the XRD results above. By affecting the immersion time of mpSi in the etchant solution, etching time is therefore able to modify the surface area, pore volume while the pore size of the porous system is mainly determined by the etching current applied in the electrochemical preparation of mpSi.

3.3.4 Characterisation results of HPS-mpSi

All the mpSi samples studied above were derived from moderately boron-doped *p*-type silicon wafer (PS in Table 2.1) of which the intrinsic resistivity is 1-10 Ω·cm. In this section, heavily boron-doped p-type silicon wafer (HPS in Table 2.1) with lower resistivity as 0.001-0.01 Ω·cm was employed in the preparation of mpSi materials with unique morphological characteristics as revealed below.

3.3.4.1 FE-SEM images of HPS-mpSi

Figure 3.22 exhibits the FE-SEM images of HPS-150-10 sample. As observed in the plane view mode (A and B), numerous nanopores were formed and distributed uniformly on the surface with thicker pore walls and larger pore openings compared to the moderately doped mpSi samples as mentioned above. The average diameter of the pores was measured as 12.4 nm based on the FE-SEM micrographs. The cross sectional FE-SEM images (C and D) clearly recorded the remarkable straightness of the pore arrays as they were shown to be orderly aligned along Si (100) plane and isolated by

thin walls of crystalline Si. The undulate surface feature due to numerous open pores was observable in the AFM image of HPS-150-10 while the surface of PS-60-15 appeared to be very smooth due to the very small pore openings as discovered previously.

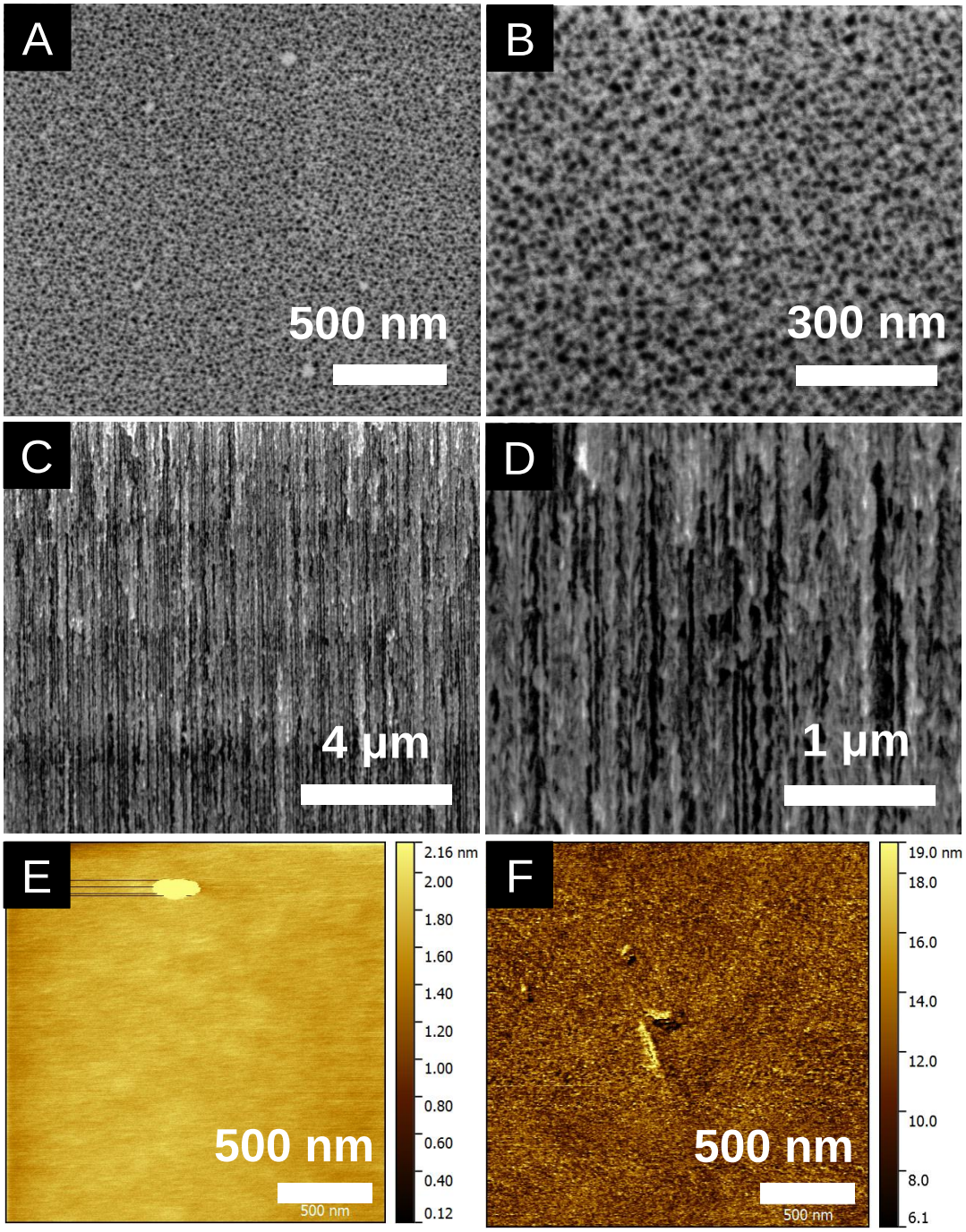

Figure 3.22 FE-SEM images of HPS-150-10 (plane view: A, B and cross sectional: C, D); AFM images of the top surface of PS-60-15 (E) and HPS-150-10 (F), respectively.

3.3.4.2 Raman scattering of HPS-mpSi

Raman scattering spectrum of HPS-150-10 was presented in Figure 3.23. A symmetric peak was centred at 519 cm^{-1} which was close to 521 cm^{-1} of well-defined Si crystal, indicating the framework crystallinity of HPS-150-10 was preserved considerably well after electrochemical etching in contrast to PS-60-15 studied in the earlier discussion. The laser power was reduced to 10 mW to minimize lattice expansion and spectral redshift caused by laser-induced heat generated on the crystalline framework.[35]

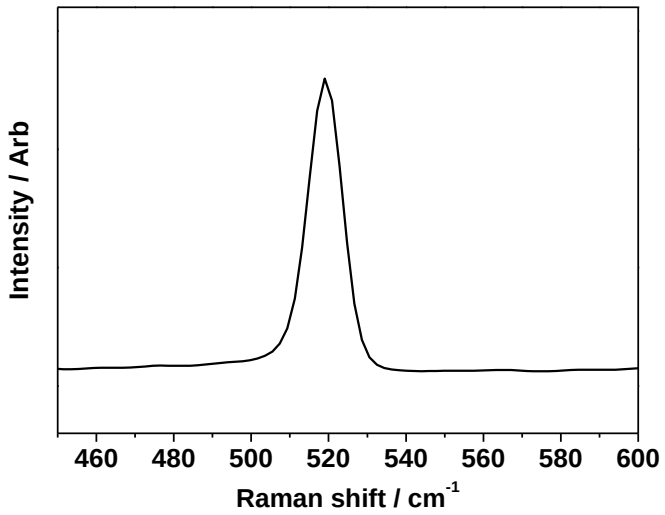

Figure 3.23 Raman spectrum of HPS-150-10.

3.3.4.3 ATR-IR spectrum of HPS-mpSi

The IR spectrum of HPS-150-10 presented in Figure 3.24 was similarly composed by six of the main characteristic bands as featured in the IR spectra of PS samples which were respectively maximized at 624, 663, 909, 2087, 2107, 2138 cm^{-1} from Si-Si and various vibration modes of Si-H. Detailed explanation of their origins can be referred to the discussion above of the PS samples.

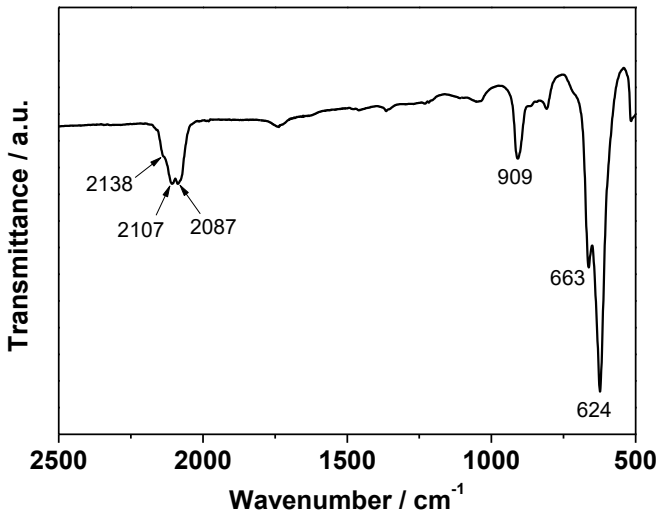

Figure 3.24 ATR-IR spectrum of HPS-150-10.

3.3.4.4 Nitrogen sorption analysis of HPS-mpSi

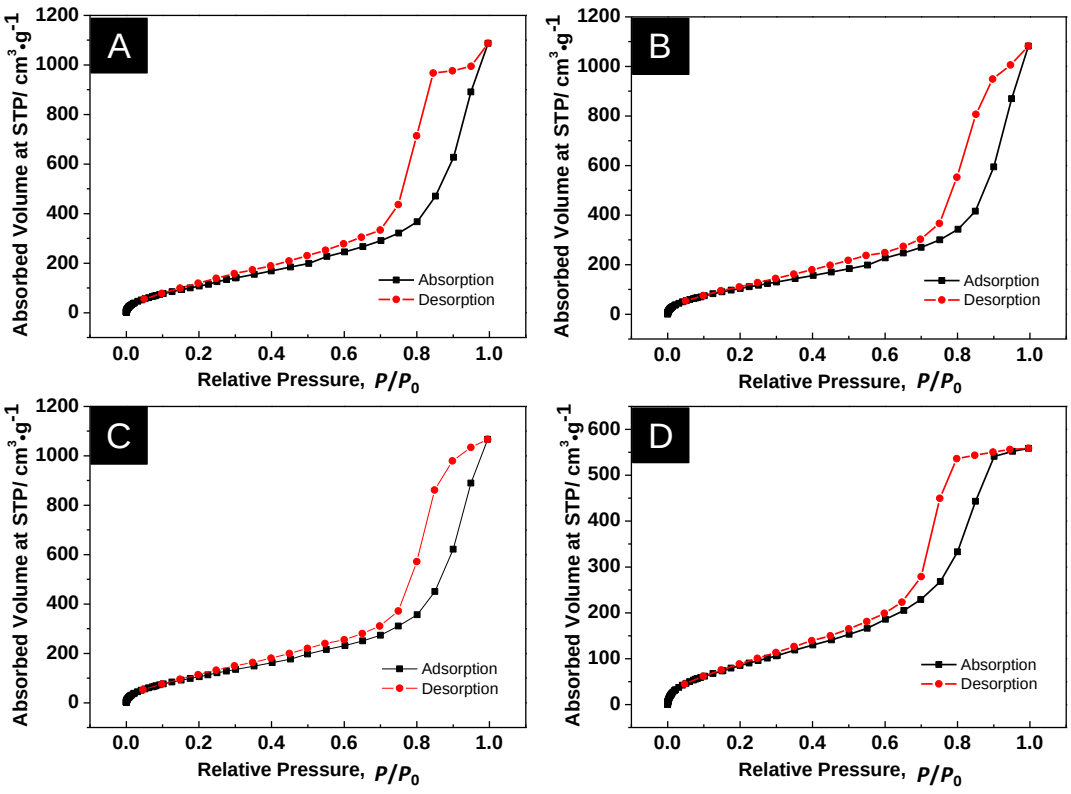

Figure 3.25 Nitrogen sorption isotherms of HPS-150-05 (A), HPS-150-10 (B), HPS-150-15 (C) and HPS-60-15 (D).

The isothermal analysis was carried out for a more precise examination of the surface and mesoporous structure of HPS samples. Including HPS-150-10, the nitrogen sorption isotherms of four different HPS samples are summarized in Figure 3.25 and characterised as IV-H1 pattern according to the IUPAC classification.[33] Meanwhile, the capillary condensation phenomenon occurred at relative pressure P/P_0 around 0.7, which was markedly higher than the turning point of PS samples that often took place at 0.4 relative pressure, representing larger mesopores possessed by these HPS structures. The average pore diameter of HPS-150-10 was 9.55 nm which has a mesopore volume (V_{meso}) as 1.72 $cm^3 \cdot g^{-1}$ and a specific surface area (S_{BET}) as 455.3 $m^2 \cdot g^{-1}$. The data of other HPS samples were shown in Table 3.5.

Table 3.5 Textural properties of heavily doped mesoporous silicon derived from nitrogen sorption isotherms.

Mesoporous silicon samples	S_{BET} / $m^2 \cdot g^{-1}$	V_{meso} / $cm^3 \cdot g^{-1}$	d_{pore} / nm
HPS-150-05	458.5	1.76	9.55
HPS-150-10	455.3	1.72	9.55
HPS-150-15	467.0	1.71	9.55
HPS-60-15	369.7	0.90	7.82

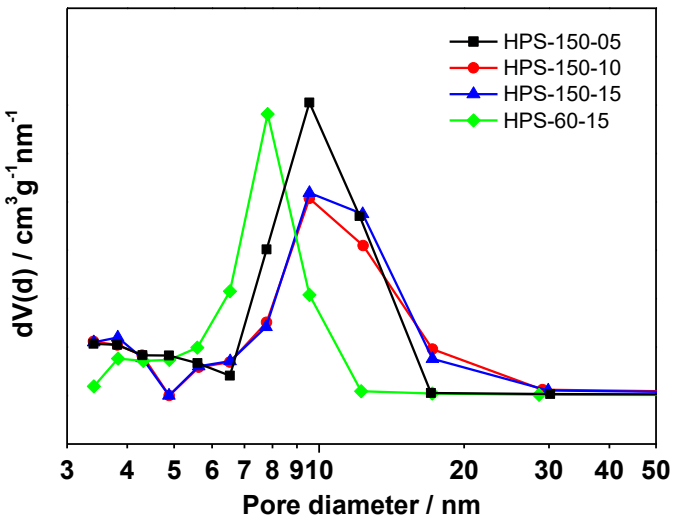

Figure 3.26 Pore size distribution curves of HPS samples (HPS-150-05, HPS-150-10, HPS-150-15 and HPS-60-15).

By comparing HPS-60-15 and HPS-150-15, the influences of etching current density on the surface and pore properties of HPS samples were revealed. As revealed in Table 3.5 and Figure 3.26, it is also very effective in shaping the porous structure of heavily doped HPS materials and has similar effect as on the moderately doped PS samples which is that under higher etching current density, the produced mpSi possesses larger specific surface area, pore volume and pore diameter.

While etching time was observed to have little effect on the porous morphology of HPS structures with respect to HPS-150-05, HPS-150-10 and HPS-150-15 of which the S_{BET}, V_{meso} and d_{pore} were almost identical as shown in Table 3.5 above. This is partly consistent with the previous findings on PS samples, which also contained very similar pore dimension but the S_{BET}, V_{meso} of PS samples were increased as electrochemical process prolonged. This is likely associated with the different degrees of crystallinity of mpSi materials. In contrast to the nanocrystalline or amorphous-like PS samples, the Si matrix of HPS samples was much better crystallized which endowed a stronger resistance to chemical dissolution in HF etchant during electrochemical etching process.

3.3.4.5 Layer thickness of HPS-mpSi

Figure 3.27 and Figure 3.28 exhibited the cross sectional images and mpSi layer thickness values of various HPS samples (HPS-150-05, HPS-150-10, HPS-60-05 and HPS-60-15) prepared under different etching current density (60 or 150 $mA \cdot cm^{-2}$) and etching time (5, 10, 15 min). Similarly, the layer thickness or the pore depth increases as a function of the etching duration.

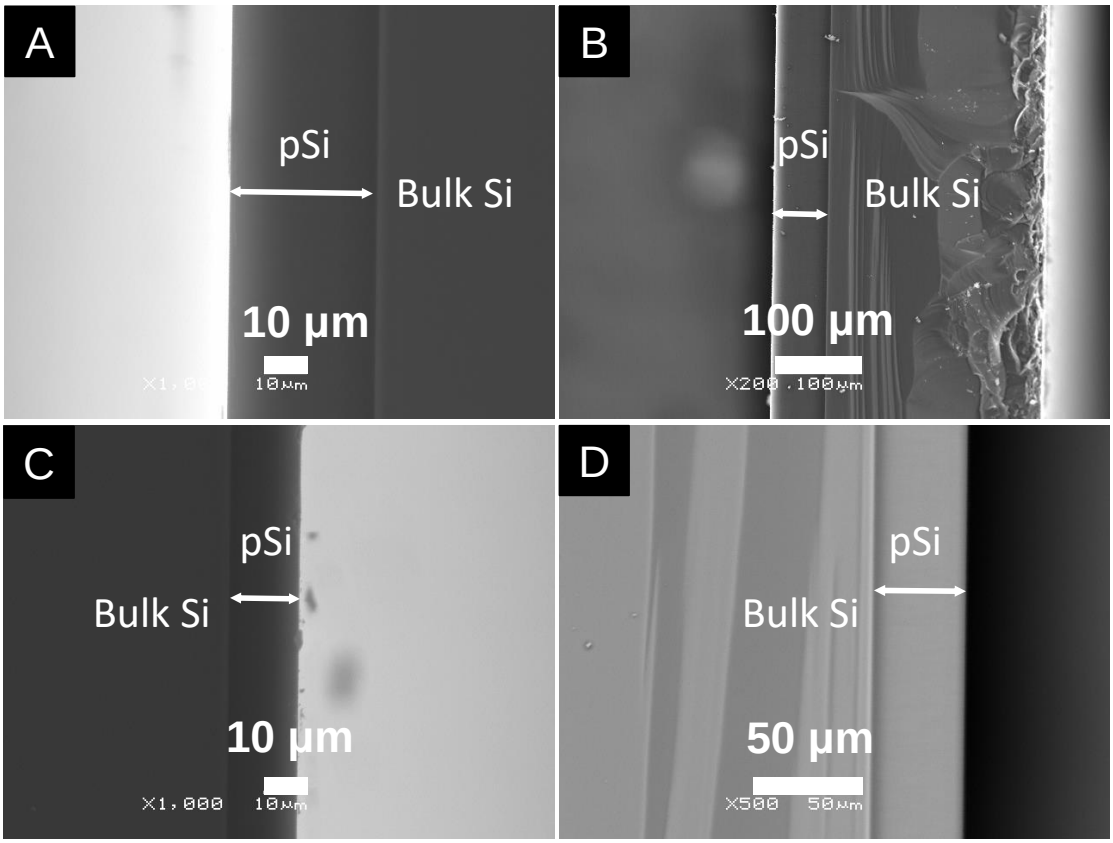

Figure 3.27 Cross sectional SEM images of HPS-150-05 (A), HPS-150-10 (B), HPS-60-05 (C) and HPS-60-15 (D).

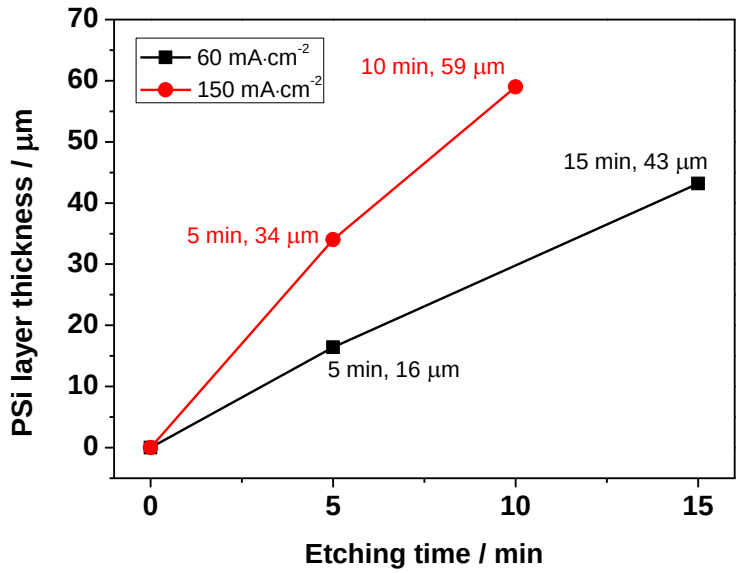

Figure 3.28 The layer thickness of heavily doped mesoporous silicon materials prepared under different etching current density (60 or 150 $mA \cdot cm^{-2}$) and etching time.

3.3.5 Free-standing mpSi disk and microflakes

The feasibility of the proposed post-treatments in preparing free-standing mesoporous silicon was investigated in this section by means of FE-SEM, IR and nitrogen sorption techniques.

3.3.5.1 Characterisation results of mpSi disk

Free-standing HPS-150-10 was prepared by lifting the mpSi layer off the substrate via 4 $mA \cdot cm^{-2}$ pulse etching as described in Chapter 2. Its physical appearance is observable in Figure 3.29, showing a dark coloured round disk shape. The FE-SEM image confirmed the identical honeycomb-like mesoporous structure and similar pore dimension as the original sample before the detachment.

While HPS disks were mostly stable and could be readily transferred by using a razor blade or spatula, PS disks were less likely to remain intact during vacuum drying and subsequent handling because of the layer thinness and highly porous texture. This situation can be rectified to some extent by supercritical liquid drying as suggested by previous studies.[34, 36-37]

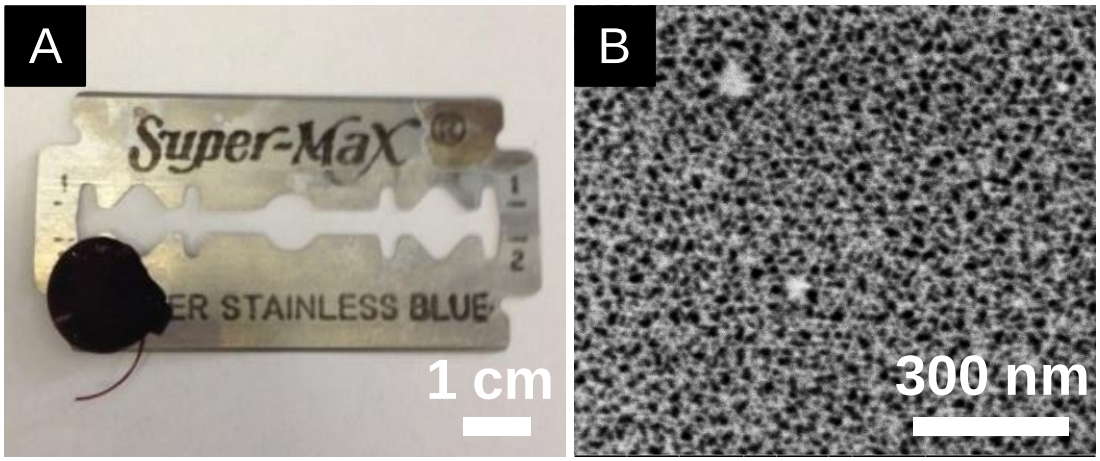

Figure 3.29 Photograph (A) and FE-SEM image (B) of HPS-150-10-D.

3.3.5.2 Characterisation results of mpSi microflakes

After pulse etching, the dried mpSi disks were then subjected to ultrasonication and transformed into free-standing microflakes as pictured in Figure 3.30 showing the physical appearance of so-obtained PS-60-15-F (A) and HPS-150-10-F (B).

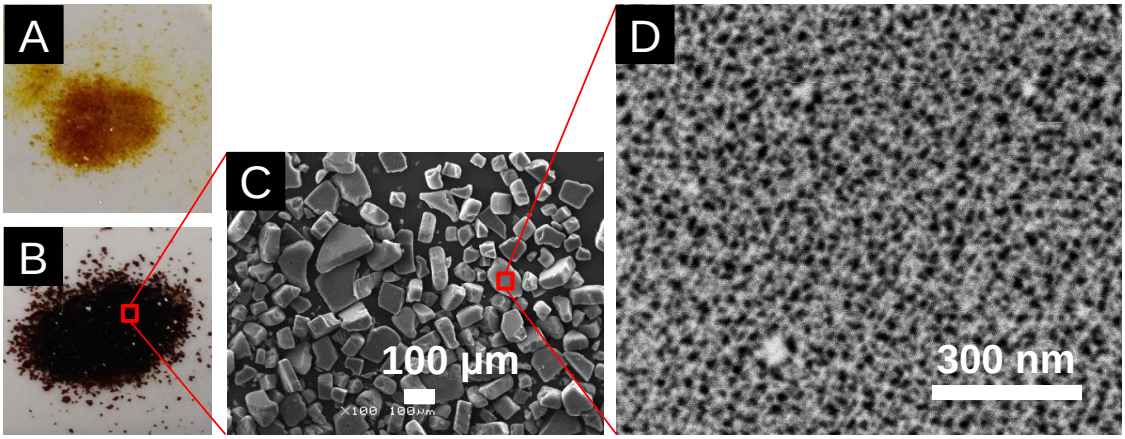

Figure 3.30 Photographs of PS-60-15-F (A) and HPS-150-10-F (B); plane-view SEM images (C, D) of HPS-150-10-F.

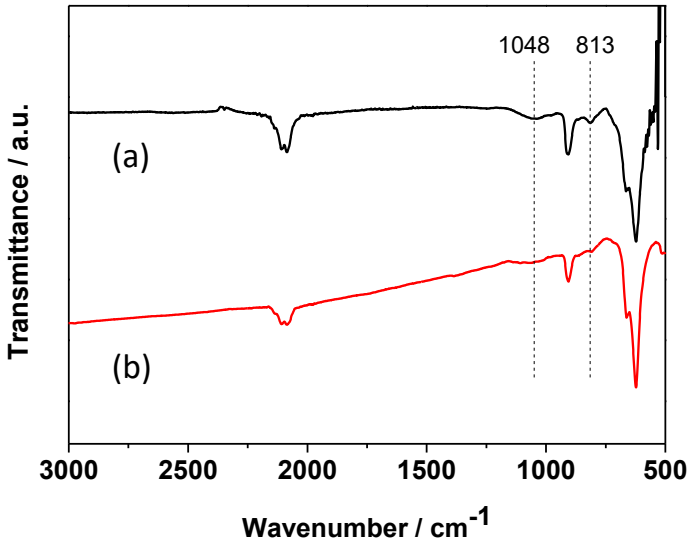

Figure 3.31 ATR-IR spectra (D) of PS-60-15-F (a) and HPS-150-10-F (b).

The ATR-IR spectra (Figure 3.31) clearly show that the surface of both samples was still hydrogen passivated with observable IR peaks from Si-H bonds at 664, 912, 2088, 2110, 2140 cm^{-1}. Minor oxidation was also detected on the surface of PS-60-15-F sample, indicated by the IR peaks at 813 cm^{-1} and 1048 cm^{-1}, assuming to be related to its large surface area and relatively poor structural crystallinity.

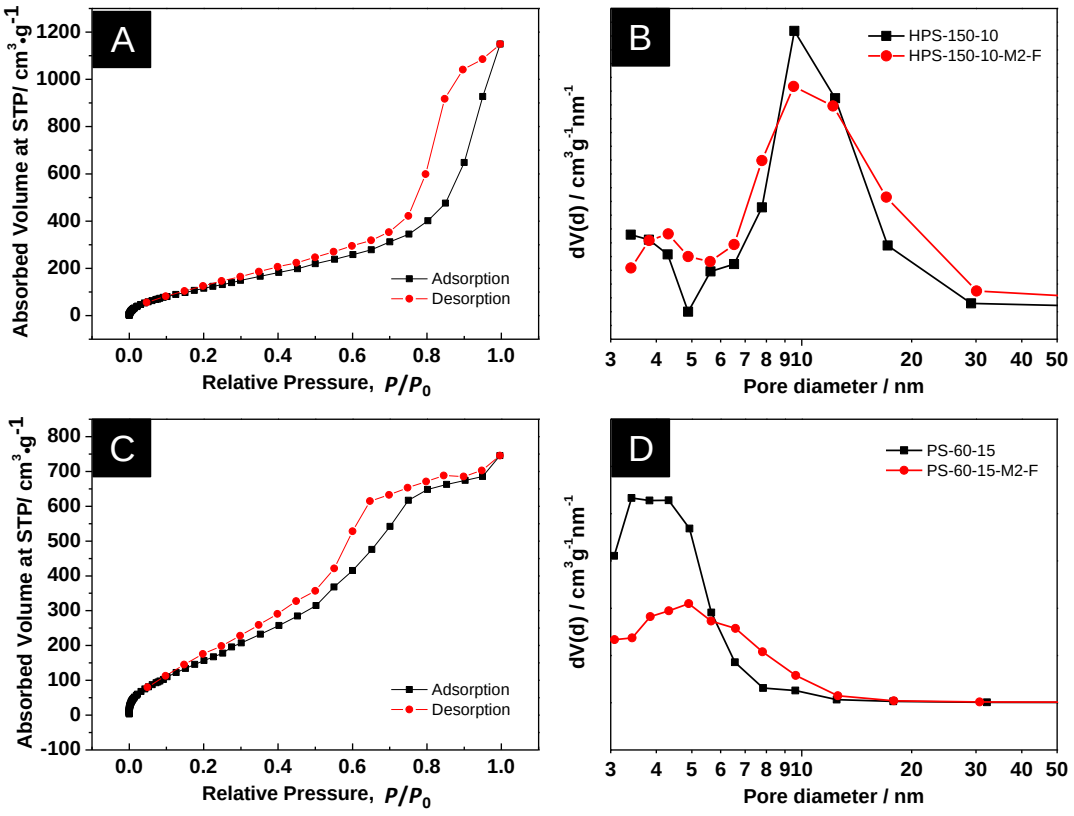

Figure 3.32 Nitrogen sorption isotherms (A, C) and pore size distribution (B, D) of HPS-150-10-F (A and B) and PS-60-15-F (C and D).

The surface and pore properties of PS-60-15-F and HPS-150-10-F microflakes were further examined by nitrogen sorption isotherms (Figure 3.32) and a summary of S_{BET}, V_{meso} and d_{pore} data was presented in Table 3.6 below. The average pore diameter of HPS-150-10-F was measured as 9.50 nm, which is very similar to the untreated HPS-150-10 sample. The similarity was also reflected in the total pore volume which was marginally increased to 1.82 $cm^3 \cdot g^{-1}$ after being processed into free-standing microflakes. Due to fragmentation, the specific surface area of HPS-150-10-F was

increased to 527.0 $m^2 \cdot g^{-1}$. However, the surface area and total pore volume of PS-60-15-F were both reduced compared to the as-etched PS-60-15 sample. This is likely caused by the sonication-induced structural alteration which resulted in the variation of pore dimension and pore size distribution as seen in Figure 3.32.

Table 3.6 Textural properties of mesoporous silicon microflakes and as-etched mesoporous silicon.

Mesoporous silicon samples	S_{BET} / $m^2 \cdot g^{-1}$	V_{meso} / $cm^3 \cdot g^{-1}$	d_{pore} / nm
HPS-150-10	455.3	1.72	9.55
HPS-150-10-F	527.0	1.82	9.50
PS-60-15	994.4	1.36	3.82
PS-60-15-F	699.9	1.16	4.91

3.3.6 Characterisation results of thiol-capped mpSi

As revealed above, the vast internal surface of both as-etched moderately doped PS and heavily doped HPS samples are purely hydrogen-terminated. By covalently binding with other organic molecules through silicon hydrosilylation that can be initiated by heat, light, radicals or metal catalysts etc., the surface of porous silicon can be modified with various functionalities. Here allyl mercaptan was intended to be grafted onto the surface of H-terminated mpSi materials with large surface area and open mesoporous structure. With –SH as functional end groups on the mpSi surface, modified mpSi material can be conjugated with many biologically active species through disulphide bond, which can be selectively cleaved inside the cells. On the other hand, thiol-functionalized mpSi can also be used as catalyst support in anchoring and stabilizing metal nanoparticles.[38-40]

A comparison of grafting efficiency among three different heating methods including oil bath, conventional oven and domestic microwave oven was provided below which shows the superior performance of microwave irradiation in thiol capping.

3.3.6.1 Oil bath

By refluxing the reaction mixture of allyl mercaptan and toluene solvent with as-etched PS-60-05 for certain amount of time, it is possible to trigger the addition reaction between Si-H and C=C bond. By adjusting the reflux time, a series of experiments were performed and the IR results were shown in Figure 3.33.

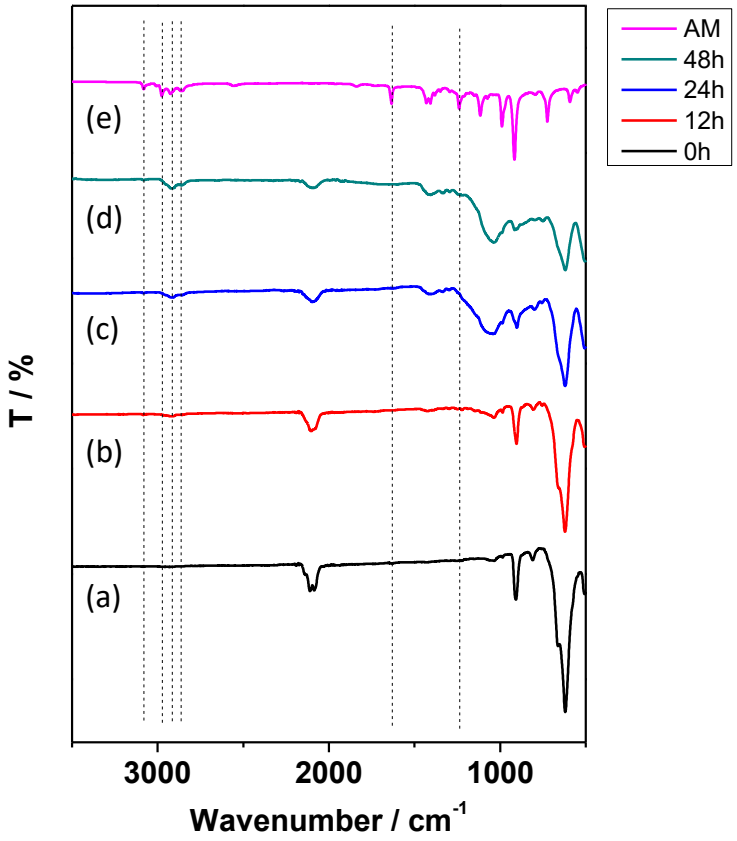

Figure 3.33 ATR-IR spectra of as-etched PS-60-05 (a), thiol-capped PS-60-05-RF samples obtained under various reflux time in oil bath (b: 12 hours; c: 24 hours; d: 48 hours) and allyl mercaptan (e) as a reference.

As demonstrated in Figure 3.33, hydrosilylation took place with silicon hydride consumption despite the occurrence of oxidation that could also contribute to the depletion of surface SiH_x. As reaction time increased from 12 h to 48 h, the IR peaks of SiH_x at 2080-2140 cm^{-1} became weaker while saturated hydrocarbon signals in the range of 2800-3000 cm^{-1} intensified accordingly, implying an increasing number of

organic ligands successfully linked to the surface of mpSi material. The absence of sp^2 C-H stretching mode at 3081 cm^{-1} and C=C stretching mode at 1634 cm^{-1} that featured in the IR spectrum of allyl mercaptan further confirmed the binding result, suggesting the alkene group of allyl mercaptan was successfully saturated by the surface hydrides of mpSi which resulted in the covalent ligandization by forming the new Si-C bond of which the IR absorption was also found at 1260 cm^{-1}.

3.3.6.2 Conventional oven

The hydrosilylation reaction was also carried out in a PTFE lined autoclave reactor in combination with a conventional oven so that the reaction temperature can be elevated above the boiling point of toluene solvent in order to enhance the formation of thiol linkages. As exhibited in Figure 3.34, the surface hydrides were completely extinguished with no organic signals observable in the IR spectrum, suggesting the inefficiency of this heating approach.

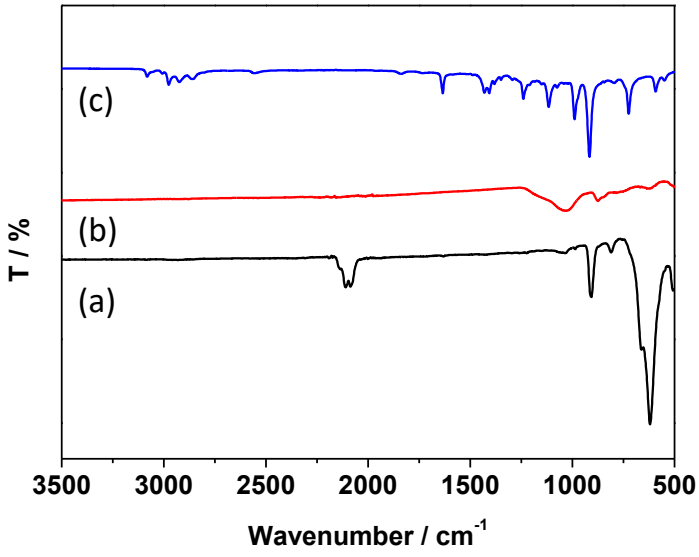

Figure 3.34 ATR-IR spectra of as-etched PS-60-05 (a), PS-60-05-AC prepared in an autoclave (b) and allyl mercaptan (c).

3.3.6.3 Microwave irradiation

The above two conventional heating methods allow the heat to be transferred to reaction system through thermal conduction and convection, which is often recognized as indirect and of low-efficiency.[41] Microwave-assisted thermal-driven hydrosilylation was thus explored in this study. Benefitting from the direct, rapid, volumetric and non-contact heating characteristics, microwave energy has shown its superiority in accelerating reaction rate and improving product selectivity under mild conditions in various studies.[41-43]

Doped silicon is known to absorb microwave energy efficiently.[44] The heat transfer to the near surface of the material will lead to a temperature gradient, which is expected to influence the reaction rate during the chemical treatment of H-terminated mesoporous silicon with organic reagents. The resistivity of the silicon wafer used to prepare PS-60-05 is 1-10 Ω·cm, which is right in the range of the maximum absorption of MW irradiation.[45] While toluene employed in the reaction system as solvent is non-polar and hence microwave transparent. These different interaction behaviours with microwave irradiation is expected to impact on the course and rate of the hydrosilylation reaction rate.

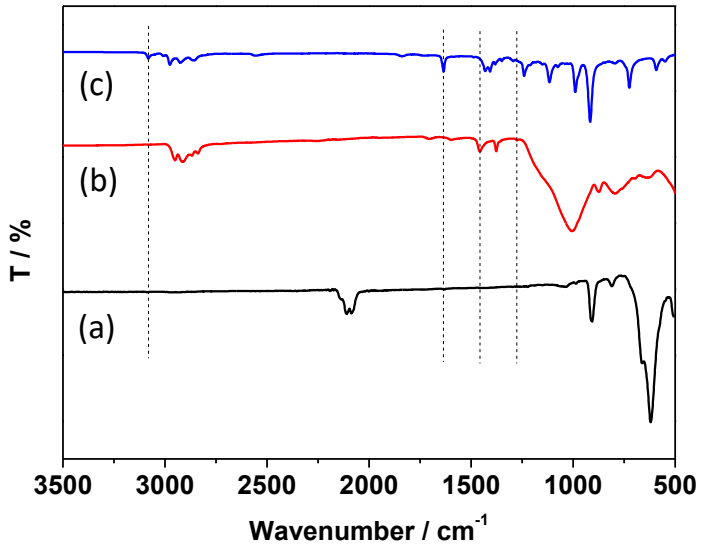

Figure 3.35 ATR-IR spectra of as-etched PS-60-05 (a), thiol-capped PS-60-05-MW obtained under microwave irradiation (b) and allyl mercaptan (c) as a reference.

As shown in Figure 3.35, Si-C stretching peaks were detected at 1260 cm^{-1} and 1460 cm^{-1}. Additional peaks characteristic of the alkyl chain also appeared at 2850-3000 cm^{-1} in the spectrum of PS-60-05-MW. The absence of signals from C=C bond at 1634 cm^{-1} and sp^2 C-H bond at 3081 cm^{-1} verified the fact that final product was free of physically absorbed organic molecules. Meanwhile, a large decrease of the ν_{SiHx} (2080-2140 cm^{-1}), δ_{SiH2} (910 cm^{-1}), and ρ_{SiHx} (669 cm^{-1}) peaks was also observed, indicating the reaction was efficient within 6 min by consuming silicon hydrides. It is worth noting that the vibration absorption band of thiol S-H at 2550-2620 cm^{-1}, however, was not identifiable in the spectrum of the capped sample. This is probably because the absorption signal is commonly known as weak and broad as evidenced by the IR spectrum of the neat allyl mercaptan in Figure 3.35c.

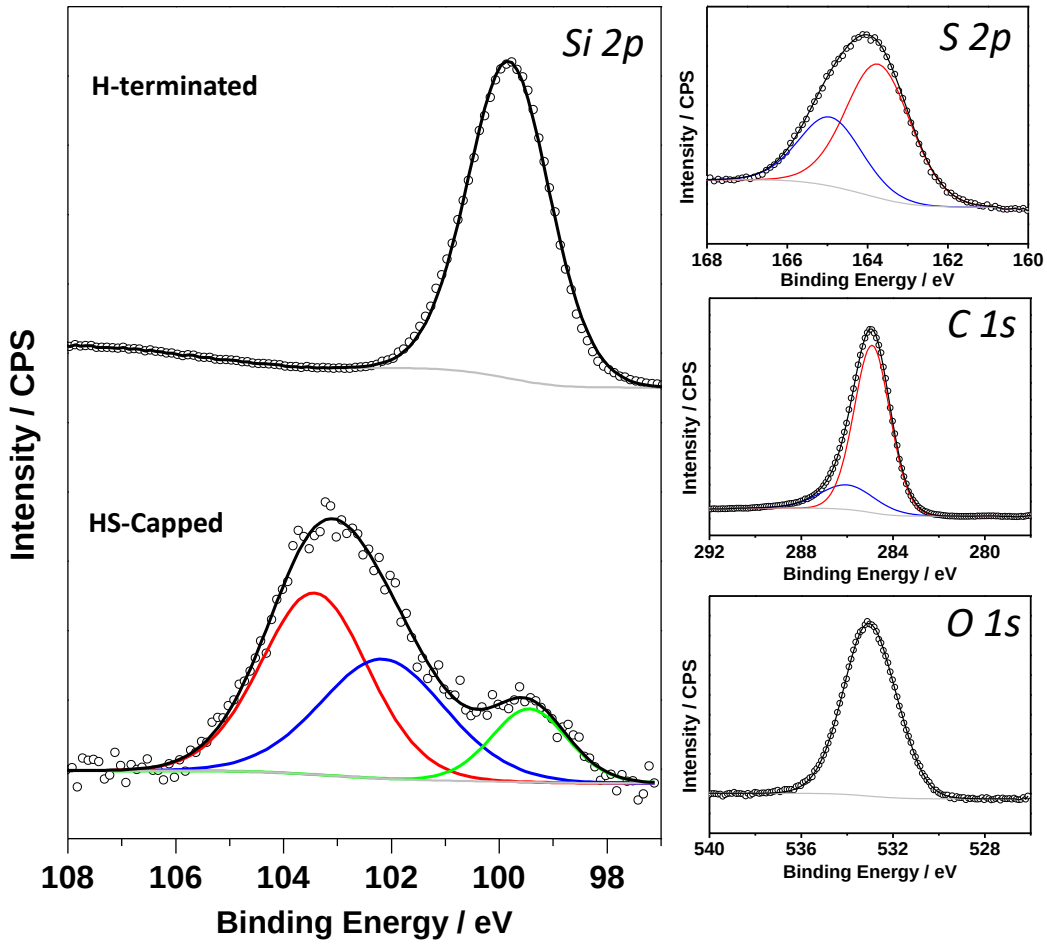

Figure 3.36 Deconvoluted XPS spectra of Si 2*p*, S 2*p*, C 1*s* and O 1*s* regions of PS-60-05-MW and Si 2*p* of freshly prepared PS-60-05.

The chemical bonding of thiol-capped PS-60-06-MW sample was also revealed in the XPS analysis (Figure 3.36). For comparison, the Si 2*p* XPS spectrum of freshly made PS-60-05 was also recorded which saw the distinctive single peak at 99.8 eV from Si-Si in accordance with its surface nature as described previously. While the Si 2*p* spectrum of thiol-capped product was fitted by three components of which the respective B.E. was centred at 103.4, 102.2, 99.4 eV, attributable to Si-O, Si-C and Si-Si. The preservation of thiol functionality after ligand grafting was affirmed by the presence of S 2*p* peak at 164.0 eV in the XPS spectrum, which comprised two sub-peaks in a 1:2 area ratio at 165.0 eV and 163.8 eV belonging to S $2p^{1/2}$ and S $2p^{3/2}$ from C-SH bond. By calculating the peak area of Si-C and Si-O spectra, thiol coverage was estimated as 43.6% of the total surface in this study.

3.4 Summary

This chapter is devoted to the preparation of mesoporous silicon via electrochemical etching method. By anodically etching the mono-crystalline Si wafer, mesoporous silicon was produced on the Si chip which shows intriguing morphological characteristics of large surface area, mesoporous system and ample hydrogen termination. The existence of abundant Si nanocrystallites on the framework is also an important feature as they not only give rise to the high surface area but also are able to influence the electronic band structure and optical properties of mesoporous silicon. The high surface area and open mesoporous network could enhance the mass transport in liquid phase applications although it is also largely dependent on the actual pore dimension and interconnectivity, which can be altered by adjusting the etching variables. An interconnected 3D porous network and a nicely ordered 1D channel arrays were characterised in the moderately doped and heavily doped mesoporous silicon, respectively. Free standing mpSi can be gained through pulse etching and thiol capped mpSi can be prepared via microwave-assisted hydrosilylation which was proved to be very efficient because of the selective heating of Si.

3.5 References

1. Wang, B.; Li, X.; Qiu, T.; Luo, B.; Ning, J.; Li, J.; Zhang, X.; Liang, M.; Zhi, L., High volumetric capacity silicon-based lithium battery anodes by nanoscale system engineering. *Nano Lett.* **2013,** *13* (11), 5578-5584.

2. Ge, M.; Fang, X.; Rong, J.; Zhou, C., Review of porous silicon preparation and its application for lithium-ion battery anodes. *Nanotechnology* **2013,** *24* (42), 422001.

3. Thakur, M.; Sinsabaugh, S. L.; Isaacson, M. J.; Wong, M. S.; Biswal, S. L., Inexpensive method for producing macroporous silicon particulates (MPSPs) with pyrolyzed polyacrylonitrile for lithium ion batteries. *Sci. Rep.* **2012,** *2*, 795.

4. Szczech, J. R.; Jin, S., Nanostructured silicon for high capacity lithium battery anodes. *Energy Environ. Sci.* **2011,** *4* (1), 56-72.

5. Li, X.; Gu, M.; Hu, S.; Kennard, R.; Yan, P.; Chen, X.; Wang, C.; Sailor, M. J.; Zhang, J. G.; Liu, J., Mesoporous silicon sponge as an anti-pulverization structure for high-performance lithium-ion battery anodes. *Nat. Commun.* **2014,** *5*, 4105.

6. Park, J. H.; Gu, L.; von Maltzahn, G.; Ruoslahti, E.; Bhatia, S. N.; Sailor, M. J., Biodegradable luminescent porous silicon nanoparticles for in vivo applications. *Nat. Mater.* **2009,** *8* (4), 331-336.

7. Gu, L.; Park, J. H.; Duong, K. H.; Ruoslahti, E.; Sailor, M. J., Magnetic luminescent porous silicon microparticles for localized delivery of molecular drug payloads. *Small* **2010,** *6* (22), 2546-2552.

8. Gu, L.; Hall, D. J.; Qin, Z.; Anglin, E.; Joo, J.; Mooney, D. J.; Howell, S. B.; Sailor, M. J., In vivo time-gated fluorescence imaging with biodegradable luminescent porous silicon nanoparticles. *Nat. Commun.* **2013,** *4*, 2326.

9. Anglin, E. J.; Cheng, L. Y.; Freeman, W. R.; Sailor, M. J., Porous silicon in drug delivery devices and materials. *Adv. Drug Deliv. Rev.* **2008,** *60* (11), 1266-1277.

10. Salonen, J.; Kaukonen, A. M.; Hirvonen, J.; Lehto, V. P., Mesoporous silicon in drug delivery applications. *J. Pharm. Sci.* **2008,** *97* (2), 632-653.

11. McInnes, S. J. P.; Voelcker, N. H., Porous silicon-based nanostructured microparticles as degradable supports for solid-phase synthesis and release of oligonucleotides. *Nanoscale Res. Lett.* **2012,** *7*(1), 385.

12. Sailor, M. J.; Wu, E. C., Photoluminescence-based sensing with porous silicon films, microparticles, and nanoparticles. *Adv. Funct.l Mater.* **2009,** *19* (20), 3195-3208.

13. Kotkovskiy, G. E.; Kuzishchin, Y. A.; Martynov, I. L.; Chistyakov, A. A.; Nabiev, I., The photophysics of porous silicon: technological and biomedical implications. *Phys. Chem. Chem. Phys.* **2012,** *14* (40), 13890-13902.

14. Harraz, F. A., Porous silicon chemical sensors and biosensors: a review. *Sens. Actuators B Chem.* **2014,** *202*, 897-912.

15. Dai, F.; Zai, J.; Yi, R.; Gordin, M. L.; Sohn, H.; Chen, S.; Wang, D., Bottom-up synthesis of high surface area mesoporous crystalline silicon and evaluation of its hydrogen evolution performance. *Nat. Commun.* **2014,** *5*, 3605.

16. Su, J.; Yu, H.; Quan, X.; Chen, S.; Wang, H., Hierarchically porous silicon with significantly improved photocatalytic oxidation capability for phenol degradation. *Appl. Catal. B* **2013,** *138-139*, 427-433.

17. Dasog, M.; Kraus, S.; Sinelnikov, R.; Veinot, J. G. C.; Rieger, B., CO_2 to methanol conversion using hydride terminated porous silicon nanoparticles. *Chem. Commun.* **2017,** *53* (21), 3114-3117.

18. Ye, M.; Qian, C.; Sun, W.; He, L.; Jia, J.; Dong, Y.; Zhou, W., Dye colour switching by hydride-terminated silicon particles and its application as an oxygen indicator. *J. Mater. Chem. C* **2016,** *4* (20), 4577-4583.

19. Yang, X.-Y.; Chen, L.-H.; Li, Y.; Rooke, J. C.; Sanchez, C.; Su, B.-L., Hierarchically porous materials: synthesis strategies and structure design. *Chem. Soc. Rev.* **2017,** *46* (2), 481-558.

20. Schneider, D.; Mehlhorn, D.; Zeigermann, P.; Kärger, J.; Valiullin, R., Transport properties of hierarchical micro–mesoporous materials. *Chem. Soc. Rev.* **2016,** *45* (12), 3439-3467.

21. Venuta, A.; Wolfram, J.; Shen, H.; Ferrari, M., Post-nano strategies for drug delivery: multistage porous silicon microvectors. *J. Mater. Chem. B* **2017,** *5* (2), 207-219.

22. Naderi, N.; Hashim, M. R.; Amran, T. S. T., Enhanced physical properties of porous silicon for improved hydrogen gas sensing. *Superlattices Microstruct.* **2012,** *51* (5), 626-634.

23. Bisi, O.; Ossicini, S.; Pavesi, L., Porous silicon: a quantum sponge structure for silicon based optoelectronics. *Surf. Sci. Rep.* **2000,** *38* (1-3), 1-126.

24. Canham, L. T., Silicon quantum wire array fabrication by electrochemical and chemical dissolution of wafers. *Appl. Phys.Lett.* **1990,** *57* (10), 1046-1048.

25. Santos, A.; Kumeria, T., Electrochemical etching methods for producing porous silicon. **2015,** *220*, 1-36.

26. Canham, L., *Handbook of porous silicon*. Springer International Publishing: 2014.

27. Lehmann, V.; Gosele, U., Porous silicon formation - a quantum wire effect. *Appl. Phys. Lett.* **1991,** *58* (8), 856-858.

28. Dasog, M.; Kehrle, J.; Rieger, B.; Veinot, J. G., Silicon nanocrystals and silicon-polymer hybrids: synthesis, surface engineering, and applications. *Angew. Chem. Int. Ed. Engl.* **2016,** *55* (7), 2322-2339.

29. Deshmukh, A. B.; Devarapalli, R. R.; Shelke, M. V., Functional silicon nanostructures derived from drying-mediated self-assembly of gold nanoparticles. *Journal of Nanoparticle Research* **2014,** *16* (5).

30. Patterson, A. L., The scherrer formula for X-Ray particle size determination. *Phys. Rev.* **1939,** *56* (10), 978-982.

31. Xifré Pérez, E. Design, fabrication and characterization of porous silicon multilayer optical devices. Universitat Rovira i Virgili., 2007.

32. Lenshin, A. S.; Kashkarov, V. M.; Seredin, P. V.; Spivak, Y. M.; Moshnikov, V. A., XANES and IR spectroscopy study of the electronic structure and chemical composition of porous silicon on n- and p-type substrates. *Semiconductors* **2011,** *45* (9), 1183-1188.

33. Thommes, M.; Kaneko, K.; Neimark, A. V.; Olivier, J. P.; Rodriguez-Reinoso, F.; Rouquerol, J.; Sing, K. S. W., Physisorption of gases, with special reference to the evaluation of surface area and pore size distribution (IUPAC Technical Report). *Pure Appl. Chem.* **2015,** *87* (9-10), 1051-1069.

34. Loni, A.; Canham, L. T.; Defforge, T.; Gautier, G., Supercritically-dried porous silicon powders with surface areas exceeding 1000 m^2/g. *ECS J. Solid State Sci. Technol.* **2015,** *4* (8), 289-292.

35. Gouadec, G.; Colomban, P., Raman Spectroscopy of nanomaterials: How spectra relate to disorder, particle size and mechanical properties. *Prog. Cryst. Growth Charact. Mater.* **2007,** *53* (1), 1-56.

36. Joo, J.; Defforge, T.; Loni, A.; Kim, D.; Li, Z. Y.; Sailor, M. J.; Gautier, G.; Canham, L. T., Enhanced quantum yield of photoluminescent porous silicon prepared by supercritical drying. *Appl. Phys. Lett.* **2016,** *108* (15), 153111.

37. Canham, L. T.; Cullis, A. G.; Pickering, C.; Dosser, O. D.; Cox, T. I.; Lynch, T. P., Luminescent anodized silicon aerocrystal networks prepared by supercritical drying. *Nature* **1994,** *368* (6467), 133-135.

38. Walcarius, A.; Etienne, M.; Bessière, J., Rate of access to the binding sites in organically modified silicates. 1. Amorphous silica gels grafted with amine or thiol groups. *Chem. Mater.* **2002,** *14* (6), 2757-2766.

39. Wang, C.; Flynn, N. T.; Langer, R., Controlled structure and properties of thermoresponsive nanoparticle–hydrogel composites. *Adv. Mater.* **2004,** *16* (13), 1074-1079.

40. Yang, H.; Wang, Y.; Huang, H.; Gell, L.; Lehtovaara, L.; Malola, S.; Hakkinen, H.; Zheng, N., All-thiol-stabilized Ag_{44} and $Au_{12}Ag_{32}$ nanoparticles with single-crystal structures. *Nat. Commun.* **2013,** *4*, 2422.

41. Oliver Kappe, C., Microwave dielectric heating in synthetic organic chemistry. *Chem. Soc. Rev.* **2008,** *37* (6), 1127-1139.

42. Dallinger, D.; Kappe, C. O., Microwave-assisted synthesis in water as solvent. *Chem. Rev.* **2007,** *107* (6), 2563-2591.

43. Zhu, Y. J.; Chen, F., Microwave-assisted preparation of inorganic nanostructures in liquid phase. *Chem. Rev.* **2014,** *114* (12), 6462-6555.

44. Boukherroub, R.; Petit, A.; Loupy, A.; Chazalviel, J. N.; Ozanam, F., Microwave-assisted chemical functionalization of hydrogen-terminated porous silicon surfaces. *J. Phys. Chem. B* **2003,** *107* (48), 13459-13462.

45. Moreno, T., *Microwave Transmission Design Data*. Dover Publications Inc.: New York: 1948.

Chapter 4

Hydrogen-Terminated Mesoporous Silicon as Visible-Light-Active Photocatalyst in Dye Degradation

Abstract

On the basis of a detailed analysis of the morphological, optical and electronic band properties, the use of mesoporous silicon with hydrogen termination in visible-light-driven methyl orange photo-degradation as a model system have been investigated in-depth in study with gained insights into the varied effects of structural factors, the roles of surface species and a deepened mechanistic understanding of its intriguing photocatalytic behaviours which is primarily expressed as an interrelated combination of photo-generated charge-driven processes and an enhanced hydrogen transfer process upon light irradiation.

4.1 Overview

As it is free and abundant, the use of sunlight to store and transfer energy is of great importance to environmental protection. Over the past few decades, various photo-active nanomaterials (transition metal oxides, chalcogenides, plasmonic metal nanoparticles etc.)[1-2] were developed to harness the renewable solar energy, aiming to meet the clean energy demand,[3] to tackle climate change,[4] and to control the deteriorating pollution crisis.[5] The large surface area, unique electron conduction properties, size dependent effects, etc.[6] largely contributed to the excellent photocatalytic performance of nanomaterials in eliminating environmental pollutants, purifying contaminated wastewater due to heavy metal ions and harmful organic compounds such as dyeing agents as one of the main causes.[7-8] Despite the remarkable progress over the years, narrow light responsive range, fast charge recombination rate, high cost of raw materials and associated environmental risks, as well as poor catalyst separation efficiency, still substantially limit their engineering applications.[9]

As a promising metal-free semiconductor, silicon nanostructures have received great attention owing to the environmental friendliness, natural abundance, low production cost and tuneable visible light responsiveness.[10-12] Significant efforts have been dedicated to exploiting the photo-activity of silicon quantum dots (Si QDs),[13-14] silicon nanowires (Si NWs)[15-21] and porous silicon (pSi),[22-26] which often show a broad absorption over entire spectral range as featured in various studies. As a result, nano-engineered silicon structures were discovered to possess a comparable photocatalytic capability as other inorganic materials in triggering diverse range of redox reactions, such as CO_2 fixation,[13, 19, 27] water splitting,[11, 24, 28] organic synthesis[29-30] and pollutant degradation (e.g. methyl orange, methylene blue, Rhodamine B, phenol and nitroaromatics)[13, 15-18, 22, 26, 31-34] under visible light irradiation. However, the photocatalytic behaviour of silicon nanomaterials is still not so clear yet especially for porous silicon which possesses much more complex micro- and nano-structural features that will strongly influence the performance compared with the low dimensional Si QDs, Si NWs etc.

In the last chapter focusing on the synthesis and characterisation of mesoporous silicon (mpSi) via electrochemical etching method, two distinctive porous morphologies have been discovered, depending on the dopant concentration of the initial wafer material. Moderately boron-doped mpSi samples ("PS-*J*-*t*") presented a 3D mesoporous network with large surface area while the heavily doped counterparts ("HPS-*J*-*t*") can be descried as ordered 1D channel arrays with relatively large pore width. By tuning the etching variables (*J*, *t*), structural properties (surface area, pore size, pore length, Si nanocrystallites) of mpSi material can be controllably altered of which the impacts on the optical properties and photocatalytic activity of mpSi in degrading methyl orange (MO) under visible light illumination will be revealed in this study.

This chapter summarized the kinetic results of MO degradation reaction by H-terminated mesoporous silicon with various morphologies in the presence and absence of external light irradiation. The essential roles of the existence of silicon nanocrystallites and hydrogen passivation on the porous surface were affirmed in our experiments with deciding effects on the material's activity and degradation behaviours. Large surface area, large mesopores, open mesoporous structure and abundant surface hydrides facilitated the mass transport and promoted the photo-degradation process while the activity of ordered 1D channel arrays of heavily doped samples was further enhanced by the well-defined crystalline framework and better electrical conductivity. By analysing the organic carbon content, active species and band potentials, the photocatalytic mechanism of H-terminated mesoporous silicon materials was proposed, which illustrated the different photochemical and chemical degradation pathways of MO molecules simultaneously occurring on the Si interface. Last but not the least, as shown later in this study, monolithic mpSi samples can also be efficiently separated from the reaction system and an excellent reusability was exhibited with a remaining 88% of the initial efficacy after 10 cycles of photo-degradation.

4.2 Experimental section

4.2.1 Photocatalyst preparation

H-terminated mesoporous silicon were prepared by electrochemical etching of mono-crystalline Si wafers (Table 2.1) following the same experimental procedure as described in Chapter 2. All the monolithic mesoporous silicon samples engaged in this study and their respective etching conditions (*J* and *t*) are summarized in Table 4.1.

Table 4.1 List of as-etched mesoporous silicon studied in Chapter 4 and the corresponding etching conditions applied in the electrochemical preparation.

Mesoporous silicon samples	**Etching current density / mA·cm^{-2}**	**Etching time / min**
PS-10-15	10	15
PS-30-05	30	05
PS-30-15	30	15
HPS-150-05	150	05
HPS-200-05	200	05
HPS-400-05	400	05

Besides, free-standing H-terminated mpSi microflakes (PS-30-15-F and HPS-200-05-F) and oxidized mpSi materials (PS-30-15-[O] and HPS-150-05-[O]) were also obtained via methods included in Chapter 2 and their activities in MO degradation under visible light irradiation were also investigated.

4.2.2 Photocatalyst characterisation

The structural morphologies of mpSi samples were recorded using FE-SEM and HRTEM techniques. The optical properties and electrical band gap were measured by UV-Vis and fluorescence spectrometers with DCM used as dispersion medium. FTIR spectra of mpSi materials were also collected to reflect the surface chemistry during reaction process. All measurement parameters were the same as described in Chapter 2 unless otherwise

stated. Notably, many samples listed in Table 4.1 including PS-10-15, PS-30-15 and HPS-150-05 had already been characterised by a range of techniques in Chapter 3. Thus, these results were also selectively mentioned in this chapter when necessary.

4.2.3 Photocatalytic evaluation

The photocatalytic behaviours and structural effects of H-terminated mesoporous silicon were assessed by the photo-degradation of methyl orange (MO) under visible light irradiation at room temperature. The unreacted dye concentration and organic carbon content of MO solution were measured respectively by UV-Vis spectrometer and TOC analyser at different time intervals of photocatalytic process. Apparent rate constants were analysed which revealed the effects of various surface and pore factors of mpSi on the photocatalytic efficiency. A series of trapping experiments using 2-propanol, ethanol, and triethanolamine (TEOA) were carried out to identify the main active species involved in the organic decomposition process and the lifetime of mpSi photocatalyst was evaluated through cycle test. All experimental procedures and instrumental parameters were the same as outlined in Chapter 2 unless otherwise specified.

4.3 Results and discussion

4.3.1 Characterisation of mesoporous silicon photocatalysts

Prior to the investigation of photocatalytic activity, the structural morphology and optical properties of PS-30-15 and HPS-150-05 fabricated by electrochemical etching method were first examined and discussed.

4.3.1.1 Structural features of PS-mpSi

The interconnected 3D porous network of PS-30-15 is evident in the FE-SEM images as shown in Figure 4.1 and HRTEM images in Figure 4.2. The average pore size was

measured as 4.7 nm as seen in the PSD curve in inset Figure 4.1A, which is slightly bigger than the mean pore diameter (3.43 nm) determined by BJH approach based on nitrogen adsorption isotherms. In fact, as mentioned in the IUPAC Technical report published in 2015, it was shown that the Kelvin equation based procedures, such as the BJH method, tend to underestimate the pore size for narrow mesopores, e.g. for pore diameter < 10 nm, the pore size will be underestimated by 20%-30%.[35] HRTEM images show clearly a matrix of isolated silicon nanocrystallites. Lattice fringes of Si (111) plane with a 0.313 nm inter-planar spacing were observed in a 5.4 nm Si nanoparticle recorded in Figure 4.2B inset. The SAED pattern shows distorted diffraction spots which are attributable to the (111), (202), (220) planes of the diamond cubic crystal structure of silicon as marked in Figure 4.2C.

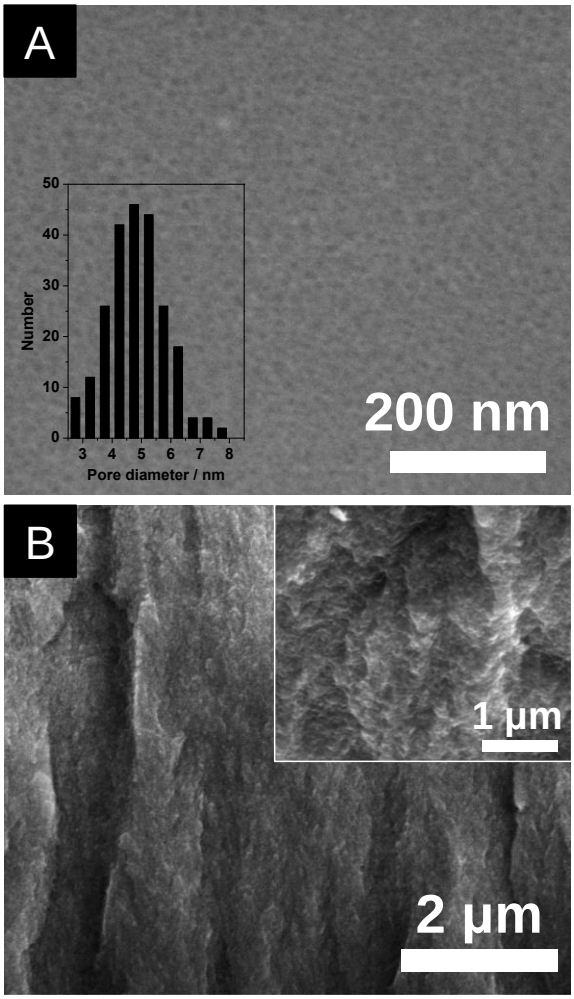

Figure 4.1 Plane view (A) and Cross section (B) FE-SEM images of PS-30-15. Inset A: histogram of pore size distribution derived from FESEM micrographs.

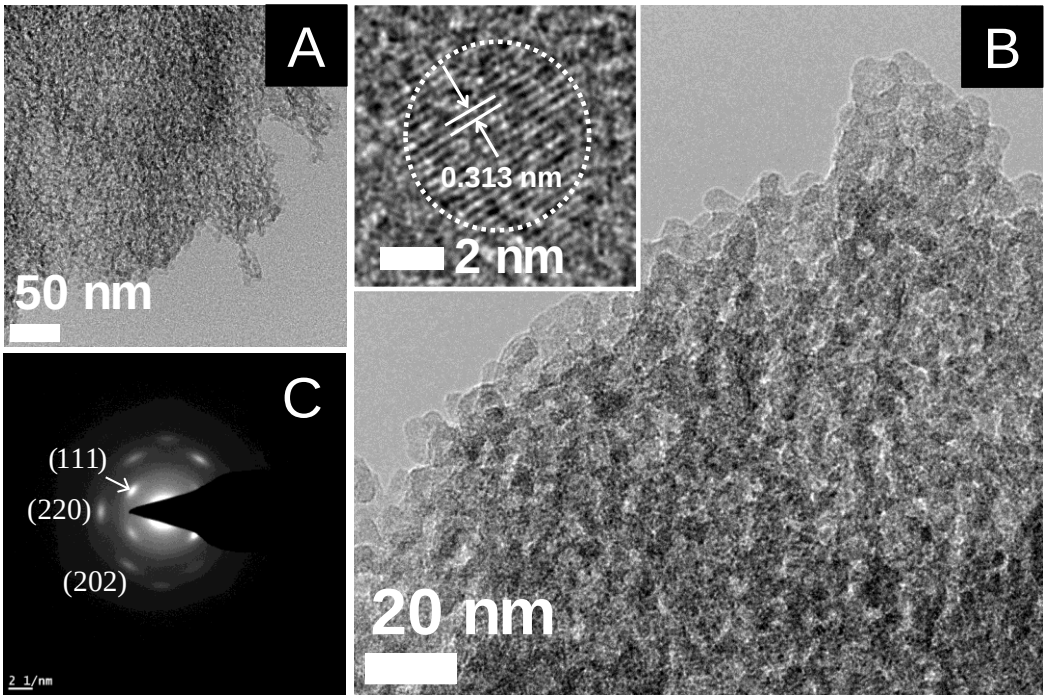

Figure 4.2 HRTEM images (A, B) and SAED pattern (C) of PS-30-15.

4.3.1.2 Structural features of HPS-mpSi

In agreement with the previous findings in chapter 3, a nicely ordered 1D channel array was featured in HPS-150-05. The high degree of order was clearly reflected in the FE-SEM (Figure 4.3) and HRTEM images (Figure 4.4), showing very straight and parallel channels along the [100] direction. The 9.4 nm channel width revealed in the HRTEM image is consistent with the BJH analysis result (9.55 nm, Table 3.5) and very close to the value derived from the FESEM images (10.5 nm). The bright diffraction spots in the SAED pattern and the Si (111) lattice fringes observed on the pore walls confirm the well-defined crystalline structure of HPS-150-05 sample. The much thicker pore walls ensured a good crystallinity and mechanical stability of the primary structure, and maintained the isolation of the pores as well.

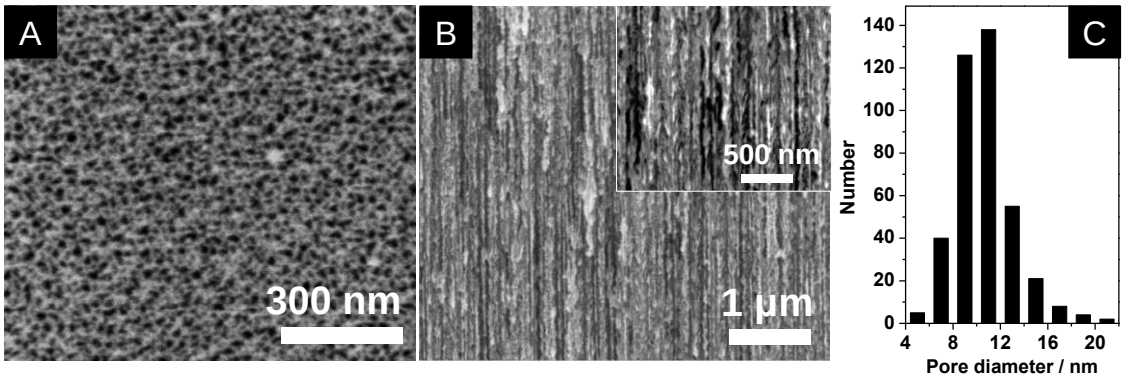

Figure 4.3 Plane view (A) and Cross section (B) FE-SEM images of HPS-150-05; Histogram of pore size distribution (C) of HPS-150-05 derived from FE-SEM micrographs.

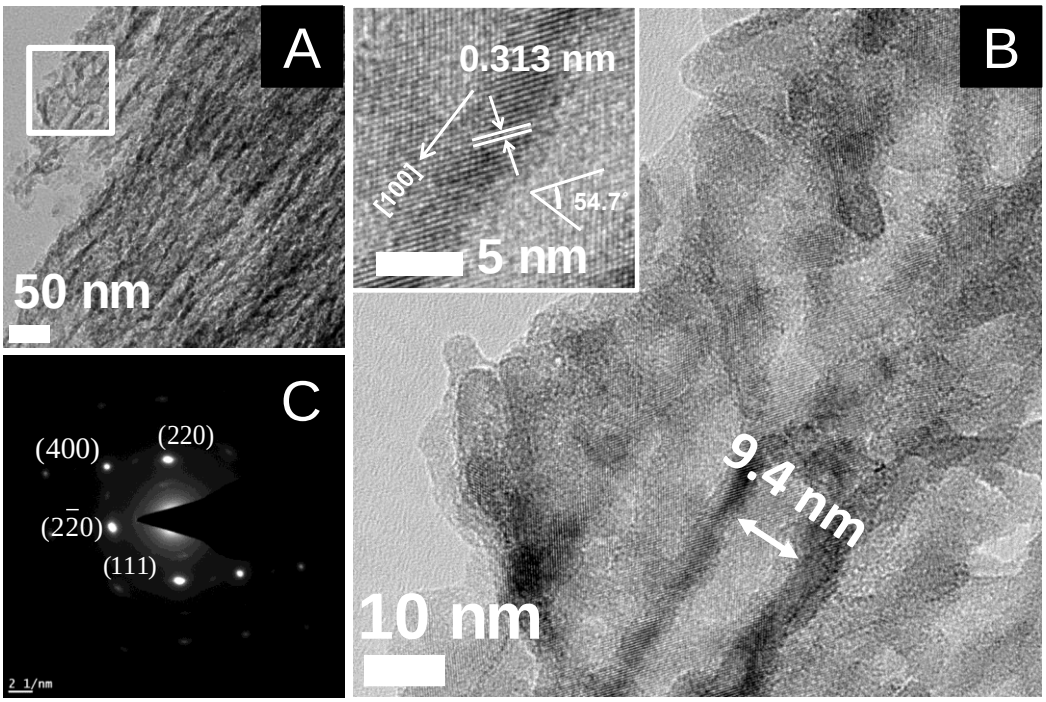

Figure 4.4 HRTEM images (A, B) and SAED pattern (C) of HPS-150-05.

4.3.1.3 Optical analysis of PS-mpSi and HPS-mpSi

4.3.1.3.1 Light absorption

As presented in Figure 4.5, UV-Vis absorption spectra of PS-30-15 (a) and HPS-150-05 (b) were collected, showing a broad absorption band maximized at 254 nm, 290 nm respectively. The substantial blue shift of the peak position in comparison to the near-IR absorption wavelength of Si bulk crystal (c. 1100 nm) indicates a significantly widened bandgap between the conduction and valence bands due to the quantum confinement effects of the constituted Si nanocrystals.[36] Therefore, the absorption efficiency of incident photons with energies between 1.8 eV and 3.1 eV corresponding to visible light range 700-400 nm was effectively increased. As an indirect bandgap semiconductor, the absorption coefficient of Si is often very low.[37] However, the mesoporous structure of mpSi samples partially made up for the deficiency by suppressing the broadband reflection of light at the interface.[10, 18] Therefore, more photons in a broad wavelength range were absorbed by these structures and more visible light energy could hence be harnessed to separate electron/hole (e^-/h^+) pairs by mpSi materials.

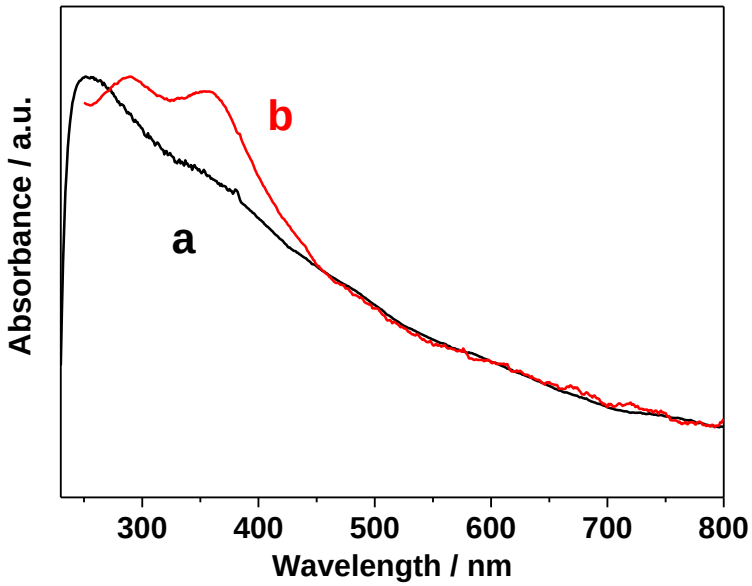

Figure 4.5 UV-Vis absorption spectra of freshly made PS-30-15 (a) and HPS-150-05 (b).

4.3.1.3.2 Light emission

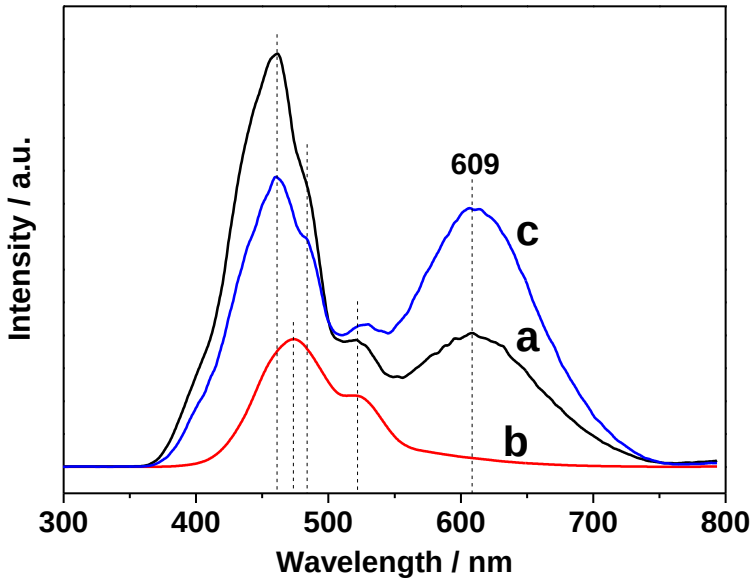

Figure 4.6 PL emission spectra of freshly made PS-30-15 (a), HPS-150-05 (b) and aged PS-30-15 (c). Excitation wavelength = 320 nm, 390 nm cut-off.

Multiple PL bands were featured in the PL emission spectra shown in Figure 4.6, at 460 nm, 521 nm and 609 nm for PS-30-15, 474 nm and 520 nm for HPS-150-05. Although the origin of the photoluminescence emitted by pSi is still under debate, many studies suggest a number of combined factors could contribute to the light emitting process, such as quantum confinement effect, structural defects, surface oxidation, framework distortion etc.[38-39] For example, the red emission at 609 nm seen in the spectrum of freshly made PS-30-15 is often associated with an oxidation effect.[40-41] As displayed in the emission spectrum of the aged PS-30-15 which was left in the air for several days under ambient conditions, the same 609 nm signal clearly was intensified. Surface oxides and existing defects are known as radiative recombination sites for excitons hence impairing the lifetime of photo-generated e^-/h^+ that are key to driving the reductive photochemical reactions aimed for.[42]

Moreover, it is well acknowledged that the lower fluorescence intensity represents a higher separation efficiency of e^-/h^+ pairs, which indicates a better photocatalytic activity of the nanomaterials. Thus, HPS-150-05 is very likely to produce longer-lived

photo-induced free charges, indicated by the considerably lower emission intensity and the absence of 609 nm signal despite the fact that it absorbed more incident photons (λ_{ext} = 320 nm) than PS-30-15. This enhancement in e^-/h^+ stability can be reasonably explained by the improved charge mobility across the surface of HPS-150-05 because of better electrical conductivity, lattice integrity, and higher resistance to oxidation than PS-30-15.

4.3.2 Photocatalytic activities of mesoporous silicon in dye degradation

This section displays the photocatalytic activity of PS-30-15 and HPS-150-05 in methyl orange photo-degradation under visible light irradiation taking advantage of the broad light absorption capability and large surface area.

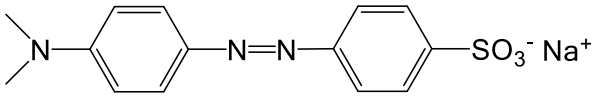

Scheme 4.1 Molecular structure of methyl orange.

4.3.2.1 Control experiments

Figure 4.7 presented several examples of the control experiments including the self-decomposition of dye molecules, adding moderately-doped or heavily doped Si chip with/without external visible light illumination. As shown, the peak absorbance of MO molecule at 464 nm almost retained its intensity as the initial value at different time intervals. The photolysis of MO on its own was negligible and MO molecules were also very stable in the presence of any Si chip under visible light irradiation.

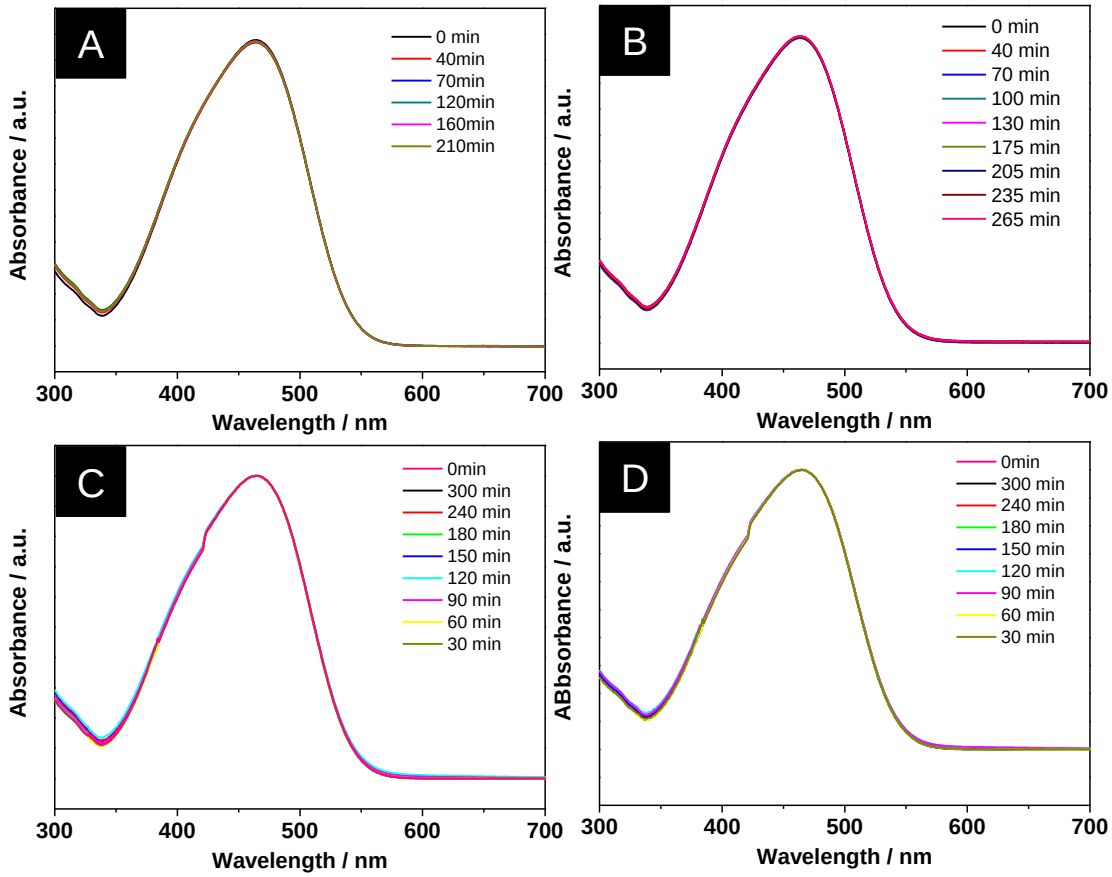

Figure 4.7 UV-Vis absorption spectra of 50 µM MO solution at different time intervals, on its own under visible light irradiation (A), with heavily doped p-type Si chip under visible light irradiation (B), with moderately doped p-type Si chip (C: under visible light irradiation, D: in the dark).

4.3.2.2 The photocatalytic activity of PS-mpSi in dye degradation

Figure 4.8 shows the variation of MO absorbance as a function of degradation time in the presence of PS-30-15 under visible light irradiation (Figure 4.8A) and the same correlation for the unirradiated PS-30-15 (Figure 4.8B). Under visible light irradiation, MO absorbance was gradually reduced to less than 5% of the initial intensity after 5 hours, accompanied by the bleaching of the aqueous solution as photographed in Figure 4.8 inset, revealing a concentration decay of the dye solution in accordance with the degradation process. The peak position was shifted from 464 nm to 466 nm which is possibly attributable to the monohydoxylated product of MO molecule, representing the oxidation in the aromatic ring.[43]

Interestingly, without any illumination, the absorption intensity of the organic dye over PS-30-15 was still observed to be dwindling although at a slower rate and with a constant peak position at 464 nm. The disappearance of MO under dark condition is expected to be related to physical adsorption and the surface hydrides of mpSi. The "dark" behaviour of mpSi material will be discussed with more examples and experimental evidence in the latter part of this chapter.

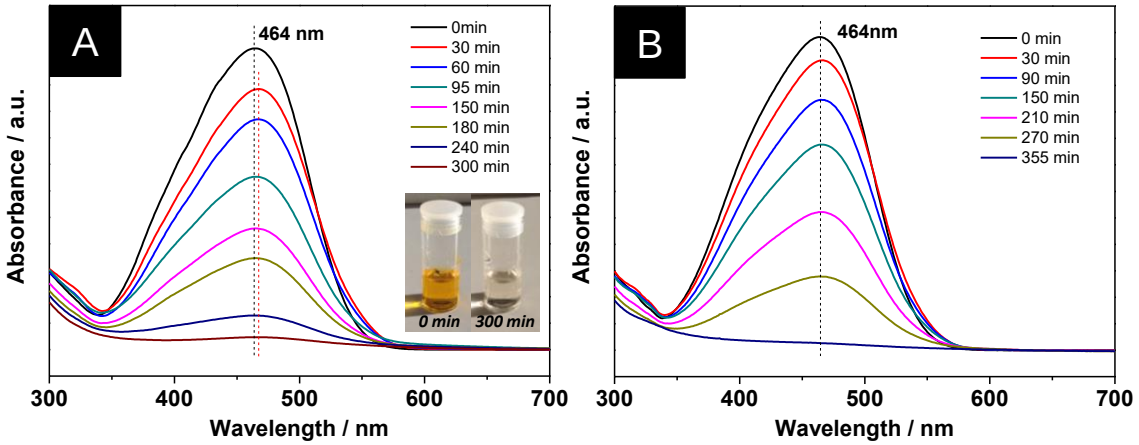

Figure 4.8 UV-Vis absorption spectra of MO solution before and after adding PS-30-15 as a function of degradation time in the presence (A) / absence (B) of visible light illumination.

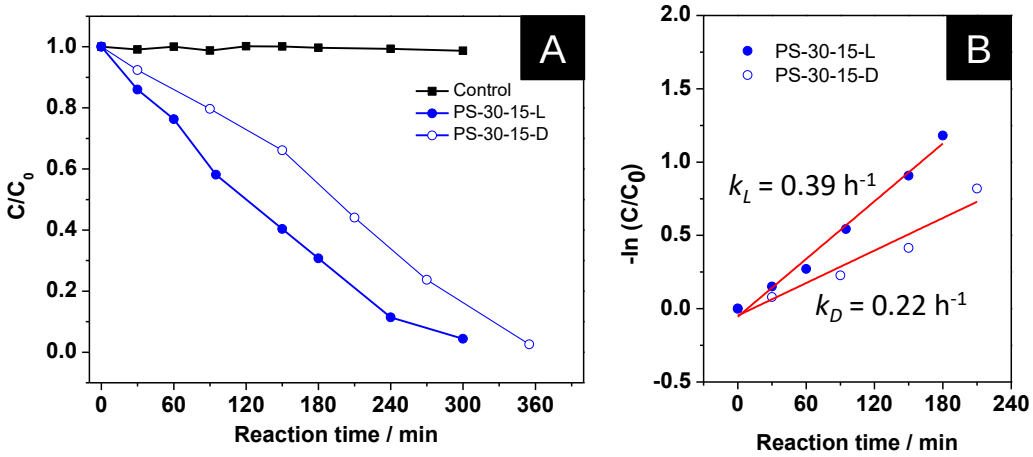

Figure 4.9 The degradation rates (A) and first order kinetics (B) of MO degradation over PS-30-15 (light on: closed circle; light off: open circle). Photolysis of MO solution on its own was plotted as reference (square).

As presented in Figure 4.9A, the concentration ratios of unreacted MO molecules derived from the UV-Vis absorption data were plotted against the decomposition time. A first order reaction model was applied to determine the reaction rate constant (Figure 4.9B).[44] It was revealed as 0.39 h^{-1} under visible light irradiation and 0.22 h^{-1} in the dark for PS-30-15. As observed the plot of dark condition in Figure 4.9A was in fact based on a zero order reaction model of which the rate constant was calculated as 0.17 h^{-1}. This is likely due to an insufficient active sites on the surface of PS-30-15 for organic substrates to react with, implying different reaction pathways between unirradiated sample and irradiated sample under visible light illumination.

4.3.2.3 The photocatalytic activity of HPS-mpSi in dye degradation

The photocatalytic activity of HPS-150-05 in degrading MO molecules was also evaluated. As exhibited in Figure 4.10A, MO molecules were completely diminished within 210 min under visible light irradiation. In contrast, under dark condition, the decay was noticeably slower. The peak shift from 464 nm to 470 nm is attributed to the formation of hydroxylated degradation products of MO, a part of the photocatalytic oxidation process. According to the published HPLC/MS results in previous studies of MO photo-degradation, the hydroxylated intermediate was possibly some derivative form of the *m*/*z* = 322 compound shown below which has an absorption peak wavelength at 470 nm.[43]

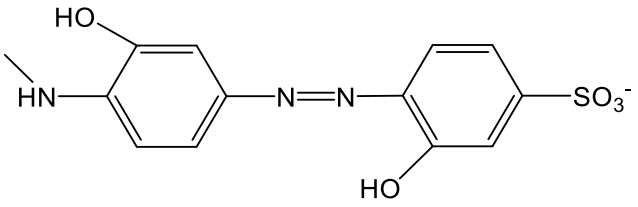

m/z: 322.05

Scheme 4.2 Structural formula of methyl orange degradation intermediate with *m*/*z* = 322.

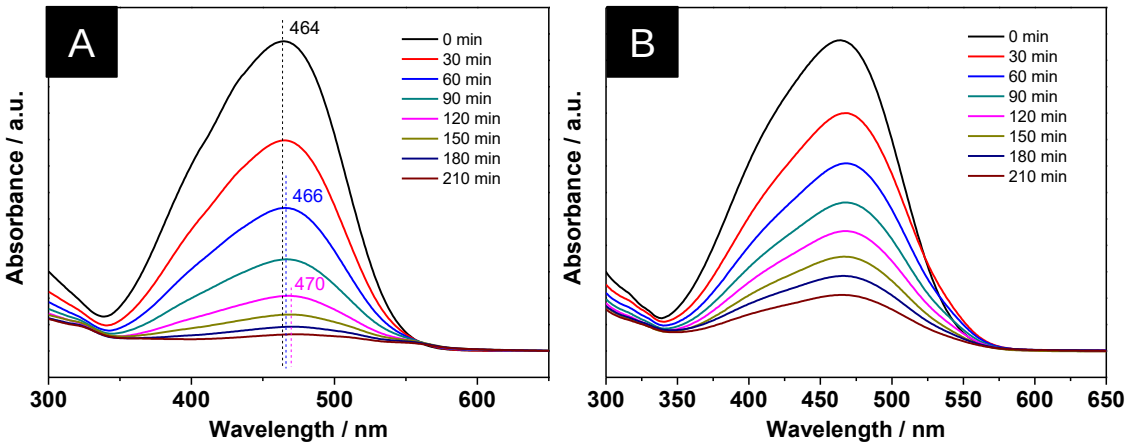

Figure 4.10 UV-Vis absorption spectra of MO solution before and after adding HPS-150-05 as a function of degradation time in the presence (A) / absence (B) of visible light.

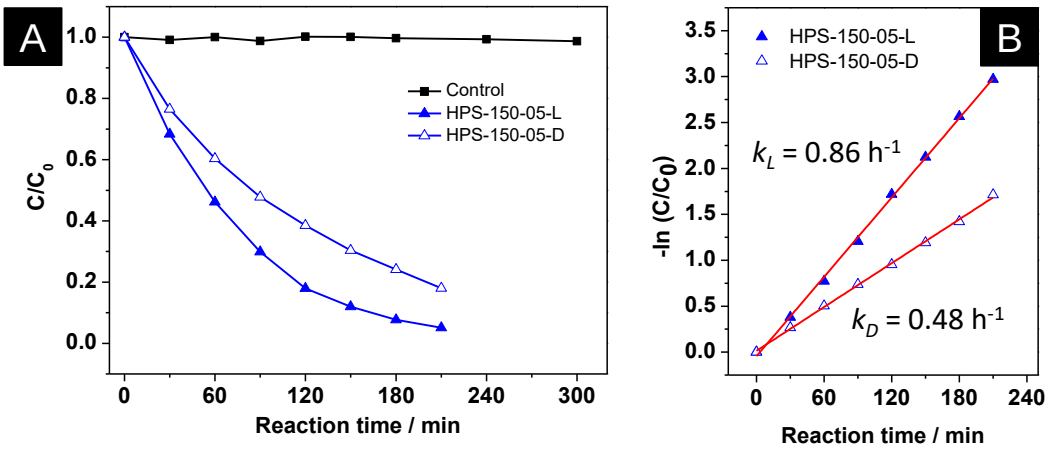

Figure 4.11 The degradation rates (A) and first order kinetics (B) of MO degradation over HPS-150-05 (light on: closed up triangle; light off: open up triangle). Photolysis of MO solution on its own was plotted as reference (square).

Likewise, the degradation kinetics of HPS-150-05 were also analysed. As seen in Figure 4.11, the apparent reaction rate constant (k) was calculated as 0.86 h^{-1} for the irradiated HPS-150-05 and 0.48 h^{-1} for the same sample in the dark.

As shown in these examples of PS-30-15 and HPS-150-05, the commonly required physisorption equilibrium between porous material and organic substrates in the aqueous solution prior to external illumination was difficult to achieve in this study as

any physical contact between pSi and MO molecules leads to the destruction of the organic structure rapidly due to the reactivity of hydrogen termination on the Si surface which can be referred to further discussion in 4.3.4. Nonetheless, it's clear that the physical adsorption by pSi indeed contributed to the overall decrease in MO concentration thus further evidence is necessary to estimate this impact by e.g. taking UV-Vis absorption spectra of the substances washed off the catalyst surface. Some insight was also reflected in the results of adsorbed MO by oxidized PS-30-15 and HPS-150-05 as shown in 4.3.3.6 that the extent of pure physisorption was relatively small which is likely related to the total amount of surface area available.

4.3.3 Impact of various factors on photocatalyst performance

In addition to PS-30-15 and HPS-150-05, other mpSi samples were also prepared via electrochemical etching by adjusting the etching conditions or adding some post-etching treatments. And their photocatalytic activity in MO degradation under visible light irradiation was assessed. The varied effects of porous morphology, silicon nanocrystallites, pore depth, light responsiveness, as well as free-standing mpSi microflakes and surface oxidation will be investigated in this section.

4.3.3.1 Porous morphology

Firstly, the comparison was drawn between PS-30-15 and HPS-150-05 to understand the influences of porous morphology in determining the photocatalytic performance of H-terminated mpSi materials. It is widely acknowledged that a large surface area of photocatalyst is appreciable as it can efficiently promote the surface-initiated photochemical reactions for example of the MO photo-degradation in this study. As disclosed in Chapter 3, PS-30-15 (SSA = 907.0 $m^2 \cdot g^{-1}$, Table 3.4) possesses a considerably larger surface area than HPS-150-05 (SSA = 458.5 $m^2 \cdot g^{-1}$, Table 3.5). However, the kinetic analysis displayed above of photocatalytic degradation over PS-30-15 and HPS-150-05 shows the benefits of the significantly larger surface area were greatly compromised by some other factors so the actual degradation efficiency of PS-30-15 is lower than

HPS-150-05 with or without irradiation. In fact, the unirradiated experimental results further confirm the influences of porous morphology as the higher photocatalytic activity exhibited by HPS-150-05 is also partly contributed by its better light responsiveness and longer lifetime of the excited e^-/h^+ charge carriers.

Since the external surface area of these monolithic mpSi samples is very limited, most mass/energy transfer took place inside the mesopores but the accessibility to the abundant internal surface is predominantly governed by the pore features. In this study although the porous morphology of both mpSi samples could be interpreted as vertically aligned mesopores along the [100] direction but the pore width and pore interconnectivity varied largely. The mean pore size was calculated as 3.43 nm for PS-30-15 and 9.55 nm for HPS-150-05 as mentioned above. The layer thickness of PS-30-15 and HPS-150-05 was 20.7 µm and 34.0 µm respectively. The larger pore size and better ordered straight channel structure of HPS-150-05 could effectively ease the diffusion resistance for MO molecules and therefore the degradation reaction was accelerated. Whereas the interconnected porous network of PS-30-15 increased the travel distance for substrate compound to reach the active surface site to be converted.

4.3.3.2 Silicon nanocrystallites

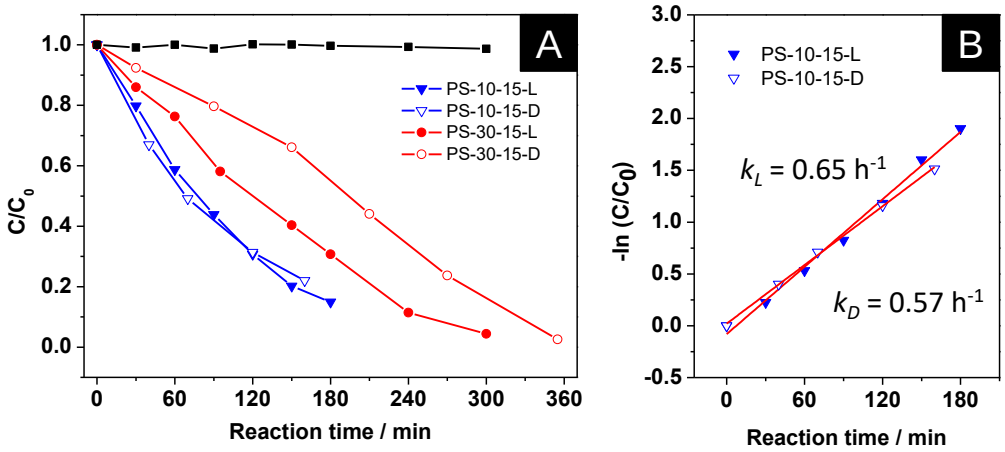

Figure 4.12 The degradation rates (A) and first order kinetics (B) of MO degradation over PS-10-15 (light on: closed down triangle; light off: open down triangle) and PS-30-15 (light on: closed circle; light off: open circle). Photolysis of MO solution on its own was plotted as reference (square).

As known from previous results in Chapter 3, the size of Si nanocrystallites embedded on the pore walls was estimated as 7.08 nm for PS-30-15 and 11.22 nm for PS-10-15 based on their XRD profiles, which might be slightly overestimated as the crystal size of PS-30-15 appeared to be 5.4 nm from the HRTEM measurement (Figure 4.2). Nonetheless, the photocatalytic performance of PS-10-15 was also investigated under visible light irradiation, as shown in Figure 4.12. The apparent rate constant is 0.65 h^{-1}, or 0.011 min^{-1} which appears to be quicker than PS-30-15, likely due to the thinner layer thickness and less interconnectivity of porous system. Interestingly, like PS-30-15 sample, MO disappearance was also observed without any illumination which also followed a pseudo first order reaction model[44] and the rate constant was calculated as 0.57 h^{-1}, or 0.010 min^{-1} for unirradiated PS-10-15.

According to quantum confinement theory, the impact of spatial confinement is not the same for different materials, as it depends on characteristic length scales of a given property, the so-called Bohr exciton radius (a_0), a physical dimension describing the most probable distance between the electron and hole in an exciton by analogy to the Hydrogen atom, which ranges from ~2 to ~50 nm depending on the semiconductor's chemical composition and structure.[45] Spatial confinement begins to affect the exciton wave function as the size of the nanocrystals approaches a_0, giving rise to discrete energy levels and widened CB/VB bandgap. The value of a_0 for silicon is known as 4.3 nm,[46] which is smaller than the size of Si nanocrystallites of PS-10-15 mentioned above. Therefore the impact of quantum confinement was no longer observable which eventually led to the poor photo-activity as revealed.

4.3.3.3 Pore depth

The effect of pore depth was revealed in the study of PS-30-05 as displayed in Figure 4.13. Its apparent rate constant in MO photo-degradation under visible light irradiation was determined as 0.85 h^{-1}, which is significantly higher than the 0.39 h^{-1} of PS-30-15 that was made under the same etching current density (30 $mA \cdot cm^{-2}$). As discussed above, the photocatalytic behaviour and degradation rate depend heavily on

the porous morphology of photocatalyst and various pore properties such as geometrical size and shape. According to the previous finding in Chapter 3, the impact of etching time on the pore size of mpSi is insignificant, which indicates identical pore dimensions for PS-30-05 and PS-30-15 (d = 3.43 nm, Table 3.4). However, the layer thickness of PS-30-05 was only 5.5 µm due to the much shorter etching duration. The thinner layer of mpSi means shorter pore length and diffusion path for dyes thus promoted the photo-degradation process.

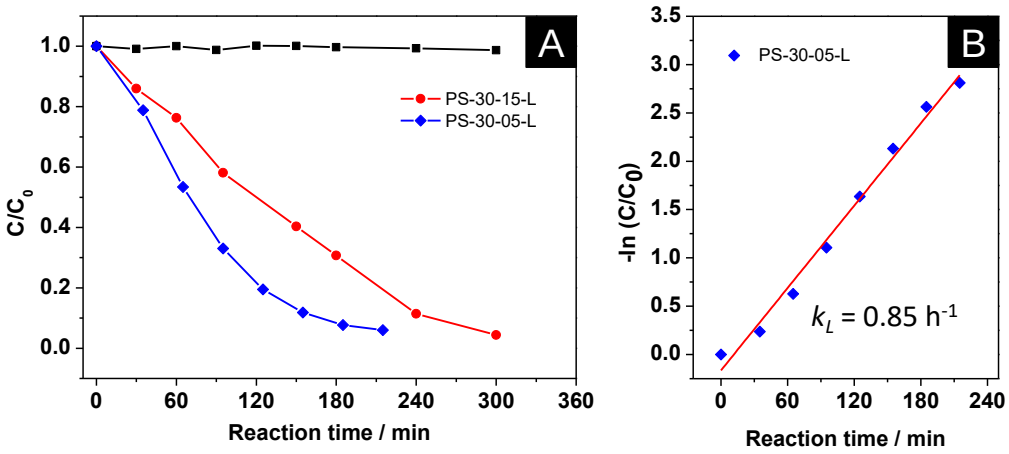

Figure 4.13 The degradation rates (A) and first order kinetics (B) of MO degradation over PS-30-05 (closed diamond) and PS-30-15 (closed circle) under visible light irradiation. Photolysis of MO solution was plotted as reference (square).

4.3.3.4 Visible light responsiveness

HPS-200-05 was fabricated by electrochemical etching and its porous structure was examined by nitrogen adsorption technique. As shown in Figure 4.14A, the specific surface area of HPS-200-05 was 408.6 $m^2 \cdot g^{-1}$ and its average pore diameter was 12.26 nm which is larger than the 9.55 nm of HPS-150-05 due to the higher etching current density applied in the preparation of HPS-200-05. It also had stronger light absorption ability in the visible light spectral range at wavelength greater than 400 nm, as conveyed by the UV-Vis absorption spectrum in Figure 4.14B. This result implies that more energy from the visible light photons can be utilized in charge separation by HPS-200-05 to generate more energized e^-/h^+ for triggering MO degradation.

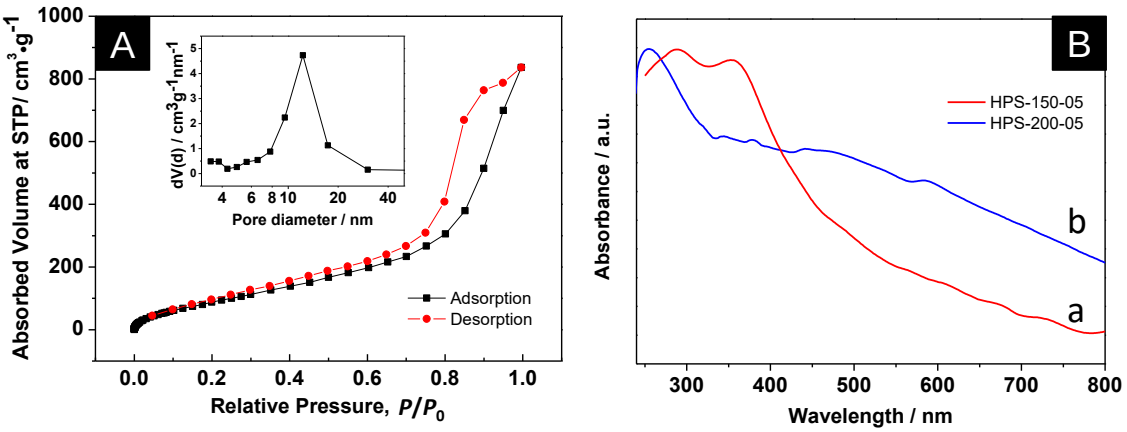

Figure 4.14 Nitrogen sorption isotherms (A) of HPS-200-05, inset pore size distribution curve acquired by BJH approach; UV-Vis absorption spectra (B) of HPS-150-05 (a) and HPS-200-05 (b).

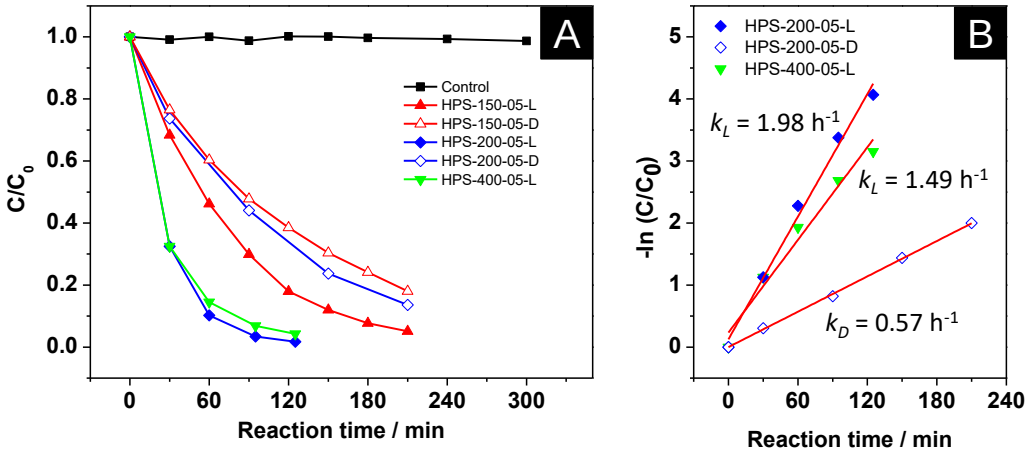

Figure 4.15 The degradation rates (A) and first order kinetics (B) of MO degradation over HPS-200-05 (light on: closed diamond; light off: open diamond), HPS-150-05 (light on: closed up triangle; light off: open up triangle) and HPS-400-05 (light on: closed down triangle). Photolysis of MO solution on its own was plotted as reference (square).

As shown in Figure 4.15, the actual rate constant was 1.98 h^{-1} for HPS-200-05, which is remarkably quicker than the 0.86 h^{-1} of HPS-150-05. Meanwhile, its unirradiated experiment also shows a faster reaction rate (k = 0.57 h^{-1}) than the unirradiated HPS-150-05 (k = 0.48 h^{-1}) because of the enhanced mass transfer by the larger pores of HPS-200-05 structure, although the improvement was not as significant as the irradiated

condition. Further increasing to 400 mA·cm^{-2}, the photocatalytic activity of HPS-400-05 was evaluated as well with a reaction rate constant of 1.49 h^{-1}.

It is clear to see that HPS-150-05, HPS-200-05 and HPS-400-05 outperformed PS-30-15 and PS-30-05 undoubtedly due to the ordered channel system, wider mesopores, and well-defined crystallinity of the heavily doped mpSi samples. The morphological qualities enabled them to be more efficient in mass transportation and charge separation/transfer during MO photo-degradation under visible light irradiation.

4.3.3.5 Free-standing microflakes

As discussed previously in Chapter 3, as-etched mpSi layer can be lifted off the un-etched substrate and further treated with sonication to make micrometre sized mpSi flakes. Here free-standing PS-30-15-F and HPS-200-05-F microflakes were prepared. As shown in the IR spectra (Figure 4.16), the hydrogen passivated surface was well preserved after ultrasound-induced pulverization and only very few oxides were formed on the surface.

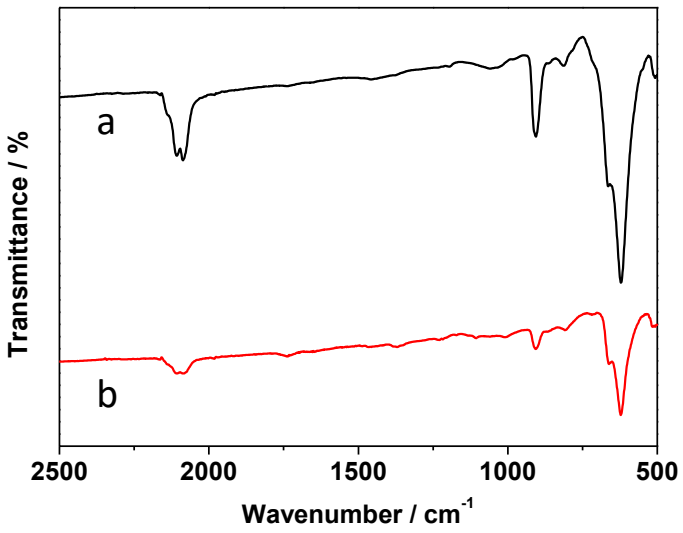

Figure 4.16 ATR-IR spectra (A) of PS-30-15-F (a) and HPS-200-05-F (b)

The photocatalytic performance of PS-30-15-F and HPS-200-05-F were demonstrated in Figure 4.17 with the rate constant determined as 0.68 h^{-1} and 2.31 h^{-1}, respectively. After

mpSi layer was freed from its mother chip, both ends of the pores became wide open so that substrate molecules gained the access to the internal surface more easily. Therefore, the mass exchange between the dye solution and the porous system was accelerated. Besides, varied degrees of the reaction rate enhancement were observed, which is 73% for PS-30-15 and 17% for HPS-150-05. This result further emphasized the influence of aforementioned porous morphology. As the diffusion barrier encountered in the porous system of PS-30-15 was effectively reduced after the internal surface sites became more available to the outside environment by making pore completely open.

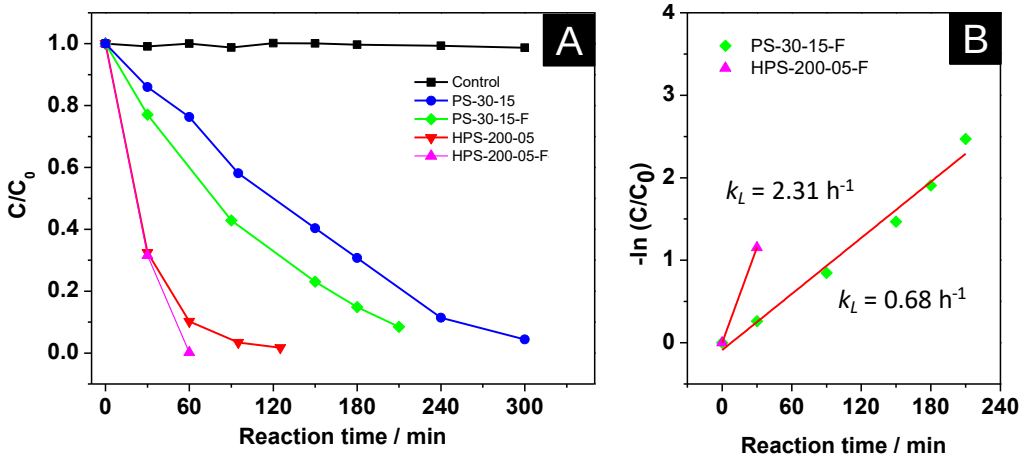

Figure 4.17 The degradation rates (A) and first order kinetics (B) of MO degradation over PS-30-15 (circle), PS-30-15-F (diamond), HPS-200-05 (down triangle) and HPS-200-05-F (up triangle) under visible light irradiation. Photolysis of MO solution on its own was plotted as reference (square).

4.3.3.6 Surface chemistry

Silicon hydrides are known to be reactive and essential to the performance of porous silicon obtained by electrochemical etching.[16, 47-49] The bond dissociation energy of Si-H is 318 kJ·mol^{-1} which is even higher than the 222 kJ·mol^{-1} of Si-Si bond.[50] Despite this, the bond polarity enhances the reactivity of Si-H bond which may affect the charge distribution on the surface of H-terminated porous silicon due to electron deficiency.[50] By using oxidizers such as H_2O_2, surface hydrides can be effectively quenched, resulting in increased hydrophilicity and stability of post-treated porous silicon in water solution,

which is commonly used in biomedical studies of porous silicon-based materials.[51-54] As indicated in the IR spectra of HPS-150-05-[O] and PS-30-15-[O] (Figure 4.18), SiH_x signals were completely disappeared. Instead, the spectrum was dominated by a broad absorption at 1050 cm^{-1} from Si-O-Si stretching mode, while Si-Si bond at 615 cm^{-1} was still visible in the IR spectra.

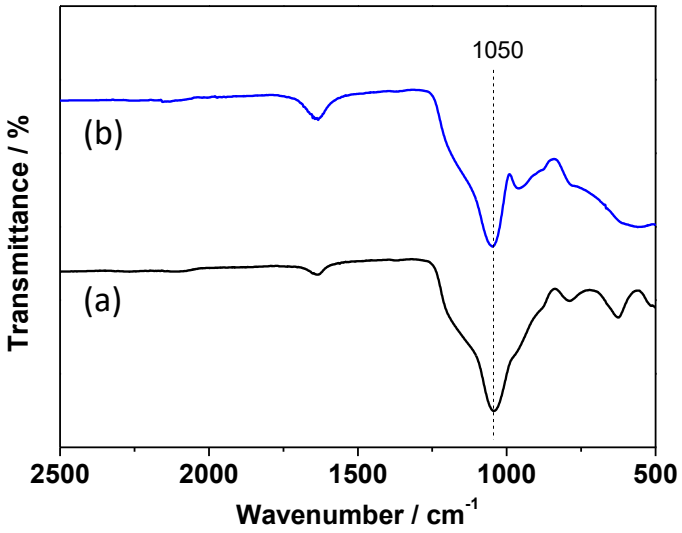

Figure 4.18 ATR-IR spectra of (a) HPS-150-05-[O] and (b) PS-30-15-[O].

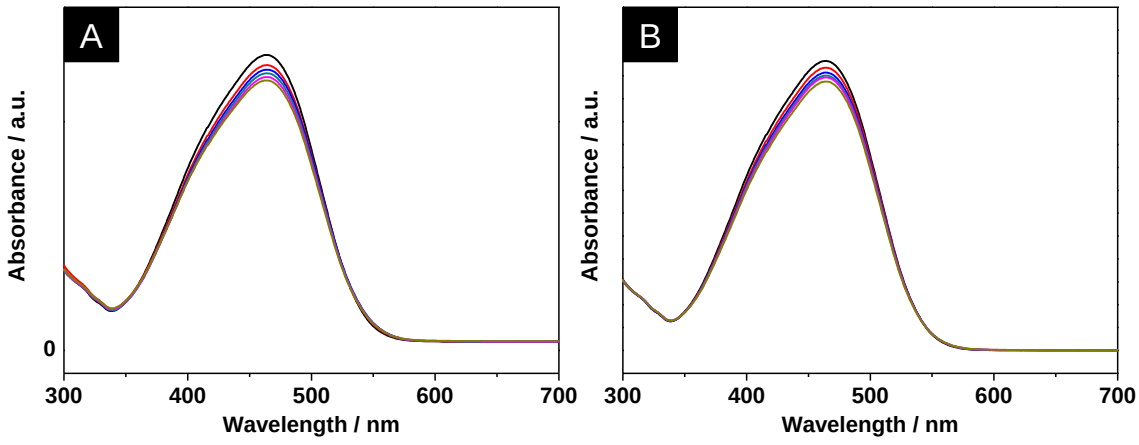

Figure 4.19 UV-Vis absorption of MO solution before and after adding HPS-150-05-[O] (A), PS-30-15-[O] (B) at different time intervals under visible light irradiation for 5 hours.

The evaluation of photocatalytic results (Figure 4.19) clearly show that the photocatalytic activity of HPS-150-05-[O] and PS-30-15-[O] were completely inhibited and only a slight reduction in MO concentration was detected which is mainly due to the physical adsorption by the porous structure and implies that SiH_x is largely responsible for the observed activity of H-terminated mpSi towards MO molecules under dark condition as well. This experimental result provided solid evidence that silicon hydrides formed on the surface of mpSi is the determinant factor in the activity and behaviours of H-terminated mpSi with or without any light irradiation.

4.3.4 Dye degradation behaviour under dark conditions

The surface state of mpSi is crucially important in the photocatalytic performance under visible light irradiation. In fact, surface hydrides are also directly related to the "dark" activity exhibited by H-terminated mpSi in MO degradation as shown in the previous results summarized in Table 4.2 below.

Table 4.2 The MO degradation rate constant and degradation efficiency of H-terminated mesoporous silicon samples with or without visible light irradiation.

Mesoporous silicon	Visible light illumination	Rate constant, k / h^{-1}	Decomposition efficiency, η [a] / %
PS-10-15	ON	0.65	41.2
	OFF	0.57	44.9
PS-30-15	ON	0.39	23.7
	OFF	0.22	13.7
HPS-150-05	ON	0.86	53.9
	OFF	0.48	40.0
HPS-200-05	ON	1.98	89.7
	OFF	0.57	41.0

[a] Decomposition efficiency (η): the concentration ratio of decomposed MO molecules after 60 min with or without external illumination.

Apart from PS-10-15, other three mpSi samples with various porous morphologies (PS-30-15, HPS-150-05 and HPS-200-05) all presented a considerable ability to bleach methyl orange through chemical conversion in the dark, more clearly seen in Figure 4.20 derived from the kinetic data in Table 4.2 above. Due to their varied surface and pore properties, the MO decomposition efficiency was different as HPS-150-05 and HPS-200-05 showed the fastest degradation rate for more efficient mass transfer in and out of the porous framework. Detailed explanation can be referred to the results and discussion illustrated in 4.3.3.1 and 4.3.3.4.

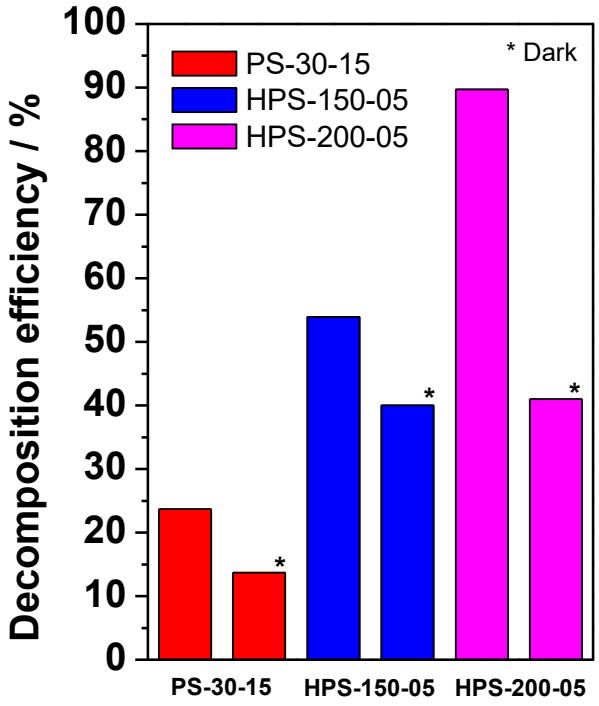

Figure 4.20 The column chart of decomposition efficiency (η) of PS-30-15, HPS-150-05 and HPS-200-05 in MO degradation with or without external illumination for 60 min.

Comparing with other photocatalytic investigations of porous silicon in literature, our H-terminated mpSi samples exhibited outstanding activity toward MO without light irradiation due to the abundant surface area and open mesoporous morphology possessed by mpSi materials in this study. Meanwhile the surface tension created by the highly porous nanostructure of mpSi, is also likely to enhance the reactivity of SiH_x groups on the roughened surfaces, as suggested by previous studies.[55]

As we know, the reduction activity of Si-H bond contained by nanostructured Si materials is widely exploited in surface modification with alkene, alkyne, aldehyde etc.,[56-59] and in electroless deposition of metallic nanoparticles via in situ reduction of metal ions such as Ag^{+}, $[PtCl_4]^{2-}$, Cu^{2+}, Ni^{2+} etc.[60-62] The versatility of its applications are also seen in the reduction of nitroarenes,[48] CO_2,[49, 63] and the dehydrogenation of secondary alcohol[64] by Si NWs and NWs arrays of which the activity was reported to be comparable to many functional inorganic materials used in photochemical or electrochemical transformations including P-doped TiO_2, Pt nanoparticles.[47] More importantly, the Si-H bond has also shown its reduction capability for fabric azo dyes such as Remazol dyes,[55] methylene blue[65] in several studies of Si NWs prepared by metal-assisted chemical etching approaches. Considering these experimental results, the following degradation pathway was proposed in this study (Scheme 4.3). By reducing the azo bond via hydrogen transfer from the surface hydrides of H-terminated mesoporous silicon, MO molecules were converted into sulfanilic acid and dimethyl-4-phenylenediamine.

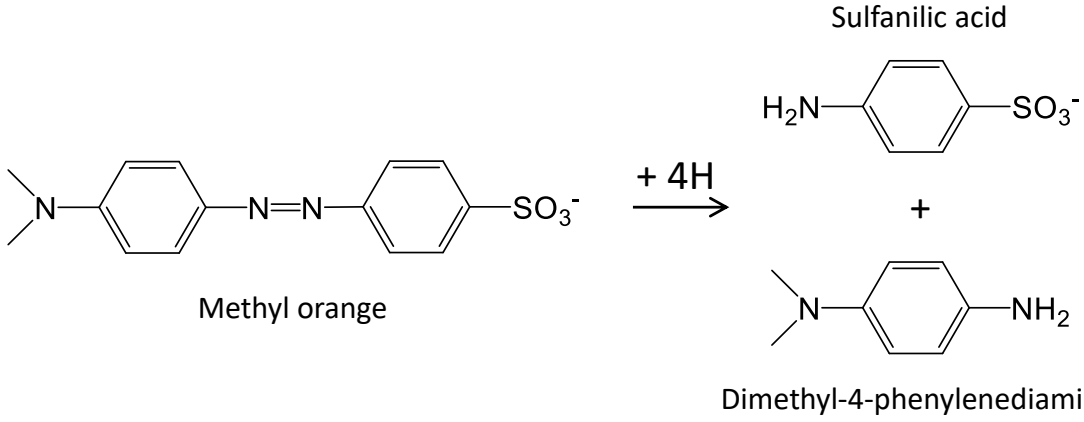

Scheme 4.3 Proposed decomposition pathway of methyl orange by H-terminated mesoporous silicon.

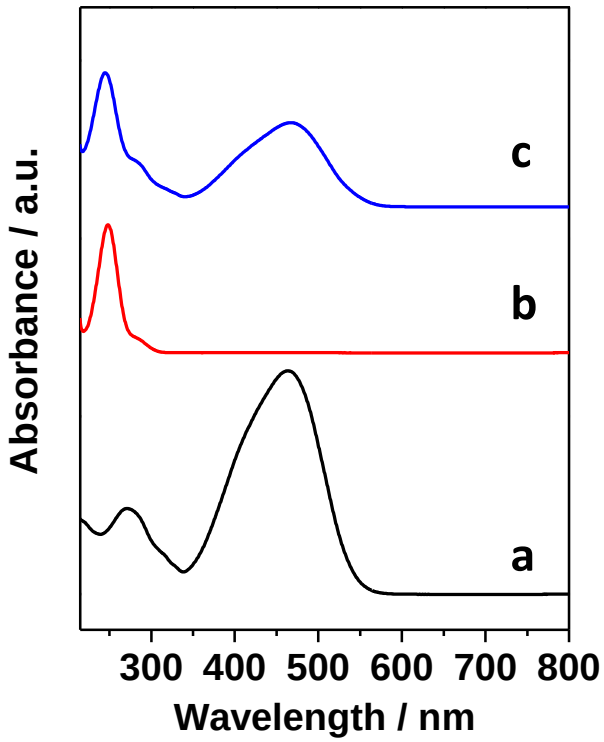

Figure 4.21 UV-Vis absorption spectra of methyl orange (a), sulfanilic acid (b) and unreacted MO solution in the presence of PS-30-15 after 210 min without external illumination.

As shown in Figure 4.21, the UV-Vis absorption spectrum of methyl orange solution is mainly composed by two absorption bands at 464 nm and 271 nm originated from the π-conjugated system. After adding mpSi, the intensity of these two peaks decayed as the azo bonds of methyl orange molecules were destroyed over time. Meanwhile, the appearance and gradual growth of a new peak at 246 nm was also observed at different time intervals, which is likely contributed by the two end products, described above. As Figure 4.21b clearly shows the characteristic absorption maximum for sulfanilic acid (SA) is at 248 nm while it has been reported around 242 nm for dimethyl-4-phenylenediamine (DMPD) as well.[66]

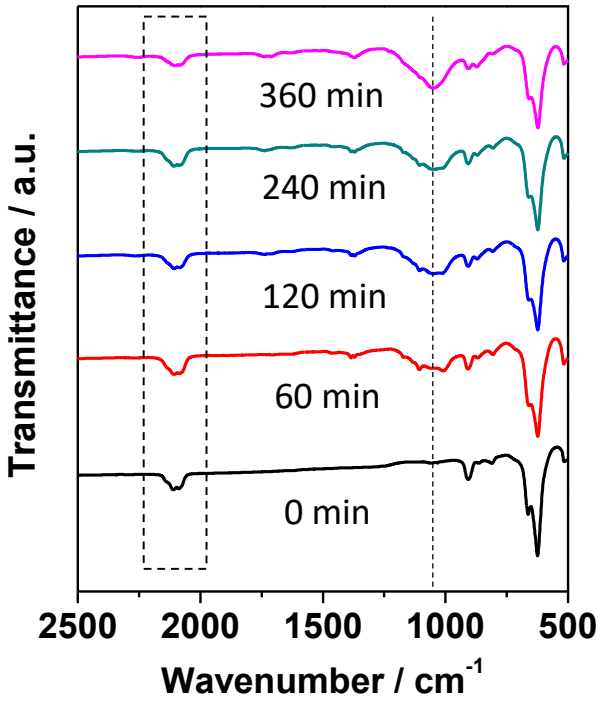

Figure 4.22 ATR-IR spectra of PS-30-15 at different time intervals during MO degradation without light illumination, 0 min, 60 min, 120 min, 240 min and 360 min, respectively.

Figure 4.22 shows the IR spectra of PS-30-15 at different time intervals of MO degradation under dark condition. The vibrational signals of Si-H bond at 2080-2140 cm^{-1} and 910 cm^{-1} decreased accordingly with the Si-O-Si absorption peak at 1000-1100 cm^{-1} intensified, confirming the consumption of surface hydrides by organic dyes and the formation of surface oxides on mpSi.

4.3.5 Dye degradation behaviour under visible light irradiation

The photocatalytic mechanism of MO degradation under visible light irradiation by H-terminated mesoporous silicon was proposed based on the analysis of total carbon content, active species, and electronic band structure of mesoporous silicon.

4.3.5.1 Accelerating effect of visible light irradiation

After visible light irradiation was applied, the behaviours of mpSi toward MO was immediately altered and the degradation rate was accelerated significantly. As displayed in Figure 4.23, in the presence of HPS-200-05, MO concentration was first measured twice every 30 min in the dark and then the lamp was switched on and the system was irradiated by the visible light source for another 120 min. The 1st order reaction rate was estimated as 1.72 h^{-1} under visible light irradiation, in accordance with the previous result (k = 1.98 h^{-1}).

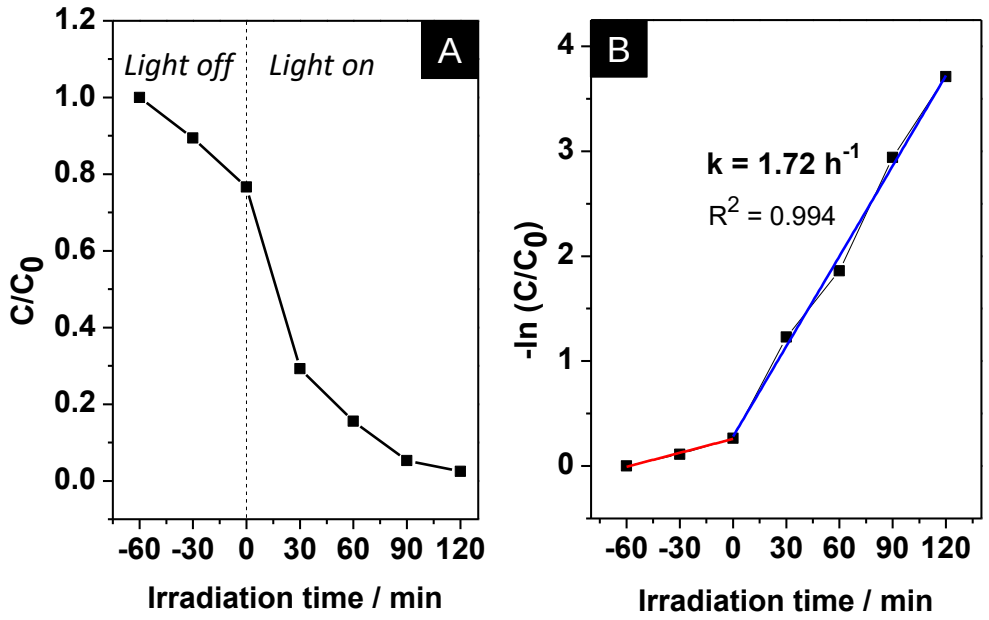

Figure 4.23 The temporal course (A) and first-order kinetics (B) of MO degradation in the light off/on experiment of HPS-200-05 (lamp was turned on after 60 min in the dark).

As mentioned previously, MO molecules were likely being converted into SA and DMPD as shown in Scheme 4.3 by mpSi through hydrogen transfer, which accounts for the major degradation activity in the dark. In fact, the presence of these products was also observed under visible light irradiation at room temperature. As displayed in Figure 4.24, the increasing rate of the peak intensity of 246-247 nm centred is far greater than that of the dark condition, which signifies an elevated reactivity of Si-H bond under visible

light illumination. As the visible light is not sufficiently energetic to cleave the surface Si-H bond which requires a minimum wavelength of approximately 354 nm,[67] and also not capable of inducing total ejection of the electrons photogenerated in the conduction band as suggested in previous studies of UV-promoted hydrosilylation.[68] Therefore, the activation barrier for hydrogen transfer was lowered. This is more likely to be a result of its own solid-state electronics and surface environment by localizing photogenerated charge carriers at specific surface sites, probably Si-H sites, in which way the reductive activity was enhanced. To back this assumption up, similar proposal was also found in literature which discovered so called exciton-based mechanism in the study of surface hydrosilylation of H-terminated Si nanomaterials.[69]

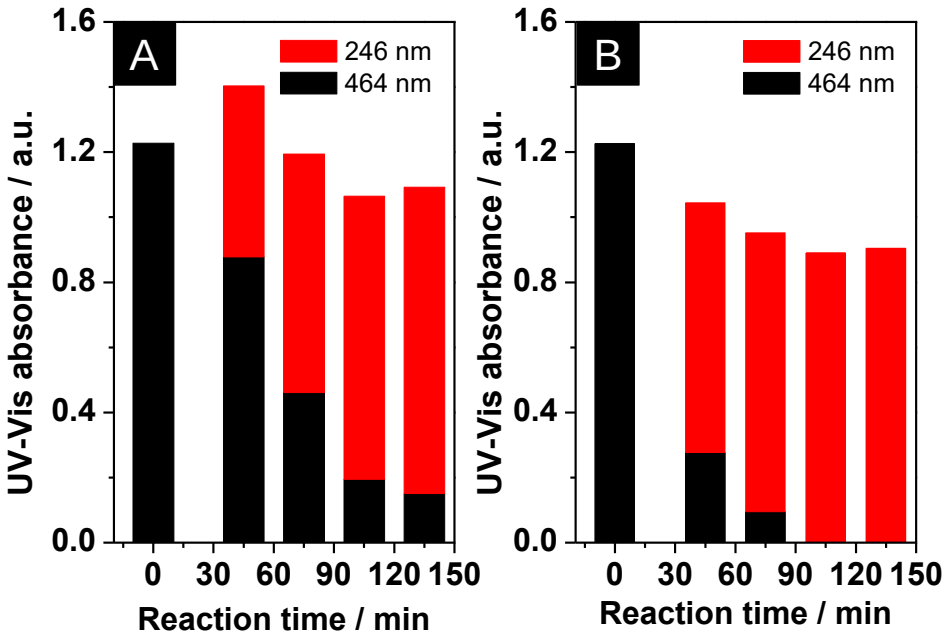

Figure 4.24 UV-Vis absorbance of absorption peaks at 464 nm and 246 nm of MO solution over HPS-200-05 at different time intervals in the dark (A), and under visible light irradiation (B).

4.3.5.2 Total organic carbon analysis

By measuring the organic carbon content of unreacted MO solution during photocatalysis, the progress of photochemical degradation was monitored. As presented in Figure 4.25 below, the total organic carbon (TOC) content declined by 10.1%

after 60 min irradiation and 20.4% after 120 min irradiation time for HPS-150-05, showing a mineralization process occurred to dye molecules in the reaction system by mpSi under visible light irradiation.

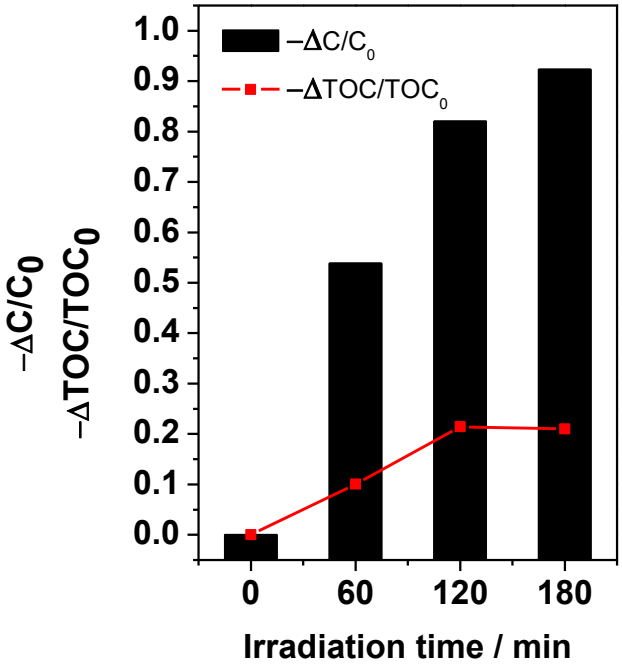

Figure 4.25 The evolution of MO concentration ($-\Delta C/C_0$) and total carbon content ($-\Delta TOC/TOC_0$) of the 50 µM MO solution degraded by HPS-150-05 under visible light irradiation.

According to photo-mineralization mechanism, organic matter is ultimately converted into CO_2, H_2O and inorganic ions (e.g. NO_3^-, NH_4^+, SO_4^-), through photocatalytic oxidation which is initiated by photon-generated holes (h^+), or by reactive oxygen-related species (ROSs) produced on the CB/VB of irradiated semiconductor photocatalyst (Scheme 4.4). Superoxide anion radical ($\cdot O_2^-$), hydroxyl radical ($\cdot OH$), hydrogen peroxide (H_2O_2) and singlet oxygen ($^1O_2$) are amongst the most active ROSs that are capable of oxidizing various organic substances because of their high oxidation potential.

$$h^+/ROSs + MO \longrightarrow intermediates \longrightarrow \longrightarrow CO_2 + H_2O + SO_4^{2-} + NO_3^- + NH_4^+$$

Scheme 4.4 Mineralization process of methyl orange by photo-generated species.

It is also known that the TOC removal rate is naturally slower than the reduction in the concentration of organic substrate. Rather than simply destroying the chromophore group of the azo dye, photo-mineralization involves various reaction intermediates formed by bond cleavage, demethylation and hydroxylation, etc. during the fragmentation of the substrate molecules, since the radical species are not so selective in general.[43, 70]

Notably the carbon loss became stagnant after 120 min irradiation time while the concentration of MO molecules constantly decayed. Due to the active participation of silicon hydrides in MO reduction as described above, oxides were gradually formed on the surface of mpSi as shown in Figure 4.22, and reduced the photo-oxidative activity of mpSi. In fact, surface oxides are reported to be able to compete with Si-H on the electron extraction and strongly influence the separation efficiency of photon-induced e^-/h^+ pairs.[21] While Si-H functionalities can act as electron sinks, trapping photo-excited electrons, therefore preventing the e^-/h^+ recombination, and consequently enhancing the oxidizing ability of mpSi photocatalyst.[15]

4.3.5.3 Active species analysis

To further explore the photocatalytic mechanism, a series of trapping experiments were performed to determine the primary active species involved in the photocatalytic process of MO degradation over mpSi material under visible light irradiation. The results of adding different radical scavengers into the system are displayed in Figure 4.26.

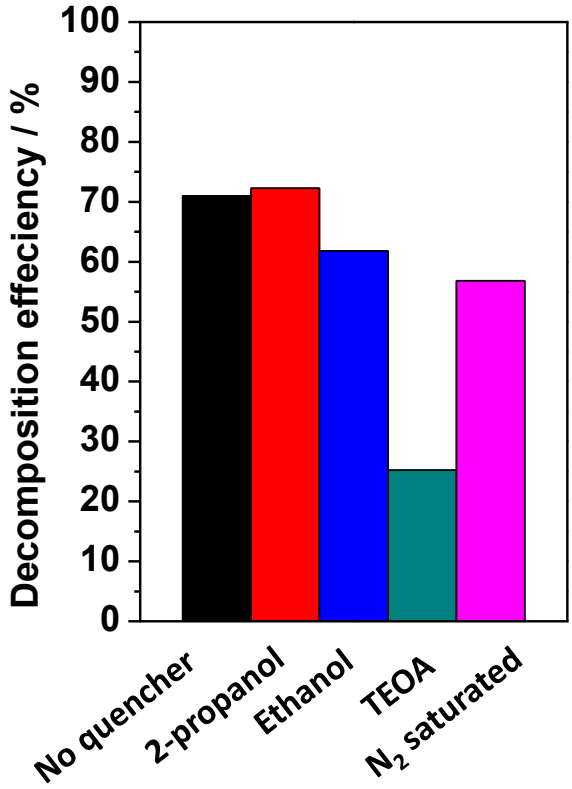

Figure 4.26 Decomposition efficiency of MO degradation by HPS-200-05 added with different quenchers (2-propanol, ethanol, triethanolamine) under visible light irradiation for 30 min.

When isopropyl alcohol (a quencher for hydroxyl radical, ·OH) was introduced into the reaction system, the photocatalytic reaction rate was almost unaffected after 30 min. Thus, hydroxyl radicals were unlikely among the active species in the photo-degradation of MO by mpSi.

After saturating the MO solution with N_2, the degradation efficiency declined by 20% after 30 min irradiation time as shown in Figure 4.26. It is worth noting that despite the depletion of oxygen in the aqueous solution, 56.8% MO molecules were still converted which also signifies the influences of visible light irradiation on the action of surface hydrides since the disappearance of only ~26% MO was observed in the dark (Figure 4.15).

As known, by accepting the photo-induced electrons generated on the conduction band of a semiconductor photocatalyst (Equation 4.1), superoxide radicals ($\cdot O_2^-$), one of the

most important active species, can be formed (Equation 4.2) which lead to the rapid oxidation of substrate molecules. Thus, without dissolved O_2, superoxide radical species could not be generated thereby the photocatalytic degradation progress of MO was inhibited profoundly. Further proof was given by the quenching result of ethanol alcohol (a quencher for electrons) which shows the decomposition was hindered after its addition into the system. In fact, its electronic band structure as revealed below also indicated very similar results.

$$Si \xrightarrow{h\nu} e^-_{cb} + h^+_{vb} \qquad \text{Equation 4.1}$$

$$O_2 + e^- \longrightarrow \cdot O_2^- \qquad \text{Equation 4.2}$$

Another quencher tested is triethanolamine (TEOA) for the detection of holes (h^+). As seen in Figure 4.26 , the photocatalytic reaction was inhibited dramatically with only around 25% of initial MO were converted after 30 min irradiation. As we also observed the release of gases from HPS-200-05, supposedly H_2, due to the nucleophilic attack on the electron deficient Si-H bond on the surface of mpSi (Equation 4.3). Thus, the inactivity is likely due to the depletion of surface hydrides by TEOA quencher.

$$(HOCH_2CH_2)_3N: \cdots \overset{\delta+}{Si}\text{-}\overset{\delta-}{H} + H_2O \longrightarrow Si\text{-}OH + H_2\uparrow \qquad \text{Equation 4.3}$$

4.3.5.4 Photocatalytic mechanism

Based on the aforementioned results, a possible photocatalytic mechanism was proposed. The bandgap energy (E_g) of mpSi was first estimated by the Tauc method based on the UV-Vis absorption data of HPS-150-05 and HPS-200-05 (Figure 4.14). As shown in Figure 4.27, it was 2.10 eV for HPS-150-05 and 2.05 eV for HPS-200-05, within the reported range of 1.8-2.2 eV for porosified silicon materials.[71-72]

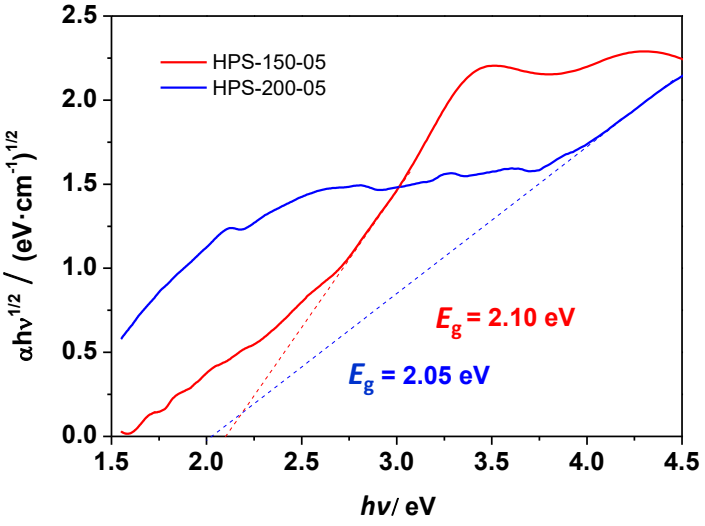

Figure 4.27 Tauc plots of HPS-150-05 and HPS-200-05.

The CB/VB band edge potential (E_{CB} and E_{VB}) of semiconductor can be calculated according to the following formulas:

$$E_{CB} = \chi - E_C - 0.5E_g \quad \text{Equation 4.4}$$

$$E_{VB} = E_{CB} + E_g \quad \text{Equation 4.5}$$

E_g is the bandgap energy of semiconductor. E_c is the energy of free electrons on the hydrogen scale, 4.50 eV. χ is the absolute electronegativity of the component atoms, 4.77 eV for Si atom.[73]

Table 4.3 The bandgap and band edge potentials of mesoporous silicon materials versus Normal Hydrogen Electrode (NHE).

	E_g / eV	E_{CB} vs NHE/ V	E_{VB} vs NHE / V
HPS-150-05	2.10	-0.78	1.32
HPS-200-05	2.05	-0.75	1.30
Si[74]	1.10	-0.50	0.60

As shown in Table 4.3, the bandgap of mpSi was significantly widened compared to Si crystal due to the quantum confinement effects of the Si nanocrystallites embedded on the pore walls of the mesoporous structure, rendering the material to be visible light responsive and photo-catalytically active. The CB potential of mpSi shifted negatively by 0.2-0.3 V, which implies an improved reduction capability of CB electrons excited by visible light photons. More significantly, its VB potential shifted downwards to 1.30-1.32 V from 0.60 V of the pristine Si. This positive shift is indicative of an enhanced oxidation ability possessed by the valence band holes of mpSi. In fact, the photocatalytic activity of Si-based nanostructures is often reported to be restricted by the shallow VB band level which results in poor oxidation performance.[10]

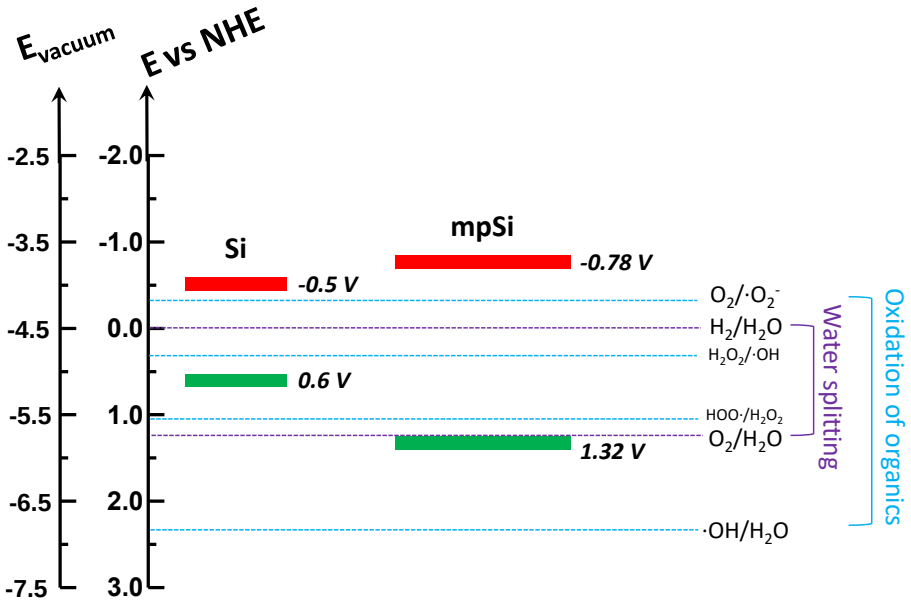

Figure 4.28 Band edge positions of Si crystal and mesoporous silicon sample (HPS-150-05) relative to NHE (normal hydrogen electrode) and the vacuum level. For comparison, the reduction potentials (E^0_{red}) of various ROS (e.g. $\cdot O_2^-$, $\cdot OH$, H_2O_2) are also presented.

As we know, the probability of charge transfer is determined by a relative position of the valence and conductance zones of semiconductor photocatalyst and the value of the oxidation-reduction potential (ORP) of the substrate.[75] As seen in Figure 4.28, the CB/VB energy levels of Si crystal and mesoporous silicon (HPS-150-05 for example) were aligned with the reduction potential of multiple ROS couples that are most commonly

discovered in heterogeneous photocatalysis. The widened bandgap of HPS-150-05 enabled it to absorb visible light energy and induce e^-/h^+ charge separation by exciting electrons to conduction band. The energetic CB electrons of mpSi can reduce the dissolved molecular oxygen into superoxide radical anions ($\cdot O_2^-$), in agreement with the previous quenching experiment. The insignificance of hydroxyl radicals (·OH) in the photocatalytic process is also confirmed by the position of valence band edge of HPS-150-05 shown in Figure 4.28 against E^0_{red} ($\cdot OH/H_2O$). Despite this, the increased VB energy of mpSi is now greater than the H_2O oxidation potential, suggesting water splitting by mpSi without a sacrificial electron acceptor would be possible and will be explored in the future. Figure 4.28 clearly affirmed the results of previous trapping experiments, showing superoxide radical anions produced by one-electron reduction of dissolved oxygen as the main reactive oxygen species in mpSi-catalysed MO photo-degradation under visible light irradiation. Besides, the band structure also indicated the possibility of the production of H_2O_2 and ·OH through the reduction of protonated $\cdot O_2^-$ during the photodegradation process. The existence of ·OH species was also evidenced in the earlier analysis of the UV-Vis spectra of the unreacted solution (Figure 4.10) which implied the generation of hydroxylated intermediates of methyl orange.

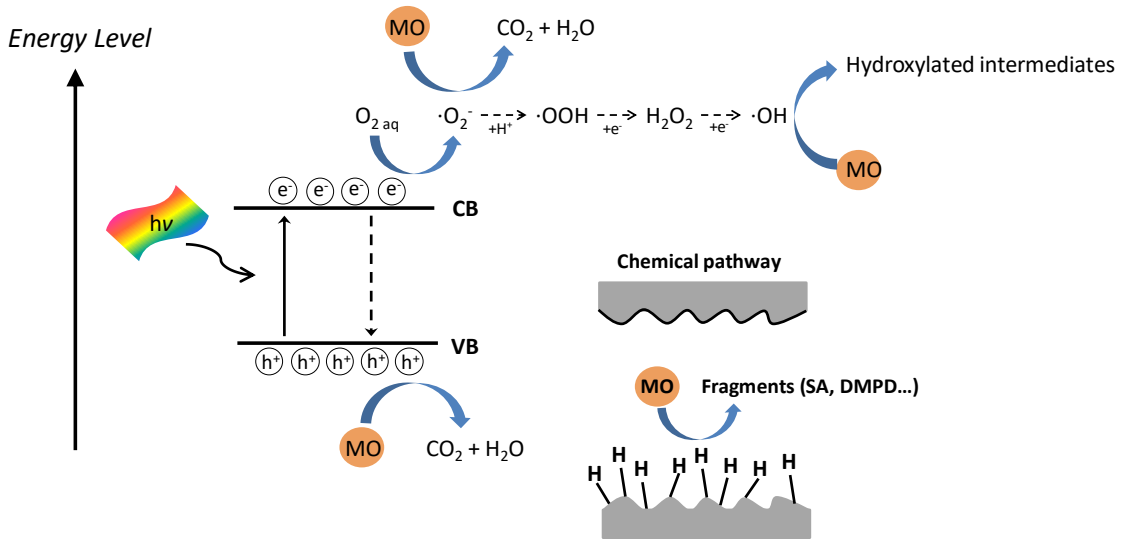

Figure 4.29 The proposed photocatalytic mechanism of the degradation of methyl orange by H-terminated mesoporous silicon under visible light irradiation and the fragmentation of methyl orange by surface hydrides of mesoporous silicon via hydrogen transfer.

The photocatalytic mechanism of MO degradation by H-terminated mesoporous silicon under visible light irradiation is summarized in Figure 4.29. When the mpSi sample is irradiated by visible light source, it absorbs supra-bandgap incident photons ($h\nu > E_g$) and generates photo-excited electrons and holes in its conduction band and valence band, respectively. The conduction band electrons then transfer to the mpSi/solution interface and reduce dissolved molecular oxygen into superoxide radicals ($\cdot O_2^-$) which oxidise methyl orange molecule into non-toxic gaseous products such as CO_2 and H_2O. In the meantime, hydroxyl radicals (·OH) are also likely to be formed through the protonation and reduction of $\cdot O_2^-$ which leads to the production of hydroxylated intermediates during the photocatalytic process. However, the effect of ·OH is believed to be minor given the low concentration at pH≈7, since the initial protonation of $\cdot O_2^-$ occurs at pH ≤ 4.8. On the valence band side, dye molecules can be oxidized directly as well but the oxidation ability of valence band holes are rather limited by the relatively high band edge position thus the production of ·OH by the oxidation of H_2O or OH^- is much excluded. Apart from the charge-driven pathway, chemical decomposition of methyl orange via the reductive degradation of the azo linkage also takes place, which collaborates with the photochemical pathway and accelerates the decoloration and decomposition of organic substances. Interestingly, the reactivity of Si-H bond of the irradiated mpSi appears to be stimulated by photons or photo-induced charges, which is still uncertain at this stage. Since both chemical and photochemical pathway require accessible silicon hydrides, the consumption of active surface hydrides by the chemical pathway eventually leads to the decay of photo-oxidation capability of mesoporous silicon by affecting e^-/h^+ separation and recombination.

4.3.6 Lifetime study of mesoporous silicon in dye degradation

The recyclability of H-terminated mesoporous silicon photocatalyst in MO decomposition under visible light irradiation was assessed. As featured in Figure 4.30 , an excellent reusability up to 10 cycles was exhibited. For the first three cycles, HPS-200-05 demonstrated parallel reaction efficiency and it was very well maintained even after 8 cycles, only slightly decreased to 88% of the initial efficacy as the number of cycles went

up to 10. Thus, it is reasonable to assume that a comparable activity will be able to last for even longer time. To our best knowledge, this is by far the best reuse performance ever achieved on Si-based elemental photocatalysts.

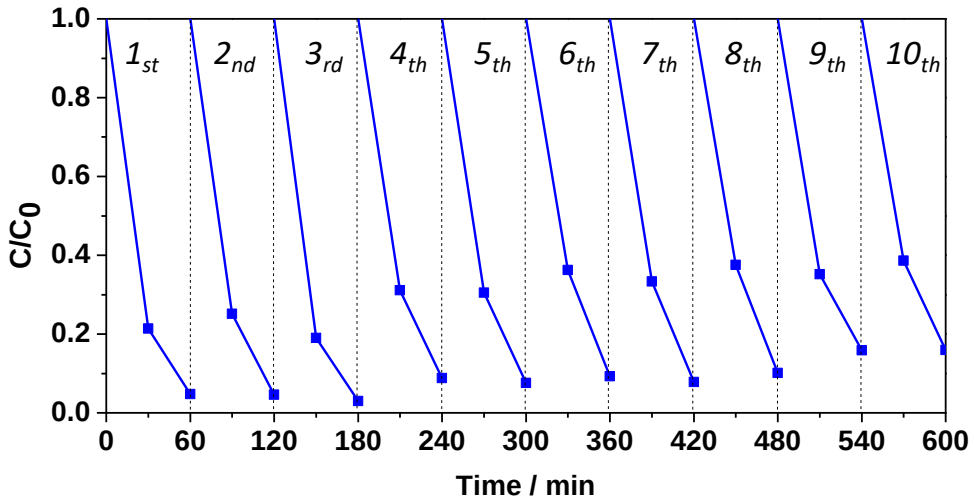

Figure 4.30 The cycle runs of HPS-200-05 in visible light driven photo-degradation of methyl orange. HPS-200-05 was simply washed with 5 wt. % aqueous HF prior to the next cycle.

Without HF cleaning procedure prior to each cycle, the activity of mesoporous silicon upon visible light irradiation decayed rapidly (Figure 4.31). This is largely due to the consumption of surface hydrides species and simultaneous formation of surface oxides as explained above.

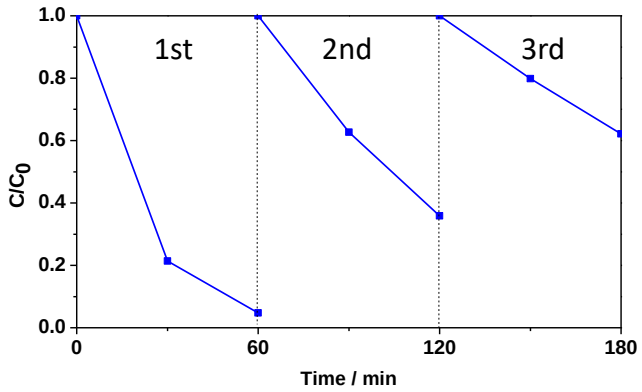

Figure 4.31 The cycle runs of HPS-200-05 in visible light driven photo-degradation of methyl orange without HF washing in between each cycle.

Interestingly, we also tested the reusability of H-terminated mesoporous silicon in MO degradation without any illumination using the same regeneration approach by HF washing. As presented in Figure 4.32, its activity was maintained and only slightly reduced after 5 runs. This result shows H-terminated mesoporous silicon is also a promising candidate as a rechargeable hydride source, which can be exploited in many applications such as H_2 generation, CO_2 reduction and organic synthesis for fine chemicals.

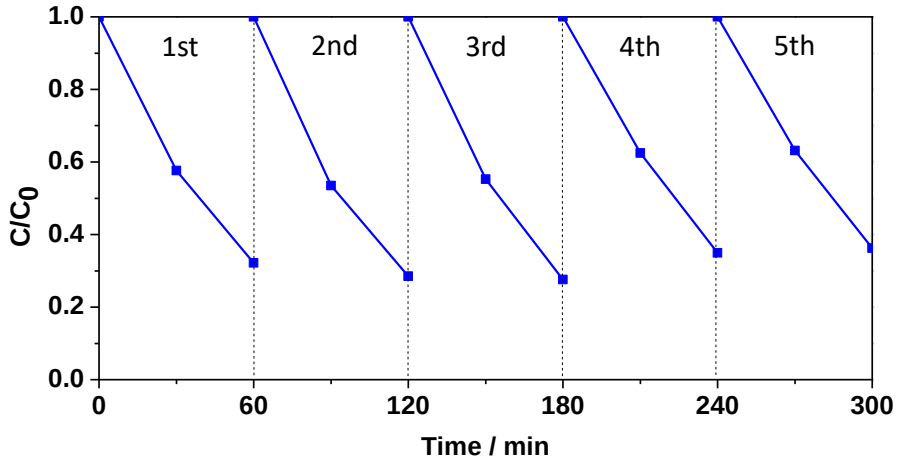

Figure 4.32 The cycle runs of HPS-200-05 in degrading methyl orange in the absence of light. HPS-200-05 was simply washed with 5 wt. % aqueous HF prior to the next cycle.

4.4 Summary

In this study, a highly reusable metal-free photocatalyst in visible-light-driven methyl orange photo-degradation was developed via electrochemical etching of monocrystalline Si. By absorbing visible light photons with energies equal to or higher than the 2.05-2.10 eV bandgap ($\lambda \approx 598$ nm) of H-terminated mesoporous silicon enlarged by quantum confinement of silicon nanocrystallites, electron-hole pairs were generated and separated with electrons excited to the conduction band creating a chemical potential (E_{CB} = -0.78 V, E_{VB} = 1.32 V vs NHE, e.g. HPS-150-05) that triggered the generation of reactive oxygen species, mainly superoxide radicals ($^{\cdot}O_2^-$) through single electron transfer and other redox events involved in the dye degradation process under

visible light irradiation. The broad visible light responsive range, vast accessible surface area and significantly released diffusion resistance by the open mesoporous system, largely contributed to the excellent decomposition efficiency of mesoporous silicon with organic molecules rapidly decolorized and mineralized.

The complex and important roles played by the surface hydrides of mesoporous silicon were also reflected in the reductive degradation of the azo linkage of methyl orange without light illumination and the determining influences on the course and rate of photochemical activities exhibited by irradiated mesoporous silicon toward methyl orange. The reactivity of the Si-H bond not only enabled unsaturated organics to be chemically fragmented into smaller molecules, but also led to the competition against charge-mediated photochemical degradation that is also strongly reliant on them as silicon hydrides can improve the lifetime of separated e^-/h^+ pairs. Notably, we also observed an acceleration in the chemical pathway after applying visible light irradiation suggesting the reduction capability of surface Si-H bond was stimulated by most likely the photo-induced charges considering the energy of incident photons are too weak to break any chemical bonds. Further investigation will be necessary to confirm this result, proposedly directed to understand the possible interaction and coupling between surface species of mesoporous silicon and the incident photons and photo-induced charges.

The effects of different structural factors on the photocatalytic performance were also discussed in this chapter, which revealed the varied influences of pore order, pore size, pore depth, sizes of Si nanocrystals on the photon absorption, and mass diffusion processes during dye degradation. As found the ordered 1D channel array of heavily doped mesoporous silicon is more efficient in degrading methyl orange molecules than the interconnected porous network of moderately doped mesoporous silicon for the improved mass transfer facilitated by the larger mesopores and straight pore alignment.

Last but not the least, the lifetime of H-terminated mesoporous silicon photocatalyst was also examined which shows an excellent reusability and its activity can be maintained very well even after 10 cycles of dye degradation.

4.5 References

1. Linic, S.; Christopher, P.; Ingram, D. B., Plasmonic-metal nanostructures for efficient conversion of solar to chemical energy. *Nat. Mater.* **2011,** *10* (12), 911-921.

2. Martha, S.; Sahoo, P. C.; Parida, K. M., An overview on visible light responsive metal oxide based photocatalysts for hydrogen energy production. *RSC Adv.* **2015,** *5* (76), 61535-61553.

3. Kamat, P. V., Meeting the clean energy demand: nanostructure architectures for solar energy conversion. *J. Phys. Chem. C* **2007,** *111* (7), 2834-2860.

4. Habisreutinger, S. N.; Schmidt-Mende, L.; Stolarczyk, J. K., Photocatalytic reduction of CO_2 on TiO_2 and other semiconductors. *Angew. Chem. Int. Ed. Engl.* **2013,** *52* (29), 7372-7408.

5. Chen, C.; Ma, W.; Zhao, J., Semiconductor-mediated photodegradation of pollutants under visible-light irradiation. *Chem. Soc. Rev.* **2010,** *39* (11), 4206-4219.

6. Zhu, H.; Lian, T., Wavefunction engineering in quantum confined semiconductor nanoheterostructures for efficient charge separation and solar energy conversion. *Energy Environ. Sci.* **2012,** *5* (11), 9406-9418.

7. Dong, S.; Feng, J.; Fan, M.; Pi, Y.; Hu, L.; Han, X.; Liu, M.; Sun, J.; Sun, J., Recent developments in heterogeneous photocatalytic water treatment using visible light-responsive photocatalysts: a review. *RSC Adv.* **2015,** *5* (19), 14610-14630.

8. Cai, Z.; Sun, Y.; Liu, W.; Pan, F.; Sun, P.; Fu, J., An overview of nanomaterials applied for removing dyes from wastewater. *Environ. Sci. Pollut. Res. Int.* **2017,** *24* (19), 15882-15904.

9. Spasiano, D.; Marotta, R.; Malato, S.; Fernandez-Ibanez, P.; Di Somma, I., Solar photocatalysis: Materials, reactors, some commercial, and pre-industrialized applications. A comprehensive approach. *Appl. Catal. B* **2015,** *170*, 90-123.

10. Liu, G.; Niu, P.; Cheng, H. M., Visible-light-active elemental photocatalysts. *ChemPhysChem* **2013,** *14* (5), 885-892.

11. Chandrasekaran, S.; Nann, T.; Voelcker, N. H., Nanostructured silicon photoelectrodes for solar water electrolysis. *Nano Energy* **2015,** *17*, 308-322.

12. Liu, X.; Coxon, P. R.; Peters, M.; Hoex, B.; Cole, J. M.; Fray, D. J., Black silicon: fabrication methods, properties and solar energy applications. *Energy Environ. Sci.* **2014,** *7* (10), 3223-3263.

13. Kang, Z.; Tsang, C. H.; Wong, N. B.; Zhang, Z.; Lee, S. T., Silicon quantum dots: a general photocatalyst for reduction, decomposition, and selective oxidation reactions. *J. Am. Chem. Soc.* **2007,** *129* (40), 12090-12091.

14. Kang, Z.; Liu, Y.; Lee, S. T., Small-sized silicon nanoparticles: new nanolights and nanocatalysts. *Nanoscale* **2011,** *3* (3), 777-791.

15. Shao, M.; Cheng, L.; Zhang, X.; Ma, D. D.; Lee, S. T., Excellent photocatalysis of HF-treated silicon nanowires. *J. Am. Chem. Soc.* **2009,** *131* (49), 17738-17739.

16. Qu, Y.; Zhong, X.; Li, Y.; Liao, L.; Huang, Y.; Duan, X., Photocatalytic properties of porous silicon nanowires. *J. Mater. Chem.* **2010,** *20* (18), 3590-3594.

17. Megouda, N.; Cofininier, Y.; Szunerits, S.; Hadjersi, T.; Elkechai, O.; Boukherroub, R., Photocatalytic activity of silicon nanowires under UV and visible light irradiation. *Chem. Commun.* **2011,** *47* (3), 991-993.

18. Wang, F. Y.; Yang, Q. D.; Xu, G.; Lei, N. Y.; Tsang, Y. K.; Wong, N. B.; Ho, J. C., Highly active and enhanced photocatalytic silicon nanowire arrays. *Nanoscale* **2011,** *3* (8), 3269-3276.

19. Liu, R.; Yuan, G. B.; Joe, C. L.; Lightburn, T. E.; Tan, K. L.; Wang, D. W., Silicon nanowires as photoelectrodes for carbon dioxide fixation. *Angew. Chem. Int. Ed.* **2012,** *51* (27), 6709-6712.

20. Liao, F.; Wang, T.; Shao, M., Silicon nanowires: applications in catalysis with distinctive surface property. *J. Mater. Sci. Mater. Electron.* **2015,** *26* (7), 4722-4729.

21. Liu, D.; Li, L.; Gao, Y.; Wang, C.; Jiang, J.; Xiong, Y., The nature of photocatalytic "water splitting" on silicon nanowires. *Angew. Chem. Int. Ed. Engl.* **2015,** *54* (10), 2980-2985.

22. Su, J.; Yu, H.; Quan, X.; Chen, S.; Wang, H., Hierarchically porous silicon with significantly improved photocatalytic oxidation capability for phenol degradation. *Appl. Catal. B* **2013,** *138-139*, 427-433.

23. Meekins, B. H.; Lin, Y. C.; Manser, J. S.; Manukyan, K.; Mukasyan, A. S.; Kamat, P. V.; McGinn, P. J., Photoactive porous silicon nanopowder. *ACS Appl. Mater. Interfaces* **2013,** *5* (8), 2943-2951.

24. Dai, F.; Zai, J.; Yi, R.; Gordin, M. L.; Sohn, H.; Chen, S.; Wang, D., Bottom-up synthesis of high surface area mesoporous crystalline silicon and evaluation of its hydrogen evolution performance. *Nat. Commun.* **2014,** *5*, 3605.

25. Xu, H.; Xiao, H.; Pei, H.; Cui, J.; Hu, W., Photodegradation activity and stability of porous silicon wafers with (100) and (111) oriented crystal planes. *Microporous Mesoporous Mater.* **2015,** *204*, 251-256.

26. Li, T.; Li, J.; Zhang, Q.; Blazeby, E.; Shang, C.; Xu, H.; Zhang, X.; Chao, Y., Hydrogen-terminated mesoporous silicon monoliths with huge surface area as alternative Si-based visible light-active photocatalysts. *RSC Adv.* **2016,** *6* (75), 71092-71099.

27. Peng, F.; Wang, J.; Ge, G. L.; He, T.; Cao, L. X.; He, Y. H.; Ma, H.; Sun, S. Q., Photochemical reduction of CO_2 catalyzed by silicon nanocrystals produced by high energy ball milling. *Mater. Lett.* **2013,** *92*, 65-67.

28. Oh, I.; Kye, J.; Hwang, S., Enhanced photoelectrochemical hydrogen production from silicon nanowire array photocathode. *Nano Lett.* **2012,** *12* (1), 298-302.

29. Lee, H. Y.; Ryu, J.; Kim, J. H.; Lee, S. H.; Park, C. B., Biocatalyzed artificial photosynthesis by hydrogen-terminated silicon nanowires. *ChemSusChem* **2012,** *5* (11), 2129-2132.

30. Lee, S. H.; Ryu, G. M.; Nam, D. H.; Kim, J. H.; Park, C. B., Silicon nanowire photocathodes for light-driven electroenzymatic synthesis. *ChemSusChem* **2014,** *7* (11), 3007-3011.

31. Lian, S. Y.; Tsang, C. H. A.; Kang, Z. H.; Liu, Y.; Wong, N.; Lee, S. T., Hydrogen-terminated silicon nanowire photocatalysis: benzene oxidation and methyl red decomposition. *Mater. Res. Bull.* **2011,** *46* (12), 2441-2444.

32. Wang, J.-F.; Chen, J.-S.; Zhou, Z.-F., Preparation of porous silicon by sodiothermic reduction of zeolite and photoactivation for benzene oxidation. *Eur. J. Inorg. Chem.* **2015,** *2015* (8), 1330-1333.

33. Ameen, S.; Park, D.-R.; Shin, H. S., Silicon nanowires arrays for visible light driven photocatalytic degradation of rose bengal dye. *J. Mater. Sci. Mater. Electron.* **2016,** *27* (10), 10460-10467.

34. Fellahi, O.; Barras, A.; Pan, G.-H.; Coffinier, Y.; Hadjersi, T.; Maamache, M.; Szunerits, S.; Boukherroub, R., Reduction of Cr(VI) to Cr(III) using silicon nanowire arrays under visible light irradiation. *J. Hazard. Mater.* **2016,** *304*, 441-447.

35. Thommes, M.; Kaneko, K.; Neimark, A. V.; Olivier, J. P.; Rodriguez-Reinoso, F.; Rouquerol, J.; Sing, K. S. W., Physisorption of gases, with special reference to the evaluation of surface area and pore size distribution (IUPAC Technical Report). *Pure Appl. Chem.* **2015,** *87* (9-10), 1051-1069.

36. Dohnalova, K.; Gregorkiewicz, T.; Kusova, K., Silicon quantum dots: surface matters. *J. Phys. Condens. Matter.* **2014,** *26* (17), 173201.

37. Rajkanan, K.; Singh, R.; Shewchun, J., Absorption coefficient of silicon for solar cell calculations. *Solid-State Electron.* **1979,** *22* (9), 793-795.

38. Ioannis Leontis, A. O. a. A. G. N., Structure, morphology, and photoluminescence of porous Si nanowires: effect of different chemical treatments. *Nanoscale Res. Lett.* **2013,** *8*, 383.

39. Kumar, P., Effect of silicon crystal size on photoluminescence appearance in porous silicon. *ISRN Nanotechnology* **2011,** *2011*, 163168.

40. Wang, K.; Wang, Q.; Chao, Y., Simple fabrication of nanostructured silicon and photoluminescence. *Appl. Phys. A* **2012,** *109* (2), 437-440.

41. Coxon, P. R.; Wang, Q.; Chao, Y., An abrupt switch between the two photoluminescence bands within alkylated silicon nanocrystals. *J. Phys. D* **2011,** *44* (49), 495301.

42. Kotkovskiy, G. E.; Kuzishchin, Y. A.; Martynov, I. L.; Chistyakov, A. A.; Nabiev, I., The photophysics of porous silicon: technological and biomedical implications. *Phys. Chem. Chem. Phys.* **2012,** *14* (40), 13890-13902.

43. Baiocchi, C.; Brussino, M. C.; Pramauro, E.; Prevot, A. B.; Palmisano, L.; Marcì, G., Characterization of methyl orange and its photocatalytic degradation products by HPLC/UV–VIS diode array and atmospheric pressure ionization quadrupole ion trap mass spectrometry. *Int. J. Mass Spectrom.* **2002,** *214* (2), 247-256.

44. Hoffmann, M. R.; Martin, S. T.; Choi, W. Y.; Bahnemann, D. W., Environmental applications of semiconductor photocatalysis. *Chem. Rev.* **1995,** *95* (1), 69-96.

45. Alivisatos, A. P., Perspectives on the physical chemistry of semiconductor nanocrystals. *J. Phys. Chem.* **1996,** *100* (31), 13226-13239.

46. Canham, L. T., Silicon quantum wire array fabrication by electrochemical and chemical dissolution of wafers. *Appl. Phys. Lett.* **1990,** *57* (10), 1046-1048.

47. Lee, H. Y.; Kim, J. H.; Son, E. J.; Park, C. B., Silicon nanowires as a rechargeable template for hydride transfer in redox biocatalysis. *Nanoscale* **2012,** *4* (24), 7636-7640.

48. Xu, Y.; Wang, L.; Jiang, W.; Wang, H.; Yao, J.; Guo, Q.; Yuan, L.; Chen, H., Silicon nanowire arrays - a new catalyst for the reduction of nitrobenzene derivatives. *ChemCatChem* **2013,** *5* (12), 3788-3793.

49. Sun, W.; Qian, C.; He, L.; Ghuman, K. K.; Wong, A. P. Y.; Jia, J.; Jelle, A. A.; O'Brien, P. G.; Reyes, L. M.; Wood, T. E.; Helmy, A. S.; Mims, C. A.; Singh, C. V.; Ozin, G. A., Heterogeneous reduction of carbon dioxide by hydride-terminated silicon nanocrystals. *Nat. Commun.* **2016,** *7*, 12553.

50. Sailor, M. J., Fundamentals of porous silicon preparation. In *Porous Silicon in Practice: Prepration, Chracterization and Applications*. Wiley, 2012; pp 1-42.

51. Secret, E.; Leonard, C.; Kelly, S. J.; Uhl, A.; Cozzan, C.; Andrew, J. S., Size control of porous silicon-based nanoparticles via pore-wall thinning. *Langmuir* **2016,** *32* (4), 1166-1170.

52. Wang, M.; Hartman, P. S.; Loni, A.; Canham, L. T.; Bodiford, N.; Coffer, J. L., Influence of surface chemistry on the release of an antibacterial drug from nanostructured porous silicon. *Langmuir* **2015,** *31* (22), 6179-6185.

53. Joo, J.; Cruz, J. F.; Vijayakumar, S.; Grondek, J.; Sailor, M. J., Photoluminescent porous Si/SiO_2 core/shell nanoparticles prepared by borate oxidation. *Adv. Funct. Mater.* **2014,** *24* (36), 5688-5694.

54. Fry, N. L.; Boss, G. R.; Sailor, M. J., Oxidation-induced trapping of drugs in porous silicon microparticles. *Chem. Mater.* **2014,** *26* (8), 2758-2764.

55. Wang, H.; Jiang, W.; Yuan, L.; Wang, L.; Chen, H., Reductase-like activity of silicon nanowire arrays. *ACS Appl. Mater. Interfaces* **2013,** *5* (5), 1800-1805.

56. Buriak, J. M., Organometallic chemistry on silicon and germanium surfaces. *Chem. Rev.* **2002,** *102* (5), 1271-1308.

57. Behray, M.; Webster, C. A.; Pereira, S.; Ghosh, P.; Krishnamurthy, S.; Al-Jamal, W. T.; Chao, Y., Synthesis of diagnostic silicon nanoparticles for targeted delivery of thiourea to epidermal growth factor receptor-expressing cancer cells. *ACS Appl. Mater. Interfaces* **2016,** *8* (14), 8908-8917.

58. Ahire, J. H.; Behray, M.; Webster, C. A.; Wang, Q.; Sherwood, V.; Saengkrit, N.; Ruktanonchai, U.; Woramongkolchai, N.; Chao, Y., Synthesis of carbohydrate capped silicon nanoparticles and their reduced cytotoxicity, in vivo toxicity, and cellular uptake. *Adv. Healthc. Mater.* **2015,** *4* (12), 1877-1886.

59. Wang, Q.; Bao, Y.; Zhang, X.; Coxon, P. R.; Jayasooriya, U. A.; Chao, Y., Uptake and toxicity studies of poly-acrylic acid functionalized silicon nanoparticles in cultured mammalian cells. *Adv. Healthc. Mater.* **2012,** *1* (2), 189-198.

60. Amdouni, S.; Coffinier, Y.; Szunerits, S.; Zaïbi, M. A.; Oueslati, M.; Boukherroub, R., Catalytic activity of silicon nanowires decorated with silver and copper nanoparticles. *Semicond. Sci. Technol.* **2016,** *31* (1), 014011.

61. Polisski, S.; Goller, B.; Wilson, K.; Kovalev, D.; Zaikowskii, V.; Lapkin, A., In situ synthesis and catalytic activity in CO oxidation of metal nanoparticles supported on porous nanocrystalline silicon. *J. Catal.* **2010,** *271* (1), 59-66.

62. Kim, T.; Fu, X.; Warther, D.; Sailor, M. J., Size-controlled Pd nanoparticle catalysts prepared by galvanic displacement into a porous Si-iron oxide nanoparticle host. *ACS Nano* **2017,** *11* (3), 2773-2784.

63. Dasog, M.; Kraus, S.; Sinelnikov, R.; Veinot, J. G. C.; Rieger, B., CO_2 to methanol conversion using hydride terminated porous silicon nanoparticles. *Chem. Commun.* **2017,** *53* (21), 3114-3117.

64. El-Demellawi, J. K.; Holt, C. R.; Abou-Hamad, E.; Al-Talla, Z. A.; Saih, Y.; Chaieb, S., Room-temperature reactivity of silicon nanocrystals with solvents: the case of ketone and hydrogen production from secondary alcohols: catalysis? *ACS Appl. Mater. Interfaces* **2015,** *7* (25), 13794-13800.

65. Ye, M.; Qian, C.; Sun, W.; He, L.; Jia, J.; Dong, Y.; Zhou, W., Dye colour switching by hydride-terminated silicon particles and its application as an oxygen indicator. *J. Mater. Chem. C* **2016,** *4* (20), 4577-4583.

66. Jana, A.; Lawrence, K. N.; Teunis, M. B.; Mandal, M.; Kumbhar, A.; Sardar, R., Investigating the control by quantum confinement and surface ligand coating of photocatalytic efficiency in chalcopyrite copper indium diselenide nanocrystals. *Chem. Mater.* **2016,** *28* (4), 1107-1120.

67. Kopping, B.; Chatgilialoglu, C.; Zehnder, M.; Giese, B., Tris(trimethylsilyl)silane: an efficient hydrosilylating agent of alkenes and alkynes. *J. Org. Chem.* **1992,** *57* (14), 3994-4000.

68. Buriak, J. M., Illuminating silicon surface hydrosilylation: an unexpected plurality of mechanisms. *Chem. Mater.* **2014,** *26* (1), 763-772.

69. Huck, L. A.; Buriak, J. M., Toward a mechanistic understanding of exciton-mediated hydrosilylation on nanocrystalline silicon. *J. Am. Chem. Soc.* **2012,** *134* (1), 489-497.

70. Lai, Y. K.; Huang, J. Y.; Zhang, H. F.; Subramaniam, V. P.; Tang, Y. X.; Gong, D. G.; Sundar, L.; Sun, L.; Chen, Z.; Lin, C. J., Nitrogen-doped TiO_2 nanotube array films with enhanced photocatalytic activity under various light sources. *J. Hazard. Mater.* **2010,** *184* (1-3), 855-863.

71. Chen, Z.; Lee, T. Y.; Bosman, G., Electrical band gap of porous silicon. *Appl. Phys. Lett.* **1994,** *64* (25), 3446-3448.

72. Frederiksen, J. T.; Melcher, P. G.; Veje, E., The electrical band-gap energy of porous silicon measured versus sample temperature. *J. Porous Mater.* **2000,** *7* (1/3), 271-273.

73. Pearson, R. G., Absolute electronegativity and hardness: application to inorganic chemistry. *Inorganic Chemistry* **1988,** *27* (4), 734-740.

74. Bludau, W.; Onton, A.; Heinke, W., Temperature dependence of the band gap of silicon. *J. Appl. Phys.* **1974,** *45* (4), 1846-1848.

75. Prihod'ko, R. V.; Soboleva, N. M., Photocatalysis: oxidative processes in water treatment. *J. Chem.* **2013,** *2013*, 1-8.

Chapter 5

Hydrogen-Terminated Mesoporous Silicon/Graphitic Carbon Nitride (g-C_3N_4) Nanosheets Heterojunction Study

Abstract

In semiconductor-mediated photocatalysis, the construction of hybrids by coupling different semiconductors is an effective strategy for achieving a better performance in a given redox reaction. In contrast to the involvement of expensive metal-containing components, two dimensional graphitic carbon nitride (g-C_3N_4) material appeals to be an ideal candidate to generate earth abundant and metal-free heterojunction utilized in solar energy conversion. Here g-C_3N_4 was for the first time composited with H-terminated mesoporous silicon previously investigated via simple impregnation, which exhibited an enhanced activity in methyl orange degradation under visible light irradiation.

5.1 Overview

Two-dimensional (2D) nanomaterials, such as graphene,[1-3] MoS_2,[4-6] and hexagonal boron nitride (h-BN),[7] have attracted worldwide attention owing to their exceptional structural and electronic properties over the past decade.[8] A significant amount of effort has in particular been devoted to the development of 2D graphitic carbon nitride (g-C_3N_4) which has shown promising activities in various fields of solar energy conversion, light-emitting and sensing etc.[9-15] Ever since the first report of using g-C_3N_4 in hydrogen production in 2009 by Wang et al.,[16] its potential as photocatalyst in water splitting,[17] CO_2 fixation,[18] and pollutant regulation[9, 11] has been exploited widely due to its notable characters such as low-cost, earth abundant, non-toxic, thermal and chemical stability.[10] Moreover, its layered structure can be easily delaminated into nanosheets via thermal,[19-21] chemical,[22-24] or mechanical treatment[25-28] which is widely recognized as a novel class of nanostructured materials because of the high surface area, small vertical thickness and quantum confined effects on photoactivity.[29]

In this chapter, H-terminated mesoporous silicon (mpSi) was combined with such two-dimensional g-C_3N_4 nanosheets (g-C_3N_4 NSs), obtained through thermal condensation polymerisation of melamine followed by ultrasonic exfoliation. Firstly, the physiochemical properties of g-C_3N_4 bulk powders and g-C_3N_4 NSs were thoroughly examined by means of characterisation techniques including SEM, IR, gas sorption, thermal analysis and optical measurements, exhibiting clear differences in physical morphology (plane size, vertical thickness), surface area and optical properties leading to a more efficient photocatalytic performance of g-C_3N_4 NSs in degrading methyl orange (MO) under visible light irradiation than the large aggregated parent powders. After combined with mpSi via liquid-phase impregnation, the degradation activity of mpSi/g-C_3N_4 NSs material of 1:1 weight ratio toward MO was remarkably promoted, indicating a coupling interaction between these two semiconductor components.

5.2 Experimental section

5.2.1 Synthesis of graphitic carbon nitride bulk powders

The bulk g-C_3N_4 was fabricated by direct pyrolysis of melamine. The precursor was heated in an alumina boat covered by Al foil at 550˚C and the heating rate was 10 ˚C·min^{-1}, then kept for 2 hours at 550 ˚C under static air. After condensation, it was ground into g-C_3N_4 powders.

5.2.2 Synthesis of graphitic carbon nitride nanosheets

Graphitic C_3N_4 nanosheets were prepared by sonication assisted liquid exfoliation. Typically, 100 mg g-C_3N_4 powder as obtained above was first dispersed in 50 mL 2-propanol. Then the colloidal solution was exposed to ultrasound treatment for 10 hours at room temperature. Thereafter they were centrifuged at 3000 rpm and then g-C_3N_4 NSs were obtained in the supernatant layer.

5.2.3 Synthesis of the composites (mpSi/g-C_3N_4 NSs)

H-terminated mesoporous silicon (mpSi) was obtained by electrochemical etching of monocrystalline Si wafers in HF/ethanol electrolyte at room temperature. Among various mpSi samples that had been studied in previous chapters, HPS-200-05-F samples exhibited the most impressive photocatalytic activity in methyl orange degradation due to the wide visible light responsiveness and its unique structural features according to the findings in Chapter 4 (Figure 4.17). Thus, it was adopted here to be combined with g-C_3N_4 nanosheets in varied weight ratio as 4:1, 1:1 and 1:4 respectively, through the procedure described in 2.2.3 in Chapter 2.

5.2.4 Sample characterisation

The structural morphology and physiochemical properties of g-C_3N_4 bulk powders and g-C_3N_4 nanosheets were examined by means of SEM, FTIR, nitrogen adsorption, TGA-DSC, UV-Vis and fluorescence spectroscopic techniques with H_2O used as dispersion medium for the optical measurements. The IR, UV-Vis absorption, photoluminescence emission spectra of mpSi/g-C_3N_4 NSs composites were also recorded. All measurement parameters were the same as described in Chapter 2 unless otherwise stated.

5.2.5 Photocatalytic evaluation

The photocatalytic activities of g-C_3N_4 materials and the heterojunction were measured by the photo-degradation of methyl orange (MO) under visible light irradiation. The unreacted dye concentration of MO solution was measured by UV-Vis spectrometer at different time intervals of the photocatalytic process. Apparent rate constants were also derived from the UV-Vis data of MO based on first order reaction model for the clarification of reaction efficiency. All experimental procedures and instrumental parameters were the same as outlined in Chapter 2 unless otherwise specified in the text.

5.3 Results and discussion

5.3.1 Characterisation and photocatalytic activity of g-C_3N_4 materials

As described above, graphitic carbon nitride (g-C_3N_4) bulk particles were synthesized through thermal-driven condensation polymerisation of melamine, which were then used to prepare g-C_3N_4 nanosheets (g-C_3N_4 NSs) by sonication-assisted liquid exfoliation in isopropanol. A range of characterisation tools (SEM, FTIR, gas sorption, thermal analysis, UV-Vis absorption and fluorescence spectroscopies) were employed to confirm this result. Then the photocatalytic performance of g-C_3N_4 powders and g-C_3N_4 NSs in MO decomposition under visible light irradiation were also examined in this section.

5.3.1.1 SEM images and elemental analysis of g-C_3N_4 materials

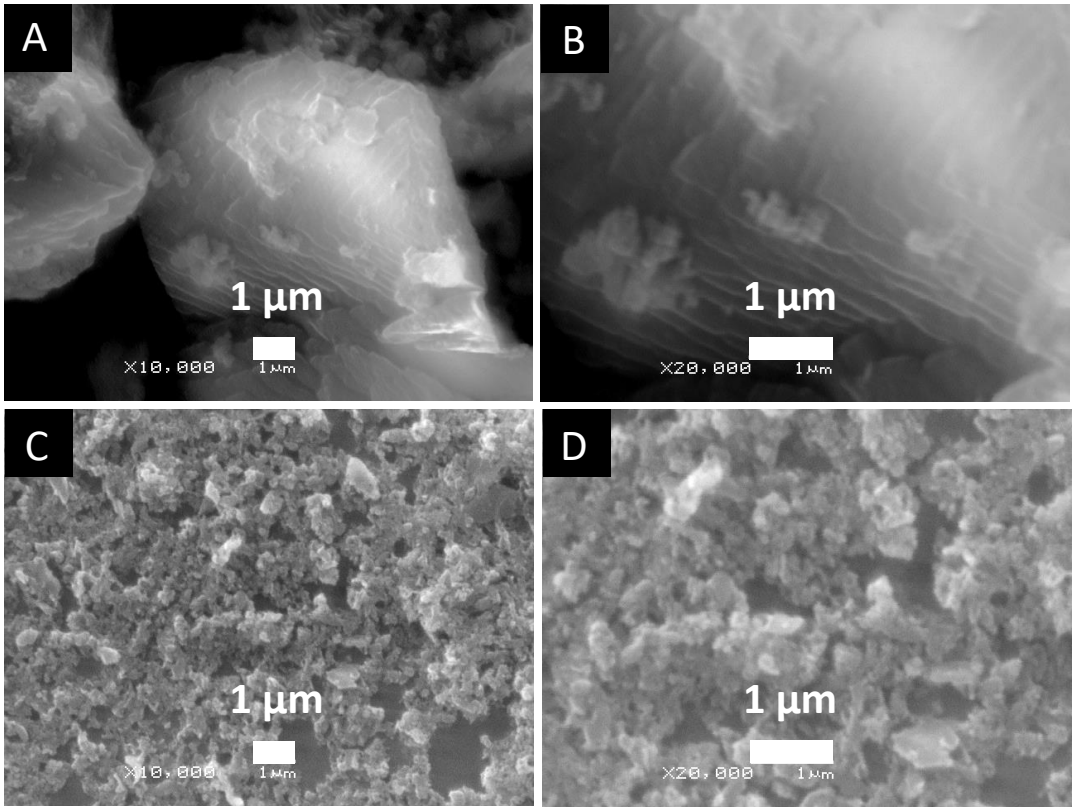

Figure 5.1 SEM images of g-C_3N_4 bulk powders (A, B) and g-C_3N_4 nanosheets (C, D).

As shown in Figure 5.1, the particle size of g-C_3N_4 nanosheets (C and D) was significantly reduced after exfoliation, in stark contrast to the bulky particles of parent g-C_3N_4 powders (A and B) as well as the thinness, while the typical graphite-like 2D layered structure was distinctly featured in the bulk g-C_3N_4. The theoretical thickness of g-C_3N_4 monolayer is about 0.325 nm[21] which would be greatly desirable to be used in the following photocatalytic application because of the much enlarged interface area it possesses for mass and charge transport. However, as known from graphene related research, multilayer or buckled single layer have been demonstrated to be more stable than the infinite flat plane.[30] Therefore as analogy to graphite, g-C_3N_4 nanosheets were composed of a variety of multilayers, which still enabled a thin vertical thickness and a large surface area, as revealed in the nitrogen adsorption desorption data below.

The average C/N molar ratio was revealed as 1.09 and 1.00 for g-C_3N_4 powders and g-C_3N_4 nanosheets respectively. The theoretical C/N ratio of the ideally crystallized g-C_3N_4 is 0.75. However, due to the incomplete condensation, the C/N ratio of g-C_3N_4 product is often slightly lower than 0.75, indicating a partially polymerised structure.[19-20] Nevertheless, the similar C/N ratios between g-C_3N_4 powders and g-C_3N_4 nanosheets samples represent the elemental composition was not affected by exfoliation.

Table 5.1 C/N atomic ratio of g-C_3N_4 bulk powders and g-C_3N_4 nanosheets measured by EDS analysis.

Samples	C/N atomic ratio
g-C_3N_4 bulk powders	1.09
g-C_3N_4 nanosheets	1.00

5.3.1.2 ATR-IR spectra of g-C_3N_4 materials

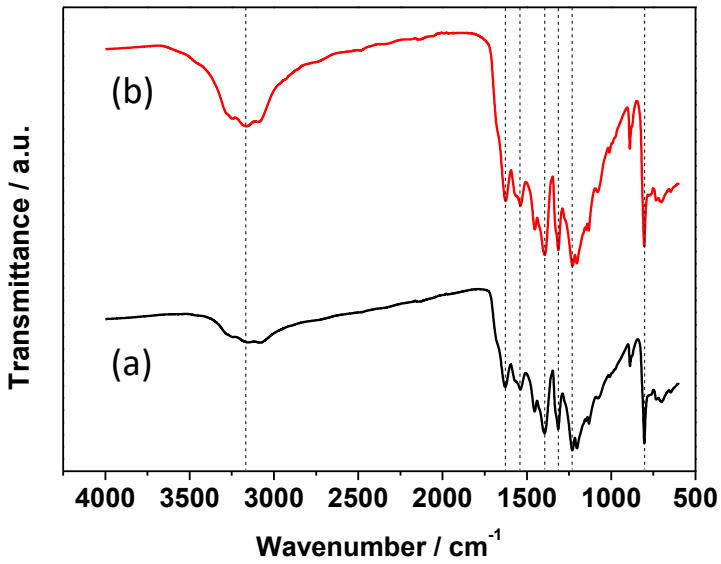

Figure 5.2 ATR-IR spectra of g-C_3N_4 bulk powders (a) and g-C_3N_4 nanosheets (b).

The IR spectra of g-C_3N_4 powder and g-C_3N_4 nanosheets are presented in Figure 5.2 displaying various signs of typical stretching modes of CN heterocycles.[31] For example, the IR absorption bands at 1628 cm^{-1} and 1539 cm^{-1} originate from the C=N bonding of the melem structure. Other signals at 1395 cm^{-1}, 1314 cm^{-1} and 1231 cm^{-1} are attributed to C-N bonding of aromatic secondary and tertiary amines. The strong peak at 804 cm^{-1} represents the characteristic breathing mode of tri-s-triazine units, which confirms the basic building block of the graphitic network of g-C_3N_4 materials. Meanwhile the broad band at 3000-3500 cm^{-1} was also observed which is indicative of the uncondensed terminal amino groups (-NH_2 or =NH groups) on the conjugated framework due to incomplete deamination. Overall, the FTIR results are in good accordance with precious reports of g-C_3N_4 materials prepared by thermal polymerization method, and affirm the identical chemical state of g-C_3N_4 powder and g-C_3N_4 nanosheets.

5.3.1.3 Nitrogen sorption isotherms of g-C_3N_4 materials

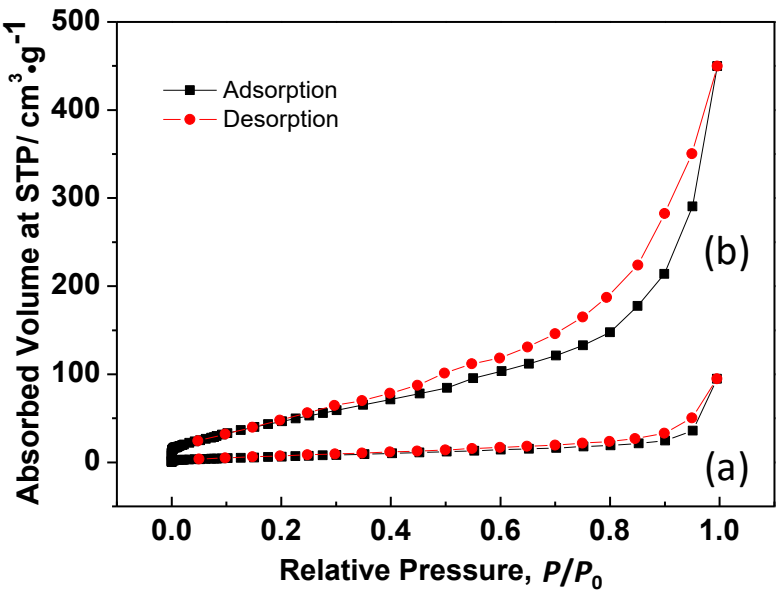

Figure 5.3 Nitrogen sorption isotherms of g-C_3N_4 bulk powders (a) and g-C_3N_4 nanosheets (b).

A Type IV shape with H3 hysteresis was found in the nitrogen sorption isotherms of both samples. The specific surface area value (S_{BET}) was derived by the application of the BET approach on the adsorption branch which was determined as 25.66 $m^2 \cdot g^{-1}$ for the bulk powders, in line with the reference value between 5-30 $m^2 \cdot g^{-1}$ depending on the exact calcination temperature. After exfoliation, a dramatic rise in surface area was observed, over 8 times to 209.2 $m^2 \cdot g^{-1}$ for g-C_3N_4 nanosheets as well as a larger pore volume from the increased interparticle space due to smaller particle size. For nanostructural semiconductor, the enlarged surface area is greatly advantageous for promoting surface photo-redox reactions by providing more reactive sites and shortened migration distance for photoexcited charge carriers.

Table 5.2 Textual properties of g-C_3N_4 bulk powders and g-C_3N_4 nanosheets

Samples	S_{BET} / $m^2 \cdot g^{-1}$	V_{pore} / $cm^3 \cdot g^{-1}$
g-C_3N_4 bulk powders	25.66	0.14
g-C_3N_4 nanosheets	209.2	0.68

5.3.1.4 Thermal gravimetric analysis of g-C_3N_4 materials

Through thermal gravimetric analysis, the exfoliated nature of g-C_3N_4 nanosheets was further revealed. As shown in Figure 5.4A, g-C_3N_4 powders started to lose weight slowly at 490˚C due to the condensation of terminal amino groups and distortion of the graphitic network. These phase transformation and degradation processes developed rapidly as the temperature was further elevated, resulting in a sharp drop of the TG curve accompanied by an intense endothermic DSC peak maximized at 742˚C. In contrast, the g-C_3N_4 nanosheets sample shows less thermal resistance than the parent powders against the ramping temperature as seen in Figure 5.4B. Although the mass loss occurred at the same temperature level as the powders, the degradation of carbon nitride evidently progressed at a much faster rate due to its higher surface area and less ordered structure, with the DSC curve peaked at 683˚C. The whole temperature range

was 490˚C-700˚C for g-C_3N_4 nanosheets, 65˚C short of the 490˚C-765˚C for the bulk counterpart due to the finer physical dimensions and less defined stacking order of nanosheets.

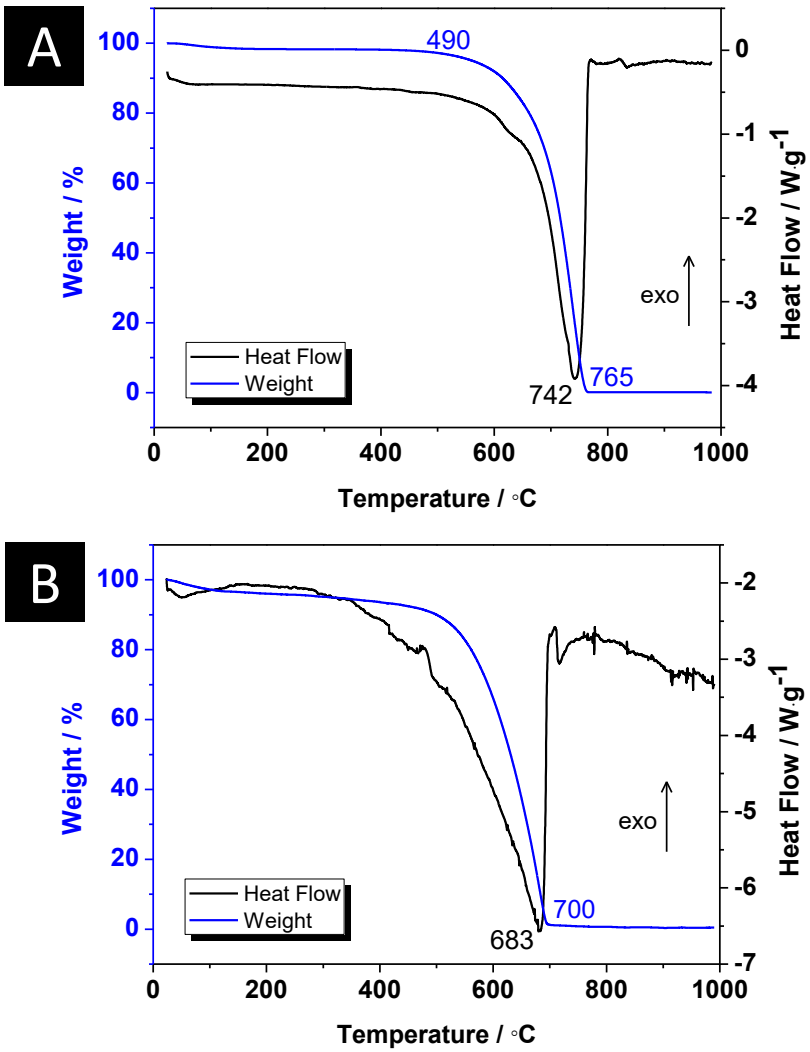

Figure 5.4 TGA-DSC curves of g-C_3N_4 bulk powders (A) and g-C_3N_4 nanosheets (B).

5.3.1.5 UV-Vis absorption spectra of g-C_3N_4 materials

As exhibited in the UV-Vis absorption spectra in Figure 5.5, both g-C_3N_4 samples show a broad visible light absorption with a absorption maximum at 322 nm, 311 nm for g-C_3N_4 powders and g-C_3N_4 nanosheets, respectively. As a consequence of the quantum confinement effect of semiconductor materials, the nanosheet sample with smaller in-

plane size and vertical thickness after ultrasound treatment has a widened CB/VB energy gap than the bulk material, by shifting conduction and valence bands in opposite directions which can contribute to a stronger redox ability of the photon-induced e^-/h^+ thus improving the photocatalytic activity in redox reactions.

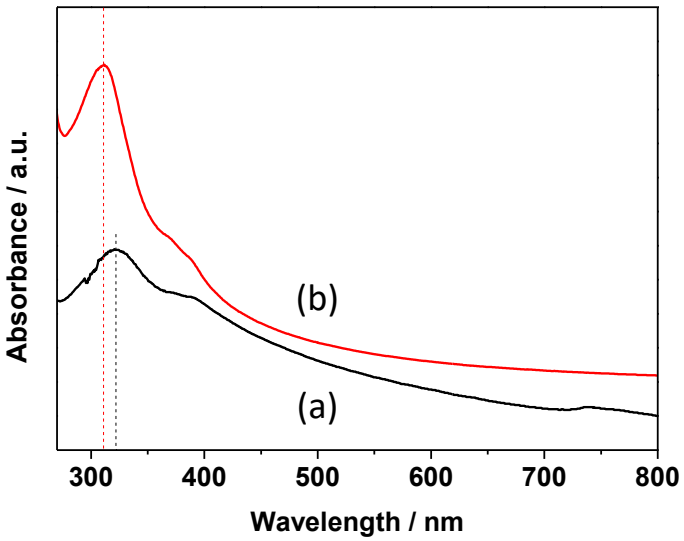

Figure 5.5 UV-Vis absorption spectra of g-C_3N_4 bulk powders (a) and g-C_3N_4 nanosheets (b).

5.3.1.6 Photoluminescence spectra of g-C_3N_4 materials

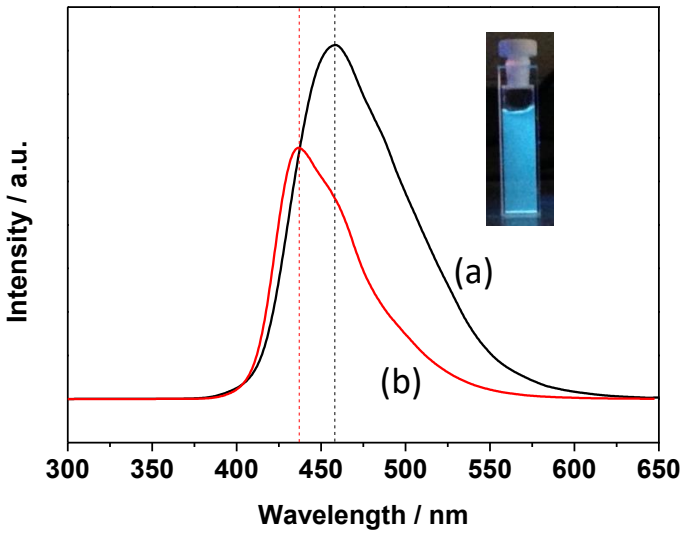

Figure 5.6 Photoluminescence spectra of g-C_3N_4 bulk powders (a) and g-C_3N_4 nanosheets (b). Inset is the photograph of aqueously dispersed g-C_3N_4 nanosheets under the irradiation of 365 nm UV lamp, emitting blue luminescence at room temperature.

In agreement with the UV-Vis absorption data above, the emission peak position of g-C_3N_4 nanosheets also shifted downwards to the lower wavelength side, from 458 nm of bulk powders to 437 nm, as featured in Figure 5.6. Likewise, the blue shift phenomenon is also the result of quantum confinement effect due to the reduction of crystal size after exfoliation.

5.3.1.7 Fluorescence quantum yield of g-C_3N_4 materials

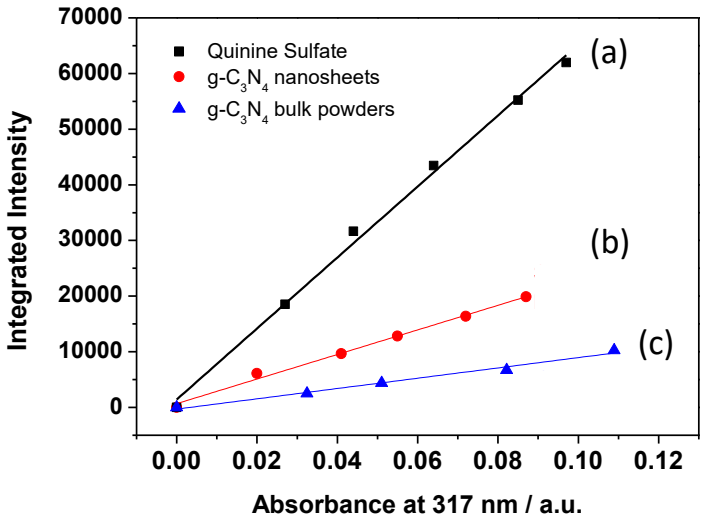

Figure 5.7 The gradients of integrated emission intensity versus the absorbance of UV-Vis absorption at 317 nm for (a) quinine sulfate standard (λ_{Em} = 449 nm), (b) g-C_3N_4 nanosheets (λ_{Em} = 437 nm) and (c) g-C_3N_4 bulk powders (λ_{Em} = 458 nm).

Table 5.3 The fluorescence quantum yield data of quinine sulfate, g-C_3N_4 bulk powders and g-C_3N_4 nanosheets.

	Slope	**Refractive index**	**Quantum yield**
Quinine sulfate	6.38×10^5	1.33	54.0%
g-C_3N_4 bulk powders	9.25×10^4	1.36	8.19%
g-C_3N_4 nanosheets	2.21×10^5	1.33	18.7%

The respective ϕ_F value for g-C_3N_4 nanosheets and g-C_3N_4 bulk powders were calculated by measuring the integrated fluorescence intensity in aqueous dispersed g-C_3N_4 nanosheets and g-C_3N_4 powders in ethanol against quinine sulfate in 0.1M H_2SO_4 aq solution. As shown in Figure 5.7, each series of the data points were linearly fitted and the fitted slopes were listed in Table 5.3 as well as the quantum yield values calculated by Equation 2.5. As displayed, the ϕ_F value of g-C_3N_4 nanosheets was profoundly improved to 18.7%, in agreement with the DFT calculation results published by other researchers in which the g-C_3N_4 nanosheets shows an clear increase of the density of states (DOS) with respect to the bulk material on its conduction band which enables improved photoresponsivity.[25]

5.3.1.8 Photocatalytic activities of g-C_3N_4 materials in dye degradation

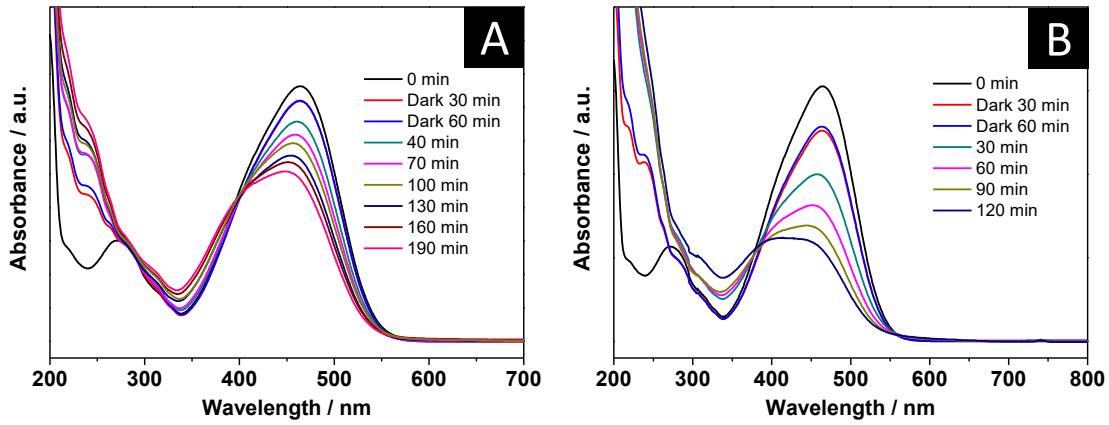

Figure 5.8 UV-Vis absorption spectra of MO solution (15 mL, 30 µM) before and after adding 45 mg g-C_3N_4 powders (A) and 45 mg g-C_3N_4 nanosheets (B) as a function of degradation time under visible light irradiation. Before irradiation, the reaction system was stirred in the dark for 60 min.

Figure 5.8 showed the variation of MO absorbance as a function of degradation time in the presence of g-C_3N_4 powders (A) and g-C_3N_4 nanosheets (B) under visible light irradiation. The peak intensity at 464 nm was gradually reduced and its position was observably shifted to the lower wavelength range representing the continuous attack upon the molecular structure of organic dyes and eventually degraded into CO_2 and H_2O

by oxidative species driven by the photon-induced e^-/h^+ charges produced on the conduction and valence band of g-C_3N_4 materials after photon absorption.[31-32] Since g-C_3N_4 is chemically inert and stable in aqueous dye solution, no absorption peaks around 246 nm from sulfanilic acid or dimethyl-4-phenylenediamine were detected during the photodegradation processes, reflecting different photocatalytic behaviours between g-C_3N_4 nanosheets and H-terminated mesoporous silicon studied in the previous chapter where MO was also decomposed chemically by the reductive silicon hydrides of mpSi into fragment compounds, as discovered in Chapter 4.

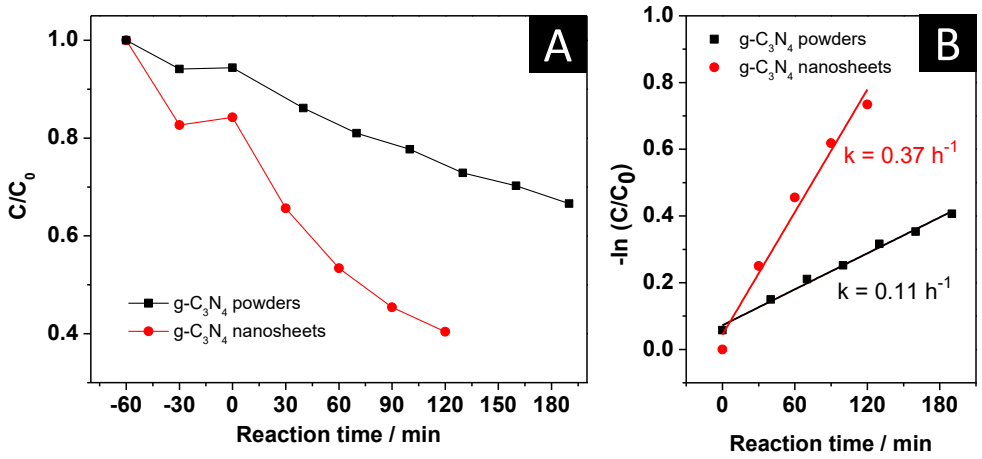

Figure 5.9 The degradation rates (A) and first order kinetics (B) of MO degradation over g-C_3N_4 powders (square) and g-C_3N_4 nanosheets (circle) under visible light irradiation. Before irradiation, the reaction system was stirred in the dark for 60 min.

Figure 5.9 displays the degradation rate of MO degradation with g-C_3N_4 powders and g-C_3N_4 nanosheets and the respective rate constant derived from the UV-Vis absorption data. As shown, the apparent 1st order rate constant (k) was 0.37 h^{-1} for g-C_3N_4 nanosheets, clearly more photo-catalytically efficient than the parent powders (k = 0.11 h^{-1}), despite the higher fluorescence quantum yield as revealed above. The significance of available surface area is also shown in the varied percentages of physically absorbed dye molecules after stirred rigorously in the dark for 60 min before carrying out the photocatalytic reaction, which was 15.8% by g-C_3N_4 nanosheets at equilibrium, and merely 5.4% by g-C_3N_4 bulk powders due to the limited surface area, 25.66 $m^2 \cdot g^{-1}$ as shown in Table 5.2.

5.3.2 Photocatalytic activities of mpSi/g-C_3N_4 composites in dye degradation

Free standing H-terminated mesoporous silicon (mpSi), HPS-200-05-F sample was hybridized with g-C_3N_4 nanosheets as characterised above via impregnation to form mpSi/g-C_3N_4 NSs composites (mpSi/g-C_3N_4-S1, mpSi/g-C_3N_4-S2, mpSi/g-C_3N_4-S3) with various weight ratios as *m*(mpSi): *m*(g-C_3N_4 NSs) = 4:1, 1:1 and 1:4 respectively. Since the amount of photocatalyst used per unit of MO solution was decreased to about 6.67 g·mol^{-1}, the photocatalytic rate constant of g-C_3N_4 NSs was thus reduced to 0.04 h^{-1} in this set of experiments.

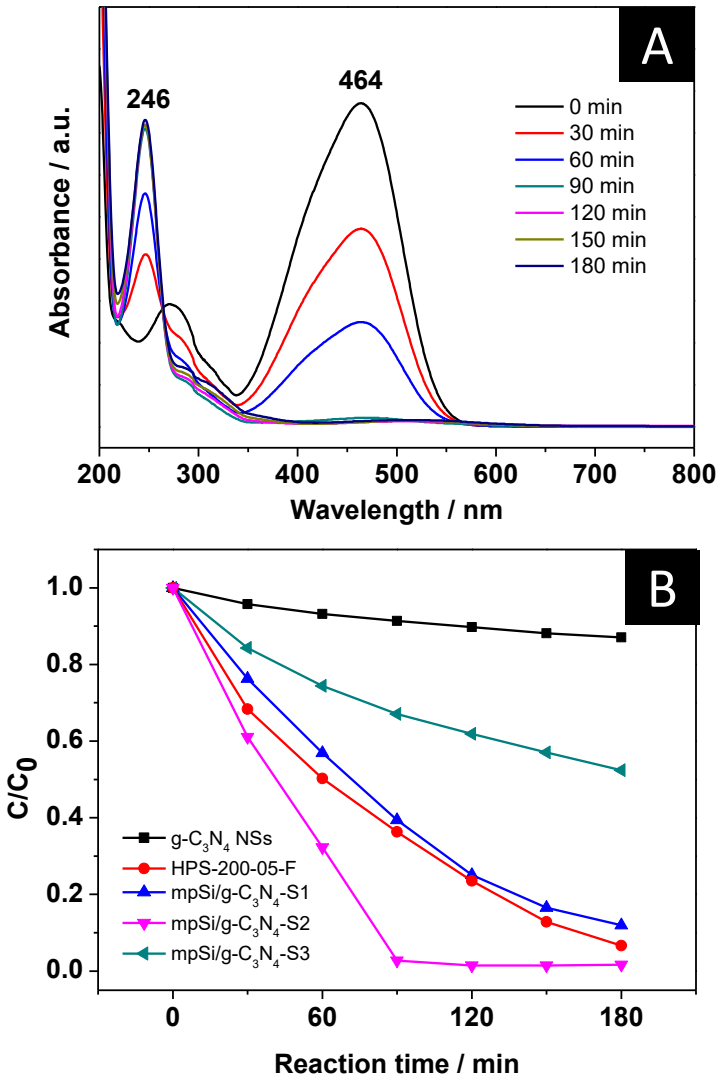

Figure 5.10 A: UV-Vis absorption spectra of MO solution before and after adding mpSi/g-C_3N_4-S2 as a function of degradation time under visible light illumination; B: MO degradation rates over HPS-200-05-F, g-C_3N_4 nanosheets, and mpSi/g-C_3N_4 NSs composites (S1, S2, S3) under visible light irradiation.

As shown in Figure 5.10A, the 464 nm peak intensity of MO decreased rapidly over mpSi/g-C_3N_4-S2 sample and completely decayed after 90 min while ~40% of the initial amount of organic molecules were still unreacted in the dye solution of mpSi under similar conditions. As found from the previous chapter, the fast rate of MO disappearance over irradiated mpSi material is a combined result of charge-driven photocatalysis and surface hydride-involved reduction. Likewise, the appearance and growth of the absorption band at 247 nm during MO degradation was also presented here in the study of mpSi/g-C_3N_4-S2, indicating a similar behavioural pattern of the composite in MO photodecomposition.

As further disclosed in Figure 5.10B, the activity of mpSi/g-C_3N_4 NSs composites in MO decomposition was varied to a large extent corresponding to the weight ratio between mpSi and g-C_3N_4 NSs components. By adding increasing amounts of mpSi into the composite structure, the degradation rate of mpSi/g-C_3N_4-S1 with 4:1 weight ratio was revealed to be similar to mpSi itself. Whereas the performance of mpSi/g-C_3N_4-S3 was significantly inhibited by the very high compositional ratio of g-C_3N_4 NSs.

According to the reported band structure of g-C_3N_4, the CB and VB band positions of g-C_3N_4 appear at -1.12 V and 1.58 V, respectively with a 2.7 eV energy gap.[33-35] As well as the band positions of mpSi (HPS-200-05) revealed in Chapter 4 as -0.75 V and 1.30 V, the band alignment of mpSi/g-C_3N_4 NSs heterojunction is drawn in Figure 5.11.

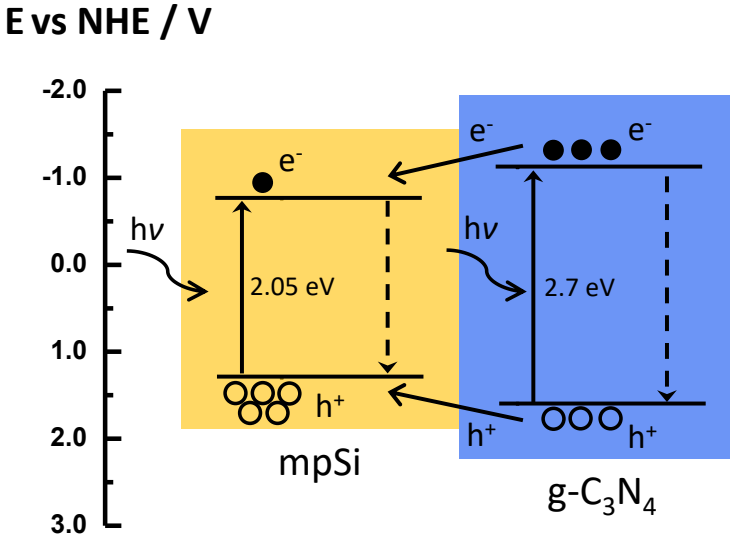

Figure 5.11 Band diagram of mpSi/g-C_3N_4 heterojunction.

As shown the semiconductor composite is defined as a Type I straddling heterostructure,[36] in which the photogenerated electrons and holes would mainly accumulate on the conduction and valence band of one component, mpSi in this case as the charge acceptor which would gain the energy. As found in Chapter 4, the reductive capability of Si-H bond of mpSi in converting MO appeared to be accelerated under visible light irradiation through the proposed exciton-related mechanism as Si-H is known as electron deficient and hence has the tendency to extract free electrons. Since mpSi is a p-type semiconducting system with excess hole supply in the valence band, the flow of photoexcited electrons may occur more frequently to the conduction band of g-C_3N_4 to mpSi and is likely to be promoted by the above mentioned stimulation effect on the hydrogen transfer process, eventually resulting in the fast disappearance of MO molecules in the presence of mpSi/g-C_3N_4 NSs as shown here. According to the electronic structure of g-C_3N_4 revealed in the DFT calculations, the valence and conduction bands of g-C_3N_4 are mainly composed of the nitrogen p_z orbitals and carbon p_Z orbitals, respectively.[16] Thus to be more specific, the charge transfer in the heterostructure is proposed to go through the C atom of g-C_3N_4 component to the surface hydrides (SiH_x) of mpSi material.

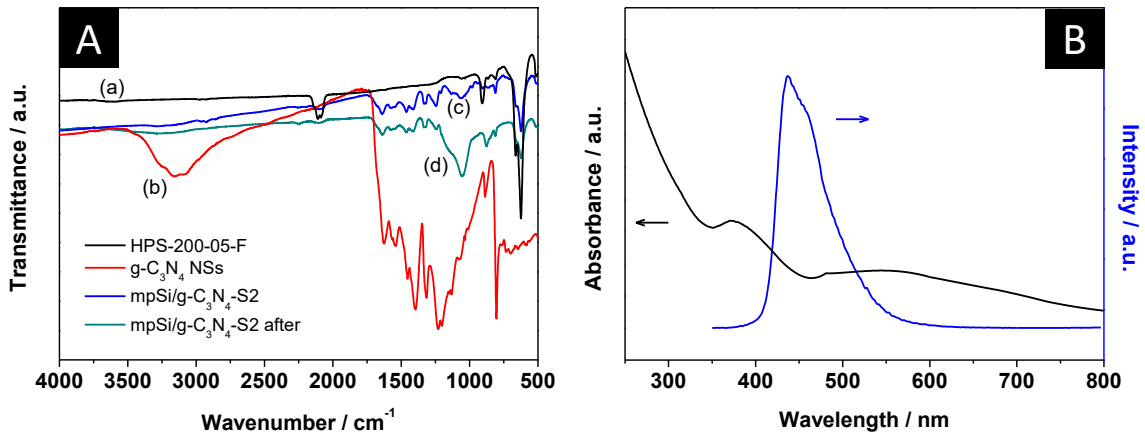

Figure 5.12 A: ATR-IR spectra of HPS-200-05-F (a), g-C_3N_4 NSs (b), mpSi/g-C_3N_4-S2 before (c) and after (d) MO degradation; B: UV-Vis absorption and emission spectra of mpSi/g-C_3N_4-S2.

Table 5.4 IR absorption wavenumbers of C=N, C-N stretching vibrations and the breathing mode of tri-s-triazine ring of g-C_3N_4 bulk powders, g-C_3N_4 nanosheets and mpSi/g- C_3N_4 composite.

	g-C_3N_4 bulk powders	**g-C_3N_4 nanosheets**	**mpSi/ g-C_3N_4-S2**
$\varpi_{C=N}$ / cm^{-1}	1628	1626	1639
	1539	1539	1545
ϖ_{C-N} / cm^{-1}	1395	1394	1411
	1314	1314	1321
	1231	1230	1246
$\varpi_{breathing}$ / cm^{-1}	804	804	811

As shown in Figure 5.12A, the FTIR spectra of mpSi/g-C_3N_4-S2 before and after photocatalytic evaluation were recorded which exhibited characteristic IR signals from both semiconductor components, confirming the existence of mesoporous silicon and g-C_3N_4 in the composite which was also consistent through the degradation reaction and catalyst recycling. Interestingly, the various IR peak positions of g-C_3N_4 NSs were all blueshifted after being hybridized with mpSi, which is unlikely to be related to the exfoliated nature of g-C_3N_4 NSs. As we can see, the IR bands of g-C_3N_4 NSs and bulk powders were all situated in identical positions in Table 5.4.

In addition, a new UV-Vis band at 550 nm also emerged in the absorption spectrum of mpSi/g-C_3N_4-S2 (Figure 5.12B). As featured, the 376 nm signal is commonly observed in g-C_3N_4 synthesis and derived from the π-π* transition of the aromatic system. However, the 550 nm peak induced by n-π* transition is rarely seen in the characterisation of g-C_3N_4 as this electronic excitation is intrinsically forbidden by symmetry but can be activated by structural distortion, especially in-plane distortion to the 2D flat morphology.[37-38] For example, the buckled configuration of g-C_3N_4 monolayer or multilayer was reported to have increased spectral response in the visible region for photon absorption and enhanced photocatalytic activity in H_2 generation due to this distinct optical feature.[39]

Thus, as suggested by the above results, some valuable insights into the coupling effects of mpSi and g-C_3N_4 NSs semiconductors were provided of which some influences had been shown on the bonding environment and structural morphology of g-C_3N_4 component, leading to the optical variations of g-C_3N_4 nanosheets. Although the nature of the interfacial interaction between mpSi and g-C_3N_4 NSs in the composite is still not yet clear in this stage. It can be better elucidated in the future with more detailed characterisation results and in-depth investigation of the physical, chemical and electronic effects on the photocatalytic behaviours of the coupled material.

5.4 Summary

In this chapter, photoactive hydrogen-terminated mesoporous silicon (mpSi) and graphitic carbon nitride nanosheets (g-C_3N_4 NSs) were coupled into mpSi/g-C_3N_4 NSs composite via impregnation, which presented an enhanced degradation capability toward methyl orange under visible light irradiation. Since both components can be facilely prepared from low cost, earth abundant raw materials, mpSi/g-C_3N_4 NSs heterojunction is very promising as a metal-free, visible light responsive candidate in utilizing the renewable solar energy on a large scale. On one hand, the large surface area and accessible porous system of mesoporous silicon fabricated via electrochemical etching facilitated the diffusion of reactants and products. Its widened optical bandgap and well-defined crystal structure also enhanced the visible light absorption and lifetime of photoinduced charge carriers. Meanwhile, the large surface area and small vertical thickness possessed by g-C_3N_4 nanosheets also promoted the absorption of reactants and reduced the charge migration distance. On the other hand, some synergistic effects on the photocatalytic behaviour of the heterojunction are reasonably expected as indicated in our preliminary results, which have shown stimulated activity of hydrogen termination on mesoporous silicon surface and n-π^* electronic transition mode of g-C_3N_4 in the composite, although the nature of the electronic/physiochemical interaction still remains largely unknown and will be the subject of future exploration.

5.5 References

1. Geim, A. K.; Novoselov, K. S., The rise of graphene. *Nat. Mater.* **2007,** *6* (3), 183-191.

2. Rao, C. N.; Sood, A. K.; Subrahmanyam, K. S.; Govindaraj, A., Graphene: the new two-dimensional nanomaterial. *Angew. Chem. Int. Ed. Engl.* **2009,** *48* (42), 7752-7777.

3. Zhang, N.; Zhang, Y.; Xu, Y. J., Recent progress on graphene-based photocatalysts: current status and future perspectives. *Nanoscale* **2012,** *4* (19), 5792-5813.

4. Hinnemann, B.; Moses, P. G.; Bonde, J.; Jorgensen, K. P.; Nielsen, J. H.; Horch, S.; Chorkendorff, I.; Norskov, J. K., Biomimetic hydrogen evolution: MoS_2 nanoparticles as catalyst for hydrogen evolution. *J. Am. Chem. Soc.* **2005,** *127* (15), 5308-5309.

5. Jaramillo, T. F.; Jorgensen, K. P.; Bonde, J.; Nielsen, J. H.; Horch, S.; Chorkendorff, I., Identification of active edge sites for electrochemical H_2 evolution from MoS_2 nanocatalysts. *Science* **2007,** *317* (5834), 100-102.

6. Gao, M. R.; Xu, Y. F.; Jiang, J.; Yu, S. H., Nanostructured metal chalcogenides: synthesis, modification, and applications in energy conversion and storage devices. *Chem. Soc. Rev.* **2013,** *42* (7), 2986-3017.

7. Golberg, D.; Bando, Y.; Huang, Y.; Terao, T.; Mitome, M.; Tang, C.; Zhi, C., Boron nitride nanotubes and nanosheets. *ACS Nano* **2010,** *4* (6), 2979-2993.

8. Bhimanapati, G. R.; Lin, Z.; Meunier, V.; Jung, Y.; Cha, J.; Das, S.; Xiao, D.; Son, Y.; Strano, M. S.; Cooper, V. R.; Liang, L.; Louie, S. G.; Ringe, E.; Zhou, W.; Kim, S. S.; Naik, R. R.; Sumpter, B. G.; Terrones, H.; Xia, F.; Wang, Y.; Zhu, J.; Akinwande, D.; Alem, N.; Schuller, J. A.; Schaak, R. E.; Terrones, M.; Robinson, J. A., Recent advances in two-dimensional materials beyond graphene. *ACS Nano* **2015,** *9* (12), 11509-11539.

9. Ong, W.-J.; Tan, L.-L.; Ng, Y. H.; Yong, S.-T.; Chai, S.-P., Graphitic carbon nitride ($g\text{-}C_3N_4$)-based photocatalysts for artificial photosynthesis and environmental remediation: are we a step closer to achieving sustainability? *Chem. Rev.* **2016,** *116* (12), 7159-7329.

10. Thomas, A.; Fischer, A.; Goettmann, F.; Antonietti, M.; Müller, J.-O.; Schlögl, R.; Carlsson, J. M., Graphitic carbon nitride materials: variation of structure and morphology and their use as metal-free catalysts. *J. Mater. Chem.* **2008,** *18* (41), 4893-4908.

11. Lam, S. M.; Sin, J. C.; Mohamed, A. R., A review on photocatalytic application of g-C_3N_4/semiconductor (CNS) nanocomposites towards the erasure of dyeing wastewater. *Mater. Sci. Semicond. Process.* **2016,** *47*, 62-84.

12. Liu, J.; Wang, H.; Antonietti, M., Graphitic carbon nitride "reloaded": emerging applications beyond (photo)catalysis. *Chem. Soc. Rev.* **2016,** *45* (8), 2308-2326.

13. Mamba, G.; Mishra, A. K., Graphitic carbon nitride (g-C_3N_4) nanocomposites: a new and exciting generation of visible light driven photocatalysts for environmental pollution remediation. *Appl. Catal. B* **2016,** *198*, 347-377.

14. Feng, L.; He, F.; Yang, G.; Gai, S.; Dai, Y.; Li, C.; Yang, P., NIR-driven graphitic-phase carbon nitride nanosheets for efficient bioimaging and photodynamic therapy. *J. Mater. Chem. B* **2016,** *4* (48), 8000-8008.

15. Liu, J.-W.; Luo, Y.; Wang, Y.-M.; Duan, L.-Y.; Jiang, J.-H.; Yu, R.-Q., Graphitic carbon nitride nanosheets-based ratiometric fluorescent probe for highly sensitive detection of H_2O_2 and glucose. *ACS Appl. Mater. Interfaces* **2016,** *8* (49), 33439-33445.

16. Wang, X.; Maeda, K.; Thomas, A.; Takanabe, K.; Xin, G.; Carlsson, J. M.; Domen, K.; Antonietti, M., A metal-free polymeric photocatalyst for hydrogen production from water under visible light. *Nat. Mater.* **2009,** *8* (1), 76-80.

17. Liang, Q.; Li, Z.; Huang, Z. H.; Kang, F.; Yang, Q. H., Holey graphitic carbon nitride nanosheets with carbon vacancies for highly improved photocatalytic hydrogen production. *Adv. Funct. Mater.* **2015,** *25* (44), 6885-6892.

18. Xu, J.; Shang, J.-K.; Jiang, Q.; Wang, Y.; Li, Y.-X., Facile alkali-assisted synthesis of g-C_3N_4 materials and their high-performance catalytic application in solvent-free cycloaddition of CO_2 to epoxides. *RSC Adv.* **2016,** *6* (60), 55382-55392.

19. Niu, P.; Zhang, L.; Liu, G.; Cheng, H.-M., Graphene-like carbon nitride nanosheets for improved photocatalytic activities. *Adv. Funct. Mater.* **2012,** *22* (22), 4763-4770.

20. Qiu, P.; Chen, H.; Xu, C.; Zhou, N.; Jiang, F.; Wang, X.; Fu, Y., Fabrication of an exfoliated graphitic carbon nitride as a highly active visible light photocatalyst. *J. Mater. Chem. A* **2015,** *3* (48), 24237-24244.

21. Han, Q.; Wang, B.; Gao, J.; Cheng, Z.; Zhao, Y.; Zhang, Z.; Qu, L., Atomically thin mesoporous nanomesh of graphitic C_3N_4 for high-efficiency photocatalytic hydrogen evolution. *ACS Nano* **2016,** *10* (2), 2745-2751.

22. Chen, L.; Huang, D.; Ren, S.; Dong, T.; Chi, Y.; Chen, G., Preparation of graphite-like carbon nitride nanoflake film with strong fluorescent and electrochemiluminescent activity. *Nanoscale* **2013,** *5* (1), 225-230.

23. Xu, J.; Zhang, L.; Shi, R.; Zhu, Y., Chemical exfoliation of graphitic carbon nitride for efficient heterogeneous photocatalysis. *J. Mater. Chem. A* **2013,** *1* (46), 14766-14772.

24. Shi, L.; Chang, K.; Zhang, H.; Hai, X.; Yang, L.; Wang, T.; Ye, J., Drastic enhancement of photocatalytic activities over phosphoric acid protonated porous g-C_3N_4 nanosheets under visible light. *Small* **2016,** *12* (32), 4431-4439.

25. Zhang, X.; Xie, X.; Wang, H.; Zhang, J.; Pan, B.; Xie, Y., Enhanced photoresponsive ultrathin graphitic-phase C_3N_4 nanosheets for bioimaging. *J. Am. Chem. Soc.* **2013,** *135* (1), 18-21.

26. Han, Q.; Hu, C.; Zhao, F.; Zhang, Z.; Chen, N.; Qu, L., One-step preparation of iodine-doped graphitic carbon nitride nanosheets as efficient photocatalysts for visible light water splitting. *J. Mater. Chem. A* **2015,** *3* (8), 4612-4619.

27. Han, Q.; Zhao, F.; Hu, C. G.; Lv, L. X.; Zhang, Z. P.; Chen, N.; Qu, L. T., Facile production of ultrathin graphitic carbon nitride nanoplatelets for efficient visible-light water splitting. *Nano Res.* **2015,** *8* (5), 1718-1728.

28. Zhu, K. X.; Wang, W. J.; Meng, A.; Zhao, M.; Wang, J. H.; Zhao, M.; Zhang, D. L.; Jia, Y. P.; Xu, C. H.; Li, Z. J., Mechanically exfoliated g-C_3N_4 thin nanosheets by ball milling as high performance photocatalysts. *RSC Adv.* **2015,** *5* (69), 56239-56243.

29. Zhang, J.; Chen, Y.; Wang, X., Two-dimensional covalent carbon nitride nanosheets: synthesis, functionalization, and applications. *Energy Environ. Sci.* **2015,** *8* (11), 3092-3108.

30. Carlsson, J. M., Graphene: buckle or break. *Nat. Mater.* **2007,** *6* (11), 801-802.

31. Yan, S. C.; Li, Z. S.; Zou, Z. G., Photodegradation performance of g-C_3N_4 fabricated by directly heating melamine. *Langmuir* **2009,** *25* (17), 10397-10401.

32. Sun, L.; Yang, M.; Huang, J.; Yu, D.; Hong, W.; Chen, X., Freestanding graphitic carbon nitride photonic crystals for enhanced photocatalysis. *Adv. Funct. Mater.* **2016,** *26* (27), 4943-4950.

33. Peng, B.; Zhang, S.; Yang, S.; Wang, H.; Yu, H.; Zhang, S.; Peng, F., Synthesis and characterization of g-C_3N_4/Cu_2O composite catalyst with enhanced photocatalytic activity under visible light irradiation. *Mater. Res. Bull.* **2014,** *56*, 19-24.

34. Xu, H.; Gan, Z.; Zhou, W.; Ding, Z.; Zhang, X., A metal-free 3C-SiC/g-C_3N_4 composite with enhanced visible light photocatalytic activity. *RSC Adv.* **2017,** *7* (63), 40028-40033.

35. Jiang, W.; Luo, W.; Wang, J.; Zhang, M.; Zhu, Y., Enhancement of catalytic activity and oxidative ability for graphitic carbon nitride. *J. Photochem. Photobiol. C: Photochem. Rev.* **2016,** *28*, 87-115.

36. Selinsky, R. S.; Ding, Q.; Faber, M. S.; Wright, J. C.; Jin, S., Quantum dot nanoscale heterostructures for solar energy conversion. *Chem. Soc. Rev.* **2013,** *42* (7), 2963-2985.

37. Li, Y.; Zhang, J.; Wang, Q.; Jin, Y.; Huang, D.; Cui, Q.; Zou, G., Nitrogen-rich carbon nitride hollow vessels: synthesis, characterization, and their properties. *J. Phys. Chem. B* **2010,** *114* (29), 9429-9434.

38. Jorge, A. B.; Martin, D. J.; Dhanoa, M. T. S.; Rahman, A. S.; Makwana, N.; Tang, J.; Sella, A.; Corà, F.; Firth, S.; Darr, J. A.; McMillan, P. F., H_2 and O_2 evolution from water half-splitting reactions by graphitic carbon nitride materials. *J. Phys. Chem. C* **2013,** *117* (14), 7178-7185.

39. Chen, Y.; Wang, B.; Lin, S.; Zhang, Y.; Wang, X., Activation of n → π* transitions in two-dimensional conjugated polymers for visible light photocatalysis. *J. Phys. Chem. C* **2014,** *118* (51), 29981-29989.

Chapter 6

Conclusions and Future Work

Abstract

In this chapter, the aim of the research described in the thesis is outlined. The main conclusions are summarized and proposals for future work indicated by this research are suggested.

6.1 Conclusions

Aiming for utilizing the abundant solar energy efficiently and cost-effectively, this thesis was focused on the study of silicon and silicon-based semiconducting systems, which are known as low-cost, earth-abundant, metal-free and eco-friendly, potentially useful in resolving various global challenges we're facing with such as water pollution.

Mesoporous silicon (mpSi) was facilely prepared by galvanostatic anodization which created a Si-based open mesoporous system with a large accessible surface area to promote mass diffusion and charge transfer in liquid phase photoreactions. In general, two different structural morphologies were constructed within the Si crystalline matrix: an interconnected porous network and an orderly aligned meso-channel array. Despite the distinct differences in pore properties, several common similarities were also shared including the hydrogen terminations and abundant Si nanocrystallites on the surface. By taking advantage of the surface hydrides, thiol-capped mesoporous silicon with allyl mercaptan was synthesised successfully under microwave field within a significantly shortened reaction time.

By tuning the etching conditions, a variety of structural properties (layer thickness, crystallinity, surface area, pore size distribution and Si nanocrystal sizes) of as-etched mpSi material were correspondingly modified. As found, the resulting Si structure was dominantly affected by the etching current density applied in the fabrication process. As etching current density increased, it was rendered with higher specific surface area, larger pore volume and pore size, and smaller nanocrystalline Si particles. The effect of etching duration was comparatively moderate as the surface area slightly increased after longer immersion time in the etchant due to the occurrence of chemical dissolution.

As a result of the high surface area, framework crystallinity and abundant surface hydrides, hydrogen-terminated mesoporous Si channel array with ordered pore alignment and large pore size showed an excellent activity in degrading methyl orange (MO) under visible light irradiation. Its widened bandgap induced by the quantum confinement effect of the constituted Si nanocrystallites endowed a broad absorption of visible light range photons. While the less efficient performance of the interconnected

porous network in MO photodegradation was largely caused by its poor crystallinity, lower electrical conductivity and higher oxidation tendency resulting in faster recombination rate of photoexcited electrons (e-) and holes (h^+), as well as by the branched, narrower mesopores that were not as effective in enhancing the access to the vast internal surface as the ordered channels. By further improving the visible light responsiveness and surface availability of the meso-channel array, MO decomposition over free-standing mpSi microparticles was further accelerated with 88% of the initial efficacy remained after 10 cycles of photoreactions.

Hydrogen termination on the surface of mesoporous silicon was revealed to be a prominent factor in destroying the molecular structure of MO by reducing its azo linkage which was also the main responsible process occurred in the dark for MO decomposition over mpSi. This degradation pathway was further promoted by enhancing the reduction activity of the surface hydrides species under visible light irradiation of which the underlying mechanism is assumed to be related to the localized excitons at Si-H sites. In addition, photo-oxidation of MO was also initiated and proceeded simultaneously, driven by the reactive oxygen species (ROSs), primarily superoxide radical anions ($\cdot O_2^-$) formed in the conduction band of mpSi. Upon irradiation, mpSi absorbed supra-bandgap incident photons and generated photoexcited e^- and h^+ in its conduction band and valence band. The conduction band electrons then transferred to the interface and reduced dissolved O_2 into $\cdot O_2^-$. In this process, surface Si-H bond is also critically important as it prevented the undesired e^-/h^+ recombination by trapping the photoinduced e^-. As a result of the competing degradation pathway mentioned earlier, the photo-oxidation capability of mpSi gradually declined.

An enhanced visible-light-driven photo-reduction of MO was achieved by combining mesoporous silicon with graphitic carbon nitride nanosheets (g-C_3N_4 NSs). As indicated by the Type-I heterojunction structure of the semiconductor composite, the reductive capability of Si-H bonds in mpSi was likely promoted in the presence of g-C_3N_4 NSs, because of an excess of photoinduced e^- on the conduction band of mpSi donated from the higher conduction band of g-C_3N_4 component, which eventually led to a faster degradation rate against MO molecules according to the exciton-related mechanism.

In this thesis, the microscopic structural characteristics of mesoporous silicon prepared by electrochemical etching have been examined thoroughly which can provide a useful guide in the applications of porous Si-based materials. The potential of H-terminated mesoporous silicon in photocatalytic degradation of methyl orange has been assessed and the importance of mass diffusion within the porous structure has been highlighted as largely regulated by the pore properties. The mechanistic study of the degradation behaviour toward methyl orange has revealed the significant roles of the surface hydrides with or without visible light irradiation. And the exploitable reduction power of Si-H bond by the action of external light and other photoactive semiconductors also suggests a potential research direction in tuning the activity to purposely guide a photochemical/chemical transformation.

6.2 Future work

Considering the current progress of this work, some recommendations for future work are:

- To conduct a more detailed product analysis and intermediates generated through the degradation process of methyl orange over H-terminated mesoporous silicon with or without external visible light illumination by employing sophisticated analytical tools, such as mass spectrometry.
- To monitor the electron-transfer processes that occur under visible light irradiation by using electrochemical methods for a direct observation of the charge separation, migration and recombination on mesoporous silicon and mpSi/g-C_3N_4 NSs composite.
- To understand the effect of photoinduced charge carriers on the reactivity of Si-H bond on the surface of mesoporous silicon by *in situ* characterisation technique, such as solid state NMR to be used on the irradiated sample.
- To exploit H-terminated mesoporous silicon in photoreduction of carbon dioxide,[1-2] organic compounds, metal ions etc. by making use of the abundant surface hydrides and seeking for possible site selectivity.
- To further explore the composite structure of mesoporous silicon and graphitic carbon nitride nanosheets and investigate the interfacial interaction between these two phases to guide the design of new structures.

More broadly, future exploration could be directed to:

- Expanding the applications of mesoporous silicon to other potential areas.
    - As anode material to be used in lithium-ion batteries making use of the exceedingly high theoretical energy capacity of Si (ca. 4200 mA h g^{-1}) and the large surface area and porous structure to accommodate the volume expansion during charging and discharging processes known to cause the rapid decay problem.[3-11]
    - As drug carrier or imaging agent to be used in biomedical applications making use of the unique structural properties, light-emitting ability, biocompatibility and biodegradability.[12-21]

- Developing mesoporous silicon-based heterostructures with other photoactive materials.[22-24]
- Creating novel structured porous silicon by bottom-up magnesiothermic reduction.[4, 25]

6.3 References

1. Sun, W.; Qian, C.; He, L.; Ghuman, K. K.; Wong, A. P. Y.; Jia, J.; Jelle, A. A.; O'Brien, P. G.; Reyes, L. M.; Wood, T. E.; Helmy, A. S.; Mims, C. A.; Singh, C. V.; Ozin, G. A., Heterogeneous reduction of carbon dioxide by hydride-terminated silicon nanocrystals. *Nat. Commun.* **2016,** *7*, 12553.

2. Dasog, M.; Kraus, S.; Sinelnikov, R.; Veinot, J. G. C.; Rieger, B., CO_2 to methanol conversion using hydride terminated porous silicon nanoparticles. *Chem. Commun.* **2017,** *53* (21), 3114-3117.

3. Liu, L. H.; Lyu, J.; Li, T. H.; Zhao, T. K., Well-constructed silicon-based materials as high-performance lithium-ion battery anodes. *Nanoscale* **2016,** *8* (2), 701-722.

4. Liang, J.; Li, X.; Hou, Z.; Zhang, W.; Zhu, Y.; Qian, Y., A deep reduction and partial oxidation strategy for fabrication of mesoporous Si anode for lithium ion batteries. *ACS Nano* **2016,** *10* (2), 2295-2304.

5. Du, F. H.; Wang, K. X.; Chen, J. S., Strategies to succeed in improving the lithium-ion storage properties of silicon nanomaterials. *J. Mater. Chem. A* **2016,** *4* (1), 32-50.

6. Yersak, T. A.; Shin, J.; Wang, Z.; Estrada, D.; Whiteley, J.; Lee, S. H.; Sailor, M. J.; Meng, Y. S., Preparation of mesoporous Si@PAN electrodes for Li-ion batteries via the in-situ polymerization of PAN. *ECS Electrochem. Lett.* **2015,** *4* (3), A33-A36.

7. Westover, A. S.; Freudiger, D.; Gani, Z. S.; Share, K.; Oakes, L.; Carter, R. E.; Pint, C. L., On-chip high power porous silicon lithium ion batteries with stable capacity over 10,000 cycles. *Nanoscale* **2015,** *7* (1), 98-103.

8. Han, X.; Chen, H.; Liu, J.; Liu, H.; Wang, P.; Huang, K.; Li, C.; Chen, S.; Yang, Y., A peanut shell inspired scalable synthesis of three-dimensional carbon coated porous silicon particles as an anode for lithium-ion batteries. *Electrochim. Acta* **2015,** *156*, 11-19.

9. Li, X.; Gu, M.; Hu, S.; Kennard, R.; Yan, P.; Chen, X.; Wang, C.; Sailor, M. J.; Zhang, J. G.; Liu, J., Mesoporous silicon sponge as an anti-pulverization structure for high-performance lithium-ion battery anodes. *Nat. Commun.* **2014,** *5*, 4105.

10. Ren, W.; Wang, Y.; Zhang, Z.; Tan, Q.; Zhong, Z.; Su, F., Carbon-coated porous silicon composites as high performance Li-ion battery anode materials: can the production process be cheaper and greener? *J. Mater. Chem. A* **2016,** *4* (2), 552-560.

11. Su, X.; Wu, Q. L.; Li, J. C.; Xiao, X. C.; Lott, A.; Lu, W. Q.; Sheldon, B. W.; Wu, J., Silicon-based nanomaterials for lithium-ion batteries: a review. *Adv. Energy Mater.* **2014,** *4* (1), 1300882.

12. Venuta, A.; Wolfram, J.; Shen, H.; Ferrari, M., Post-nano strategies for drug delivery: multistage porous silicon microvectors. *J. Mater. Chem. B* **2017,** *5* (2), 207-219.

13. Stojanovic, V.; Cunin, F.; Durand, J. O.; Garcia, M.; Gary-Bobo, M., Potential of porous silicon nanoparticles as an emerging platform for cancer theranostics. *J. Mater. Chem. B* **2016,** *4* (44), 7050-7059.

14. McInnes, S. J.; Michl, T. D.; Delalat, B.; Al-Bataineh, S. A.; Coad, B. R.; Vasilev, K.; Griesser, H. J.; Voelcker, N. H., "Thunderstruck": plasma-polymer-coated porous silicon microparticles as a controlled drug delivery system. *ACS Appl. Mater. Interfaces* **2016,** *8* (7), 4467-4476.

15. Wu, C. C.; Hu, Y.; Miller, M.; Aroian, R. V.; Sailor, M. J., Protection and delivery of anthelmintic protein Cry5B to nematodes using mesoporous silicon particles. *ACS Nano* **2015,** *9* (6), 6158-6167.

16. Wang, M.; Hartman, P. S.; Loni, A.; Canham, L. T.; Bodiford, N.; Coffer, J. L., Influence of surface chemistry on the release of an antibacterial drug from nanostructured porous silicon. *Langmuir* **2015,** *31* (22), 6179-6185.

17. Tzur-Balter, A.; Shatsberg, Z.; Beckerman, M.; Segal, E.; Artzi, N., Mechanism of erosion of nanostructured porous silicon drug carriers in neoplastic tissues. *Nat. Commun.* **2015,** *6*, 6208.

18. Herranz-Blanco, B.; Arriaga, L. R.; Makila, E.; Correia, A.; Shrestha, N.; Mirza, S.; Weitz, D. A.; Salonen, J.; Hirvonen, J.; Santos, H. A., Microfluidic assembly of multistage porous silicon-lipid vesicles for controlled drug release. *Lab Chip* **2014,** *14* (6), 1083-1086.

19. Savage, D. J.; Liu, X.; Curley, S. A.; Ferrari, M.; Serda, R. E., Porous silicon advances in drug delivery and immunotherapy. *Curr. Opin. Pharmacol.* **2013,** *13* (5), 834-841.

20. Gu, L.; Hall, D. J.; Qin, Z.; Anglin, E.; Joo, J.; Mooney, D. J.; Howell, S. B.; Sailor, M. J., In vivo time-gated fluorescence imaging with biodegradable luminescent porous silicon nanoparticles. *Nat. Commun.* **2013,** *4*, 2326.

21. Gu, L.; Park, J. H.; Duong, K. H.; Ruoslahti, E.; Sailor, M. J., Magnetic luminescent porous silicon microparticles for localized delivery of molecular drug payloads. *Small* **2010,** *6* (22), 2546-2552.

22. Sampath, S.; Maydannik, P.; Ivanova, T.; Shestakova, M.; Homola, T.; Bryukvin, A.; Sillanpää, M.; Nagumothu, R.; Alagan, V., Efficient solar photocatalytic activity of TiO_2 coated nano-porous silicon by atomic layer deposition. *Superlattices Microstruct.* **2016,** *97*, 155-166.

23. Chandrasekaran, S.; Macdonald, T. J.; Mange, Y. J.; Voelcker, N. H.; Nann, T., A quantum dot sensitized catalytic porous silicon photocathode. *J. Mater. Chem. A* **2014,** *2* (25), 9478-9481.

24. Megouda, N.; Cofininier, Y.; Szunerits, S.; Hadjersi, T.; Elkechai, O.; Boukherroub, R., Photocatalytic activity of silicon nanowires under UV and visible light irradiation. *Chem. Commun.* **2011,** *47* (3), 991-993.

25. Zuo, X.; Xia, Y.; Ji, Q.; Gao, X.; Yin, S.; Wang, M.; Wang, X.; Qiu, B.; Wei, A.; Sun, Z.; Liu, Z.; Zhu, J.; Cheng, Y. J., Self-templating construction of 3D hierarchical macro-/mesoporous silicon from 0D silica nanoparticles. *ACS Nano* **2017,** *11* (1), 889-899.

Appendix: list of publications including potential publications

[1] Li, T.; Li, J.; Zhang, Q.; Blazeby, E.; Shang, C.; Xu, H.; Zhang, X.; Chao, Y., Hydrogen-terminated mesoporous silicon monoliths with huge surface area as alternative Si-based visible light-active photocatalysts. *RSC Adv.* **2016,** *6* (75), 71092-71099.

[2] Mechanistic elucidation of the degradation behaviour of hydrogen-terminated mesoporous silicon in dye degradation. In preparation.